A Fundamental Study of Nanostructured Si Anodes for Lithium Ion Batteries

by

Bharat Gattu

Bachelor of Technology, Metallurgical and Materials Engineering, Indian Institute of Technology Roorkee, India, 2006

Master of Science, Materials Science and Engineering, Missouri University of Science & Technology (previously University of Missouri, Rolla), USA, 2009

Submitted to the Graduate Faculty of the

Swanson School of Engineering in partial fulfillment

of the requirements for the degree of

Doctor of Philosophy

University of Pittsburgh

2020

UNIVERSITY OF PITTSBURGH

SWANSON SCHOOL OF ENGINEERING

This dissertation was presented

by

Bharat Gattu

It was defended on

November 5, 2020

and approved by

Dr. Lei Li, Ph.D., Associate Professor, Department of Chemical and Petroleum Engineering, University of Pittsburgh

Dr. Susheng Tan, Ph.D., Associate Professor, Department of Electrical and Computer Engineering, University of Pittsburgh

Dr. Jay F. Whitacre, Ph.D., Professor, Department of Materials Science and Engineering, Carnegie Mellon University

Dissertation Director: Dr. Sachin Velankar, Ph.D., Professor, Department of Chemical and Petroleum Engineering, University of Pittsburgh

A Fundamental Study of Nanostructured Si Anodes for Rechargeable Lithium Ion Batteries

Bharat Gattu, Ph.D.

University of Pittsburgh, 2020

Lithium-ion (Li-ion) batteries have emerged as the flagship, ubiquitous energy storage systems for portable / stationary consumer electronic devices such as video cameras, laptops, mobile phones including the plug-in hybrid as well as in the current models of all electric vehicles (EVs). Despite the commercialization of the first prototype Li-ion battery in 1990 by Sony, commercial Li-ion battery systems currently still employ graphite/carbon having a theoretical capacity of ~372 mAh/g as the anode system. Silicon exhibits a theoretical capacity of ~4200 mAh/g and is explored as a promising anode to replace graphite in LIBs. However, silicon undergoes huge volume expansion (>300%) during lithium alloying / de-alloying resulting, in tremendous crystallographic related phase induced stresses. As a result of these stresses, there is pulverization of the active material in the electrodes resulting in loss of electronic contact with the substrate/current collector resulting in drastic and rapid reduction in capacity and subsequently, the failure of the battery.

In this work, different synthesis approaches (electrodeposition, electroless plating, hydrothermal synthesis, chemical vapor deposition, high energy mechanical milling) for generating nanoscale Si and/or Si composite nanostructures, such as (1) silicon-carbon core-shell (C@Si@C) hollow nanotubes, (2) silicon nanorods and silicon nanoflakes, (3) electrodeposition of silicon thin films and (4) Si/VACNTs directly grown on Cu serving as binder-less system, are discussed. Their electrochemical behavior has been analyzed and correlated to the synthesis process, ensuing structural changes, related structural and microstructural property, degradation

mechanism and finally their performance. The Si anodes were characterized for their structure, microstructure and electrochemical performance (first cycle irreversible loss, specific charge – discharge capacities, fade rate) in Li/Li+ system. Their behavior was correlated to morphology of nanostructures before and after electrochemical cycling, and process parameters employed during the synthesis process. X-Ray diffraction, Raman spectroscopy, SEM/TEM, BET analysis and XPS have been used to characterize the crystallographic structure and composition of these nanostructures before and after electrochemical cycling to confirm the evolution, phase and morphological stability of these nanostructures. Subsequently, effort has been made to analyze and study the electrochemical response in full cell system using LiNMC111 at critical loadings using CC-CV mode of testing.

Table of Contents

List of Tables

List of Figures

Preface

Lithium ion batteries over the past five decades have emerged to be the dominant energy storage systems due to their exceptional gravimetric and volumetric power and energy storage capability. The market of lithium ion batteries is valued at USD 20 – 30 billion with applications in portable electronics, medical devices, military accessories and more recently, in automotive industries (electric vehicles, hybrid electric vehicles, plug – in hybrid electric vehicles) and residential energy management and storage applications. The success of transition to alternate energy sources depends on the development of lithium ion batteries into more compact design with better energy and power capabilities. The major focus of the dissertation is to develop silicon-based anodes as a replacement to carbon anodes both for current and future lithium ion battery chemistries. Additionally, from a manufacturing and environmental perspective, the methods have been focused on existing technologies which can be scaled up and the progression of the work has been streamlined towards the use of environmentally friendly methods and precursors minimizing the economics involved in the development of the silicon systems.

The dissertation introduces the history of lithium ion batteries and briefly describes the evolution of different components over time. Subsequently, the motivation and issues with the silicon anode system and different methodologies have been described. A framework of research and development has been described and a study relating process, process parameters, silicon anode structures, scientific characterization, electrochemical testing and the performance of these anode systems has been conducted to establish process – material structure – material properties – performance relationship. One of the motivations of this dissertation is to merge the material science and engineering framework of material structure – material property relationship with the chemical engineering framework of process parameters – material property.

Modification of the processes and well as process parameters result in formation of various silicon – based structures such as Si nanotubes, nanoflakes, nano rods, thin films as well as composite Si – vertically aligned carbon nanotubes directly on current collector. The material properties of the Si anode resulting from the change in these process parameters vary from amorphous to nano crystalline to single crystal along with the change in morphology, architectural dimensions (such as the wall thickness), composition of the silicon, etc. These variation in the Si anode material reflect in the electrochemical performance parameters such as first cycle irreversible loss, immediate initial fade rate, long term fade rate, gravimetric specific capacities.

Different methodologies for the coin cell testing have been developed and described with an initial analysis for the performance of full cell system (LiNMC – silicon) has been conducted. The dissertation ventures into engineering design and full cell testing with a focus on the effect of areal loading, areal capacity, N/P ratio on the phenomenon of Li reaction with active anode (silicon, carbon, etc) and Li plating occurring in a full cell under constant current – constant voltage mode at different current rates. The appendix sections enlist and describe the design, development and performance of carbon based electrodes for stabilized Li metal plating followed by hybrid solid state ceramic electrolyte system based on enhanced ionic conductivity of Li ions due to low activation energy for surface migration making them feasible for room temperature operation.

Acknowledgements

I am very grateful to Dr. Susan Fullerton for guiding and supporting me through my PhD thesis. I would also like to express my gratitude to Nanomaterials for Energy Conversion and Storage Technologies (NECST, previously Kumta Lab) for the equipment, material support and electrochemical data acquisition and analysis support. Additionally, I am grateful for the scientific and equipment discussions with Dr. Rigved Epur during initial stages of my induction in the PhD program and NECST laboratory which have assisted me during my PhD work as well as research assistant at NECST laboratory. I acknowledge the interactions with community of life support technicians, supervisors, divers and hands on training from technicians at United Divers Pvt. Ltd and United Subsea Engineering Pvt. Ltd. during my previous work / entrepreneurial venture due to which I was able to modify / handle / maintain minor small scale equipment and their components available at NECST lab (such as glove boxes, CVD reactors, sputtering, installation of inert atmosphere pouch cell fabrication, plumbing, electrical, electronics, etc.) facilitating my contribution to NECST lab / Kumta Lab. I am very thankful for NECST lab, Electrochemical Society and Department of Energy for the support and allowing presentation of research at various meetings and conferences giving me the opportunity to interact with other experts in the research field. I am also thankful for Chemical Engineering seminar which allowed me to interact with Dr. Paresh Vasandani which lead to the repair and upgradation of the electrospinning setup at NECST lab / Kumta lab which was damaged trying to execute the ideas of the lab supervisor. I am thankful to NECST laboratory supervisor/manager and previous advisor, Dr. Prashant N Kumta for equipment support during my PhD program.

I would like to thank my advisor Dr. Susan Fullerton along with Dr. Lei Li, Dr. Susheng Tan, Dr. Jay Whitacre and Dr. Sachin Velankar for their support, discussions and feedback during my PhD program and dissertation both as a part of Department of Chemical engineering / NFCF as well as a part of my PhD committee. Special thanks to Dr. Ramalinga Kuruba and other members Dr. Moni K. Datta, Dr. Abhijit Roy and Dr. Oleg Velikokhatnyi for inputs on paper and being co-authors in various publications during my PhD. I would further like to extend my thanks to all the post-docs, graduate students, technicians, and administrative assistants at University of Pittsburgh for their support and making University of Pittsburgh a great place to work. I am grateful to all the graduate students (especially Dr. Rigved Epur, Dr. Prashant Jampani, Dr. Sameer Damle, Dr. Umang Desai, Dr. Pavithra Murugavel Shanti, Shrinath Ghadge, Brian Austin Day, Piyathip Thanapisithukul) in Swanson School of Engineering who have made my work life at University of Pittsburgh amazing. Additionally, I am thankful to the Chemical Engineering graduate students (induction year 2012) for the interactions/discussions during the beginning of the PhD program.

My special thanks to Dr. Rigved for accepting my assistance in CVD / PECVD operation, developing the electrodeposition set up and Dr. Prashant Jampani for setting up the CNT reactor during his PhD work which later on assisted me to assemble the system during my PhD work after the relocation of NECST lab to Energy Innovation Center. I would also like to acknowledge interactions with J. R. Gaines, Jason Hrebik from Kurt J Lesker and Tracy Watts from Anatech USA to successfully integrate the Hummer Sputtering Systems with Torus dual target magnetron sputtering; Dr. Scott Speakman and Ron Amodeo from Malvern Panalytical to try develop the in - situ transmission and reflection mode characterization of lithium ion batteries in large format.

I am thankful for the knowledge and outlook I gained from the courses at Department of Chemical and Petroleum Engineering and other courses from Department of Mechanical Engineering and Materials Science (MEMS), Department of Physics and Astronomy which have helped me in my PhD work. Additionally, I would acknowledge Department of Bioengineering at University of Pittsburgh for giving me the opportunity to directly / indirectly contribute to various project proposals resulting in awards / contracts / projects from Department of Energy in the field of lithium sulfur and Li metal anode systems. I would also acknowledge Department of Energy for giving me the opportunity to develop Li metal - based system along with establishing a protocol, experimental methodology / tools for development and demonstration of Li metal anode system for Department of Energy, enabling their vision and research.

I am indebted to my parents and family for their unconditional love, emotional support and encouragement throughout my graduate studies. I would express my deep sense of appreciation to my friends for their guidance in equipment design, repair and upgradation for NECST Lab which have led to the development of technology and systems.

1.0 Introduction

1.1 Motivation

Energy is the most essential component for the survival of mankind and has played a vital role in the development of human civilization and race for centuries. Catering the requirements of the growing global population and the extensive industrialization of worldwide nations resulting in the environmental degradation requires tapping energy resources in an efficient, environmentally favorable, affordable and sustainable manner. For example, approximately four fifths of the United States energy consumption is derived, maintained and sustained from various fossil fuels such as natural gas, petroleum and coal. The dependency on these conventional non – renewable energy sources have resulted in their depletion and near future extinction along with excessive CO_2 generation, increased carbon footprint leading to adverse consequences in nature, such as global warming, climate change, desertification, extinction of different species of flora and fauna. Alternatively, harnessing renewable clean energy sources similar to wind, solar, water, oceanogenic and geothermal heat are in great demand which are replenished naturally and can sustained indefinitely if the infrastructure is deployed in an efficient and prudent way at different geographical locations based on long term sustainability model. However, majority of these sources are immobile and geographically constrained within their region of availability, thus, limiting their direct efficient application in routine activities and hence, the energy is required to be transported in the form of electricity and stored to result in practical use. Various electrochemical energy storage devices such as capacitors (super, ultra) and batteries which convert chemical / electrochemical energy directly to electricity and vice – versa and fuel cells which convert electrochemical energy directly to electricity, offer practical solution for a wide range of applications such as electric vehicles, portable electronics, grid energy storage with potential applications in defense and space exploration. A Ragone plot (**Figure 1**) comparing the energy and power performance capabilities of these energy storage systems indicate the ability of capacitors for use in high power applications while fuel cells to be employed in massive energy generation devices.[1-2] Batteries, on the other end of spectrum, show intermediate range performance / characteristics enabling applications in a broader market segments such as portable electronics and especially, in the transportation sector for both ICE (internal combustion engine) and electric vehicles.

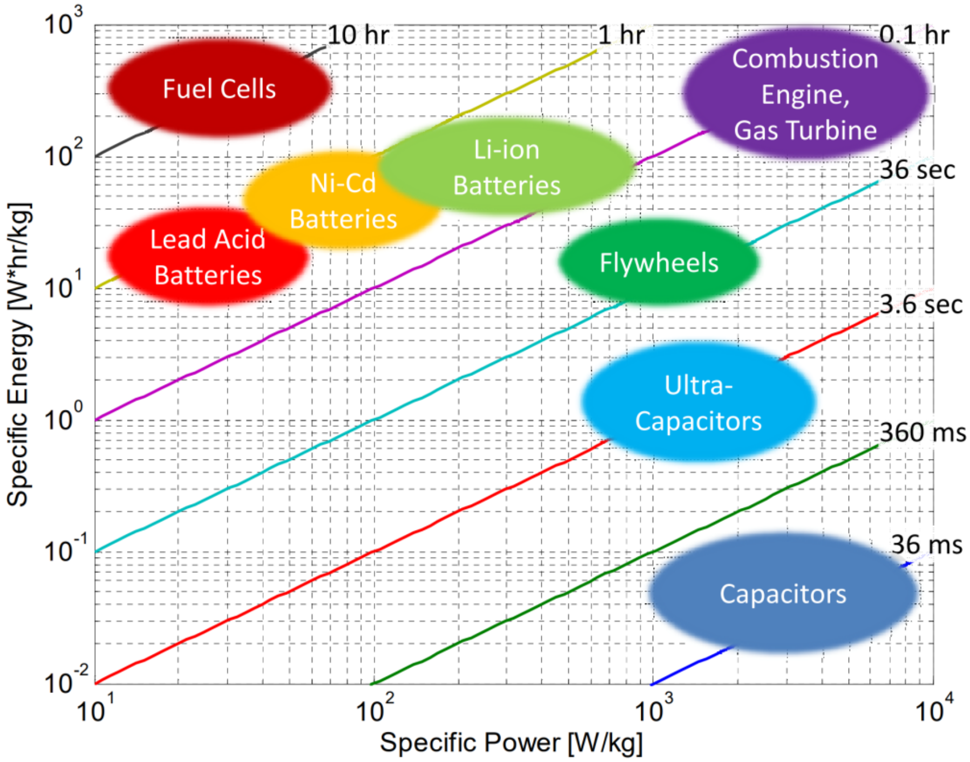

Figure 1 Ragone plot indicating performance domains of different electrochemical energy storage systems compared to traditional internal combustion gas engine

Lithium-ion batteries (LIBs), due to their high energy density and compact design, have become the popular choice for portable energy storage products, among the various battery systems which have been developed since Alessandro Volta invented the first battery in the early 19th century. Sony Corporation has been the front runner of energy storage devices for consumer electricals / electronics (cell/smart phones, laptops, portable digital assistants (PDAs), camcorders, digital cameras used in recording and communication industry) since their commercialization of the first LIB in 1990. Many improvements in terms of storage capacity, long term stability / cycle life and shelf life and safety, since the market induction has facilitated the use of LIBs in power tools and more recently, in transportation sector as Electric Vehicles (EVs) and Plug in Hybrid Electric Vehicles (PHEVs). Currently LIBs employ, $LiCoO_2$ / $LiMn_2O_4$ and their variants (with theoretical capacity of 150 - 200 mAh/g) as the cathode and graphite (with theoretical capacity of ~372 mAh/g) as the anode, resulting in a full cell level energy densities of 100 - 250 Wh/kg. Despite the improvements over time, the ever-growing demands of the EV/PHEV transportation market and the growing Asian economies demands cost – effective material development with improved rate capabilities, cyclability with high gravimetric / volumetric energy densities along with meeting the power densities.

Silicon reacts with lithium at electrode potentials (vs. Li^+/Li) close to that of graphite to form a sequence of lithium – silicon alloys leading to the formation of highly lithiated phase of $Li_{22}Si_5$, pushing it as a candidate for replacing graphite anode with theoretical charge storage capacity (~4200 mAh/g) ten times that of graphite / carbon. However, the evolution of lithiated Li - Si phase with high gravimetric content of lithium induces a huge volumetric expansion (>300%) of Si lattice, eventually causing pulverization of the material on subsequent de-alloying. This mechanical failure from continuous charging / discharging results in loss of intra – electrode and electrode – current collector electrical contact, finally leading to rapid capacity fade followed by complete cell failure.

Recent research efforts have witnessed development of several approaches to address the problem of mechanical failure which include the use of nanosized silicon particles ($\phi < 200$ nm), strain engineered 1-D dimensional nanostructures, amorphous silicon composites and active-inactive composites. [3-13] Silicon in amorphous and nanostructured forms sustain mechanical integrity free of pulverization as a result of the reduced atom to defect ratio within a nano-sized particle / grain and the 'free volume' availability due to disordered nature of amorphous silicon, resulting in higher cycle life and capacity retention. The constriction of higher atomic density along grain boundaries results in grain boundary sliding preventing fracture of silicon particles and subsequent failure of the system. Furthermore, it is predicted that the absence of long range order and presence of defects in amorphous silicon (*a*-Si), results in homogeneous distribution of both the volumetric changes and strain upon lithium alloying and effect of nucleation and growth of lattice pores and subsequent crack growth and propagation is expected to prevent catastrophic effects when compared to crystalline silicon [9, 14-15]. Hence, the extent of pulverization of the active silicon - based material is significantly reduced, thus, giving rise to enhanced performance, capacity retention and cycling performance.

This dissertation elucidates approaches, studies, methods and analytical techniques to capitalize on these aspects, thus, leading to the evolution of nanostructures of silicon such as amorphous silicon thin films, silicon nanoparticles, nanoflakes, nanorods, hollow silicon nanotubes (h-SiNTs) and Si/vertically aligned carbon nanotube (VACNT) nanostructures from a fundamental perspective along with utilizing commercially viable cost effective and high throughput methods instead of currently reported methods for producing silicon nanoparticles/nanostructures which include laser ablation, laser pyrolysis, high temperature solid state reduction and gas evaporation.[16-20] These nanostructures exhibit good electrochemical properties such as high specific capacity, coulombic efficiency, good cyclability and rate capability. The progression of the study and the development of the Si anode systems has been categorized into different strategies and approaches listed henceforth, which are the specific aims of this work.

APPROACH – I:

Silicon nanotubes (Si-NTs) and hollow silicon nanotubes (h – SiNTs) form attractive stable Si based anode system due to their ability to accommodate huge mechanical strain induced during the discharge - charge mechanism, making them less vulnerable to structural pulverization in LIBs.[13, 21-22] However, most of the reported synthesis methods involve electro-spinning and chemical infiltration which require costly precursors, are characterized by low synthesis yields along the systems show high FIR loss due to the decomposition of electrolyte [13, 22]. In this work high aspect ratio (length to radius ratio) nanowires of MgO were synthesized by hydrothermal route (high pressure reactor) which was used as a substrate/template to uniformly deposit amorphous silicon using low pressure CVD (LPCVD) reactor on the surface of these nanowires to obtain large quantities of silicon nanotubes. The MgO nanowires were then leached in acid medium (HCl) to obtain hollow silicon nanotubes (h-SiNTs) showing a potential for large scale production. Optimization of the h-SiNTs dimensions was further engineered by modifying the process parameters of the CVD deposition, resulting in controlled variation of their geometrical dimensions.

To improve the cyclability, further reduce the FIR loss and to generate a stable SEI layer, the nanotubes were coated with a thin layer of amorphous carbon by the decomposition of ethylene in a CVD based reactor to generate core−shell hollow C@Si@C tubular nanostructure. A understanding of the process/synthesis parameters and their influence on the structural dimensions of the h-SiNTs were characterized. Furthermore, the impact of the dimensions of h-SiNTs and the presence of electrolyte – carbon – silicon interface on the ensuing electrochemical response in Li/Li$^+$ system will also be undertaken to optimize the performance of the core−shell hollow C@Si@C nanotubes.

APPROACH – II:

The sacrificial template outlined in Approach – I is a major limiting factor for the large-scale synthesis of Si nanostructures. Sodium Chloride on the other hand, is commercially abundant, cheap, and environmentally benign material that, when used as a template, provides several advantages over traditional templates such as silica, anodized alumina oxide (AAO), MgO, and ZnO by avoiding the use of harsh reagents (HF, NaOH, HCl) and temperature conditions used to leach the template.

High energy mechanical milling (HEMM) is an industrially used easy and inexpensive technique when compared to high pressure reactor synthesis which can be used to generate scalable quantities of various powders and with reduced particle sizes.[23] Particle size refinement of NaCl was obtained by high energy mechanical milling (HEMM) of commercial NaCl which served as template for chemical vapor deposition of silicon. The effect of the HEMM processing conditions on NaCl particle size and the development of Si nanostructures of different morphologies was investigated and characterized. The Si nanostructures were tested as slurry coated electrodes in a Li/Li+ electrochemical cell and their electrochemical response was analyzed depending on the morphology of the Si nanostructures.

APPROACH – III:

Previously, thin films of amorphous silicon (*a-Si*) developed on copper substrates by radio frequency (RF) magnetron sputtering showed stable electrochemical performance with good capacity retention and high specific capacity [24-26]. However, sputtering suffers from unidirectional deposition / shadow effects which restricts the ability to synthesize nanostructures and has more compatibility for wafer scale production of *a-Si* thin films. Hence, electrodeposition and its variations has been employed to form *a-Si* thin films on copper substrates [27]. Electrochemical reduction of silicon tetrachloride ($SiCl_4$) dissolved in organic solvent was conducted to develop amorphous silicon (*a*-Si) thin films directly on Cu foil. The system provides binder-less approach capable of producing amorphous silicon thin films with the possible ability to produce *a*-Si at a rate of 1 – 3 $mg/cm^2/hour$ to match industrial scale requirements required to generate $3mAhcm^{-2}$ capacity electrodes [28]. Pulsed current electrodeposition (PED) technique was employed to develop Si thin films on Cu foil and the effect of various frequencies of the pulsing cycle on the morphology of *a*-Si thin film deposits on Cu foil and their performance in LIB are studied. The composition and morphology of the thin films thereby altered with the change in the frequency which correspondingly, influenced their performance in the lithium ion batteries.

APPROACH – IV: Carbon nanotubes (CNTs) due to their exceptional mechanical and electrical properties serve as good substrate for Li active materials. [29-30] Composite nanostructures with multiwalled carbon nanotubes (MWCNTs) and amorphous silicon have previously been developed using a floating catalyst chemical vapor deposition (FCCVD) approach [31] with the CNTs acting as mechanically stable support system to accommodate the mechanical strain arising from silicon and serve as direct electrical pathway to improve charge transport. However, in an effort to replace the CVD technique in Approach – I for a much simpler technique, Si electrodeposition was used to generate this nano composite electrode architecture without the use of binder.

Electroless Ni plating was employed to develop a uniform coating of Ni on Cu foils following which vertically aligned carbon nanotubes (VACNTs) were grown in a chemical vapor deposition (CVD) reactor using a vaporizable liquid-based carbon precursor and an iron - based catalyst. Silicon was then electrodeposited on these VACNTs by pulse current electrodeposition technique outlined in Approach – III to generate Si/CNT core shell nanostructures directly on a conducting substrate which was used as a binder less electrode without any additives and tested in a Li/Li^+ electrochemical cell and their electrochemical performance was systematically analyzed. Subsequently, a study on the effect of N/P areal capacity ratio on the behavior / performance of the full cell system has been carried out along with analysis of electrochemical response using LiNMC cathode system.

In this dissertation, synthesis methods such as HEMM, LPCVD, FCCVD, electrodeposition, electroless plating and hydrothermal synthesis and a combination of these processes are utilized to generate different silicon based anode systems along with electrode architecture, consisting of different morphologies of Si as well as an intrinsic mixture of both crystalline and amorphous modifications. These systems exhibit a strain-engineered nanostructure to subside the effects originating from volumetric changes and lattice strains; two major reasons which usually lead to failure of crystalline silicon-based anodes. These engineered electrode architectures and nanostructures demonstrated good specific capacity, high coulombic efficiency, reduced first cycle irreversible loss, along with low fade rate exhibiting possible application in commercial LIBs as an alternative to graphite-based anodes.

1.2 Background

1.2.1 Lithium-ion Battery (LIB)

A lithium-ion battery (LIB) is a set of electrochemical cells where lithium ions (Li^+) shuttle between the positive and negative electrodes as a part of the discharging and charging processes, respectively, connected either in parallel or in series. LIBs currently dominate the battery market owing to the high overall cell voltage and specific capacity, with other competitive systems being primary alkaline ($Zn\text{-}MnO_2$) and lead acid batteries. Lithium was used in primary batteries before the commercialization and utilization of rechargeable Li-ion systems in the energy storage market. Primary Li batteries electrolyte consist of lithium perchlorate ($LiClO_4$) dissolved in propylene carbonate (PC) solvent and lithium metal as the anode. The history of lithium-ion batteries started in 1962. The first battery was a battery that could not be recharged after the initial discharging (primary battery). The materials were lithium for the negative electrode and manganese dioxide for the positive electrode. They were first developed in the 1970's by Sanyo ($Li\text{-}MnO_2$, 1975) and Matsushita ($Li\text{-}CFx$, 1973) which were employed dominantly in artificial pacemakers, cameras, LED-fishing boats and portable memory storage applications. Li metal-based batteries (LMBs) were primary in nature and eventually discarded after single use when the chemical energy was released complete as electrical energy as a result of the electrochemical reactions. Hence, considerable attention was focused towards developing battery chemistries and materials with rechargeable capabilities to extend the life by making them reusable. Mobil Energy developed the first rechargeable battery (secondary battery) in 1985. This battery was based on lithium (negative electrode) and molybdenum sulfide (positive electrode). However, its design exhibited safety problems due to the lithium on the negative electrode and development of Li metal based rechargeable systems encountered several hindrances due to the thermal instability upon cycling resulting in melting of lithium which set forth violent reactions leading to issues with their safe operation. However, Li-ion based batteries were found to be exhibit more safety during operation, due to lithium ions (Li^+) shuttle between and into the positive and negative electrodes during discharging or charging processes, respectively. LIBs lead the energy storage market, due to this fundamental difference and safety advantage compared to LMBs, in addition to their high specific capacity and overall cell voltage compared to other systems such primary alkaline ($Zn\text{-}MnO_2$) and as lead acid batteries. The primary alkaline batteries contain manganese oxide (MnO_2) and zinc (Zn) metal as the positive and negative electrodes, respectively and are used in domestic electronics such as radios, torch lights, portable electronic devices, music players, etc. Oxidation of Zn results in formation of zinc oxide (ZnO) and MnO_2 simultaneously, reduces to form Mn_2O_3 while the name, alkaline batteries is derived due to the use of potassium hydroxide as the electrolyte. Lead acid batteries consist of positive and negative electrodes made of lead oxide (PbO_2) and lead (Pb), respectively. The system is subject to redox reactions leading to the formation of sulfate ($PbSO_4$) during discharge process on both the electrodes, while the recharge process involves $PbSO_4$ reduction to form elemental lead (Pb) and $PbSO_4$ is oxidized to form PbO_2 at negative and positive electrodes, respectively.

1.2.2 Rechargeable/Secondary Lithium-ion Batteries

The first generation rechargeable LIBs consisted of titanium disulfide (TiS_2) as cathode and Li metal anode giving an energy density of ~480 Wh/kg [32]. Subsequently, several other chemistries comprising of different cathodes (MoS_2, $NbSe_3$, conducting polymers and vanadium oxide) and Li metal as anode were developed [33]. Various rechargeable LMB systems that were developed in late 20th century (1970 – 1990) is provided in Table 1.[33] However, pure *Li* metal develops dendritic structures on repeated cycling posing safety and fire hazard issues triggered by internal short circuit and thermal run away.[34]

Table 1: Different secondary lithium based batteries developed during late 20th century [33]

System	**Voltage**	**Wh/L**	**Wh/kg**	**Company**
$Ali/LiAlCl_4\text{-}SO_2/C$	3.2	208	63	’81-85 Duracell
$Li/CDMO(Li_xMnO_2)$	3	-	-	’89 Sanyo
$Li/Li_{0.3}MnO_2$	3	140	50	’89 Tadiran
Li/MoS_2	1.8	140	52	’97 MoLi
$Li/NbSe_3$	2	250	95	’83-’86 Bell Lab
Li/TiS_2	2.1	280	130	‘78 Exxon
Li/V_2O_5	1.5	40	10	’89 Tohsiba
Li/VO_x	3.2	300	200	’90 HydroQuebec
LiAl/Polyacene	3	-	-	’91 Kanebo/Seiko
LiAl/Polyaniline	3	180	-	’87 Bridgestone
LiAl/Polypyrolle	3	180	-	’89 Kanebo
$LiAl/TiS_2$				’79 Hitachi

Efforts to resolve dendrite issue lead to the development of an alloy made from *Li* and *Al* as anode instead of pure Li metal. This alloy improved the safety of battery, but the poor mechanical properties of this alloy hindered its usage in wound cylindrical type battery. Tadiran batteries developed another approach using dioxolane based electrolytes with the battery shut down, as a safety feature, when the cell temperature increased beyond a critical value [35]. In this system, when the cell temperature reached beyond 110°C either due to increase in internal impedance or short circuit caused by dendrite formation, the dioxolane based electrolyte polymerized to form an ionically and electrically insulating barrier. The quest for the replacement of *Li* metal as anode and a material to store *Li* as Li^+ resulted in the concept of lithium-ion (Li-ion) battery and identification of carbon anode in 1980’s.Rocking Chair Electrochemical systems

In 1980's, graphitic layers were used for Li^+ intercalation at low electrode potentials, leading to the development of graphite based anodes to resolve the issue of unstable *Li* dendrite during the recharge of LMBs [36]. Analogous to graphite, lithium based transition metal oxides ($LiMO_2$, $M=Co$, Ni, Mn), especially, $LiCoO_2$, were identified and developed, which showed the ability of reversible extraction of Li^+ at higher potentials giving rise to a higher full cell voltage [37].

The graphical representation of a typical LIB with graphite and transition metal oxide as anode and cathode, respectively, and the reactions during the charge - discharge process is shown in **Figure 2**. The electrons generated from the spontaneous oxidation of Li to form Li^+ from the intercalated graphite layers (LiC_6) during the discharge process, powers the external circuit by providing energy to the energy sink. Correspondingly, the deficient cathode ($Li_{1-x}MO_2$) consumes Li^+ through the electrolyte and the external electrons, forming lithium enriched transitional metal oxide ($LiMO_2$). On the contrary, electrons driven by an energy source from the cathode cause Li^+ to de-intercalate from $LiMO_2$ and, simultaneously, intercalate into the graphitic anode system during the charging process. The reversible Li^+ ionic motion between the electrode hosts inducing the intercalation phenomenon lead to 'rocking chair' type LIBs with a high overall voltage induced by the electrochemical potential difference of the anode and cathode materials. The transfer of the Li^+ between the cathode and anode in these 'rocking chair' cell, is facilitated by an electrically insulating yet ionically conducting electrolyte acting as a medium of Li^+ transport. The initial battery composed of graphite and $LiCoO_2$ as anode and cathode, respectively was commercialized by Sony Corporation, triggering enormous interest in pursuing high energy density cathode and anode materials in LIBs for various applications.

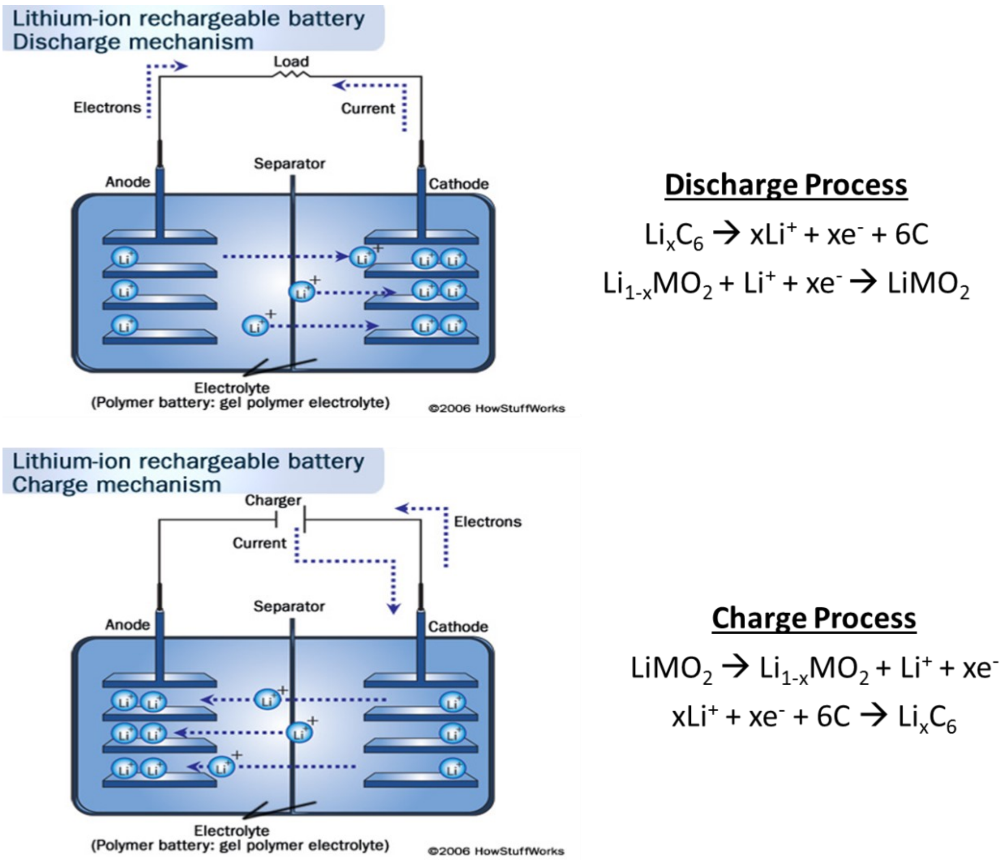

Discharge Process

$$Li_xC_6 \rightarrow xLi^+ + xe^- + 6C$$

$$Li_{1-x}MO_2 + Li^+ + xe^- \rightarrow LiMO_2$$

Charge Process

$$LiMO_2 \rightarrow Li_{1-x}MO_2 + Li^+ + xe^-$$

$$xLi^+ + xe^- + 6C \rightarrow Li_xC_6$$

Figure 2 Graphical representation of a rocking-chair type LIB with $LiMO_2$ (M=Metal) cathode and graphite / carbon anode along with their respective reactions during discharge-charge processes.

1.2.3 Selection Criteria - Theoretical Capacity, Differential Capacity and Energy Density

A thorough characterization and comparison of electrochemical energy storage systems involves several parameters that need complete understanding with theoretical capacity, energy density and differential capacity being the most important parameters for selecting the anode/cathode materials for designing a system for practical applications.

Theoretical Capacity: The total amount of charge (A·h or mA·h or coulombs) that can be stored as transportable Li^+ ions per unit weight (grams, kg) of the material is defined as the specific capacity. The theoretical capacity of an anode/cathode material (mA·h·g^{-1} or mA·h·cm^{-3}) defines the maximum ability of material to store Li^+ during the discharge/charge process.

$$Gravimetric\ Capacity = \frac{N \times F}{M} \left(\frac{Coulomb}{g}\right) = \frac{N \times F}{3.6\ M} \left(\frac{mAh}{g}\right) \quad \ldots\ldots\ldots\ldots\ldots\ldots \text{(1-1)}$$

$$Volumetric\ Capacity = Gravimetric\ (\ Capacity\ \times\ density) = \frac{N \times F}{3.6\ M} \times \rho \left(\frac{mAh}{cm^3}\right) \ldots \text{(1-2)}$$

where N = moles of transportable Li^+ ions (= no. of electrons) per each mole of material

F = Faraday's constant (= 96487 Coulomb or 26.8 Ah)

M = Formula weight of the material (g/mol)

δ= Density of the material (g/cm^3)

Energy density: The total energy which can be utilized during the discharging process or which can be stored during the charging process is defined as the energy density of the battery. The work done / energy required to move a charge (Q) across the potential gradient / potential difference (V_{avg}) inbetween the two electrodes of the battery per unit weight of the system gives the energy density of the battery. The extent of intercalation (x_m) of Li^+ or the amount of Li reacted/alloyed (depending on the system) with the material in the electrode determines the average voltage (V_{avg}). Hence, the energy density of battery is calculated using the formula below:

$$Energy\ Density = \frac{N \times F}{M} \int_0^{x_m} V\, dx \left(\frac{Wh}{kg}\right) \qquad \ldots\ldots\ldots\ldots\ldots\ldots \text{(1-3)}$$

where x_m = the maximum possible reversible degree of insertion of Li^+ or the maximum amount of Li reacting with material.

Differential capacity: During the galvanostatic charge / discharge process of the battery, the differential capacity with respect to voltage (dQ/dV) provides necessary information on different reactions and their respective voltage potentials. The electrochemical reactions are usually controlled by diffusion process of the ions that occur at the electrodes and hence, potentiostatic and galvanostatic cycling tests are employed to determine the electrochemical properties by assembling half-cells or full cells.

$$I = \left(\frac{dQ}{dt}\right) = \left(\frac{dQ}{dV}\right) \times \left(\frac{dV}{dt}\right) \qquad \text{............. (1-4)}$$

In a galvanostatic testing, voltage between electrodes in the cell due to various processes (faradaic and non-faradaic) is monitored by applying a constant current to the system while in a potentiostatic testing condition, a constant voltage is applied between the two electrodes and the current is recorded. Under galvanostatic cycling condition, different voltage plateau are observed at various electrode potentials which indicate the existence of two phases due to Li intercalation (or alloying reaction) due to trivial variation in the voltage with time during the respective reactions following the Gibbs phase rule. Under galvanostatic conditions, change in stored charge with respect to potential (dQ/dV) shows a significant value especially when the reaction induces a phase change thus representing the onset potential, peak potential and completion potential of the respective, reaction. Accordingly, the reaction peaks obtained from the differential capacity (*dQ/dV*) vs. potential provide information on different phenomenon and electrochemical reactions occuring during the process.

1.2.4 Designing of Materials in Battery for Energy Storage

A rechargeable battery operates on the basic principle of conversion of electrical energy to chemical energy during the charge process and vice versa during the discharge process. The energy conversion electrochemical reactions occur at electrode-electrolyte interface with the electrolyte filtering the flow of electrons and allowing for the transport of Li^+ inbetween the electrodes. During the discharge process, oxidization process occurs at the anode leading to generation of electrons. These generated electrons flow from the anode into external circuit, through the energy sink and consumed at the cathode for the reduction reaction. Hence, the anode and cathode are also termed as the negative electrode and positive electrode, respectively. The lithium ions simultaneously move from anode to cathode through the electrolyte. During the charge process, the energy sink is replaced with a power source in the electrical circuit which draws the electrons from the cathode (positive electrode) and drives them to the anode (negative electrode). The anode consumes the electrons due to the reduction reaction and converts the electrical energy to store as chemical energy, for the subsequent discharge process.

When the external electrical circuit is open with no current drawn from the battery, the electrostatic driving force is balanced the opposing chemical driving force on the transportable Li^+ species. The chemical driving force, is calculated using the change in standard – state Gibbs free energy per mole of ions, represented by $\Delta G_r^0 = \mu_a - \mu_c$, where μ_a and μ_c are the thermodynamic chemical activity / potentials of the anode and cathode, respectively.

The electrochemical free energy per mole is given by $\Delta G_r^0 = -n \times F \times E^0$, where n is the number of electrons transferred per mole of reactants/charged species and E^0 is the standard potential difference between the anode and cathode in equilibrium. Hence, the voltage of the system is derived from $\Delta G_r^0 = -n \times F \times E^0 = \mu_a - \mu_c$ and given by the equation $E^0 = \frac{\mu_a - \mu_c}{-n \times F}$, indicating that obtaining higher energy densities requires the battery's overall capacity and cell voltage to be increased. The overall full cell voltage is an intrinsic material property (μ^{Li}, chemical potential) of the cathode and anode materials and difference in the chemical activity potentials should not have a detrimental affect on the stability of the electrolyte. The Fermi energy level (**Figure 3**) of the cathode (E_c) is greater than highest occupied molecular orbitals (HOMO) while that of the anode is lower than lowest unoccupied molecular orbitals (LUMO) of the electrolyte to prevent instantaneous oxidation and reduction at cathode and anode, respectively.[38] Therefore, the difference in free energies (E_a-E_c or eV_{oc}) of cathode and anode materials selected or designed are required to be less than the electrolyte band gap (E_g) for the electrochemical system to be stable.

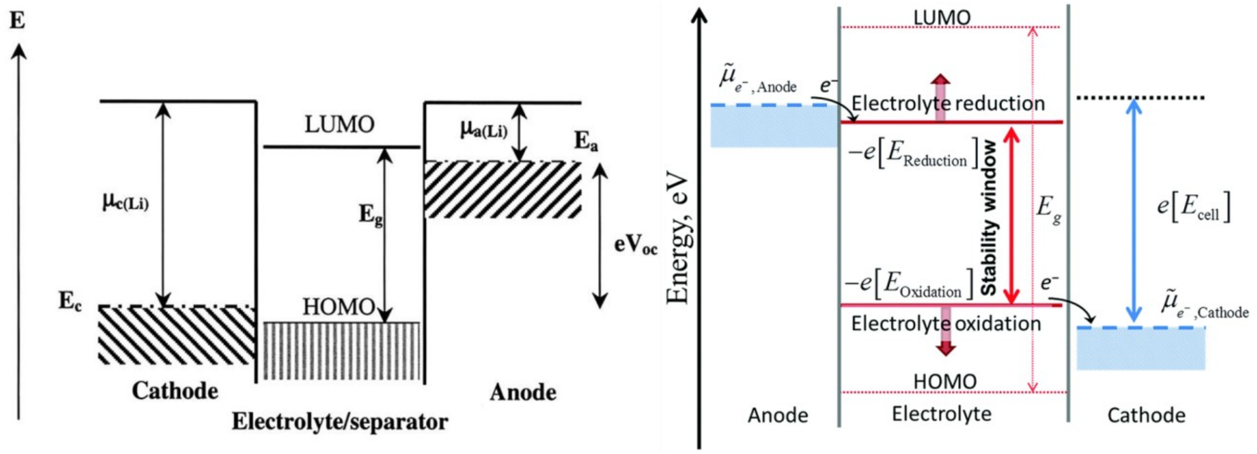

Figure 3 Graphical representation of relative energies of electrolyte, electrodes and interfaces along with energy gap along with appropriate notation [38-39]

The standard potential difference ($E°$) is expressed as the open circuit voltage (E_{oc}) of cell at thermodynamic equilibrium when the system is devoid of any electrochemical activity induced by external sources/sinks of energy. However, the electrolyte resistance to ionic transport both in bulk and at the electrode-electrolyte interface along with the electrical resistance of the cell components contribute to internal cell impedance during practical operation. The internal resistance of the electrochemical system is represented as R_{cell} given by the equations

$$R_{cell} = R_{el} + R_{int} + R_e \qquad \text{……………} \quad (1\text{-}5)$$

where R_{int} is the interfacial charge transfer resistance at the electrode-electrolyte interface,

R_e is the contribution of electrical resistances arising cell components such as electrical interfaces, electrode substrate, additives and active materials,

$$R_{el} = \left(\frac{L_{effective}}{\sigma_{el} \times A_{effective}}\right) \qquad \text{…………} \quad (1\text{-}6)$$

represents the electrolyte resistance between the two electrodes and is determined by effective distance ($L_{effective}$) between the cathode and anode influenced by the thickness of the anode/cathode/separator, the effective area in between the electrodes ($A_{effective}$) influenced by the porosity of the anode/cathode/separator and the ionic conductivity of the electrolyte (σ_{el})

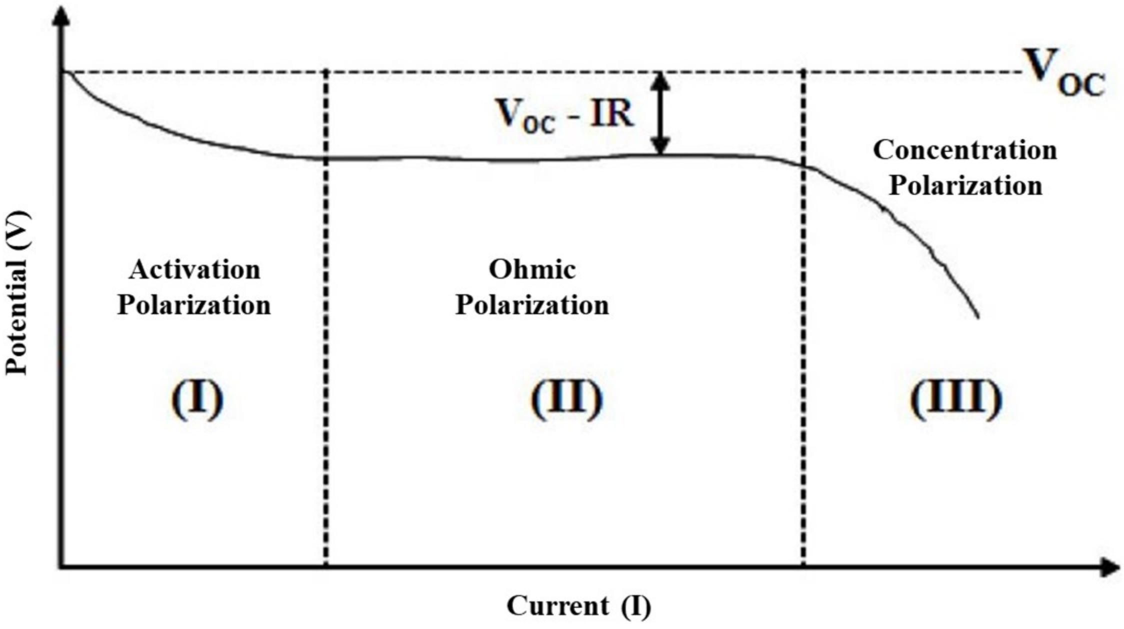

Figure 4 General voltage polarization curve of a battery system

When a resistance load is connected or energy is withdrawn from a battery, there is a decrease in the nominal potential due to the internal impedance/resistance given by $E = E_{oc} - I \times R_{cell}$.

The polarization of an electrochemical cell is determined by the difference in the voltage at thermodynamic equilibrium and the voltage output as a function of current. The polarization curve is given by the voltage-current characteristic curve of the electrochemical cell (**Figure 4**). The kinetic limitations of the electrochemical reactions and other parallel parasitic processes determine the shape of the curve. The slope of the curve can be divided into three distinct regions based on the current applied during the battery operation.

Region-I referred to as activation polarization is marked by a rapid decrease in voltage with the impedances determined by the kinetics involved during the charge-transfer reactions occuring at the electrode/electrolyte interface of the electrodes. Region-I is followed by ohmic polarization (Region – II) marked by a slight change in voltage with impedance contribution from all the cell resistances origination due to various cell components such as current collectors, electrolyte, active materials present in the electrode and the interface of electrode coating - current collector foil. Subsequently, concentration polarization as shown in the region-III induces a rapid decrease in voltage. The electroactive species consumed by the reaction at the electrode-electrolyte interface needs to be continuously replenished from the bulk, a process which suffers from limited diffusion of species at higher current densities. Hence, an electrolyte with good ionic conductivity is required to facilitate the ion transport to the active interface rapidly to sustain the charge transfer reactions. Electrode materials with enhanced electrical conductivity also assist this charge transfer process by facilitating the faster transport of electrons in parallel to ions leading to lower internal impedances.

1.2.5 Prototype / Commercial Configurations of Lithium-Ion Battery

Lithium ion batteries used in energy storage device or the battery pack are designed according to certain dimensions and geometry depending on the application constraints and utility. The commercial Li-ion batteries are available in the formats described as follows:

1.2.5.1 Coin Cell / Button Cell

This format of battery is a small single cell typically 5 to 25 mm (0.197 to 0.984 in) in diameter and 1 to 6 mm (0.039 to 0.236 in) high shaped as a flat cylinder — resembling a button with flat compact geometry with the ability to be stacked to obtain higher voltages. IEC 60086-3 defines an alphanumeric coding system (such as CR 2032), wherein, the first and second letters represent the chemistry (C = Lithium) and geometry (R = round/cylindrical), respectively (**Figure 5**). The first two numbers describe the cell diameter in millimeter (‘20’ = 20mm) followed by the height of the cell (32’=3.2mm), expressed in one - tenths of millimeter. The button cells are used in miniature electrical applications such as wristwatches, biomedical devices, industrial electronic instruments and for material development phase during initial research.

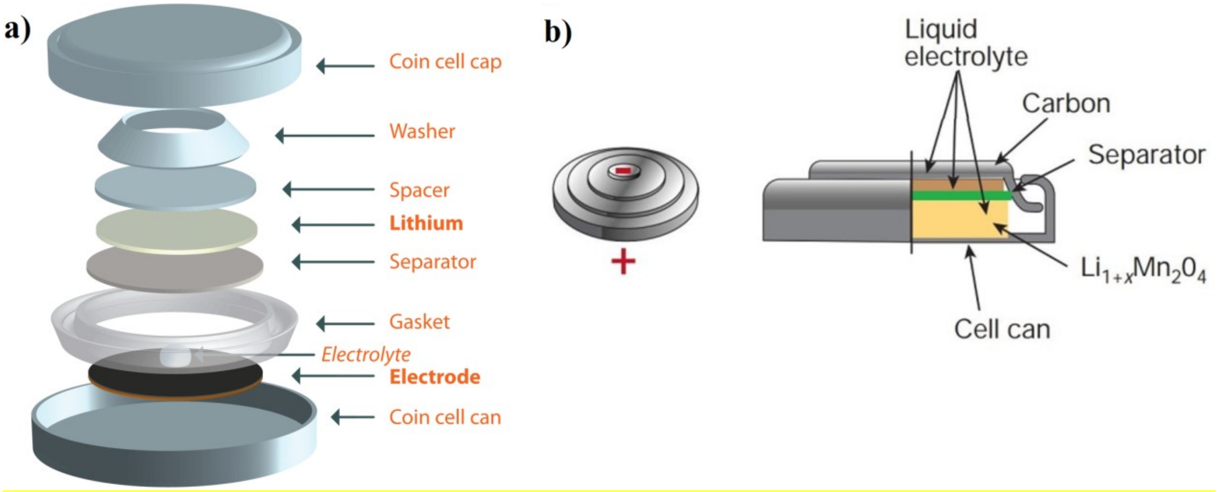

Figure 5 Representation of a) assembly and b) crimped lithium ion coin/button cell [40-41]

1.2.5.2 Prismatic Battery / Cell

The prismatic cell predominantly used in cell phones, PDAs, laptops and tablets is marked by flat geometry with thin and lean pack sizes and foil type polymer laminate case with variable dimensions and product specifications depending on the manufacturer and application without any universal format/nomenclature (**Figure 6**). Despite their advantages such as minimal weight, efficient packaging and elegant design compared to the cylindrical cells, they suffer from lower energy/power densities and mechanical instability.

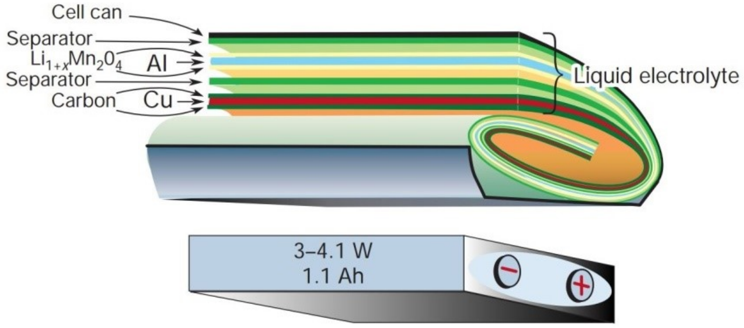

Figure 6 Graphical illustration of a Li-ion prismatic cell [41]

1.2.5.3 Cylindrical Battery / Cell:

Currently, the cylindrical cell is the popularly used format for LIBs due to good mechanical stability and ease of assembly (**Figure 7**). The prevalent cylindrical Li-ion cell in market is 18650, with the first two digits of nomenclature '18' representing the cell diameter in millimeters while the subsequent three digits, for example, '650' represents the cell length (in tenths of a millimeter). These configurations are used in medium sized portable devices, power tools, laptops, wireless communication devices and more recently in electric vehicles (EV/PHEV/HEV).

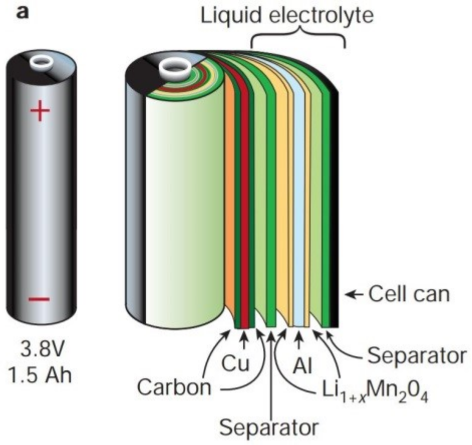

Figure 7 Schematic representation of a cylindrical Li-ion battery (18650, 14500, etc) [41]

1.2.5.4 Stacked Pouch cell

In the pouch cell configuration, the electrodes welded to conductive tabs along with electrolyte are encapsulated in a mechanically flexible and heat sealable foil with the entire system sealed airtight inside a pouch (**Figure 8**) offering a flexible, lightweight and simple solution to battery design.

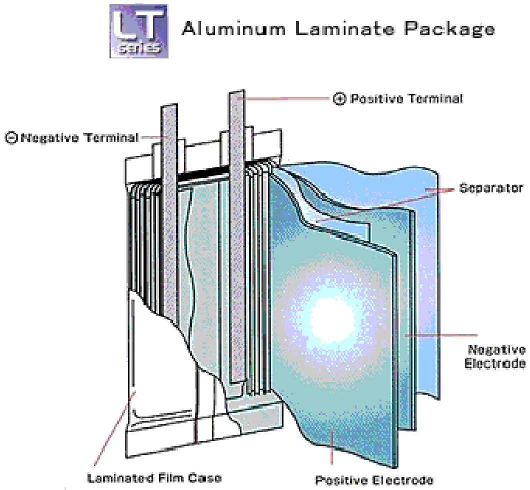

Figure 8 Schematic illustration of a Li-ion pouch cell[42]

These cell configurations are used in military devices, mobile phones and more recently, manufacturing large format battery modules in auto industry, especially for electric vehicles. Some stack pressure is recommended but allowance for swelling must be made. The pouch cells can deliver high load currents, but it performs best under light loading conditions and with moderate charging. Pouch cells exhibit highest gravimetric energy density; however, still require an external means of containment for general structural stability of the battery pack and prevent expansion of the system.

A complete battery pack module used for practical applications consists of different components such as the separators, electrode materials, current collectors, electrolyte, packaging material and battery management system (BMS).

1.2.6 Translational Testing Protocol Development of Lithium-ion Batteries

The development of LIBs from concept to a prototype product requires a translational testing process along with performance analysis at different stages of the product development. The high - level translational testing protocol depicting various stages involved developed by Bharat Gattu at Nanomaterials for Energy Conversion and Storage Technology, Energy Innovation Center, Pittsburgh is shown in **Figure 9**. The initial stages (Stage I and Stage II) of the development focused on the material development involves half-cell testing of anode and cathode systems separately to determine the performance of the systems according to the targeted practical application in a coin cell format. Subsequently, Stage III of the process performed in a single layer pouch cell format is targeted to establish the performance of the system and validate / record the performance of the system before moving to the multi-layer pouch cell prototype testing. A general list of testing scenarios includes rate capability, long term cycling and electrochemical impedance analysis to determine the specific capacity, columbic efficiency, internal impedance and fade rate exhibited by the anode / cathode system at different parameters / variables such a gravimetric current rates, depth of charge / discharge and areal loadings.

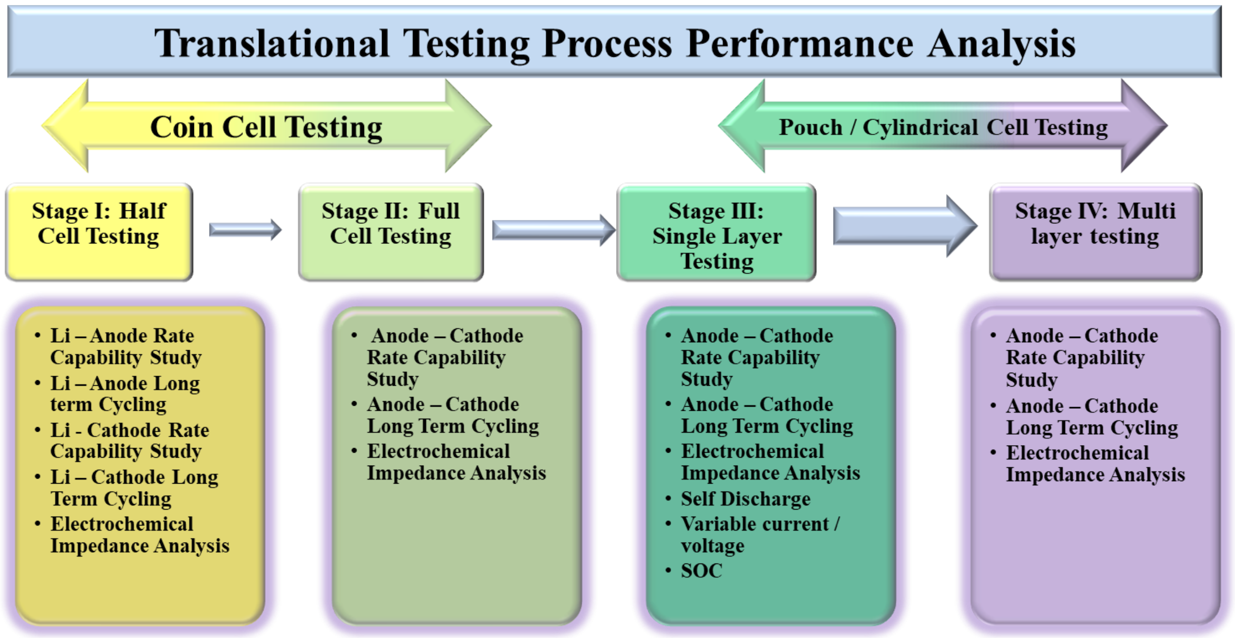

Figure 9 Translational Testing Process for development of Lithium ion batteries

Each and every stage of this translational testing process involves optimization of different components of the electrochemical system at various stages of system development (**Figure 10**). Stage I and Stage II (coin cell testing) involves optimization of different materials, process parameters and variables such as active material system/composition, slurry composition, coating thickness, electrolyte content and formulation, types of binder and additives and areal capacity. Subsequently, an intermediate single layer testing (Stage III) which marks the transition to large format system involves the optimization of uniformity of coating, porosity and packing of the cathode/anode material, calendaring and sealing pressure cycle, electrolyte content, formation cycle, external pressure and performance of the system at different temperatures.

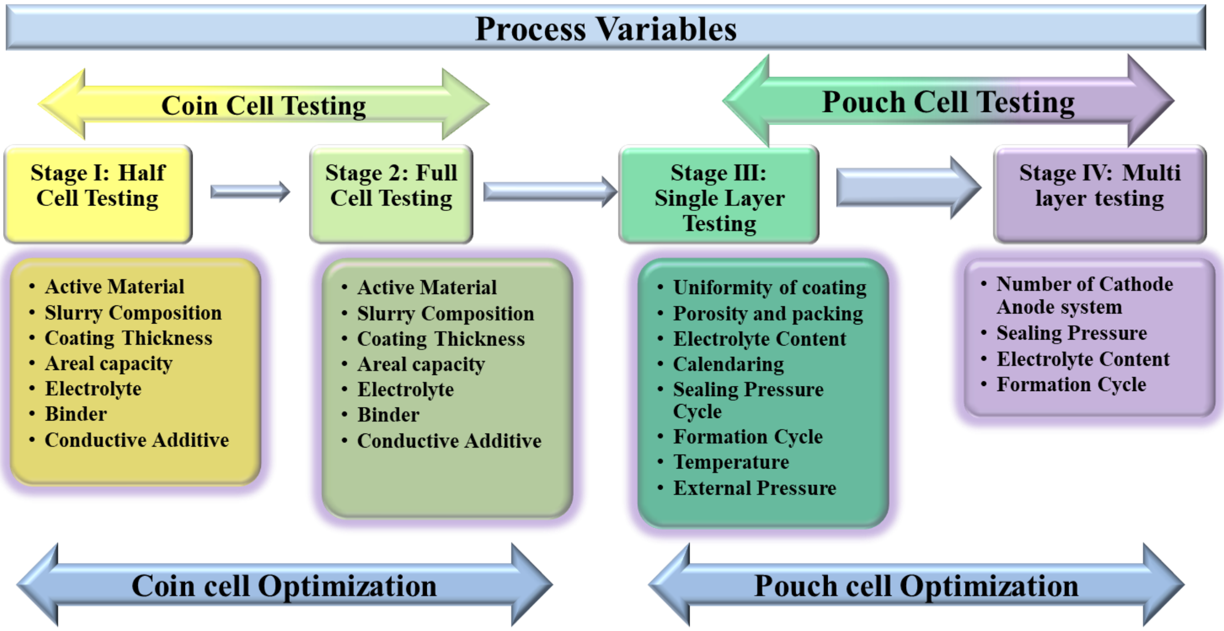

Figure 10 Process Variables at different stages of translational testing protocol developed at NECST.

The multilayer testing (Stage IV) involves optimization of number of cathode / anode systems, the sealing pressure (external/internal), electrolyte content and formation cycles targeted at achieving a desired capacity and voltage of the battery based on application and gravimetric/volumetric energy density of the battery.

An example of the development of the lithium ion battery from coincell to pouch cell using commercial graphite and LiNMC111 has been shown in **Figure 11**. The results indicate replicable transition from coin cell to pouch cell when analyzed in terms of gravimetric capacity when tested at different rate capabilities matching the areal capacities of the anode and cathodes along with electrolyte content. The rate capability tests of graphite and LiNMC111 at different current rates was performed at different stages of the development protocol and finally assembled in a single layer pouch cell.

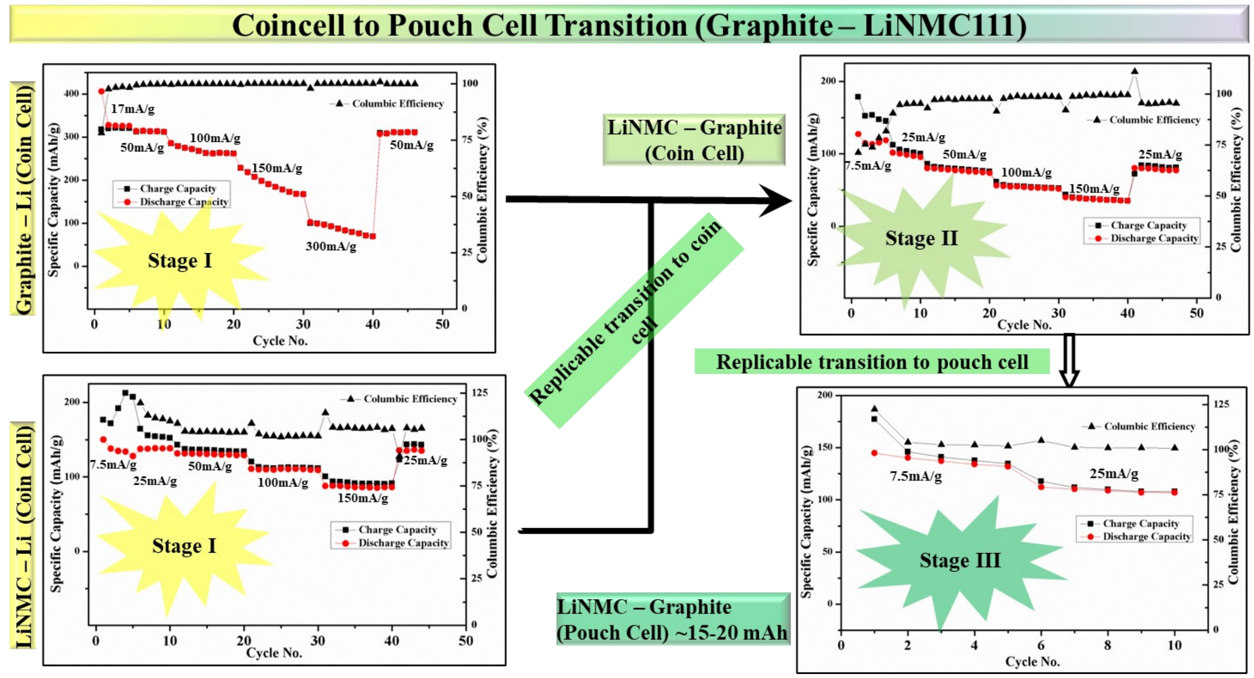

Figure 11 Replicable transition of commercial graphite – LiNMC111 system following the translational testing protocol

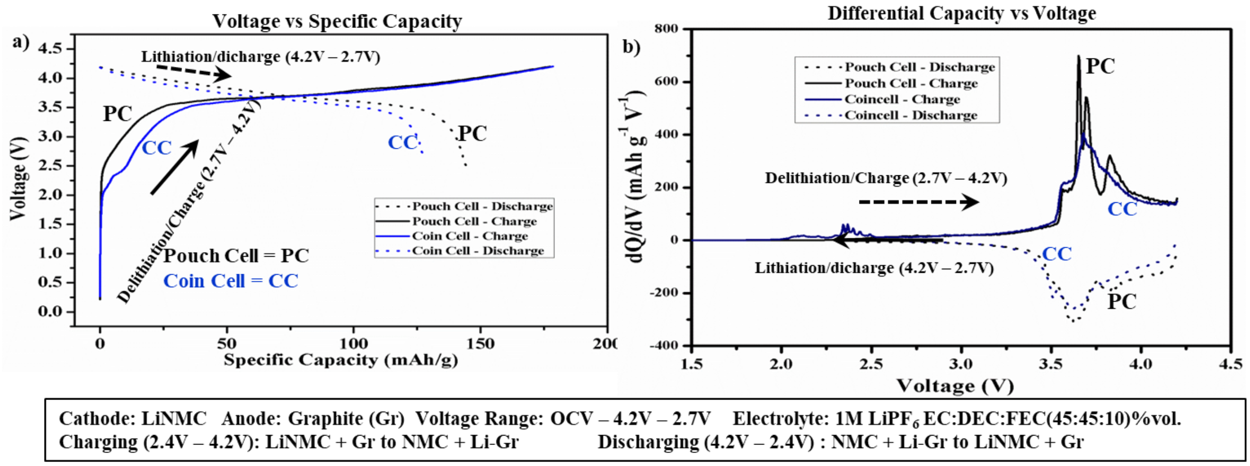

Cathode: LiNMC Anode: Graphite (Gr) Voltage Range: OCV – 4.2V – 2.7V Electrolyte: 1M $LiPF_6$ EC:DEC:FEC(45:45:10)%vol.
Charging (2.4V – 4.2V): LiNMC + Gr to NMC + Li-Gr Discharging (4.2V – 2.4V) : NMC + Li-Gr to LiNMC + Gr

Figure 12 Comparison of electrochemical signal of Stage II and Stage III testing a) Voltage vs Specific capacity plot and b) differential capacity vs voltage profiles indicating the reaction peaks of LiNMC111 – Graphite system

A comparative analysis of the pouch cell and coin cell electrochemical testing (Figure 12) indicates overlap of the voltage vs specific capacity curves as well as the differential capacity vs voltage profile between Stage II and Stage III of the development process. Major reactions are observed between 3.5 – 4V in both pouch cell and coin cell with the pouch cell showing three distinct peaks corresponding to that of graphite intercalation / deintercalation overlapping with LiNMC111 deintercalation / intercalation during the charging / discharging process. The complete initial presentations and data results are available at NECST LAB, Energy Innovation Center at University of Pittsburgh.

1.2.7 Cathode materials for Lithium-ion Batteries

Commercial LIBs consist of layered oxide compounds such as $LiNiO_2$, $LiCoO_2$ and their variations; manganese based spinel oxides – $LiMn_2O_4$; olivine oxide based $LiFePO_4$ materials as cathode materials. which act as a host to accommodate energy in the form of intercalated Li^+ ion species. However, for practical applications requiring high energy density a material must meet the below list of conditions:

i. Increased Gibbs free energy for the lithiation or discharge reaction to exhibit higher full cell voltage to provide more energy stroage density.

ii. Good reversibility and efficient oxidation / reduction ability during electrochemical reaction between Li^+ and transition metal (M^{n+}) ion for high coulombic efficiency.

iii. Reversible intercalation of maximum Li^+ with the material exhibiting improved specific capacity.

iv. Higher coupled diffusion and transport of Li^+ in the host material and optimum electrical conductivity of the host material to exhibit good rate capability.

v. Good structural stability within the operational voltage range along with good chemical stability in different electrolytes used in LIBs.

vi.Lower production cost, environmentally benign, low toxicity and have good recyclability.

The cathode materials developed initially for rechargeable Li-batteries consisted of di and tri chalcogenides such as vanadium diselenide (VSe_2), titanium disulfide (TiS_2), molybdenum disulfide (MoS_2) and niobium triselenide ($NbSe_3$). The crystal lattice of these materials consist of a hexagonal closed pack (HCP) structure with *metallic* ions *(Ti, V, Nb, Mo)* occupying the octahedral sites and the sulfur sheets alternating these layers, forming an ABAB stacking sequence. The weak van der Waals forces hold the individual metal sulfide (TiS_2) sheets together separated by a vacant *gallery space,* which can be occupied by active guest species such as Li^+. This space between the alternating metal sulfide sheets can be occupied by Li^+, enabling reversible intercalation forming a single phase Li_xTiS_2 structure ($0 \leq x \leq 1$), with good cyclability. Exxon employed and commercialized this technology in the form of button cells consisting of TiS_2 cathode and *LiAl* anodes which were used in small electronic devices and wrist watches, during 1977-79. Similar, VSe_2 also exhibits electrochemical activity as cathode material, however, undergoing a two-phase transition behavior forming Li_2VSe_2 [43]. The initial intercalation leads to formation VSe_2 / Li_xVSe_2 two-phase region which are in equilibrium with another two – phase transition region consisting of $LiVSe_2$ and Li_xVSe_2. This process finally results in a two-phase region consisting of $LiVSe_2$ and Li_2VSe_2 as the final reaction product. Despite the formation of multi-phase regions, the octahedral structure of the formed phases undergoes minimum crystal deformation enabling reversible cycling of VSe_2 based cathodes.

MoliEnergy in 1980 commercialized , Group VI sulfides such as MoS_2 which were expected to be inactive for electrochemical insertion, however, have the ability to act as an active cathode material by conversion of molybdenum coordination to octahedral coordination from trigonal prismatic enabling one mole *Li* insertion per mole of MoS_2. The Bell Laboratories identified trichalcogenides (such as $NbSe_3$) as another class of materials, which could be used as cathode materials which reversibly react with lithium to form electrochemically active Li_3NbSe_3.[44] However, it was found that $NbSe_3$, exhibited lower operating voltages, lower rate capability and suffered from major degradation problems[45].

1.2.7.1 Lithium Cobalt Oxide ($LiCoO_2$)

The use of $LiCoO_2$ as a potential cathode material in LIBs was first reported by Goodenough in 1980, which was identified to have a layered structure similar to the earlier developed chalcogenide based cathodes.[37] $LiCoO_2$ exhibits $R\overline{3}m$ structure with the ability to reversibly cycle 0.5 Li per Co could in $Li_{1-x}CoO_2$, giving rise to a theoretical capacity of ~130 mAh/g [37]. The material exhibits a smaller change in the discharge/charge voltage and high operating voltage (3.1-4.2V) associated with high chemical potential of lithium μ^{Li+} that is associated with the $Co^{3+/4+}$ redox couple during the lithium extraction/insertion, establishing it as a potential candidate for practical high energy density cathodes[37]. However, the layered structure of $LiCoO_2$ undergoes crystallographic distortion from hexagonal to monoclinic due to the collapse of the layered stacking along with cobalt dissolution when extracting more lithium (x>0.5) by charging it beyond 4.2 V as shown in Figure 13 [46] [47].

Several approaches have been developed to overcome the challenges of capacity fade and capacity limitation of only half of Li ions to be extracted per mole of $LiCoO_2$ caused by the structural degradation and chemical instability. Coating the $LiCoO_2$ surface with a protective layer of oxides such as Al_2O_3, ZrO_2 and TiO_2 prevents the dissolution of Co, arising from its interaction with acidic species such as HF present in the electrolyte. [48-51] Furthermore, limited natural cobalt sources, high cost and toxicity of cobalt has triggered exploration of other alternative cathode materials exhibiting higher capacity, lower cost and ecological nature.

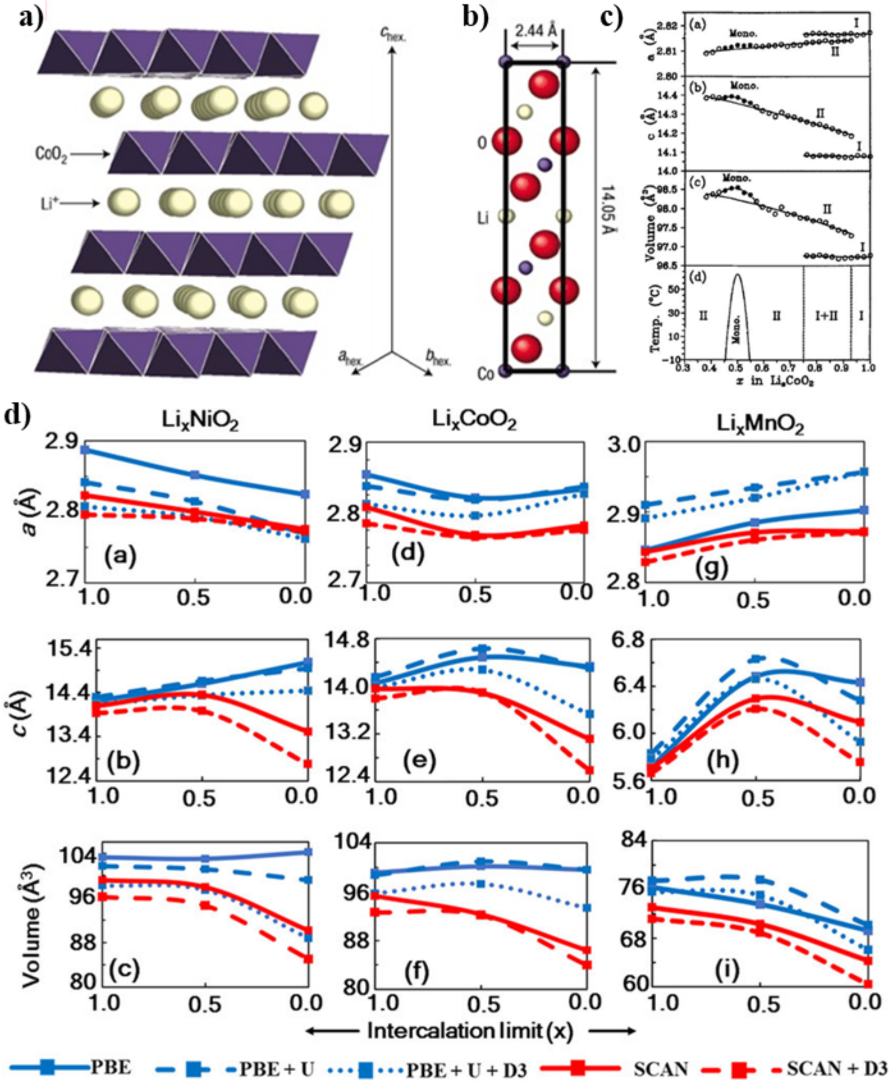

Figure 13 Graphical representation of a) layered LiCoO2 and b) unit cell with atomic arrangement. c) unit cell parameters, constants, cell volume variation along with the phase diagram resulting from electrochemical characterization of Li_xCoO_2, d) simulated unit cell parameters of $LiNiO_2$, $LiCoO_2$ and $LiMnO_2$ with respect to extent of intercalation. [52] [46, 53]

1.2.7.2 Lithium Nickel Oxide ($LiNiO_2$)

The discovery of $LiCoO_2$, lead to extensive study of several other transition metal oxides as potential cathode systems. $LiNiO_2$, another layered compound from the same family of materials, generated great interest as a replacement for $LiCoO_2$ due to its better reversible capacity, lower toxicity and cost compared to *Co* analogue. [54-55] However, the tendency of Ni^{3+} ions to inter migrate and diffuse from the *Ni* plane to *Li* plane poses a great challenge for synthesizing defect free $LiNiO_2$ causing non-stoichiometry and pinning of NiO_2 layers.[56] Hence, the system suffers from poor lithium ion diffusion coefficient reflecting in large capacity fade, large polarization leading and poor rate capability in the electrochemical system. Additionally, $LiNiO_2$ is susceptible to undergo tetragonal structural distortion (Jahn-Teller distortion) due to the high energy of the low spin electron in the degenerate orbital of $Ni^{3+}: d^7(t_{2g}^6 e_g^1)$ ion inducing irreversible phase transformations occurring during electrochemical cycling [57-59]. Substitutional replacement of *Ni* with other cations such as *Co*, suppresses Jahn-Teller distortion[59], while induction of *Mg* in the rhombohedral site of crystal lattice results in $Li_{1+x}NiMg_xO_{2(1+x)}$ phase preventing the phase distortion and transformation inducing better thermal stability and increase in the retention of electrochemical capacity[60].

1.2.7.3 Spinel Structure Based Cathodes

Lithiated manganese spinel, $LiMn_2O_4$ based compounds as a cathode material were developed by Thackeray *et al.* and showing advantages such as economical, environmentally favorable in nature and better handling safety compared to $LiCoO_2$ [61-62]. These spinels belongs to the $Fd\overline{3}m$ structure with *Mn* and *Li* engaged in the 16d (octahedral) and 8a (tetrahedral) sites, respectively, resulting in a three dimensional channel for Li^+ diffusion occurring in lattice structure compared to a two dimensional diffusion path occuring in the case of the layered compounds. This phenomenon makes it an attractive system for LIB requiring high power capability especially in electric vehicles, however, with limitations such as specific capacity fade associated with the system's non-stoichiometry, structural and chemical instability [63]. The discharge/charge reaction is categorized into two different regions / steps (Figure 14) with the lithium extraction from the 8a tetrahedral sites initiating at 4V to form the λ-MnO_2 structure preserving the initial cubic symmetry however, with a decrease in lattice parameter due to the oxidation of Mn^{3+} to Mn^{4+}.[64-67] The second reaction of delithiation during charging commences at 3V from $Li_2Mn_2O_4$ with the *Li* occupying the empty 16c octahedral sites and 8a tetrahedral sites.

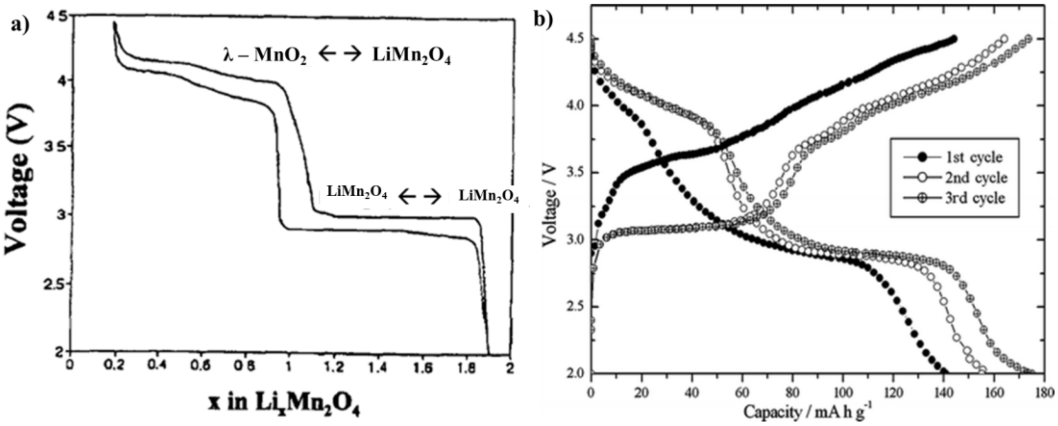

Figure 14 The electrochemical charge / discharge profile of $LiMn_2O_4$ with respect to Li/Li$^+$ ($0<x<2$) [67-68]

The second step causes the *Li*, existing in the 8a sites (tetrahedral) to occupy the *16c* sites (octahedral) during the diffusion process to minimize the electrostatic repulsion and the free energy of the system along with the increase in oxidation state of Mn ion > 3.5. This leads to the formation of a distorted tetragonal structure from the initial cubic crystal structure, a phenomenon characteristic to the Jahn-Teller distortion due to the high spin of Mn^{3+} in the degenerate orbitals of the coordinate crystal structure resulting in the increase in lattice strain causing rapid capacity fade in the electrochemical system.

Doping different elements such as *Ni, Co, Fe*, *Cr*, *Mg* stabilizes the crystal structure [69-71] and employing metal oxide coatings such as V_2O_5 and Al_2O_3 prevents the dissolution of *Mn* ions from the cathode material into the liquid electrolyte leading to improved performance and cyclability in the electrochemical system. [38, 70, 72]

1.2.7.4 Other Derivatives of Layered Oxide

Layered oxides based on *Mn* have high capacity from the layered structures and attracted interest as materials for cathode owing to the advantages of manganese chemistry. $LiMnO_2$ forms a layered structure similar to $LiCoO_2$ and $LiNiO_2$ with a theoretical specific capacity of ~285 $mAh{\cdot}g^{-1}$. This metastable layered crystal structure is formed using low temperature synthesis method (ion exchange/ hydrothermal processes), while the thermodynamically stable orthorhombic analogue is synthesized at high temperature. Bruce *et al*[73], synthesized $LiMnO_2$ by ion exchange process from $NaMnO_2$ which despite its higher capacity suffered from large capacity fade due to the irreversible layered – spinel phase transition during the charging process. [74-75] On formation of $Li_{0.5}Mn$, the *Mn* and *Li* ions due to the stabilization obtained by charge disproportionation of Mn^{3+} to Mn^{2+} (tetrahedral) and Mn^{4+} (octahedral) move to the tetrahedral sites surrounded by *Li* vacancies[76-77]. Many studies involving doping with different atoms (*Co, Ni, Cr* etc) have been conducted to stabilize the layered metastable structure of $LiMnO_2$ [77-80]. Equivalent amounts of the three transition metals (*Ni, Mn* and *Co)* form $Li(Ni_{1/3}Mn_{1/3}Co_{1/3})$, Li-NMC111 exhibit high capacity (~ 160 $mAh{\cdot}g^{-1}$) [79] and better rate capability [81-82] and more recently Ni:Mn:Co = 8:1:1 exhibits a specific capacity of ~200 $mAh{\cdot}g^{-1}$.

1.2.7.5 Olivine Structure-Based Cathodes

Cathodes consisting of $LiFePO_4$ based olivine compounds exhibit good attributes such as reversible Li^+ extraction to form $FePO_4$, high capacity, environmentally benign and lower cost [83]. These olivine structure have one dimensional (1-D) channels, which enable easy diffusion of Li^+

during the de-intercalation / intercalation processes. During charging process (Figure 15), the orthorhombic structure *$LiFePO_4$* converts into *$FePO_4$* having a trigonal quartz like structure [84]. This transformation occurs by the formation of a two - phase transition region (*$LiFePO_4$ / $FePO_4$*) exhibiting a plateau at ~3.4 V in the discharge profile. When compared to *$LiCoO_2$* based LIBs, *$LiFePO_4$* cathode exhibits higher capacities of ~170 mAh/g with a discharge potential of ~3.4 V. Owing to minimal crystal structural distortion during the *$LiFePO_4$ - $FePO_4$* transition provides better cycling stability. However, *$LiFePO_4$* exhibits lower *Li^+* diffusivity (~1.8 x 10^{-14} $cm^2 \cdot s^{-1}$) and lower electrical conductivity (in the range of 10^{-8} - 10^{-10} $S \cdot cm^{-1}$) due to small polaron hopping, which restricts the use in high power applications [85]. Different methods were explored to improve the electrical conductivity and *Li^+* diffusivity by particle size reduction [78, 86-87], doping of metallic element [88-90] and conductive coatings [91-93]. Doping $LiFePO_4$ with aliovalent metallic ions and coating with conducting materials such as carbon have shown to improve the conductivity and hence, the ability to successfully intercalate / de-intercalate *Li^+* at high charge - dicharge rates [88, 91, 94-95].

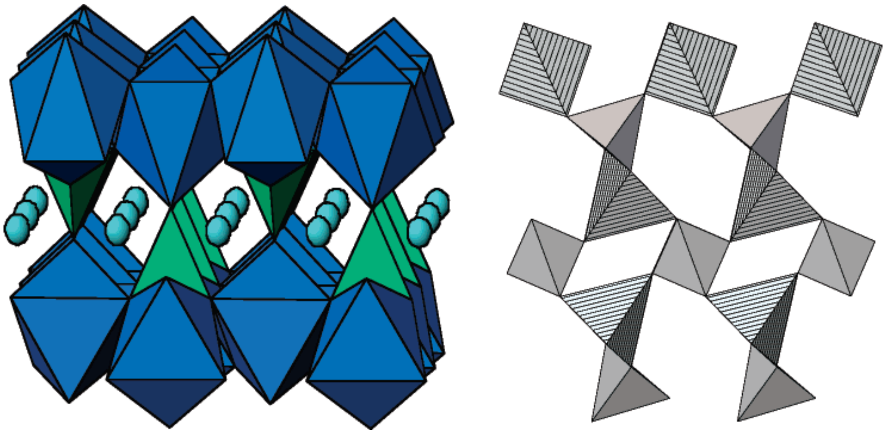

Figure 15 Crystallographic structures of olivine based materials (orthorhombic LiFePO4 and trigonal quartz-like FePO4) [84]

1.2.8 Lithium-ion Battery Electrolytes

An important component of a lithium-ion battery is the electrolyte which acts as the medium for the Li^+ ion transfer during the discharge-charge process and contains one or more lithium salts, which serve as the source of mobile Li^+ species along with mixtures of solvent. [96-97] The electrolyte present in between the cathode - anode of the electrochemical system is in constant contact with the electrodes filling in the porosity of the electrode. [98] Therefore, selection of the electrolyte which is compatible with the working conditions, power requirements and electrode materials for the required application is very important. [99-101] Electrolyte used in LIBs should fullfill the below list of operational / fundamental criteria and properties:

i. They should be electronically insulating (to prevent cell short circuiting and / or self-discharge) however, have high Li^+ conduction (reduces the internal cell resistance).[102-103]

ii. Ability to exhibit broad electrochemical stability window to prevent decomposition at beyond the operating voltages (>4 V). [104-105]

iii. Exhibit good electrochemical / chemical stability to prevent parasitic side reactions on electrode surfaces.

iv. Should be inert to other battery components (current collectors / separators / other packaging materials).

v. Have high and low boiling and melting points, respectively.

vi. Low toxicity towards life forms for industrial production, recycling and handling.

vii. Have low production / manufacturing costs with longer shelf life.

Electrolytes for LIBs are sub - categorized as liquid electrolytes (non-aqueous), polymer/gel based electrolytes and solid electrolytes based on the nature and fundamental operating principle[106-108109-121].

1.2.8.1 Liquid Electrolytes (Non-Aqueous)

Different salts of lithium used in commercial LIBs, their physical properties, conductivities and compatilbility are shown in **Table 2** [96]. Di atomic lithium salts with simpler molecular structure (for example, *LiCl* and *LiF*) cannot be used as dominant salt in LIB electrolyte due to poor solubility in organic solvents resulting from smaller ionic radius of Li^+.

The current LIBs consist of complex anionic salts (such as $LiPF_6$) where a stabilizing Lewis acid and an anion core are usually employed. The resonance effect causes the negative charge of F^- to be well distributed in the Lewis acid complex (- PF_5), thus, resulting in lower melting point/ good solubility. [96] **Table 3** gives the list of solvents used for lithium ion batteries along with their electrochemical stability window in different lithium salts.

Table 2: Different salts of lithium used in electrolyte [96]

Salt	Structure	M. Wt	T_m/ °C	$T_{decomp.}$, / °C in solution	Al-corrosion	σ /mScm^{-1} (1.0 M, 25 ° C)	
						in PC	in EC/DMC
$LiBF_4$	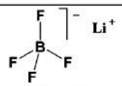	93.9	293 (d)	> 100	N	3.4 [a]	4.9 [c]
$LiPF_6$	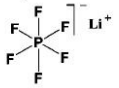	151.9	200 (d)	~ 80 (EC/DMC)	N	5.8 [a]	10.7 [d]
$LiAsF_6$	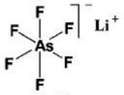	195.9	340	> 100	N	5.7 [a]	11.1 [c]
$LiClO_4$	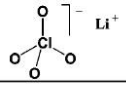	106.4	236	>100	N	5.6 [a]	8.4 [d]
Li Triflate	$Li^+ CF_3SO_3^-$	155.9	>300	>100	Y	1.7 [a]	
Li Imide	$Li^+ [N(SO_2CF_3)_2]^-$	286.9	234 [b]	>100	Y	5.1 [a]	9.0 [e]
Li Beti	$Li^+ [N(SO_2CF_2CF_3)_2]^-$				N		

Table 3: Stability of electrolyte systems/solvents in electrochemical system: Non active electrodes

Solvent	Salt/Conc (M)	Working Electrode	E_a^a	E_c^b
DEC	GC	Et_4NBF_4/0.65	6.7	
	Au, Pt	$LiClO_4$/0.1		1.32
	Pt	$LiAsF_6$	4.2	
2-Me-THF	Pt	$LiClO_4$	4.1	
	GC	$LiAsF_6$/1.0	4.15(0.1)	
	GC	$LiAsF_6$/1.0	4.2	
	Pt	$LiAsF_6$	4.1	
DMC	GC	Et_4NBF_4/0.65	6.7	
	Au, Pt	$LiClO_4$/0.1		1.32
	GC	$LiPF_6$/1.0	6.3	
	GC	LiF	5	
THF	GC	Et_4NBF_4/0.65	5.2	
	Pt	$LiClO_4$	4.2	
	GC	$LiAsF_6$/1.0	4.25(0.1)	
EC	GC	Et_4NBF_4/0.65	6.2	
	Ni	Bu_4NPF_6		0.9
	Au, Pt	$LiClO_4$/0.1		1.36
EMC	GC	Et_4NBF_4/0.65	6.7	
	GC	$LiPF_6$/1.0	6.7	
γBL	Au, Ag	$LiAsF_6$/0.5		1.25
PC	GC	Et_4NBF_4/0.65	6.6	
	Ni	Bu_4NPF_6		0.5
	Au, Pt	$LiClO_4$/0.1		1.0-1.2
	Porous Pt	$LiClO_4$/0.5	4	
	Pt	$LiClO_4$	4.7	
	Au	$LiClO_4$	5.5	
	Pt	$LiAsF_6$	4.8	
DME	GC	Et_4NBF_4/0.65	5.1	
	Pt	$LiClO_4$	4.5	
	Pt	$LiAsF_6$	4.5	

[a]Anodic and [b]cathodic limits, potential referred to Li^+/Li. [c] Ultramicroelectrode technique was employed for the salt-free condition.

1.2.8.2 Solid Electrolyte Systems

There are two major classification of solid electrolytes (SE) are mainly based on their structure: crystalline/ceramic electrolytes and glassy/amorphous electrolytes. Glassy/amorphous electrolytes (**Table 4**) have generated interest owing to their strategic advantages related to ease of production, isotropic uniform ionic conductivity and absence of grain boundaries. The lack of grains / grain boundaries in a SE is important for the safety of battery operation since they resist ionic (Li^+) mobility while improving the motion of other ions thus, reducing the chances of undesirable dendrite growth and short circuiting of LIBs. Oxide based glasses which were initially used as glass based electrolytes were later doped/mixed with *Boron* / *Selenium* to enhance their conductivity [117]. The next class of materials containing glasses based on phosphorus oxynitride (LIPON), were developed by Oak Ridge National Laboratory (ORNL) which attracted attention due to their feasible practical applications, strategically in thin film LIBs [118]. The LIPON films made by nitrogen ion beam based thermal evaporation or by sputtering in nitrogen plasma from Li_3PO_4 target [119-120] show excellent chemical/electrochemical stability allowing for minimal self-discharge under fully charged/ discharged state for extended periods of time. [121]

Table 4: Ionic conductivities of lithium oxide (*Li_2O*) based glasses at respective temperatures

Materials	**Conductivity**	**Measurement**
(Composition)	**(S/cm)**	**Temperature (°C)**
Li_2O- B_2O_3 (63-37)	6.3 x 10^{-11}	25.0
$LiPO_3$-LiF (60-40)	6.7 x 10^{-9}	25.0
Li_2O-SiO_2 (40-60)	1.0 x 10^{-6}	100.0
$LiPO_3$-Lil (67-33)	1.0 x 10^{-3}	194.0
$Li_2B_7O_{12}Cl$	2.5 x 10^{-I}	200.0
Li_2O-LiF-B_2O_3 (20-36-44)	3.1 x 10^{-4}	200.0
Li_2O-Nb_2O_3	6.1 x 10^{-4}	200.0
$LiNbO_2$-SiO_2	1.0 x 10^{-4}	200.0
$LiPO_3$-LiCI (70-30)	1.0 x 10^{-3}	220.0
$LiPO_3$-LiBr (67-33)	1.3 x 10^{-3}	220.0
Li_2O-LiF-$Al(PO_3)_3$ (15-70-15)	1.3 x 10^{-3}	220.0
Li_2O-Al_2O_3-SiO_2 (25-25-50)	6.1 x 10^{-4}	250.0
$LiPO_3$-Li_2SO_4 (67-33)	3.5 x 10^{-3}	250.0
$Li_2B_4O_7$	1.0 x 10^{-4}	300.0
$LiBO_2$	4.0 x 10^{-3}	300.0
$Li_2B_7O_{12}Cl$	8.0 x 10^{-3}	300.0
Li_2O-Li_2Cl_2-B_2O_3 (31.8-12.3-55.9)	1.7 x 10^{-2}	300.0

Li_2O-Li_2SO_4-B_2O_3 (0.71-1.1-1)	2.1 x 10^{-2}	300.0
$Li_2Al_2Si_4$	4.0 x 10^{-4}	300.0
Li_2O-Y_2O_3-SiO_2 (40-6-54)	1.4 x 10^{-3}	300.0
B_2O_3-0.56Li_2-0.08LiF	6.3 x 10^{-4}	300.0
B_2O_3-0.56Li_2-0.08Lil	3.2 x 10^{-3}	300.0
Li_2O-LiF-$Al(PO_3)_3$ (30-50-20)	1.0 x 10^{-2}	300.0
Li_2O-Li_3PO_4-B_2O_3 (25-10-65)	1.0 x 10^{-3}	330.0
Li_2O-B_2O_3 (42.5-57.5)	6.1 x 10^{-3}	350.0
Li_2O-Li_2Cl_2-Li_2SO_4-SiO_2-B_2O_3 (35-10-30-12.5-12.5)	9.7 x 10^{-2}	350.0
Li_2O-Li_2Cl_2-B_2O_3-Al_2O_3 (29-24-3-44)	1.5 x 10^{-2}	350.0
Li_2O-Li_2SO_4-B_2O_3 (0.5-0.15-1)	2.4 x 10^{-3}	350.0
$Li_2Si_2O_5$	1.9 x 10^{-3}	350.0
Li_2O-B_2O_3-$LiNbO_3$ (40-35-25)	8.0 x 10^{-4}	350.0
Li_2O-B_2O_3-SiO_2 (39-13-48)	1.5 x 10^{-4}	350.0
$Li_2Si_2O_5$-Li_2SO_4 (71.5-28.5)	8.7 x 10^{-4}	350.0
Nb_2O_5- Li_2O_2 (50-50)	5.3 x 10^{-3}	350.0
Ta_2O_5- Li_2O_2 (50-50)	6.4 x 10^{-3}	350.0
Li_2O- B_2O_3 (63-37)	6.3 x 10^{-11}	25.0

Ceramic materials of halides, oxides, nitrides, sulfides and similar polyanions comprise the category of crystalline solid electrolytes. Perovskite structures (ABO_3) are attractive candidates as crystalline solid ion conductors because of their tolerance to ionic substitution and atomic misarrangement, resulting in open and organized lattice structures for Li^+ conduction,

Single crystals of $Li_{3x}La_{2/3-x}TiO_3$ (x=0.11) due to large number of Li site vacancies exhibit good conductivity of Li^+ (10^{-3} - 10^{-4} mS/cm).[122] However, on establishing interfacial contact with negative anode containing active lithium or lithium metal, results in the reduction of Ti^{4+} ion in the oxide. [111] This leads to the precipitation of metallic elements and increase in the electrical conductivity of the electrolyte, thus, restricting their application in commercial LIBs. NASICON (Na Super Ion Conductors) type Li analogues having a general formula of $Li_{1+x}M_2(PO4)_3$ $(M = Zr, Ti, Ge)$ have been developed as Li^+ electrolytes, where, the polyhedral corners of MO_6 and PO_4 are interconnected to form three dimensional (3D) channels for Li^+ conduction [48]. The *metallic* cation, M (usually the Ti^{4+}) also suffers from problems similar to that of perovskite structure due to the increase in electronic conductivity triggered by the reduction of *Ti* by lithium intercalation. The doping of these electrolytes with trivalent ions (such as *Al*) results in improvement of ionic conductivity by approximately two – three orders of magnitude.[48-49]

1.2.8.3 Polymer Based Electrolyte Systems for LIB

The discovery of Li^+ conductivity in polyethylene oxide (PEO) resulted in the proposition of concept of polymer electrolytes in LIBs[46]. Enormous interest has been generated in this polymer electrolyte field and the developed systems have the trade name of, LiPo or Li-Poly batteries in commercial applications. Solid polymer based electrolytes can categorized as: solvent containing gel polymer systems or solvent free systems with ionic coupling. PEO based electrolyte systems are the commonly employed solvent-free polymer-based electrolytes with the lithium salt dissolution occurring and facilitated through the formation of complex between the ether oxygen in the PEO chain and Li^+. However, with the increase in size of anion, as in the case of lithium salt of bis (trifluoromethylsulfonyl) imide [$(CF_3SO_2)N^-$], charge delocalization results in detrimental properties such as poor binding strength and dissociation of Li^+ ions.[47]

1.2.8.4 Additives for Electrolytes in LIB

Additives form a special distinct set of compounds which are dissolved into the electrolyte (especially in liquid based non-aqueous) to induce advanced and precise property such as enhanced ionic conduction, stable SEI layer formation, flame retardation, etc. More recently, electrolyte additives composed of vinylene carbonate (VC) and fluoroethylene carbonate (FEC) and their analogues have shown improved performance in terms of cycling stability, stable solid electrolyte interface (SEI) and first cycle irreversible loss.[79, 123]

1.2.9 Anode Systems for Lithium-ion Batteries

A LIB anode during the discharge process, undergoes oxidation to produce electrons and is also termed as negative electrode. The initial anode in the first-generation lithium based batteries consisted of elemental *Li* due to low molecular weight and high electro-positivity, however, suffered from severe safety problems due to internal short circuiting of the cell due to dendritic Li growth upon recharging the battery. Researchers explored an substitute material to *Li* metal; an anodic host structure to accommodate reversible insertion of the Li^+ ions thus, preventing dendrite formation during the discharge - charge processes. Sony® commercialized the first LIB with $LiCoO_2$ / graphite (*C*) serving as the cathode/anode hosts for Li^+, respectively, with an operating nominal discharge voltage of ~3.6 V and energy storage densities between 120 - 150 Wh · kg^{-1}. While $C/LiCoO_2$ is the popularly used commercial LIB in portable systems such as laptops, cell phones, PDAs, and cameras etc, major efforts are being focused continuously to develop new anode materials with better stability. The anode materials selection for LIB are based on the below listed behavior/criteria:

i. Alloying/reaction with lithium at lower electrode potentials (close to metallic Li) with Li^+ ions, to improve the overall cell voltage.

ii. Exhibit capacity retention and good cyclability for long electrochemical cycle life.

iii. Exhibit chemical stability to electrolyte/solvent in a wide potential window.

iv. Inexpensive, safe and good shelf life to handle and for commercialization.

1.2.9.1 Carbon Based (Carbonaceous) Materials

Before they found application as anode hosts in Li-ion battery, the existence of graphite - lithium intercalated compounds was well known / studied for several decades[124-125]. Efforts to intercalate Li^+ into graphite electrochemically from *Li* salt electrolytes (dissolved in DME and

DMSO) was conducted by Besenhard *et al* [126-127]. Their first use in LIBs was reported by Basu *et al* wherein, graphite intercalated compounds with lithium (GIC) were used as anodes in a *LiCl-KCl* molten salt electrolyte in 1980[128]. Subsequently, patents for the use of GIC based anodes in room temperature LIBs were applied by Basu and Ikeda in 1981[129] and 1982[130], respectively. Extensive research in developing carbon based anode was done eventually resulting in the commercialization by Sony® in 1990 of the first LIB with a carbon anode [131].

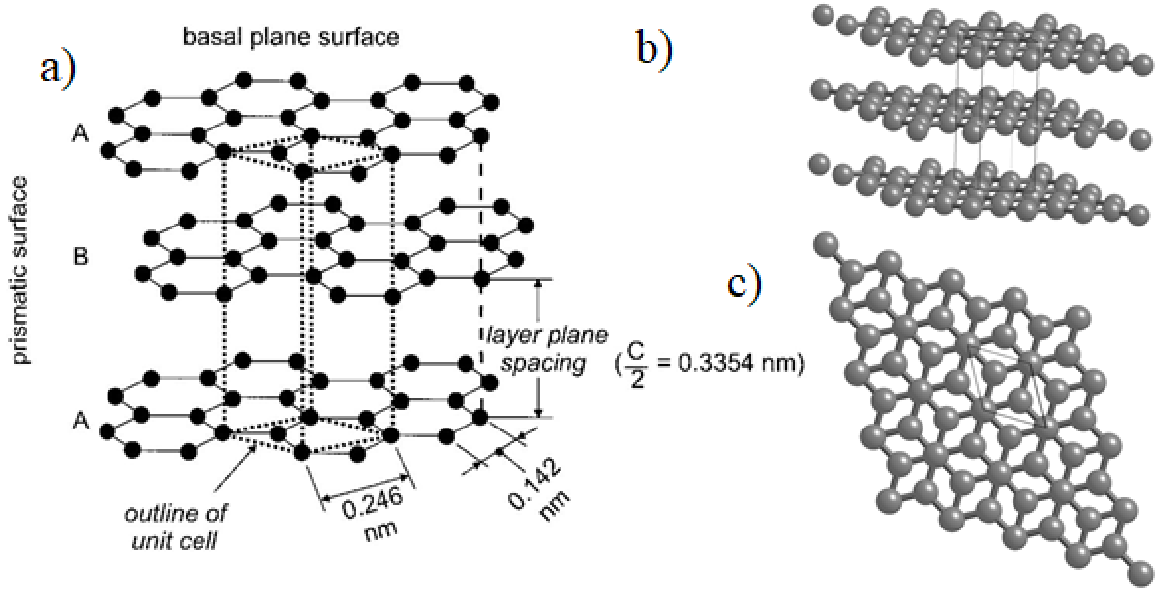

Figure 16 Schematic showing a) atomic arrangement and crystal structure of graphite unit cell (hexagonal) indicating the stacking sequence (AB layer) with prismatic surfaces and basal plane, b (SW Isometric) and c) basal plane view of graphite, Crystal Maker[38]

The carbonaceous anodes in LIBs consist of sp^2 hybridized carbon atoms arranged in a continuous hexagonal network (graphene layers), often termed as honeycomb structure. These networked sheets are stacked over each other and held together by weak low energy van der Waals forces to form different ordered structures: the 2H or α-phase ABAB stacking sequence with hexagonal symmetry and the ABCABC type stacking, showing a 3R or β-phase rhombohedral symmetry. Naturally and readily available carbons contain β-phase carbons (up to 30%), formed by mechanical treatments (during processing or handling) such as milling, shearing and ultrasonic treatments which can be converted α-phase by heating at high temperatures.[64-65] The graphitic structure of carbon induces two different surfaces, termed as the prismatic (edge) and the basal plane surfaces (Figure 16) [78].

The smooth homogenous basal planes consist of only the carbon atoms, while, the rough and heterogeneous prismatic surface can consist of other atoms (such as hydrogen/oxygen/) as functional groups on the surface (– COOH and – COH). Intercalation of lithium into graphite structure occurs through the prismatic planes while the basal planes and its constituent carbon atoms facilitate only the diffusion and are inert to any intercalation / reaction.[66, 86] Hence, understanding and controlling the quantities of the basal and prismatic planes along with their relative amounts in the carbon containing materials for making LIB anodes is very critical.

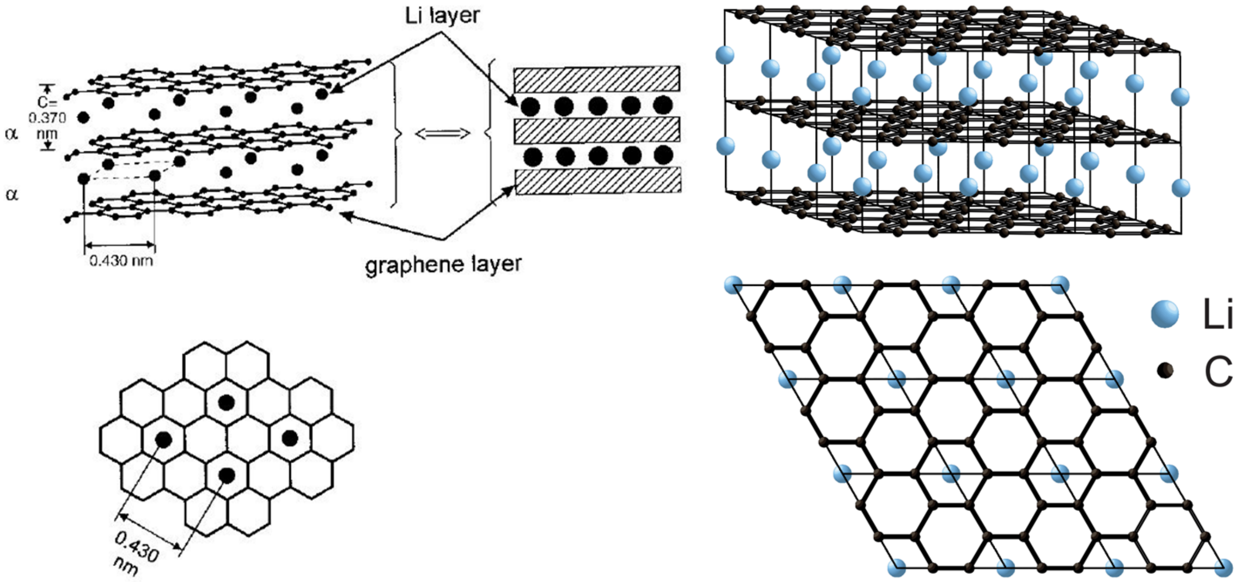

Figure 17 : Pictorial representation of Li intercalation into graphitic structure along with a view perpendicular to basal plane in LiC6 [78, 132]

The internal van der Waals forces generated by interaction of Π - electrons enable gliding of graphene layers over one another by rotational / translational modes inducing stacking faults and distortion in the carbon matrix[133-134]. This triggers loss of periodic atomic arrangement in between the stacking layers, forming turbostratic structure. The inter-planar and interatomic distances in the disordered carbon-based structures are diffused, variable and greater than that of graphitic carbon on an average. In general, the disordered carbon materials are of two types: hard and soft carbons. The turbostratic disorder in soft carbon materials can be removed by heating them in an inert atmosphere to very high temperatures (>3000°C). However, it is difficult to remove the turbostratic order in the case of hard carbons by annealing due to the presence of stable sp^3 bonding in between the layers and hence, they retain the disorder. Disordered and ordered carbons differ drastically in their electrochemical performance and properties such as gravimetric capacity, intercalation potential with respect to lithium, quality of the SEI layer, first cycle irreversible loss and rate capability.

The lithium intercalation into the prismatic graphite layers occurs in a periodic sequence (stages) involving formation of different intercalant layers, a phenomenon termed as "the staging mechanism"[135]. The structure containing 'n' number of graphene layers between two intercalated layers (layers containing Li^+ ion) is defined as the nth stage compound. In a well-ordered graphitic structure, a maximum of one Li can be accommodated for 6 carbon atoms. Therefore, stage-I results in a compound with the stoichiometric formula LiC_6 with the intercalant layer consisting Li^+ separated by single graphene layer (Figure 17) while the sites in adjacent neighboring plane for Li intercalation are avoided, causing an in-plane lithium density of LiC_6. The ABAB graphene layer sequence after intercalation, is transformed to an energetically favorable AA type stacking order. The intercalation of external ion (Li^+) results in an increase in average distance (10.3%) in between the graphene layers [87]. The mechanism of staging is observed from the voltage vs. time plot obtained by electrochemical intercalation of graphite with lithium in a galvanostatic mode

(Figure 18). The voltage plateaus (Figure 18) indicate the formation and presence of two phases or two different stage compounds, namely the stage-I and stage-II compounds, which co-exist when the voltage remains constant at ~0.1 V during the presence of two phase regime [90].

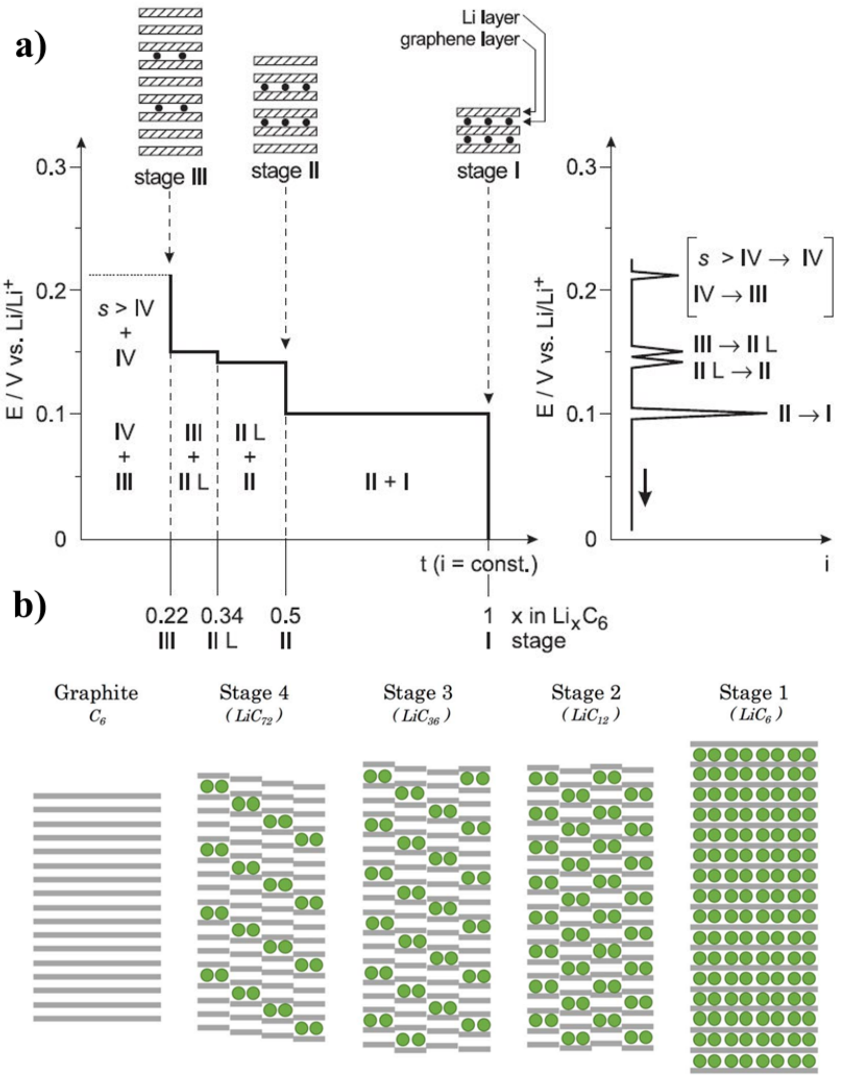

Figure 18 a) Potential vs intercalation at various stages (staged mechanism) and b) schematic of lithium intercalation into graphite during electrochemical reaction [78, 136]

The irreversible capacity arising due to the formation of solid electrolyte interphase (SEI) layer on graphitic surfaces is another important feature of the carbonaceous compounds [89, 93, 137]. This phenomenon arises from the decomposition of the solvent that occurs at around above 0.5 V (~0.8V) and also, in parallel to the Li intercalation reaction, a very damaging phenomenon, especially when employing propylene carbonate (PC) based electrolyte in LIBs. In PC based non – aqueous LIB electrolytes, the co – intercalation of solvent molecules occurs in the form of Li^+-$(solv)_y$ to form Li^+- $(solv)_y$ - C_n along with the Li^+ into graphite layers [92]. The solvated intercalation phenomenon causes expansion in the layered graphitic structure (~150%) resulting in exfoliation of layers due to loss in interplanar interactions and subsequently, loss in capacity (**Figure 19)**. To tackle this problem, carbonate based solvents (ethylene carbonate - EC, diethyl carbonate - DEC, etc.) are employed since the Li^+ interaction and their stability energy prevents the solvated intercalation reaction, instead, forming a protective SEI layer on the graphite surface[138]. Due to the viscosity of EC being very high because of its high permittivity, it is mixed with other linear carbonates, for example, diethyl carbonate (DEC) / dimethyl carbonate (DMC) enhancing the fluidity and is thus widely used in current commercial LIBs. [138]

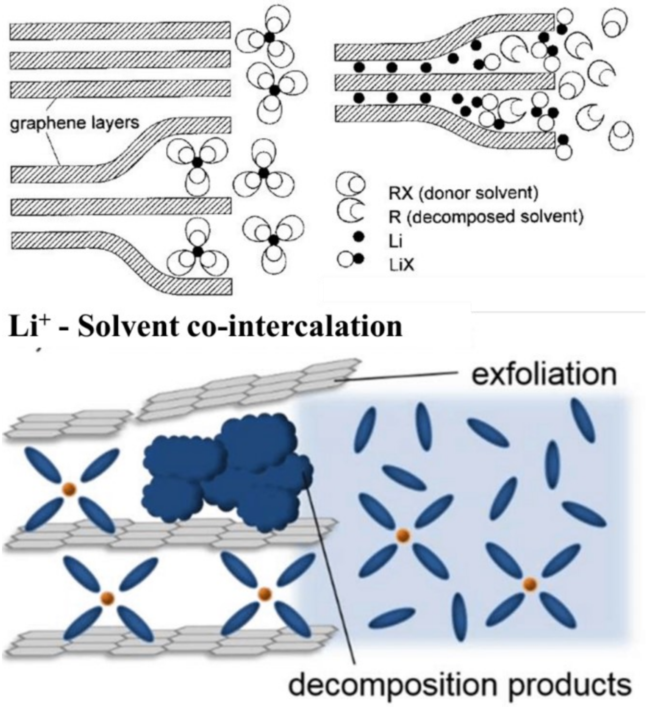

Figure 19 Exfoliation / flaking of graphitic layers from co-intercalation of solvent [92, 139]

1.2.9.2 Intermetallic / Alloy-based Lithium-ion Battery Anodes

The good cycle/ low cost of carbon-based anode has enabled the system to be used widely in commercial portable and well as large scale applications. The increase in demand for energy storage for emerging applications such as grid storage and automotive industry, has resulted in grave need for LIBs with better energy storage densities. Alloy / metallic - based anodes have generated attention as carbonaceous electrode alternatives owing to their higher gravimetric / volumetric energy storage densities. Pure metallic elements such as *Sn, Al*, *Si* and *Bi* have the ability of alloying with copious amounts of Li at low electrode potentials with respect to Li/Li$^+$ providing in higher energy storage densities according to the below reaction:

$$M \ + n\, Li^{+} + ne^{-} \rightarrow \ Li_{n}M$$

$$M \ = Sn, Si, Al, Bi, Sb, Zn$$

The theoretical specific capacity of these alloys / elements are calculated from the molar quantity of Li which can be alloyed electrochemically during lithiation reaction, the values of which are as provided in **Table 5**.

Table 5: Specific charge storage capacities and molar volumetric changes exhibited by the different anode elements during electrochemical cycling with lithium

Element	**C**	**Bi**	**Sn**	**Al**	**Si**
Maximum Lithiated phase	LiC_6	Li_3Bi	$Li_{4.4}Sn$	Li_9Al_4	$Li_{4.4}Si$
Gravimetric capacity (mAh/g)	372	385	992	2235	4200
Volumetric Capacity (mAh/cm^3)	833	3773	7247	6035	9784
Volume change (%)	12	115	257	238	297

The work on lithium based alloys and intermetallic was triggered and conducted on the systems: *Li-Al* [98-99, 105], *Li-Sn* [100-102], *Li-Mg*[103], *Li-Sb*[107-108] and *Li-Si* [110-112] by employing high temperature molten salt electrolytes (~400°C). The metallic alloy anodes undergo huge volume changes as a part of the alloying and de-alloying processes. The colossal volumetric /

crystallographic changes induce large mechanical stresses, eventually triggering the fracture of the active material, which is usually referred to as ‘crumbling’ or ‘pulverization’ of the electrode. The resulting fine secondary particles from pulverization phenomenon lack the initial inter connectivity and remain electrically insulated from the substrate / current collector, resulting in active material / capacity loss. Several approaches were designed and explored to resolve the issue of mechanical failure in the metallic alloy anode systems as listed below:

- Use of amorphous and nanostructured materials.
- Mixed conductor composite matrices: active-active and active-inactive matrix composites.

Fuji® commercialized a metallic alloy anode, in 1995, based on Li-ion battery with the trade name - Stallion® lithium-ion cell [140] which exhibited higher capacities when compared to those that use graphite based anode. The Stallion® cell employed an amorphous oxide of tin composite anode, SnO_x dispersed within a glass matrix of Al_2O_3, B_2O_3 and tin phosphate. The electrochemically active Sn which undergoes de-lithiation and lithiation during the charge – discharge processes was formed electrochemically by the following reactions:

$$SnO_x + 2xLi^+ + 2xe^- \rightarrow xLi_2O + Sn \ (irreversible\ Li_2O\ formation)$$

$$xLi_2O + Sn + yLi^+ + ye^- \leftrightarrow xLi_2O + Li_ySn \ (reversible\ alloying\ of\ Sn)$$

The electrochemically inactive matrix consisting of borate-alumina-phosphate glass acts like a supporting medium / matrix for the metallic tin nanodomains which are formed during the first in-situ reduction of SnO_x. There is an irreversible loss of capacity during the first cycle due to loss of lithium atoms as well as lithium ion as a result of the permanent reduction of the parent SnO_x phase to form Li_2O and Sn.

Another electrode system termed as the active-active concept was developed and proposed by Besenhard where *SnSb alloy* was employed as the starting material [113]. The alloying / dealloying reactions for this system with lithium are as follows:

$$SnSb \quad + \ 3Li^{+} + 3e^{-} \ \leftrightarrow \ Li_3Sb + Sn \ \ (reversible\ reaction\ )$$

$$Sn \quad + \ yLi^{+} + ye^{-} \ \leftrightarrow \ Li_ySn\ (reversible\ reaction\ )$$

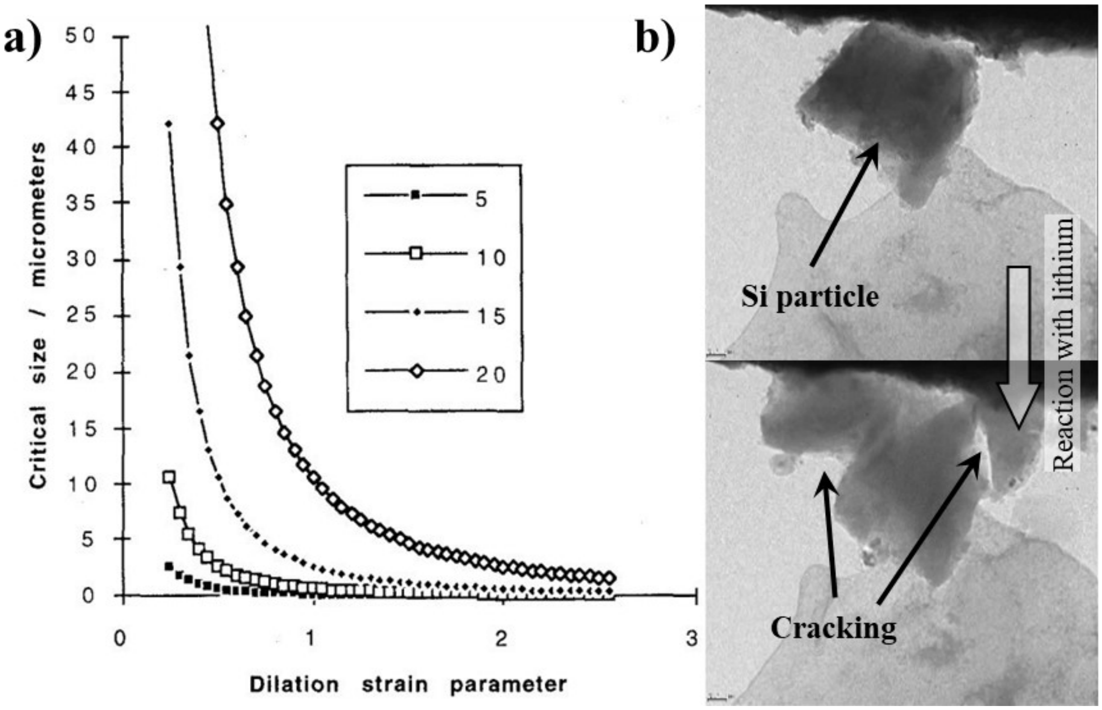

Figure 20 a) Effect of dilation strain parameter on critical geometric size to prevent fracture of materials with different fracture toughness (MPa) and b) in-situ TEM of silicon particle cracking under lithiation [141-142]

The lithium alloying phenomenon occurs in a sequential fashion, where, lithium initially alloys at higher potential with Sb to form Li_3Sb with dispersed Sn domains [114-115] following which the remaining Sn domains further alloy with Li to form Li_ySn phases. As a part of the de-lithiation process, after the entire *Li* is de-alloyed from *Sn* / *Sb*, the initial *SnSb* phase is restored. This process of phase separation and restoration phenomenon during the discharge - charge process results in a critical morphology which induces the aggregation and coalition of finely dispersed *Sn* thus, forming bigger *Sn* grains which is immediately responsible for the failure of mechanical integrity arising from large volume changes. Intermetallic phases between *Sn* and *Fe*, especially $SnFe$, Sn_2Fe, Sn_2Fe_3 and Sn_3Fe_5 were synthesized and studied by Dahn *et al* where active *Sn* alloys with *Li* forming Li_xSn alloys and *Fe* domains [117-121]. The inactive electrochemically formed *Fe* is very fine (~10 nm) and surrounds the Li alloyed *Sn* particles forming a conductive matrix improving the inter-particle conductivity. Several research studies found that reduction in the particle size of the active materials resulted in alleviation of the mechanical stresses [142-143]. Using a theoretical model, Huggins *et al* calculated the electrochemical and material conditions which results in fracture of particles due to specific volume mismatch in a two-phase structure [142]. Accordingly, a critical terminal particle size can be computed from this model, (Figure 20) below which, continued and further fracture does not happen and this value is independent of the magnitude of the volume mismatch, material, and fracture toughness of the lower specific volume phase. Additionally, the material systems with particle sizes in the sub-nanometer and nanometer range are able to undergo superplastic deformation during the de-alloying / alloying processes to accommodate the huge volumetric changes. The relationship between the applied stress (σ), strain rate ($\dot{\varepsilon}$) and grain size (d) is computed by the following equation [144]:

$$\dot{\varepsilon} = A\sigma^{n} d^{-p} D_0 \exp(-Q/RT) \qquad \ldots\ldots\ldots\ldots\ldots \quad (1\text{-}7)$$

where A is a pre exponential constant

n = stress exponential constant ($n \approx 2$)

p = the grain size exponential constant ($p \approx 2\text{-}3$)

Q = activation energy for flow / diffusion and

R = Universal gas constant.

The strain rates computed from the equation are very low for micron sized grain sizes (~10 μm) and only high temperature super plasticity can be observed and obtained. However, reducing the particle size triggers and enables the superplastic behavior even at room and cryogenic temperatures. In addition, nanostructured materials and systems have higher fraction of atoms located at the grain boundaries and surface when compared to micro materials resulting in improved mechanical performance and properties such as fracture toughness, ductility and mechanical hardness. [104]

1.2.10 Silicon Based Anodes for Lithium-ion Battery

The rise in portable electronics, miniature devices and increased demand for longer driving range / charge mileage in electric vehicles has commanded the battery research community and manufacturers to develop LIBs with the capability to store higher amount of energy without increasing the weight of the overall battery pack. Batteries with higher density of energy can be obtained by enhancing the specific capacity and/or output voltage of the individual constituent electrochemical cells. The equation for computing the total specific capacity of an individual electrochemical cell is as below:

$$C = \frac{C_a \times C_b}{C_a + C_b} \qquad \ldots\ldots\ldots\ldots \quad (1\text{-}8)$$

where C_a is the specific capacity of anode and C_c is the specific capacity of cathode.

The total capacity of the battery that can be obtained, plotted against anode capacity for two different cathodes: *$LiCoO_2$ and $LiMnO_2$* (140 mAh/g, *$LiCoO_2$* and 200 mAh/g, *$LiMnO_2$* derivative) is shown in Figure 21.[145] A higher cathode capacity is essential for an overall high specific capacity of the battery. However, it can be noted that when a cathode with a large capacity of ~200 mAh/g is employed, there is a rapid increase in overall capacity initially with the capacity of anode approaching values of ~1200 mAh/g, after which there is only a marginal improvement in total full cell capacity with further increase in the capacity of anode. Hence, while selecting anode materials to develop and design future generation of high energy density batteries, it is critical that their theoretical / operational capacity is higher than 1200 mAh/g for obtaining and maximizing the attainable capacity for a given cathode.

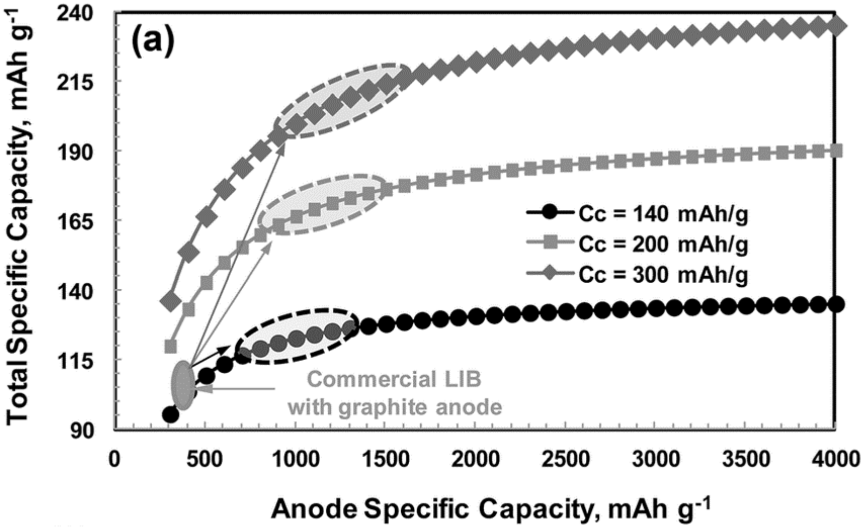

Figure 21 Total specific capacity of LIB calculated as a function of anode specific capacity for cathodes having two different capacities (140 mAh/g & 200 mAh/g) [145-146]

Graphite with a theoretical capacity of only ~372 mAh/g which is currently used as anode in all commercial Li-ion batteries thus, is certainly not a preferred candidate for designing /

developing high energy density LIBs. As previously discussed, metal alloy anode systems are suitable materials for achieving higher gravimetric capacities, among which, silicon is highly attractive because of its low cost, elemental abundance in earth's crust and high theoretical capacity of ~3500 – 4200 mAh/g, which is attributed to its ability to form the highest lithiated phase, $Li_{22}Si_5$. These attractive characteristics enable silicon - based materials to potentially replace graphite as an anode with high specific capacity.

1.2.10.1 Electrochemical Lithiation/De-lithiation Reactions in Silicon

The formation of electrochemical *Li-Si* alloys was initially demonstrated in high temperature reactor cells operating inbetween voltage range of 400°C - 500°C by Sharma and Seefurth in 1976 [111] and then followed by Huggins *et al* in 1981 [122]. The phase diagram of *Li-Si* (Figure 22) indicates the formation of different *Li-Si* phases as follows: $Li_{12}Si_7$ ($Li_{1.71}Si$), $Li_{14}Si_6$ ($Li_{2.33}Si$), $Li_{13}Si_4$ ($Li_{3.25}Si$) and $Li_{22}Si_5$ ($Li_{4.4}Si$) [147]. The formation of the highest lithiated possible phase, $Li_{22}Si_5$, therefore determined the theoretical capacity of *Si* to be 4200 mAh/g.

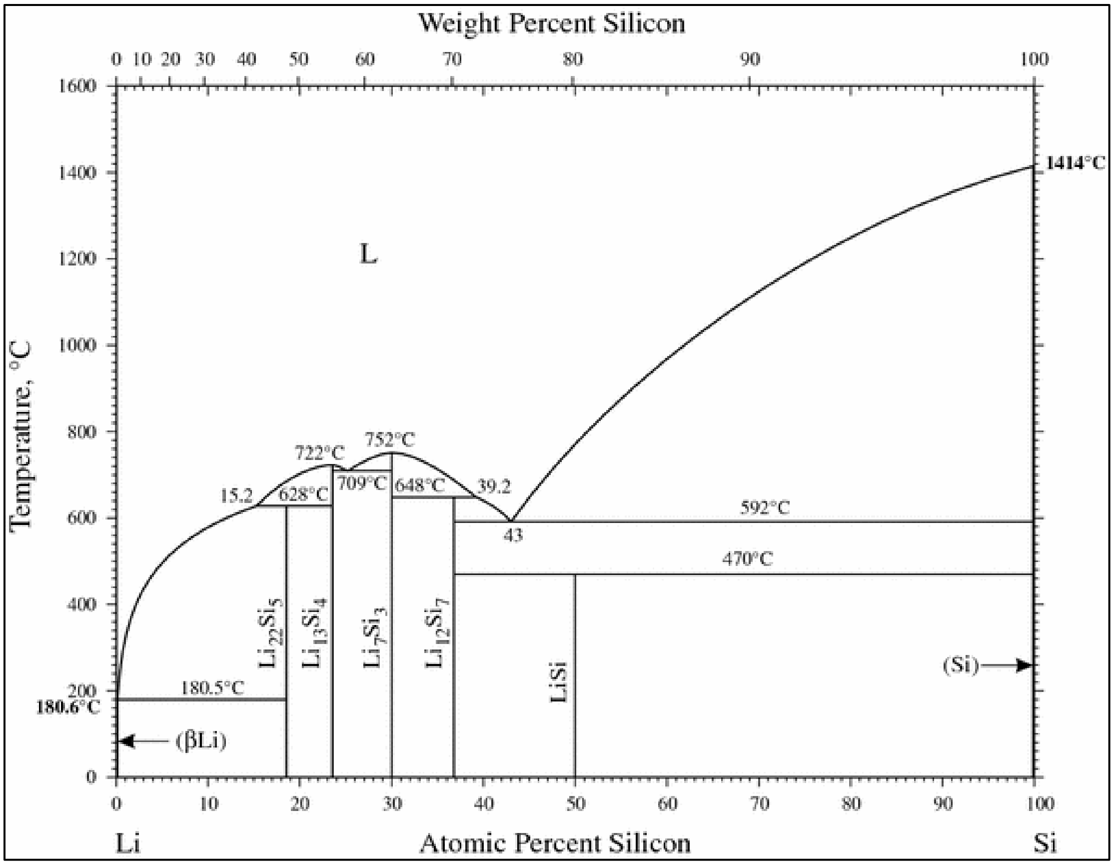

Figure 22 Phase diagram of Li – Si system [148]

The different alloys which bulk crystalline silicon forms with lithium containing various *Li-Si* phases during the discharging process are listed in Table **6** [122]. A large change in volume upon lithiation is often associated with the formation of these phases. The complete lithiation of silicon leading to the formation of the $Li_{22}Si_5$ phase results in a 400% change or four-fold increase in volume. This huge volumetric expansion is catastrophic triggering the formation of large amount of mechanical stresses in the active material leading to pulverization or cracking of the electrode.

Table 6: Unit cell volume, unit cell formula, crystallographic unit cell volume per Si atom and theoretical density of different crystal structures in the Li-Si system [122]

Compound / crystal structure	**Unit cell volume (Å)**	**Volume per silicon atom (Å)**
Silicon cubic	160.2	20.00
$Li_{12}Si_7$, ($Li_{1.71}Si$) orthorhombic	243.6	58.00
$Li_{14}Si_6$, ($Li_{1.71}Si$) rhombohedral	308.9	51.50
$Li_{13}Si_4$, ($Li_{3.25}Si$) orthorhombic	538.4	67.30
$Li_{22}Si_5$, ($Li_{4.4}Si$) cubic	659.2	82.40

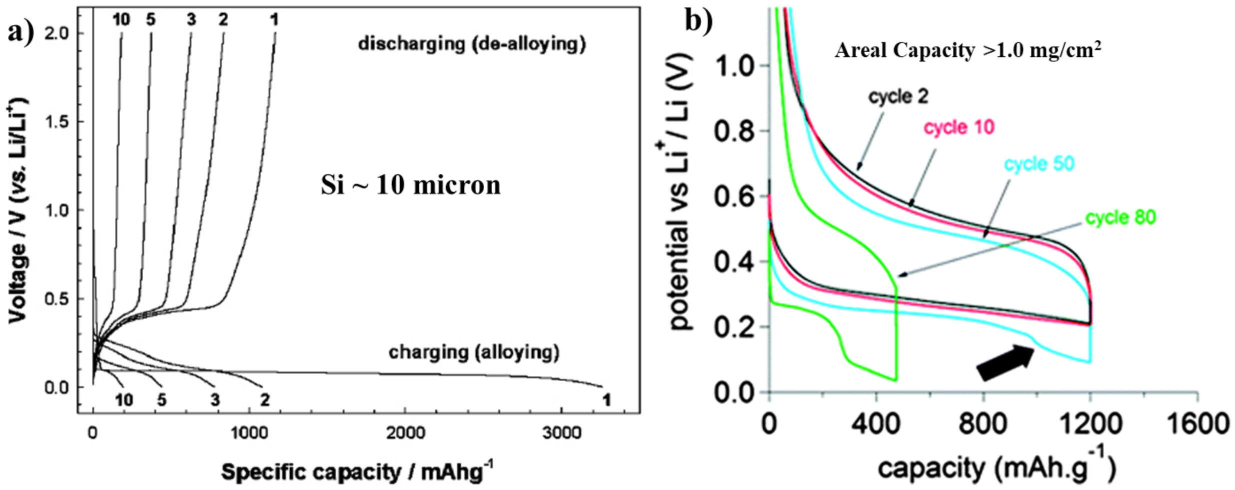

Figure 23 Discharge - charge profiles for a) micro-Si (10µm) and b) Si with areal loading > 1.0mg/cm2 under galvanostatic conditions in a voltage window of 0.0-2.0V (vs. Li/Li+) [149-150]

However, observations made through in-situ X-ray diffraction measurements by Dahn *et al* indicated that the electrochemical alloying of *Li* with crystalline *Si* at very low current rates initially resulted in the amorphization of *Si* forming Li_xSi alloys followed by recystallization to form $Li_{15}Si_4$, the highest lithiated phase having a theoretical capacity of 3579 mAh/g [124]. During the first cycle, *Li* alloys with *Si* by solid state diffusion to form a new Li_xSi phase which is amorphous in nature along with the unreacted *Si* phase. The presence of this dual phases results in a horizontal flat voltage profile during the discharge reaction, where the available free energy is consumed in the nucleation and growth of this new amorphous phase. A typical voltage profile of crystalline silicon observed during cycling at a current density of 100 mA/g is shown in Figure 23 [150]. The presence of the flattened voltage profile at ~0.2 V during the lithiation/alloying reaction in first discharge cycle indicates the presence of crystalline silicon and Li_xSi phases. A very high initial first discharge capacity of ~3700 mAh/g was observed followed by a huge initial irreversible loss of ~75%, resulting in a lower charge capacity of only ~880 mAh/g. Furthermore, the specific capacity decreases to less than ~500 mAh/g by the end of 5th cycle resulting in a poor electrochemical cycling performance of crystalline *Si*, ruling out its potential to replace graphite as a higher capacity anode.Mechanism of failure in silicon anodes

As mentioned in the previous section, bulk crystalline Si exhibits a huge first cycle irreversible (FIR) loss during the initial discharge – charge cycle followed by rapid fade in capacity, thus, limiting its use in major commercial applications. Initial studies performed to understand the failure mechanism observed that the huge first cycle irreversible loss was induced due to the material pulverization and loss of material electrical conductivity [150]. However, other operating phenomenon such as presence of surface oxides [73, 151] and solid electrolyte interphase (SEI) films [152] were also found to be responsible for the poor electrochemical performance of the bulk crystalline Si based anodes which are described in the following sections.

1.2.10.2 Loss of Active Silicon Material in Anode

The huge volumetric changes during the alloying / de-alloying reactions result in build - up of the mechanical stresses which lead to pulverization and loss of inter-particle conductivity/contact. The loss in electronic conductivity is demonstrated by measuring the internal impedance / resistance of the electrochemical cell. Galvanostatic intermittent titration technique (GITT) experiment, was conducted by Ryu *et al* by applying a current density of ~100 mA/g for

10 minutes to allow the de-lithiation / lithiation reactions to occur following which the current was switched off for the next 20 minutes [125]. Quasi open circuit voltage (QOCV) and closed circuit voltage (CCV) were monitored and measured when the system was subject to electrochemical agitation under galvanostatic conditions and at rest, and the difference between the two recorded potentials was used to calculate the internal resistance.

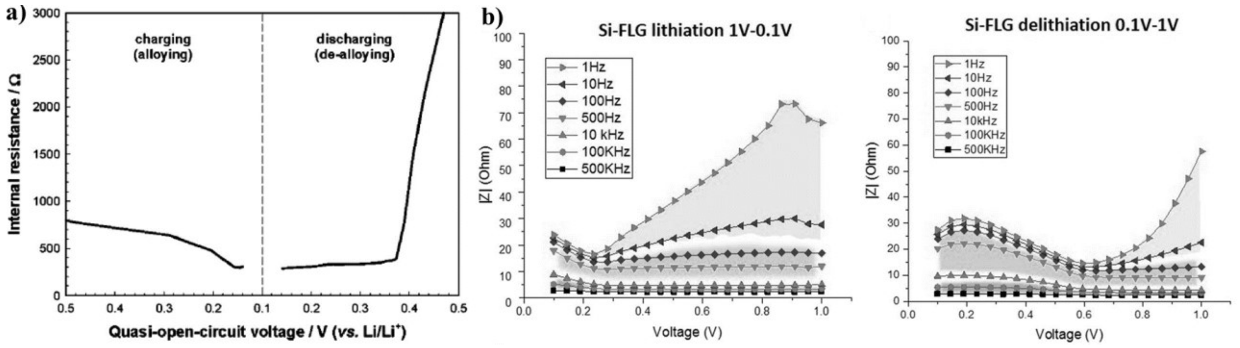

Figure 24 Variation of internal impedance with voltage in a) silicon based anode and b) Si – FLG during lithiation and delithiation [125, 153]

The variations in internal resistance (shown in Figure 24) indicates a decrease in the internal impedance / resistance due to improvement of inter-particle electrical contact induced by the volumetric expansion of the silicon particles. The Li_xSi alloys that are usually formed during the lithiation process may also influence the decrease in internal resistance.[125] However, the internal resistance increased rapidly beyond ~0.4V during the de-alloying cycle which is due to the near completion of extraction of *Li* from the Li_xSi alloys which is almost complete during the de-lithiation process. This phenomenon subjects the active material to huge tensile forces due to volume contraction. The *Si* particle in the anode undergoes cracking, resulting in a loss of conductivity or capacity due to the ease of micro-crack generation and propagation, under these tensile force fields. The formation and propagation of cracks / pulverization of the active Si material during the electrochemical charge / discharge cycling has been observed and confirmed by using in-situ AFM and SEM methods. [126-127, 143]

1.2.10.3 Formation and Effect of Solid Electrolyte Interphase (SEI):

Solid electrolyte interphase layer (commonly referred to as SEI layer) is an electrochemically generated protective film that forms / deposits on the surface of the negative electrode during the initial cycle because of electrolyte decomposition. In the case of Si, the components of the SEI layers are mainly composed of lithium alkyl carbonates such as LiF, $Li_xPO_yF_z$, Li_2CO_3, SiF_x, Li_2O etc [75-77]. The formation of SEI layer is a dynamic process which continues to progress, especially in the case of Li alloying based anodes, as a result of which, new surfaces are formed continuously. Further electrolyte decomposition or SEI formation is triggered on the fresh surfaces as a result of material cracking and pulverization. The lithium lost during the formation of the SEI layer products is irreversible, and hence, results in the first cycle irreversible (FIR) loss, lower coulombic efficiency and capacity fade[76]. Additives such as vinylene carbonate (VC) [80, 154] and fluoroethylene carbonate (FEC) [79-80] are usually added to the electrolyte to suppress and stabilize the formation of SEI which has indicated to lower the first cycle irreversible loss and improve the cyclability of the electrode. Though there are considerable controversies concerning the mechanism of SEI formation, several mechanisms are proposed and the major models to explain SEI formation are as listed below: [109, 155-157]

The Peled model (Figure 25a)

This is the primary mechanism to describe the SEI film established via a surface reaction. The surface reaction is stepwise and preferential reduction of certain electrolyte components. The formed layer is with integral structure except for several Schottky defects for Li ions migration.

The potential difference $\Delta\phi_{M/Sol}$ contains three components $\Delta\phi_{M/Sol} = \phi_{M/SE} + \phi_{SE} + \phi_{SE/Sol}$. The deposition-dissolution process of an electrode covered by an SEI involves three consecutive steps, which are described schematically as follows:

a) Electron transfer at the metal/SEI interface:

$$M^0 - ne^- \rightarrow M^{n+}{}_{M/SEI}$$

On cathodic polarization a metallic cation sheds its solvent molecules, crosses the solution / SE interface, and enters inside a vacancy in the SEI.

b) Migration of cations from one interface to the other when ${t_M}^+ = 1$ (or migration of anions when ${t_X}^- = 1$)

$$M^{n+}{}_{M/SEI} \rightarrow M^{n+}{}_{SEI/Sol}$$

The metallic cation migrates through the bulk of the SEI by Schottky vacancies mechanism.

c) Ion transfer at the solid-electrolyte interphase/solution (SEI/sol). For ${t_M}^+ = 1$

$$m(solv) + M^{n+}{}_{SEI/Sol} \rightarrow M^{n+}\ m(solv)$$

Finally, it reaches the active surface and accepts an electron from the conducting material and becomes a member of the lattice of the anode material. All the above reactions are qualified to be the rate-determining step (r.d.s.) however, it was found that ionic migration through the SEI is the rate-determining step for many systems due to the thickness of the SEI layer and poor ionic conductivity of pure solid crystals at room temperature. In addition, it was found that the rate of reaction with anode material or the nucleation of the lithium is affected by the interfacial resistance.

The Mosaic Model (Figure 25b)[158-159]

The SEI formation involves several reductive decompositions on the surface simultaneously forming a mixture of insoluble multiphase products which deposit on the anode.

The formed SEI has a mosaic morphology and the diffusion of Li ions contributed by both the defects and the grain boundaries of the products. The transport of ions through the SEI, which consists mainly of polycrystalline material, takes place by mobile point (Schottky or Frenkel) defects. As a result, the contribution of the grain boundaries of these organic/inorganic microphases must be taken into account which was absent in the initial Peled model [155].

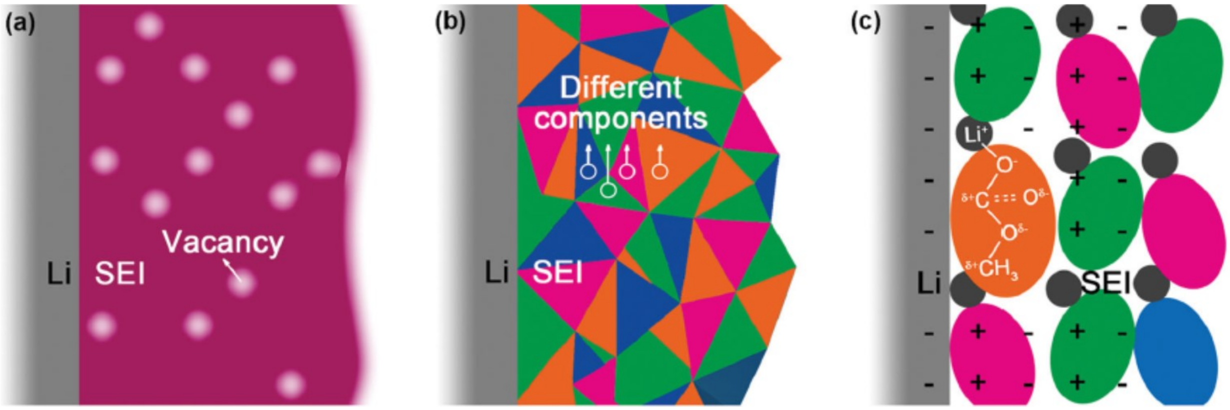

Figure 25 Schematic representation of SEI layer and its formation. a) The Peled's model, b) Mosaic model and c) Coulombic interaction mechanism

In the mosaic model, as a part of the electrical impedance studies (EIS), one layer of SEI is characterized by at least four RC elements in series combination and a Warburg impedance to the first approximation. These RC elements represent two interfaces: electrode/SE and SE/solution, SEI ionic resistance and capacitance, and grain-boundaries resistance and capacitance. Each additional sublayer adds an additional three RC elements. In some cases, the grain-boundary resistance may be larger than the ionic (bulk) resistance of the SEI.

The Coulombic interaction mechanism (Figure 25c) [157, 160]

After the surface reaction, the decomposition products are lined up with positively charged Li ion as a "head" and the partially positively charged carbons as a "foot". The unique double electric layer allows the products to attach themselves to the existing film. Compared to the other two models, the SEI layer constructed by Coulombic interaction mechanism can have superior stability due to the stronger adhesion induced by the ion pairs.

1.2.10.4 Presence of Silicon Surface Oxide Layer

Bare silicon surface depending on the synthesis method and origin usually has a surface oxide layer (SiO_2 or SiO_x) with the thickness of this oxygen containing layer dependent on the particle size. With the reduction of particle size, there is an increase in specific surface area (SSA), which results in an increase in the coverage of surface oxide. Commercial nanoparticle silicon may contain upto ~26 wt% of SiO_2 which is electrochemically inactive, resulting in low overall specific capacity of Si electrode.[73] Etching of these Si nanoparticles with hydrofluoric acid for around 30 minutes have the ability dissolve the surface oxide and the oxide-free silicon particles thus obtained have shown a significant improvement in specific capacity (**Figure 26**)[73].

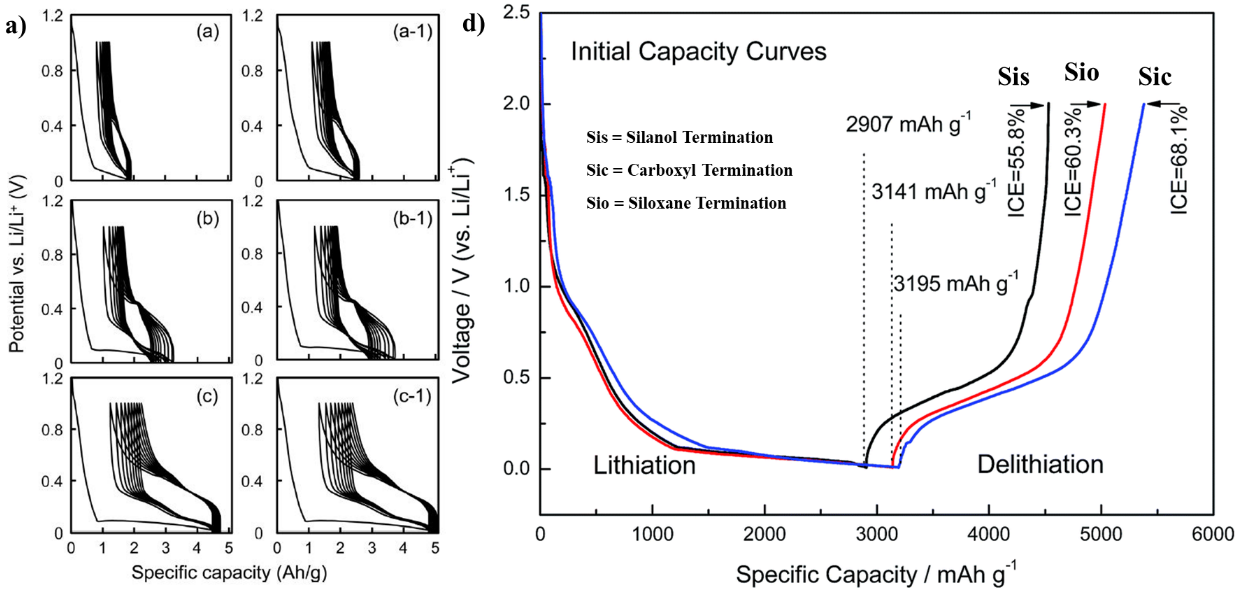

Figure 26: Specific capacity vs. potential of Si electrode during first 10 cycles. (a) and (a-1) commercial as-received Si, (b) and (b-1) etching for 10 min, (c) and (c-1) etching for 30min [73, 161]

Silicon sub oxides such as SiO_x , unlike SiO_2, are electrochemically active and can contribute to first cycle irreversible capacity loss when present on the surface of the active *Si*, due to the reduction by Li to form Li_2O and *Si* during the lithiation process [73-74]. However, the use of HF acid both in the laboratory and large-scale industry (especially for batteries in EV) poses issues with health, equipment degradation, handling, and costs (installation / running). The effect of surface oxide is highly prominent in nano particles due to high specific surface area associated with nano particles. Additionally, different synthesis methods result in different amounts of silicon suboxides and silicon surface oxide, with different surface group termination and different SEI layer thus, exhibiting different performance.

1.2.11 Approaches to Address Issues with Silicon Based Anode

To address the huge first cycle irreversible loss and rapid capacity fade associated with silicon-based anodes, several different approaches have been developed as discussed in the subsequent sections.

1.2.11.1 Nano/Sub Micro and Nanocrystalline Silicon

Several reports indicate that the reduction in the particle size or the crystallite size of the active material significantly improves the retention of specific capacity [142-143, 162-164]. Huggins *et al* suggested the existence of and determined a critical radius of Si below which, the fracture of the particle would not occur and this value depends on the fracture toughness and the lithiation extent of the lower specific volume phase [142]. Consequently, the percentage of volume expansion or the amount of strain generated in the anode material was established to be directly proportional to the amount of lithiation in the Si material. The use of silicon nanoparticles as anode was first reported by Liang *et al* and obtained a reversible specific capacity of ~1700 mAh/g by the end of the 10th cycle.[165] Although inferior to the cyclability performance of graphite-based anode systems, there was a major improvement when compared to bulk crystalline *Si* based electrodes. Over the years, many attempts have been made to synthesize nanosized silicon using different techniques and routes all of which have demonstrated better capacity retention [82, 150, 166-167]. A recent study reported a strong particle size dependence on the cyclability, where, silicon particles below 150 nm in diameter did not fracture while surface cracks developed in particles of larger sizes resulted in the fracture of material upon lithiation demonstrating the influence of reduced particle size on the electrochemical response minimizing or even eliminating the adverse catastrophic effects of the colossal volume expansion related stresses [143].

1.2.11.2 Si Composites Based on Active-Inactive Matrices

The formation and generation of the inactive phase in the electrode using *in situ* electrochemical reaction with Li^+, (for example in the case of SnO_2) results in the generation of Li_2O by irreversible consumption of Li^+, which nevertheless, serves as glassy Li^+ conductor as well as a binding matrix serving as a spectator / inactive 'glue' phase holding the active electrode material thus, accommodating the huge volume expansion of *Sn* [140]. The sub-oxides of Si (SiO_x) are also studied similar to Sn, where in the lower suboxides of silicon ($SiO_{0.8}$) exhibited higher capacity (~1600 mAh/g) however, with poor cyclability. Higher suboxides of Si (such as – $SiO_{1.1}$) however, exhibited lower capacity of ~800 mAh/g and as expected, a better capacity retention [168]. These Si suboxide based anode materials still had a huge first cycle irreversible loss of ~50%, arising from the formation of electrochemically stable Li_2O on the anode by the irreversible reaction of SiO_x by *Li* in the first discharge cycle [166].

However, the direct generation and synthesis of ‘active-inactive’ component materials via *ex situ* approaches that are non – electrochemical in nature thus, preventing the extraneous consumption of *Lithium* to form inactive species that serve to bind and hold the lithiated phase. The *ex situ* generation method of electrochemically active - inactive thermodynamically stable electrode phases serve to directly expose the active phase for Li reaction thus, significantly reducing the FIR losses to values considerably lesser than 50% as observed in the Fuji® tin oxide systems wherein the oxide is electrochemically reduced to active-inactive phases thus absorbing a large amount of *Li* that is irreversibly lost. The thermodynamic Li – inactive phase, in the *ex situ* approach, is homogenously distributed in the thermodynamic Li-active phase. This eliminates the irreversible consumption of Lithium leading to the FIR loss of *Li*. Accordingly, TiB_2, *SiC, TiN,* and *C* have been researched and studied as potential inactive matrices for silicon based anodes by the Kumta et. al. [10-12, 24, 169]. Here, mechanical milling of bulk crystalline *Si* with the above-mentioned matrices was conducted to synthesize a homogenous phase, with *Si* dispersed uniformly in the inactive electrochemical matrix. These conducting matrices are electronically conducting and assist in the charge transfer mechanism associated with lithium alloying / de-alloying with silicon. Silicon obtained from these milling approached was either amorphous or nano – crystalline with very low capacities of ~350-400 mAh/g however, with a better and improved electrochemical cyclability when compared to commercial microcrystalline silicon.

1.2.11.3 Si Composites Based on Active-Active Matrices

While improving the cyclability of the anode compared to the bulk crystalline silicon using the active – inactive matrix approaches was attained reversible capacities were significantly lower compared to silicon’s theoretical capacity since, the inactive – material was heavier decreasing the overall capacity of the electrode. A matrix that is soft, ductile and lightweight is required to overcome this problem and to alleviate the internal electrode stresses generated during the electrochemical reaction. Carbon being much lighter than previously explored nitrides or borides; and mechanically soft, thus, serving as a good secondary matrix.

Composites of silicon and carbon were first developed in 1990s by Dahn *et al* by the decomposition of polymers of silicon / carbon such as polyphenylsesquisiloxane (PPSSO) and polymethylphenylsiloxane (PMPS) in the temperature range of 900°C - 1300°C [165]. The composites obtained at temperatures of ~1000°C showed a capacity of ~500 mAh/g and the capacity dropped to ~250 mAh/g when higher decomposition temperatures (~1300°C) were used. The electrochemical formation of inactive *SiC* at higher temperatures (~1300°C) resulted in lower capacity and composites with required Si/C composition was difficult to achieve using Si */ C* systems. Other precursors use pitch polysilanes [170-173] and epoxy silanes [174] also used higher decomposition temperatures to synthesize the *Si/C* composite. The obtained capacities from these materials, were low (<500 mAh/g) exhibiting huge, large first cycle irreversible loss, possibly due to oxygen presence and formation of *silicon carbide species* at high temperatures. Hence, research was directed utilizing silane gas (SiH_4) as the silicon precursor with a low temperature decomposition of ~500°C and below. For example, nanosized silicon particles of ~10-20 nm were deposited on carbon (KS6 graphite) by the decomposition of silane gas in a thermal chemical vapor deposition (TCVD) showed a reversible capacity of ~1000 mAh/g, with a low first cycle irreversible loss of ~26% and fade rate of only ~2% [175]. The excellent cycling performance of this *Si/C* composite was due to better adhesion of the silicon nano particles (~50 nm) to the surface of KS6 graphite. Even though the system showed better capacity, higher capacity retention, the TVD process of *Si* precursor gases to control the particle size, structure and composition was difficult. Ball milling is a simple and high throughput approach, where *Si* is milled with carbon and an organic polymer serving as diffusion barrier thus, preventing the diffusive reaction between *Si* and *C* induced during the process(which usually forms inactive *SiC)*, resulting in a homogenous *Si/C anodic* composite. [122, 169, 176]

1.2.11.4 Amorphous and Disordered Silicon

Amorphous silicon (*a-Si*) is devoid of any long-range order (similar to bulk metallic glassy materials) and consists of a large number of defects and free volume. The presence of this disordered structure distributes the volumetric expansion more homogenously upon lithium insertion, and the phenomenon of crack formation and propagation is considerably less catastrophic when compared to crystalline silicon [14-15, 177]. Hence, the mechanical decrepitation and pulverization of the active material is reduced giving rise to better capacity cyclability/retention. In LIB applications, *a-Si* thin films are grown on metallic substrates using physical vapor deposition (PVD) techniques following which they are directly assembled in coin cells without the addition of any material such conductive additives and binders [15, 25-26, 178]. *a-Si* film of ~100 nm thickness was deposited on a *Ni* foil by vacuum evaporation and it exhibited a high 1st discharge capacity of ~2500 mAh/g with a reversible capacity of ~2000 mAh/g stable upto 50 cycles.[178]

Maranchi *et al* developed and studied *a-Si* films (~250 nm thick) sputtered on *Cu* foil using RF magnetron sputtering system which exhibited very high first and second discharge capacities of ~4100 mAh/g and ~3800 mAh/g, respectively [26]. The films exhibited excellent capacity retention for ~29 cycles, after which there was a rapid capacity fade, resulting in a capacity of only ~1800 mAh/g at the end of 40 cycles. The good cycling stability of amorphous silicon even for a few cycles in this system was due to the efficient binding of silicon atoms to the current collector and structural integrity of the films [26]. *a-Si* can also be synthesized using a low pressure chemical vapor deposition reactor (LPCVD) by thermal cracking of silane gas (SiH_4) in the temperature range of 485°C - 500°C [6, 179] which was utilized in developing 3-D heterostructures, nanowires, nanotubes and core-shell structures, and will be discussed in the subsequent sections. Despite displaying better electrochemical performance in LIBs compared to bulk / micro / nano crystalline silicon, *a-Si* films generated by PVD methods (like evaporation and sputtering) are usually expensive and characterized by low synthesis and manufacturing outputs, thus, preventing them from being implemented for large scale production.

1.2.11.5 Silicon - Based Nano/Micro Scale Architectures

Over the past years of Si anode development, interest was shown on anodes consisting of silicon architectures by engineering the morphology of the material to achieve desired improvement in the electrochemical performance of LIBs. The architectural parameters played important role in reducing the stresses developed during the volume expansion process, thus, preventing / delaying the onset of crack formation, which eventually leads to capacity fade and pulverization. These architectures are either single phase, containing only silicon such as nanowires, nanotubes, porous silicon, or multicomponent heterostructures such as core-shells and bio-inspired structures. These nanostructures are comprised of either the amorphous or nanocrystalline state. Among many reported literatures on Si architectures, few relevant and analogous representative systems have been selected and discussed in the subsequent sections:

1.2.11.6 Silicon Nanowire Based Electrodes

The use of Si nanowires as anode material in LIB demonstrating good gravimetric capacities along with good cyclability was initially reported by Chan *et al* [3] and immense interest to explore one dimensional (1 – D) nanostructures was generated due to their ability to offer strain relaxation as to resolve the issue of mechanical failure in Si anodes. The growth of Si – nanowires is typically guided by vapor – liquid – solid (VLS) mechanism during the decomposition of silane on various substrates (stainless steel) which were employed directly without the use of any additional binder or conductive additives (**Figure 27**). An initial low first cycle irreversible loss of ~27% and reversible capacities >3000 mAh/g were obtained during initial 10 cycles. In the case of Si nanowires, an increase in overall length and diameter resulted from the volumetric expansion and the internal stresses generated due to this were less damaging and facile, leading to superior cycling stability.

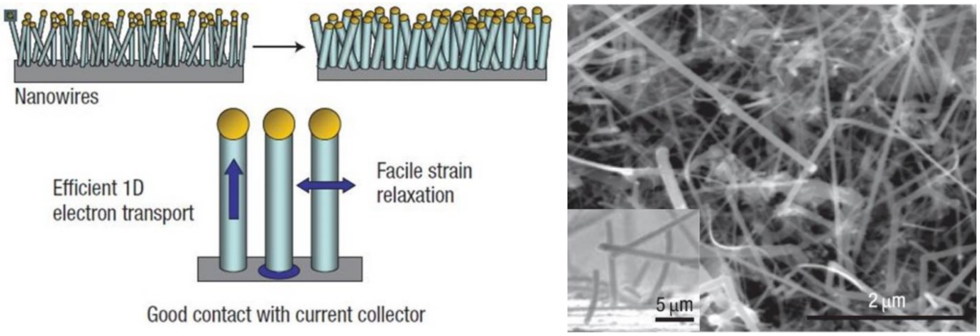

Figure 27: Pictorial representation of Si nanowires developed directly on substrate and SEM image of SiNWs [3]

Additionally, the strong adhesion of these nanowires to the underlying current collector contributed to a good electronic transport and hence, good rate characteristics. The FIR loss of these nanowires (~27%) is still higher when compared to the carbon based anodes, possibly due to SEI layer formation[3] which could be lowered by coating the nanowire surface with carbon [180-181] or copper [181], leading to decrease in electrolyte decomposition thus, improving charge transfer kinetics. The long - term stability, sustained coulombic efficiency and areal loading are issues that still need to be addressed.

1.2.11.7 Silicon Based Heterostructures

Silicon based heterostructures are multi-component electrode systems containing crystalline or amorphous silicon along with other electrochemically active/inactive phase(s). These electrode structures are usually designed employing a bottom up approach, which result in a morphology mitigating the stresses developed due to the volumetric expansion induced in silicon by lithiation. Silicon heterostructures when carefully designed are electronically conductive and offer advantages in terms of enhanced charge transfer kinetics, reduced internal impedance and better rate capability when compared to pure silicon - based nanostructures.

Over the past decades, carbon nanotubes (CNTs) due to their chemical stability, mechanical and electrical properties have generated immense interest and specialized applications. [29-30, 182] Thus, CNTs exhibit the potential to be employed as an secondary component in the electrode serving as a support (inactive matrix) for silicon. The use of Si/CNT heterostructures as high capacity Li-ion anodes was first demonstrated by Wang *et al* by using a 2-step CVD approach to generate these electrodes.[6] The method involved growth of long vertically aligned multiwall carbon nanotubes (MWCNTs) on quartz substrates followed by growth of silicon droplets by the low temperature decomposition of silane (SiH_4) (**Figure 28**). An initial low FIR loss of ~20% with reversible charge / discharge capacities > 2050 mAh/g (@ current rate of ~100 mA/g for 25 cycles) were exhibited by these structures. The development of carbon coating on similar systems by other groups improved the cyclability and coulombic efficiency of these CNT/Si heterostructures [183].

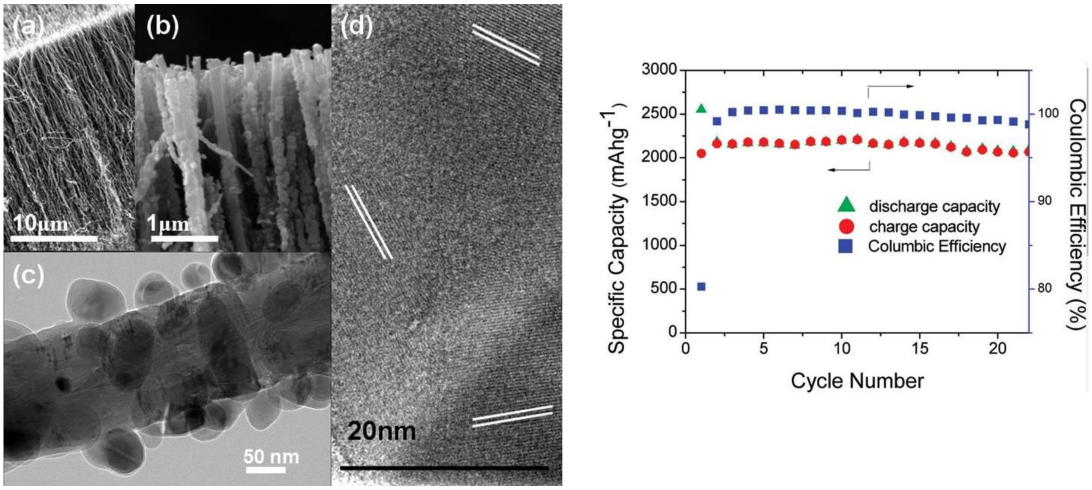

Figure 28: Left: SEM, TEM & HRTEM images of Si droplets coated on vertically aligned carbon nanotubes (VACNTs); Right- Specific Capacity plot of heterostructures cycled galvanostatically at ~100 mA/g in the voltage range of 0.02 to 1.2 V vs. Li+/Li [6]

Another study developed silicon coated as droplets on annealed carbon black particles which was later coated with carbon using CVD [184]. This slurry-based electrode resulted in a system with self-assembled hierarchical rigid sphere with open interconnected diffusion channels, delivering specific capacities close to ~2000 mAh/g (at C/20 rate) for 100 cycles. The good interface development between *C* and *Si* in these electrode structures is assumed to be critical in maintaining the mechanical integrity of the silicon droplets to the inactive system, by minimizing the strain mismatch induced by the volume changes [6]. However, the interface may fail to maintain its integrity in the heterostructure at higher current rates due to high Li flux and variation in the diffusion pathways. Krishnan *et al* developed a strain-engineered structure consisting of aluminum, silicon and carbon exhibiting good rate characteristics, to address this issue[185]. Carbonaceous nanorods were deposited on stainless steel substrates by employing oblique angle deposition (OAD) technique in a sputtering system. Subsequently, a layer of aluminum was deposited on these carbon nanorods followed by silicon to form a composite electrode with a nanoscoop like morphology, exhibiting a reversible specific capacity of ~412 mAh/g at high current rates of ~51.2 A/g for over ~100 cycles. Implementing aluminum as an interlayer at C/Si interface facilitated the transition of strain from silicon to carbon, thus, resulting in the minimization of lattice and crystallographic strain mismatch at the interfaces. In a different study, $TiSi_2$ nanonets were selected as a strong and conductive core and decorated with CVD derived silicon droplets. [186] These $TiSi_2 - Si$ heterostructures cycled at a current density of ~8.4 A/g in the voltage window 0.15 V – 3 V vs. Li^+/Li, displayed specific capacities >1000 mAh/g with a low capacity fade of ~0.1% between 20th and 100 cycles. However, the cyclability was adversely affected when the voltage window was increased by reducing the lithiation (lower) cut-off voltage to ~0.03 V. Lower voltages may result in the lithiation of the $TiSi_2$ core along with additional lithiation of Si, resulting in the disintegration of the heterostructure. Similar study on heterostructures of $TiC/C/Si$ indicated that TiC/C served as a mechanically stable and electrically conducting support core resulting in reversible specific capacities of ~3000 mAh/g (cycled at current density of ~0.84 A/g) with specific capacity retention of ~92% by the end of 100 - 120 cycles. [187]

In the more recent years, egg-yolk shell and pomegranate based electrode nanostructures inspired by nature, were developed that exhibited higher specific charge / discharge capacities and better capacity retention for over more than 1000 cycles.[188] The egg-yolk shell structure was achieved using commercial silicon nanoparticles which were sealed inside a conformal, self-supporting thin amorphous carbon shell with a void space which was designed to allow free expansion of silicon without breaking the outer shell. The system exhibited reversible specific capacity of ~2800 mAh/g (at a charge – discharge rate of C/10) for over 1000 cycles with a specific capacity retention of ~74% and a coulombic efficiency of ~99.84% in the stable region [188]. Using similar approach, these carbon encapsulated silicon hollow core shells were self-assembled to form a pomegranate type structure with hierarchical arrangement, resulting in a capacity retention of ~97% after 1000 cycles. The stabilization of SEI layer formation on the carbon and the accommodation of volumetric expansion during Si lithiation in the intra particle void spaces were inferred to be the main reasons for the improved cycling stability pomegranate and of the egg-yolk structures.

1.2.11.8 Pure Silicon Based Nanotubes

Silicon nanotubes (Si-NT) have attracted immense interest among strain engineered pure Si based structures, as Li-ion anodes, due to their good cyclability and long cycle life. The nanotubes are tubular structures / hollow cylinders of Si (based on architectural dimensions), synthesized using a sacrificial template by different methods. One-dimensional structure such as silicon nanowires exhibit facile strain relaxation, however, the nanotube structure exhibit large amount of unoccupied volume that allow the silicon to expand freely without cracking and pulverization. Park *et al* reported the use of silicon nanotubes as Li-ion anodes where nanotubes were synthesized by initially infiltrating porous alumina membranes with silicon napthalide, followed by their reductive decomposition to form silicon and etching of the alumina membranes to form hollow silicon nano tubes. [13] These Si nanotubes exhibited a reversible specific capacity of ~3200 mAh/g (at charge – discharge current of ~0.2C rate), a FIR loss of ~11%, good current rate characteristics with specific capacities approaching ~2800 mAh/g at higher current rates of ~5C (~15 A/g) and good cycling performance. The formation of a thin amorphous carbon layer on the surface of these silicon nanotube during the reductive decomposition of silicon napthalide was perceived to prevent continual electrolyte decomposition and promote the formation of a stable SEI layer.[13] A recent finding showed that double-walled silicon nanotubes consisting of a hollow inner tube composed of pure Si and an outer silicon – oxide layer (SiO_x) exhibited good cycling stability for over 6000 cycles(**Figure 29**).[22] The SiO_x layer on the exterior served as a robust mechanical layer clamping the inner tube directing the silicon to expand towards the interior, preventing the dilating surface from coming in contact with electrolyte.

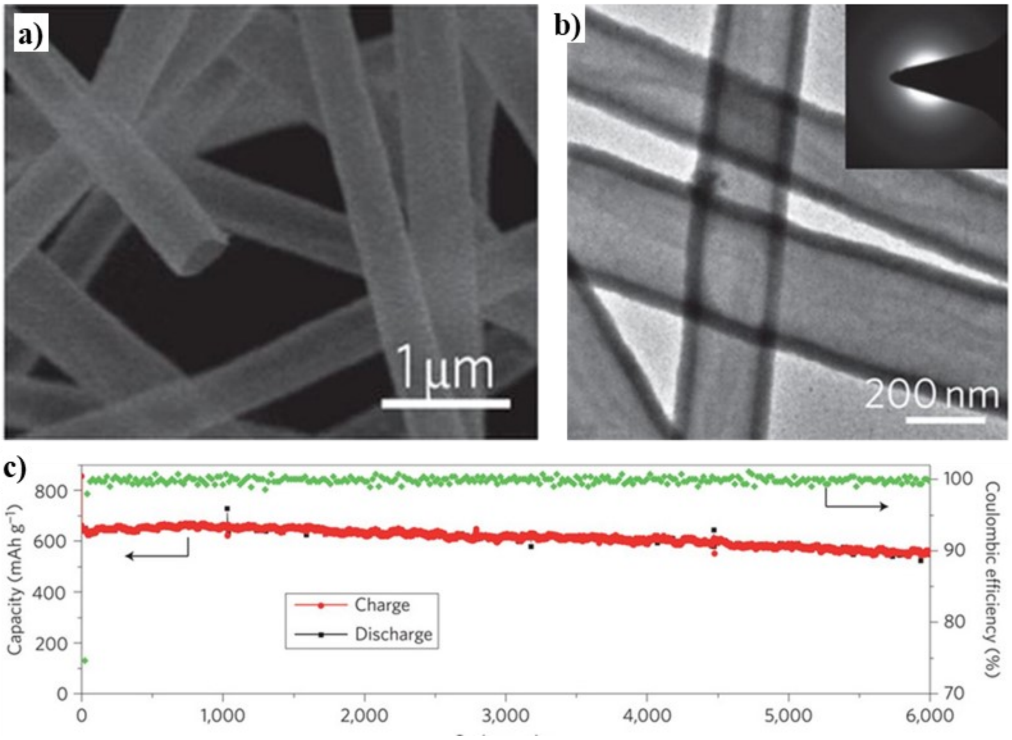

Figure 29: a) SEM and b) HRTEM images of the double walled SiNTs; c) long term cycling of double walled SiNTs at 12C [22]

Arrays of sealed vertically aligned silicon nanotubes were developed using a *ZnO* nanorod template (acting as a sacrificial system) on current collector followed by CVD deposition of silicon.[21] These free standing aligned closed end arrays of Si nanotube were directly tested in half cell configuration without employing any binders and showed good cycling, rate characteristics with an FIR loss of ~10-13% and capacity retention of ~80% after 50 cycles.

While silicon nanotubes seem to be apparent attractive choice, they suffer from major disadvantages such as the synthesis methods of these nanotubes, result in low experimental and commercial yields of the active electrode material. Furthermore, these methods employ the use of non-recyclable templating precursors and highly expensive reagents thus, increasing the overall production / manufacturing costs which may result in roadblocks and high cost of energy storage when used for actual implementation. Another major drawback is the low areal loadings obtained in these systems (<1 mg/cm^2) resulting in an overall low areal capacity (<1 mAh/cm^2) of these electrodes. In a lithium ion battery, an areal capacity in the range of 2-3 mAh/cm^2 is desired to sustain the lithium influx originating from the capacity of cathodes in full cell assembly. Hence, during the development of anode material in a LIB, it is significant to obtain a low first cycle irreversible (FIR) loss along with good cyclability and rate capability with an emphasis on obtaining high areal loading/ specific capacities and developing a synthesis approach suitable for commercial and practical production in terms of scalability and cost.

1.2.12 Effect, Importance and Impact of Synthesis Methods

Other factors playing an important role during the selection of materials for anode/cathode other than the material and its electrochemical properties, are, the cost of the raw materials / precursors, recycling costs, synthesis techniques and the environmental effects of by-products obtained on the production platform. From a commercialization perspective, significant attention is diverted towards the synthesis technique for generating electrochemically stable materials involved in the battery production since, it affects various factors such as manufacturing cost (direct, indirect, running, purchasing, maintenance, etc), availability of raw materials and subsequent environmental effects. A brief description of the synthesis methods, procedure and their respective operational principle employed in this study to generate different silicon - based anode systems are described in the subsequent sections.

1.2.12.1 High Energy Mechanical Milling

High energy mechanical milling (HEMM) is a metallurgical powder processing method which used mechanical energy of collisions to synthesize both equilibrium and metastable phases of various materials. It is primarily a top to down approach with its origin in powder metallurgy and is used for carrying out processes such as particle size reduction, alloying, solid state reactions (mechanochemical reduction reaction), amorphization (introduction of / increasing the crystallographic disorder) and mixing of materials. HEMM has become attractive technique for large-scale processing and production of materials / variety of powders due to the lower costs and faster processing times associated with it.

In this process, the initial materials (charge) are added to a milling vial (stainless steel or other hardened materials) along with a suitable grinding media (hardened steel balls, zirconia, etc) followed by sealing in an ambient or protective atmosphere. Subsequently, the vial is then subject to milling action for a desired amount of time during which the powder particles are clenched in between the milling balls and between the hardened surface of vial and the ball, thus, undergoing plastic flow under various stresses arising from the absorption of energy arising from the milling action. The stresses comprise of shear (attrition), impact (collision), impact (stroke) and compression which often result in cold welding, continuous flattening, rewelding and fracture of the particles depending on the mechanical behavior of the material. The fracturing of particles occurs due to two distinct processes: (a) the continuous action of mechanical forces resulting in work hardening and plastic deformation of the material leading to fracture by fatigue assisted failure; and/or (b) fracturing due to the development of brittle/fragile structures by work hardening. Furthermore, the secondary particles resulting from fracture process undergo rewelding to form bigger particles. Subsequently, due to the absence of driving force to form agglomerates on continuation of the process, a steady state equilibrium emerges between agglomeration and fragmentation, resulting in a decrease in average particle size due to the energy input. The milling process is also affected by other variables such as milling speed, ball to powder ratio, milling time, milling atmosphere, extent of filling the vial, etc. Hence, controlling and tailoring these process variables results in the desired reaction along with particle size and distribution.

HEMM is an inexpensive and rapid process capable of generating huge yields of the final desired material along with large scale production capability thus offering strategic advantages over conventional processing techniques. Since, HEMM is a complete solid – state processing technique which may not limited by the phase diagram stability and thus, may be utilized to synthesize alloys comprising of various immiscible elements. However, a major drawback of this process is that, longer milling times may result in the contamination of the product by the materials in the vial or milling media, influencing the properties and purity of the final product.

1.2.12.2 Electrodeposition / Electroplating

Electrodeposition / electroplating is an apparently simple technique developed and used over decades to make metal / alloy / composite coatings for decorative, protective as well as for other specific functional engineering applications (corrosion inhibition, tribological properties). The deposition process is usually conducted in an electrolytic cell by subjecting the substrate to an electric current or a voltage with respect to reference/ current collector. The electrodeposition cell is comprised of three main components distinguished by the phenomenon occurring at that component, namely, a) working electrode (where the deposition occurs); b) counter electrode, (serves as an inert or sacrificial electrode); and c) electrolyte, (serves as the medium for ionic conduction). Often a third electrode, termed as the reference electrode with a fixed potential (standard potential) is connected in the cell to accurately record the voltage of the working electrode. The deposition methods can be broadly classified into potentiostatic and galvanostatic mode. Under potentiostatic conditions, the working electrode serving as the surface for deposition, is maintained at a constant voltage with respect to the reference/sacrificial electrode; while, under galvanostatic conditions, the working electrode is subject to a constant current density resulting in the deposition. In both deposition modes, there is continuous supply of electrons to the substrate (working electrode) and the cations / positively charged species in the electrolyte deposit as a metallic / alloy / composite coating on the surface of the substrate by accepting these electrons. Variation in the deposition variables such as applied voltage, electrolyte composition, time of deposition and current density result in different morphologies of coating such as thick/thin films, nanowires, nanoparticles, nanotubes islands and core-cell structures, with the properties and nature of the deposit governed by Faraday's laws of electrolysis and electrochemical principles. Faraday's law of electrolysis was developed for the electrodeposition / electroplating system and is as follows: the amount of the material/coating deposited on the electrode is determined by the chemical change in the system which is directly proportional to the amount of electrons (measured in Coulombs, C) consumed during the process. Electroplating being a highly energy efficient, rapid and inexpensive process, has the ability to develop thin film material deposition on conducting substrates on a large scale.

Many of the electrodeposition processes developed in the industry employ aqueous based electrolytes, where ionic species are dissolved in water (solvent). They suffer from different drawbacks due to narrow electrochemical window (~1.2 to 1.8V) and thermal window (100C) due to the electrochemical instability and higher vapor pressure of water. This results in generation of unwanted hydrogen / oxygen gas (other species) during electrolysis, rapid evaporation and thermal instability restricting the operational conditions. The use of non-aqueous electrolytes such as organic solvent-based electrolytes, molten salts and ionic liquids mitigates these issues. The molten salts are usually eutectic mixtures and consist of a mixture of salts melted at high temperatures consisting the electro-active species forming the electrolyte and exhibit higher thermal stability window and good ionic conductivities. The molten salts used for plating experiments and extraction industry consist of eutectic systems ($LiCl$-KCl, KCl-$NaCl$, Na_3AlF_6 - Al_2O_3) with an operating temperature range of 400°C to 1200°C based on the system and application. On the other hand, ionic liquid based molten salt electrolytes (also termed as ionic melts, fused salts, liquid salts, ionic fluids or ionic glasses) have lower melting points and are liquid at room temperature (or in the range of -50C - 200C). Ionic liquid electrolytes are usually made of quaternary ammonium salts of linear hydrocarbons (for example tetraalkylammonium $[R_4N]^+$) or cyclic amines which can be either saturated (pyrrolidinium, piperidinium) and aromatic (imidazolium, pyridinium). Organic solvent – based electrolyte systems consist of electroactive species solvated in an organic medium (such as Propylene carbonate (PC), tetrahydrofuran (THF), acetonitrile, dimethyl sulfoxide (DMSO) and N, N dimethylformamide (DMF)) with appropriate dielectric strength. However, the ionic conductivity of electrolytes is lower than that of aqueous systems due to lower disassociation constants, lower mobility of solvated pair and a supporting electrolyte is often added to improve their conductivity.

1.2.12.3 Chemical Vapor Deposition (Low Pressure / Thermal) Method

Chemical vapor deposition (CVD) is employed to deposit discontinuous particle coatings or uniform thin films of different materials on a substrate (conducting or insulating) for products in data storage, microelectronics components, cutting tools, solar products, medical equipment, and other end-use applications. The CVD process generally involves, introduction of one or more volatile precursors into a batch / continuous reactor to decompose and/or achieve a reaction on the substrate to obtain the desired material. The reactions occurring inside the reactor are governed by chemical thermodynamic laws, (which determine the free energy change and the driving force of the reaction), as well as, by kinetic theory of reactions, which influence the diffusion and transport (or rate-control mechanism) phenomenon in the reactor. Modification of this technique as well as the process parameters results in a more uniform / desired coating on the substrate when compared to other physical vapor deposition methods such as thermal evaporation, e-Beam evaporation or DC/RF sputtering which usually from a non-conformal coverage due to low atomic migration distances and impurities. The flow rate of the carrier gases, substrate temperature, reactor pressure, etc. are different operational process parameters which influence the CVD process and different morphologies such as particles, continuous thin films, one dimensional structures (such as nanowires/nanofibers) and other complex architectures can be obtained.

Carbon nanotubes [29-30, 182], have been used in various applications such as catalyst supports [189-191], energy storage systems [5-6, 192-195], chemical / bio sensors [196-198] etc. due to their superior electrical, mechanical and corrosion resistant properties. CVD presents an economical and simple method for producing CNTs at controlled temperatures and pressures (both localized and ambient conditions) along with higher yields and purity when compared to other processes (such as laser ablation, arc discharge, etc.) used for synthesizing CNTs [199]. CNTs can be synthesized in multiple architectures, morphology and forms such as thick/thin films on substrates, powder form, coils, springs, straight or entangled and vertically aligned structures.

Better control of process as well as fundamental parameters for the growth and development of these architectures is offered by CVD, thus, making it a coveted technique for the production of CNTs. In energy storage research especially in Li-ion batteries, Si/CNT based anode nanostructures synthesized by injection of vaporized liquid or gaseous precursors using CVD method exhibited high specific capacities and better rate capabilities [5-6, 195]. The CVD process assists the CNTs to develop an architecture that is long (high aspect ratio), dense and vertically aligned on a substrate, playing a significant role in the improvement of electrochemical performance of the CNT/Si composite anode structures.

2.0 Objectives

2.1 Limitations of Silicon-Based Anodes

Although silicon has a very high theoretical specific capacity of ~4200 mAh/g, it still suffers from huge volumetric changes which occur during charge/discharge (or alloying/de-alloying) processes of the bulk crystalline silicon leading to the pulverization of the material. This phenomenon subsequently, results in the loss of intra – particle and inter – particle electrical contact along with the failure of anode / substrate interface, adversely, affecting the performance in lithium based electrochemical system such as:

➢Huge first cycle irreversible loss (>80%) resulting from the loss of active material due to pulverization

➢Increase and huge capacity fade (>5% capacity loss/cycle) in subsequent cycles from continuous breakage of the active material, restricting the long cycle life

➢Continuous formation of solid electrolyte interphase (SEI) layer on freshly formed surfaces of pulverized particles resulting in the irreversible consumption of lithium, leading to poor coulombic efficiency and capacity fade

Due to these drawbacks and disadvantages, the specific capacity of macro crystalline silicon-based anodes decreases to less than ~100 mAh/g in 20 - 25 cycles, preventing commercially available crystalline Si to replace graphite as the anode for high energy density anodes.

2.2 Hypothesis and Approach

The huge first cycle irreversible (FIR) loss followed by rapid capacity fade in Si based anode systems can be reduced by avoiding the pulverization of materials during electrochemical cycling. It is possible to minimize the mechanical strain and stresses resulting due to the volumetric changes during the lithiation and de – lithiation reactions by controlling the morphology, particle size and microstructure along with using different supporting active/inactive matrices etc. Few of the fundamental and basic principles for the different approaches and electrode designs which were developed and used in this dissertation are as follows:

➢**Reduction of particle and crystallize size:** The decrease in the crystallite / particle size to less than 200 nm diminishes the stresses / strain responsible for onset and propagation of microcracks which often lead to the fracture of bulk silicon. The dislocations generated during crystallographic transformation have shorter migration distances to the surface which result in relaxation of the internal stresses. Additionally, decreasing the particle size results in shorter Li^+ ion diffusion distances in the particle as well as in the electrode (electrolyte to silicon) suppressing the long migration of Li^+ thus, stabilizing the system as well as improving the rate characteristics of the battery.

➢**Decreasing crystallographic ordering:** Amorphous silicon has a high extent of disordered structure consisting of defects with a crystallite size of less than 10nm. The volume expansion of silicon occurs in an isotropic fashion in *a*-Si compared to that of crystalline silicon, resulting in a homogenous distribution of mechanical stresses. Additionally, the highly disordered phase suppresses the preferential migration of Li^+ in the particle thus, reducing crystallographic transformation interface.

➢**Supporting Matrix:** Designing and providing a supporting system with strong and robust mechanical properties along with continuous, long range electrical conductivity helps to accommodate the mechanical strain induced in silicon based electrode to help minimize the capacity fade contributing and improve charge transfer kinetics.

➢The design and development of strain engineered morphology and structures based on Si to withstand the volumetric expansion and maintain structural morphology without fracture upon repeated cycling.

2.3 Overall Objectives

The lithiation of silicon at low electrode potentials with respect to lithium metal forms an intermetallic alloy phase ($Li_{22}Si_5$) with the highest possible molar composition of Li. The theoretical specific capacity of this intermetallic (Li/Si = 4.4) is ~4200 mAh/g, leading to consideration of silicon as a promising anode material replace graphite for LIBs. The huge volumetric changes in the crystalline silicon as a result of de-alloying/ alloying (charge/discharge) processes cause pulverization of the electrodes from crystallographic level till macroscopic electrode level. This results in the loss of electronic continuity of the electrode along with the current collector resulting in significantly large capacity fade. The objectives of the work is to develop and study strategies to make silicon based anode nanostructures so that the anode performance improves in lithium ion battery by providing higher capacities (>1000 $mAhg^{-1}$), lower FIR loss (<15%), better capacity retention of ~80% for 300 – 1000 cycles and better rate capability delivering stable capacities @ $0.5Ag^{-1}$ – $2Ag^{-1}$; with manufacturing cost less than $125 per Wh to meet the demands of the energy storage market[200] along with obtaining a fundamental scientific and engineering understanding of the electrochemical process and material related phenomena occurring from the microstructural, structural and compositional perspective. Based on this, the work is directed towards achieving the above-mentioned goals by developing novel silicon based nanostructured composites using cost effective and scalable approaches and investigating their compositional, structural, and electrochemical characteristics.

The objectives of this dissertation are to develop cost effective strategies along with demonstrating the control to synthesize silicon – based nanostructures with an ability to deliver:

- Lower first cycle irreversible loss (FIR) (<15%)
- Higher coulombic efficiency (>99%)
- Good retention of capacity, rate capability and cyclability
- Improved specific capacity greater (~1000 mAh/g)

Additionally, efforts are made to develop scientific understanding, establish confidence in the ability of electrode design and further the knowledge about design and evolution of full cell. Based on these high-level design and requirements, the dissertation study and work are directed towards synthesizing Si based nanoparticle, nanocrystalline and amorphous composite electrodes trying to minimize the cost and improve the scalability. The specific research goals are thus outlined in the subsequent sections.

2.4 Specific Aims

The objectives of the proposal crafted in terms of the following specific aims as discussed under:

1. Specific Aim 1: To study the effect of process parameters and electrode – electrolyte interface coatings on the electrochemical performance of hollow silicon nanotubes.

MgO nanowires with high aspect ratio are synthesized by a simple hydrothermal route which are used as a template to uniformly coat amorphous silicon on the surface of the nanowires to obtain large quantities of silicon nanotubes. The MgO nanowires are leached in a mineral acid (HCl) to obtain hollow silicon nanotubes (h-SiNTs) that can potentially be extended for large scale production. Optimization of the h-SiNTs dimensions are further engineered by modifying the process parameters, resulting in controlled variation of their geometrical dimensions.

To improve the cyclability, reduce the FIR loss and to generate a stable SEI layer, the nanotubes are coated with a thin layer of amorphous carbon by the decomposition of ethylene in a CVD based reactor to generate core−shell hollow C@Si@C tubular nanostructure. The SiNTs and carbon coated SiNTs are mixed with binder and conductive additives and tested using conventional slurry-based electrodes in a Li/Li^+ electrochemical cell. A scientific understanding of the synthesis parameters and their influence on the structural dimensions of the h-SiNTs are studied and characterized. Furthermore, the impact of the dimensions of h-SiNTs and the presence of electrolyte – carbon – silicon interface on the ensuing electrochemical response in Li/Li^+ system is undertaken to optimize the performance of the core−shell hollow C@Si@C nanotubes.

2. Specific Aim 2: Synthesize and characterize silicon nanostructures from water soluble NaCl template and understand their electrochemical performance in LIBs.

The sacrificial template outlined in Specific Aim 1 is a major limiting factor for the large-scale synthesis of Si nanostructures. Sodium Chloride on the other hand, is identified as a commercially abundant, cheap, and environmentally benign material that, when used as a template, provides several advantages over traditional templates such as silica, anodized alumina oxide (AAO), MgO, and ZnO by avoiding the use of harsh reagents (HF, NaOH, HCl) and temperature conditions used to leach the template.

Particle size refinement will be obtained by high energy mechanical milling of commercial NaCl which will serve as template for chemical vapor deposition of silicon. The effect of the HEMM processing conditions on NaCl particle size and the development of Si nanostructures of different morphologies will be investigated and characterized. The Si nanostructures will be tested as slurry coated electrodes in a Li/Li^+ electrochemical cell and their electrochemical response will be analyzed depending on the morphology of the Si nanostructures.

3. Specific Aim 3: To synthesize amorphous silicon thin films using electrodeposition and study the effect of pulse current electrodeposition parameters on the morphology and electrochemical performance.

Electrochemical reduction of $SiCl_4$ from an organic solvent is conducted to obtain thin films of amorphous silicon (*a*-Si). These films are directly deposited on copper foil and assembled in the battery serving as a binder-less approach capable of producing thin films of amorphous silicon and easily scaled up to produce *a*-Si at a rate of 1-3mg/cm^2/hour to match industrial scale requirements required to generate 3mAh · cm^{-2} capacity electrodes [28]. Pulsed current electrodeposition (PED) technique will be employed to develop Si thin films on Cu foil. The effect of various frequencies of the pulsing cycle on the morphology of *a*-Si thin film deposits on Cu foil and their performance in LIB will be studied. The composition and morphology of the thin films will be thereby altered with the change in the frequency which correspondingly, will influence their performance in the lithium ion batteries.

4. <u>Specific Aim 4:</u> To synthesize vertically aligned carbon nanotube (VACNT) on copper electrode (VACNT-Cu) as versatile binder-less electrode platforms and characterize their structure, morphology and electrochemical performance for Li-ion batteries.

Electroless Ni plating is used to develop a uniform coating of Ni on Cu foils following which vertically aligned carbon nanotubes (VACNTs) are grown from a liquid-based carbon precursor and a floating iron-based catalyst. Silicon is then electrodeposited on these VACNTs by pulse current electrodeposition techniques outlined in Specific Aim 3 to generate Si/CNT core shell nanostructures. The system is used as a binderless electrode without any additives and tested in a Li/Li^+ electrochemical cell and their electrochemical performance will be systematically analyzed. Subsequently, modifications are made to the electrode to reduce the FIR loss and tested with LiNMC111 in a modified coin cell system to study the full cell performance at different negative / positive (N/P) ratio under constant current – constant voltage (CC- CV) mode resulting in modification of their electrochemical cycling performance.

<u>Characterization of the Si based nanocomposites</u>

- X-Ray diffraction and Raman spectroscopy is used to investigate the presence and nature of various phases present and also study the structure of silicon obtained by the various synthesis techniques outlined earlier.

- High resolution scanning electron microscopy (HRSEM) and transmission electron microscopy (HRTEM) is used to study the morphology of the interface structure of the nanocomposites developed. Specifically, the interface between the electrochemically active Si and the interface control agent (ICA) will be studied in detail.

- The electrochemical characteristics of the nanocomposites is investigated in detail and the structure-property correlation relating to the morphology and microstructure of the nanocomposites; the interface between the electrochemically active and the electrolyte interphase as well as the silicon and the interface control agent (ICA) and their electrochemical performance is established using a variety of galvanostatic , potentiostatic and impedance techniques with the vision to develop strategies for optimizing the synthesis parameters to develop nanoscale structures that exhibit the desired optimal performance characteristics of high capacity of (1000mAh/g), reduced FIR of (<15%) and good capacity retention of 80% at low (~25mAg^{-1} – 100 mAg^{-1}) and high (500 mAg^{-1} - 2000 mAg^{-1}) current rates as per the requirements of EV Everywhere project of Vehicle Technology Office - US Department of Energy. [201-203]

3.0 Silicon−Carbon Core−Shell Hollow Nanotubular Configuration

In recent years many approaches have been developed to address the challenges furnished by silicon anodes, few of which include reduction in particle size, use of ex-situ and electrochemically in-situ generated active-inactive nanostructured composites with strain engineering which were among the earliest approaches developed and proposed in the late 1990s and early 2000.[4-6, 204-214] These approaches demonstrated the potential of the concept to minimize and curtail the volume induced stresses.[4-6, 204-214] Although these early studies failed to achieve capacities close to the theoretical values predicted for Si, the strategies nevertheless, demonstrated the nanoscale composite architecture concept laying the pathway for achieving improved electrochemical performance by providing internal relaxation avenues for stresses generated during the lithiation and delithiation cycles.[4-6, 204-214] Subsequently, the mid and late 2000 witnessed the development of nanowires, core-shell heterostructure composite architectures, nanoshells and hollow nanotubes of silicon exploiting the nanoscale aspects further realizing the potential of the system to display high capacity, good cyclability and low capacity fade as a result of the system possessing enhanced mechanical properties due to the exploitation of the nanostructured architecture.[4-6, 204-215] Silicon nanotubes consequently, offer hoop stress/strain relaxation similar to or better than the one dimensional nanowires by restricting the thickness of the hollow tubular structures to few nanometers and moreover, providing shorter diffusion distances for Li^+ ion thus, improving the rate capability combined with the much needed cycling stability.[4, 210-211, 215] However, the synthesis processes utilized to generate these morphologies suffer from high cost, poor scalability, longer processing times and low yield of the active material, due to the use of expensive raw materials/precursors/templates, use of specialized equipment, inferior efficiencies leading to loss of material during each fabrication step, detrimental environmental effects of by products and high energy input. [4, 207, 209-212, 215]

More recently a high throughput MgO nanowire template has been used to generate hollow silicon nanotubular (h-SiNT) configuration thus, establishing the approach as a viable economical and environmentally favorable method for large scale generation of Si nanotubes.[216] The process uses a low temperature method to prepare bulk quantities of recyclable MgO nanowire template from economic precursors (e.g. magnesium acetate, urea). The MgO template can be etched easily in dilute HCl which avoids use of highly corrosive HF acid generally required to dissolve inorganic templates such as SiO_2/SiO_x used for making hollow structures.[212] The use of MgO template also cuts down on the extra processing steps such as high temperature thermal oxidation when using carbon based templates.[211] These h-SiNT structures exhibit a specific capacity of ~1000 mAh g^{-1} at a current density of 2 A g^{-1} for nearly 400 cycles. However, these structures suffer from high FIR loss (~26%-27%) characterized by poor loading densities (~0.6-0.9 mg cm^{-2}) due to the thin wall thickness.

Core-shell silicon based structures have hitherto shown considerable promise in stabilizing the silicon nanostructures.[217-219] Both experimental and simulation studies (based on density functional theory and molecular dynamics) have indicated enhanced diffusion of Li^+ in layered structures analogous to phosphorene (such as SiS, SiSe, GeS), improvement in performance of anode materials by employing layered structures similar to carbon such as nitrogen doped graphitic layers or hexagonal boron nitride as capping agents and tailoring of the concentration and stress gradient in amorphous Si core by employing SiO_2/Al_2O_3 shell coatings.[220-223] Recent experimental studies on coreshell nanostructures comprising of Si nanorod core with TiO_2, SnO_2 or Ge as shell indicate improvement in the performance of coreshell nanorod arrays for micro LIBs.[217-219]

However, very few studies have been reported on generation of core-shell structures based on hollow nanotubes and evaluation of their performance in LIBs for charge storage capacity, stability and irreversible loss. In the current study, core-shell hollow carbon/silicon nanotubular (h-SiNT/C) architectures with optimized dimensions of the silicon core have been synthesized using a high throughout approach that is very much amenable for scale-up making it attractive as potentially, a commercially viable process. Optimization of the h-SiNTs dimensions was further engineered by modifying the process parameters resulting in controlled variation of their geometrical dimensions. Control of the h-SiNT physical characteristics translated to recording their marquee electrochemical performance of much reduced FIR loss, high loading density, attractive specific capacity as well as fade rate when tested in Li/Li^+ system. The core-shell hollow C@Si@C nanotubular configuration (h-SiNT/C) exhibit hybrid behavior, combining improved cycling stability of h-SiNTs showing no mechanical/microstructural damage in tandem with reduced FIR loss and improved loading density (areal capacity) thus, rendering them viable as next generation LIB anodes.

3.1 Experimental

3.1.1 Materials Synthesis:

The process for the synthesis, analysis, characterization and testing have been described in the subsequent sections according to the synthesis method.

3.1.1.1 Synthesis of Sacrificial MgO Template

A schematic representation of the entire process used for synthesizing the core-shell C@Si@C hollow nanotubes (h-SiNT/C) is shown in **Figure 30a**. Magnesium oxide (MgO) nanowires template were synthesized according to a modified published method.[224] Briefly, 6.44 g of magnesium acetate tetrahydrate (Aldrich) and 1.2 g of urea was dissolved in 75 ml and 25 ml of DI water, respectively and urea solution was added drop wise at a flow rate of 0.5 ml min^{-1}, to the acetate solution under vigorous stirring. The mixture was transferred into Teflon lined stainless steel autoclave (125 ml total capacity), heated to 180°C at 5 °C min^{-1} for 1 h and cooled down to room temperature. A colloidal solution was observed due to the formation of a white precipitate of magnesium hydroxide ($Mg(OH)_2$), which was washed thrice thoroughly with DI water and isopropanol to remove any unwanted dissolved products and collected on 0.5 μm PTFE membrane using vacuum filtration. The obtained $Mg(OH)_2$ at the end of filtration was then dried in a 60 °C oven overnight to evaporate the solvent. The $Mg(OH)_2$ filtrate collected was calcined in 5% oxygen - argon gas by first heating from room temperature to 310 °C at a heating rate of 3 °C min^{-1} for 7 hours and then to 500 °C at 1 °C min^{-1} for 1 hour, to enable dehydration and conversion of the hydroxide into MgO wires. The hydrothermal synthesis of MgO nanowire template has an output efficiency of ~ 95%-97% (~1.17 g of MgO nanowire template from one batch) as compared to the theoretical calculated value of ~ 1.21g of MgO.

3.1.1.2 Synthesis of Hollow Silicon Nanotubes (h-SiNTs)

A uniform Si layer was coated on MgO nanowire using low pressure thermal chemical vapor deposition system (LPCVD) during which 2% silane (SiH_4) diluted in argon gas was decomposed at 500 °C for different periods of time comprising 10 minutes (denoted thereafter as Si/MgO-10), 15 minutes (denoted thereafter as Si/MgO-15), and 20 minutes (denoted thereafter as

Si/MgO-20).[5, 205, 208, 215] The mass of MgO nanowire template used in Si - LPCVD was kept constant for all the experiments. The Si coated MgO consisting of Si/MgO core-shell structure was then dispersed in 6 N HCl solution and homogenized in a bath sonicator for 2 hours to dissolve the underlying MgO nanowires. After dissolution of the MgO, the resultant hollow silicon tubes (denoted thereafter as h-SiNT-10, h-SiNT-15 and h-SiNT-20 obtained after 10 min., 15 min. and 20 min. LPCVD deposition, respectively) obtained were thoroughly washed with DI water and isopropanol, and were collected on 0.5 μm PTFE membrane filters using vacuum filtration. Finally, any adsorbed solvent from the wet h-SiNTs was removed by heating to 100°C overnight in a drying oven. After silicon deposition, ~1.43g–1.62g of Si/MgO coreshell structures were obtained from 1g of MgO template. After etching the MgO core from Si/MgO coreshell, 0.4g–0.6g of h-SiNTs were obtained per gram of MgO template used. The output of Si/MgO and h-SiNTs obtained per gram of MgO template increases with the increase in time of deposition due to the increase in the amount of Si layer deposited on MgO nanowires.

3.1.1.3 Synthesis of Core-Shell C@Si@C Hollow Nanotubes (h-SiNT-15/C)

The h-SiNTs obtained after 15min of LPCVD deposition on MgO followed by acid etching (h-SiNT-15) were coated with carbon by thermal decomposition of a gaseous mixture of Ar and propene gas in CVD tube furnace under atmospheric pressure at 700°C for 15 min. to obtain carbon coated h-SiNTs (denoted thereafter as h-SiNT-15/C). The gas flow rates of Ar and propylene was 75sccm and 15sccm, respectively.

3.1.2 Materials Characterization:

X-ray diffraction studies were performed using Philips X'Pert Pro system with Cu Kα, λ = 0.15406 nm radiation (voltage = 45 KV and current = 40 mA). Scanning electron microscopy (SEM, Philips XL 30, EDS analyzer) was used to study the morphological and compositional analysis. Raman spectroscopy was performed using a Renishaw in-via Raman microscope equipped with a 633nm red laser to evaluate the vibrational and rotational modes of h-SiNTs. High resolution transmission electron microscopy (HRTEM) studies were conducted using the JEOL JEM-2100F microscope to obtain the TEM images and SAED patterns for the h-SiNTs. Brunauer–Emmett–Teller (BET) method performed on a Micromeritics ASAP 2020 instrument was used to obtain the N_2 adsorption-desorption isotherms and measure the specific surface area (SSA).

3.1.3 Electrochemical Characterization of h-SiNTs and h-SiNT-15/C

Slurries of h-SiNTs (h-SiNT-10, h-SiNT-15, h-SiNT-20) and core-shell h-SiNT-15/C were prepared by mixing 50 wt.% of active material (h-SiNTs and h-SiNT-15/C) with 40 wt.% binder (sodium alginate, MP Biomedicals) and 10 wt.% Super-P (MTI Corp) in DI water for at least 8 hours to ensure good dispersion. The slurries were then degassed for few minutes before being cast onto copper foil current collector which were later dried in air for 1 hour and then in vacuum at 100°C for 12 h. An electrode loading in the range 1.4 -1.8 mg cm^{-2} was achieved on the copper foils for h-SiNTs and h-SiNTs-15/C.

The electrochemical characterization of h-SiNTs and h-SiNTs-15/C has been performed using CR 2025 coin cells (MTI Corp) where Li metal and Celgard 2250 served as the counter electrode and separator, respectively. The electrolyte used in all the studies was 1 M $LiPF_6$ in ethylene carbonate/diethyl carbonate/fluoroethylene carbonate (45: 45: 10, BASF). Electrochemical testing was conducted within the voltage range 0.01–1.2 V vs. Li^+/Li in a galvanostatic current mode. The positive potential used as lower cutoff in the voltage window (0.01V) prevents the plating of lithium on the copper substrate while the upper cutoff potential (1.2V) ensures complete delithiation of the charged electrode to Si in addition to preventing any kind of reaction between the Cu substrate with lithium.

To evaluate the nature of the charge-storage in h-SiNT-15 and core-shell h-SiNT-15/C, electrode materials and to understand effect of carbon coating on the electrochemical performance of these materials in Li/Li^+ system, electrochemical impedance spectroscopy (EIS) was performed using the Gamry potentiostat over a frequency range of 0.1 Hz to 100000 Hz. An alternating voltage amplitude of 5 mV was used and the spectra were obtained before cycling and after the 1st, 50th and 200th discharge - charge cycles, to observe any noticeable changes in the charge storage mechanism upon cycling. The Z-View (Scribner Associates, Inc.) software was used to design the equivalent circuit model of the impedance spectra and analyze the impedance response of the h-SiNT-15 with and without the carbon coating.

3.2 Results and Discussion

3.2.1 Synthesis and Materials Characterization of h-SiNTs

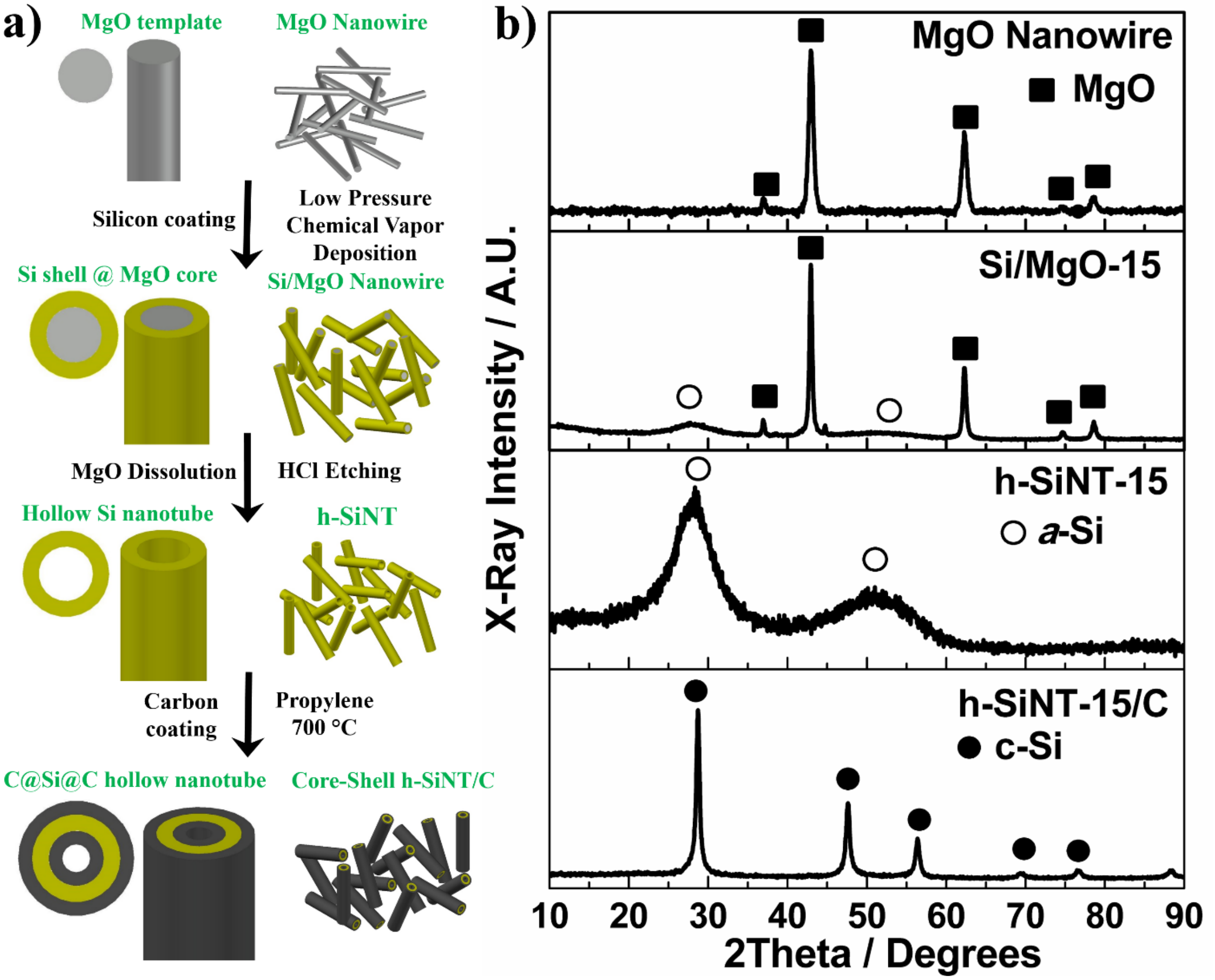

Figure 30: a) Schematic of synthesis process for the generation of core-shell C@Si@C hollow nanotubes (h-SiNT/C). b) XRD patterns of calcined MgO template, core–shell Si/MgO-15, h-SiNT-15 and core-shell h-SiNT-15/C.

The XRD pattern of the sacrificial MgO template (**Figure 30b**), obtained by the hydrothermal synthesis method following the reaction of magnesium acetate and urea confirmed the formation of MgO after heat treatment at 500 °C. The SEM analysis of the MgO template, shown in **Figure 31a**, shows the wire-like morphology of MgO with diameters 0.2 μm –0.9 μm and the length varying from 0.1 μm to few hundred μm. The high pressure and supercritical nature of the solution developed during the hydrothermal process leads to the rapid nucleation and uncontrolled growth of these MgO wires with their simultaneous fracture.[216] Hence, a wide variation in the geometrical dimensions of the wire was observed. However, it should be noted that the only morphology observed is a wire and no other morphology of particles or flakes was observed.

In order to generate the hollow Si nanotube (h-SiNTs) structure, the MgO core was removed from the Si/MgO core-shell structure by etching using HCl as discussed in detail in the experimental section. The XRD pattern of the resultant h-SiNT-15 sample obtained after acid etching of MgO from Si/MgO-15 (**Figure 31b**) shows peaks corresponding to only *a-Si* without any peaks corresponding to presence of residual MgO or $MgCl_2$ following the acid treatment thus indicating the complete dissolution of the sacrificial MgO template from the Si/MgO-15 core-shell structure. Similar XRD patterns showing the presence of only *a-Si* has been observed for h-SiNT-10 and h-SiNT-20 nanotube samples. The formation of *a*-Si has also been confirmed by Raman spectrum analysis of h-SiNTs. The Raman spectrum of h-SiNT-15 (**Figure 31e**) showed a broad peak at 480 cm^{-1} (transverse optical mode) in lieu of 520 cm^{-1} (crystalline silicon) which confirmed the amorphous nature of the deposited silicon.[225] The other small broad peaks obtained at ~380 cm^{-1}, ~301 cm^{-1} and ~150 cm^{-1} are signature of the longitudinal optical, longitudinal acoustic and transverse acoustic phonon mode for amorphous silicon, respectively.[31, 225-230] There was no major difference in the Raman spectra collected for the h-SiNTs with the change in time of deposition (h-SiNT-10 and h-SiNT-20) showing broad peaks at ~475 – 480 cm^{-1} and other small broad peaks at ~380 cm^{-1}, ~301 cm^{-1} and ~150 cm^{-1}.

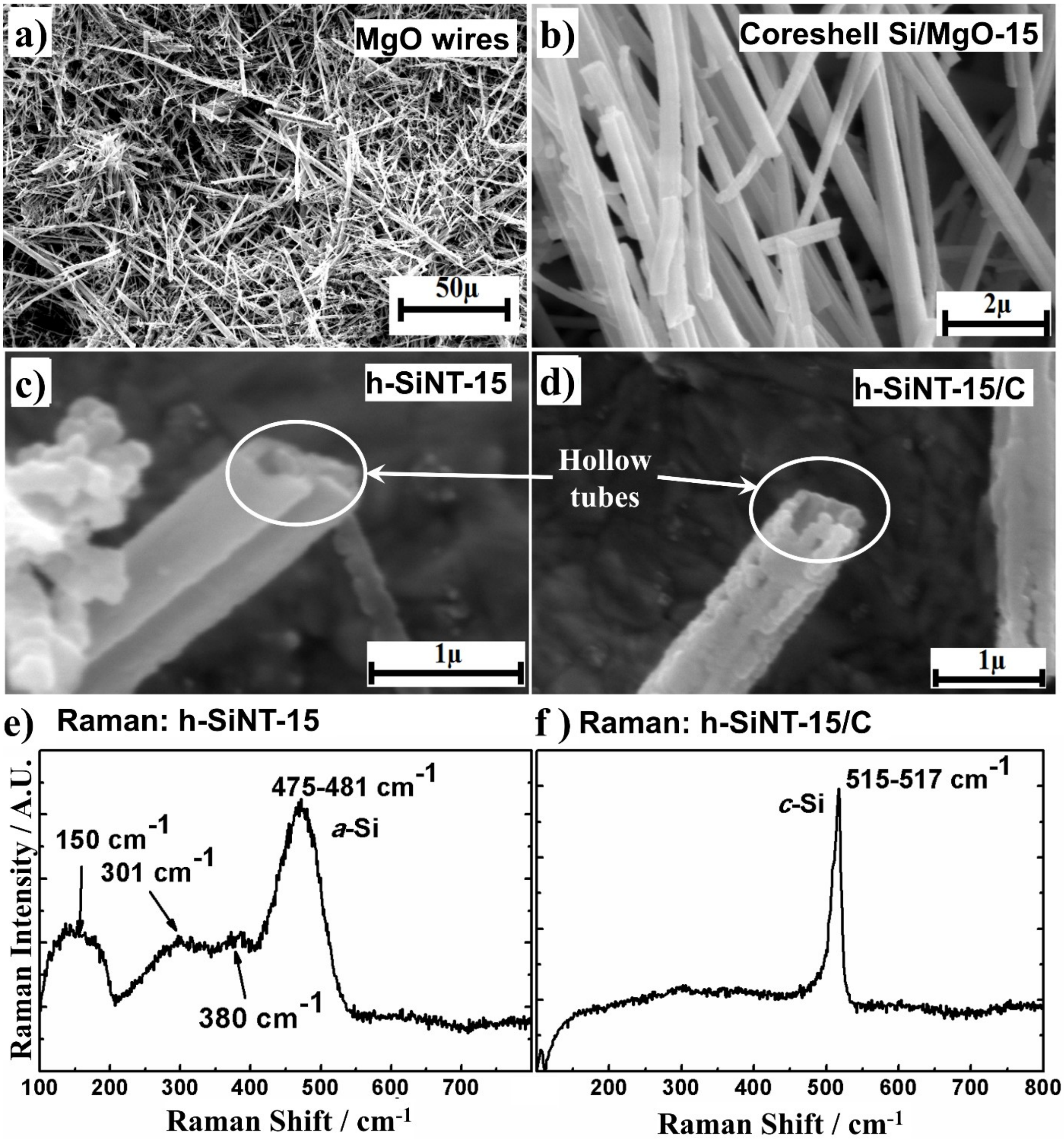

Figure 31: SEM images of a) MgO wires, b) Si/MgO-15 core-shell wires, c) h-SiNT-15 structures and d) core-shell h-SiNT-15/C structures. Raman spectra of the (e) h-SiNT-15 showing amorphous nature of Si and (f) core-shell h-SiNT-15/C showing crystalline nature of Si.

The SEM analysis of the h-SiNTs, obtained after the LPCVD of Si and etching of the MgO core, confirmed the formation of tube like *a-Si* hollow structures devoid of any particles or any other morphology as shown in **Figure 31c** for the representative nanotube sample of h-SiNT-15.

The HRTEM analysis of the obtained h-SiNTs (**Figure 32)** clearly indicates the formation of hollow tubular structures of *a-Si* showing diffuse rings corresponding to the amorphous phase in the selected area electron diffraction (SAED) pattern (**Figure 32d**), and an increase in the thickness of the wall with the increase in the time of silane deposition. h-SiNTs formed using LPCVD for 10 min (h-SiNT-10, **Figure 32a**) showed porous wall with a thickness of ~ 40-45 nm that underwent consolidation with increase in the thickness to ~60 nm and ~75 nm after 15 min (**Figure 32b**, h-SiNT-15) and 20 min (**Figure 32c**, h-SiNT-20) of silane deposition time, respectively.

The BET surface area analysis for the h-SiNTs obtained following different deposition times expectedly showed a decrease in the specific surface area (SSA) with increase in the silane deposition time (**Figure 32e, Table 1**). The specific surface area (SSA) of the tubular structure of Si with inner and outer radius, R and αR, respectively is given by

$$\left[\mathrm{SSA} = \frac{3}{\rho_{Si}\mathrm{R}} \times \frac{(\alpha+1)}{(\alpha^2+\alpha+1)}\right] \qquad \ldots\ldots\ldots\ldots \quad (3\text{-}1)$$

where, α (>1) is the ratio of outer radius to inner radius determined by the thickness of the deposited layer in LPCVD of Si on the MgO wires. Hence, the specific surface area of the h-SiNTs decreases with the increase in deposition time due to the increase in thickness (increase in α) as indicated in the above equation for the specific surface area. It is interesting to note that the increase in the time of deposition of Si during the LPCVD process leads to an increase in the wall thickness of the h-SiNTs, thus, increasing the mass of silicon in each hollow tubular structure which also improves the tap density of the Si in the nanotubular structures.

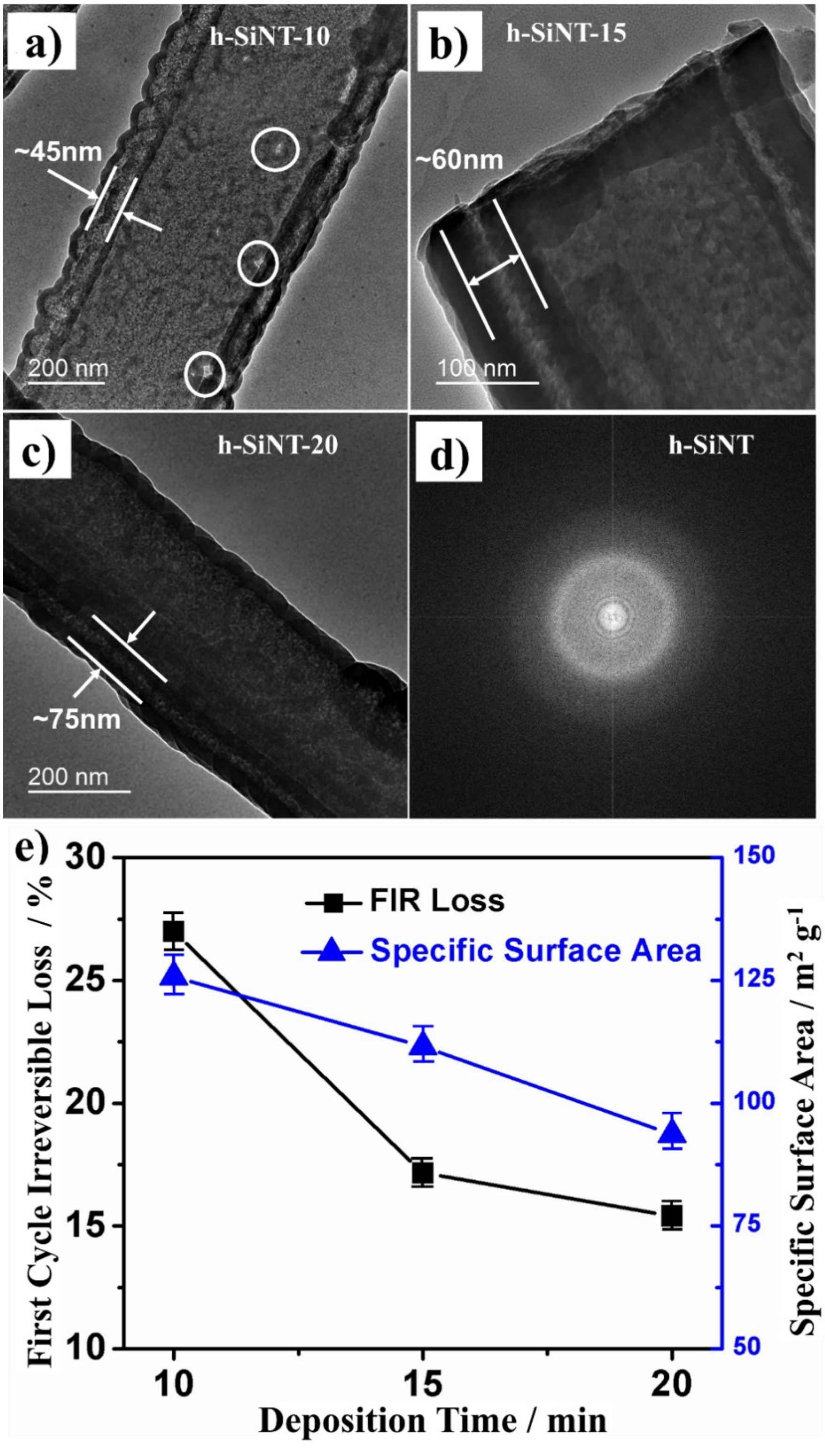

Figure 32: HRTEM images of a) h-SiNT-10, b) h-SiNT-15, c) h-SiNT-20 showing the increase in thickness of the shell with the increase in time of LPCVD-Si, d) SAED pattern of showing annular rings, and (e) specific surface area and FIR loss of h-SiNTs vs. time of LPCVD-Si.

3.2.2 Electrochemical Performance of h-SiNTs

The obtained h-SiNTs has been tested to evaluate their potential as promising anode materials for LIBs. The electrodes were generated using slurry casting of the h-SiNTs (h-SiNT-10, h-SiNT-15, h-SiNT-20) on copper current collectors and their electrochemical properties were investigated under galvanostatic conditions in Li/Li$^+$ system between the voltage range of 0.01 V – 1.2 V. It must be mentioned here that the areal loading density of the active material in the electrode increases with increase in LPCVD deposition time (~0.7 mg cm^{-2} for h-SiNT-10, ~1.35 mg cm^{-2} for h-SiNT-15 and ~1.6 mg cm^{-2} for h-SiNT-20) as tabulated in **Table 7** due to the formation of thicker walls of the *a*-Si nanotube structures with increasing time (higher tap density). **Table 7** tabulates a summary of the electrochemical performance of the h-SiNTs along with their geometrical features and specific surface area.

Table 7 Summary of performance of h-SiNTs and core-shell h-SiNT/C tested in Li/Li+ system

Material	**Wall Thickness**	**Specific Surface Area**	**Loading Density**	**Specific capacity / mAh g^{-1}**		**FIR Loss %**	**Fade Rate / % loss cycle^{-1}**
	nm	**m^2·g^{-1}**	**mg·cm^{-2}**	**Discharge**	**Charge**		
h-SiNT-10[216]	*a*-Si ~ 40 ±2.5	~125 ±3.3	~0.7 ±0.06	~2840 ±11	~2160 ±13	~25 ±0.92	~0.07
h-SiNT-15	*a*-Si ~ 60 ±1.8	~111 ±2.6	~1.35 ±0.12	~3275 ±27	~2720 ±24	~17.2 ±0.43	~0.31
h-SiNT-20	*a*-Si ~ 75 ±1.4	~94 ±1.2	~1.6 ±0.09	~2770 ±15	~2343 ±12	~15.3 ±0.34	~0.42
h-SiNT-15/C	*c*-Si ~ 60 ±2.1 C ~ 50 ±1.7	~87 ±1.3	~1.7 ±0.05	~1780 ±9	~1565 ±s6	~13.2 ±0.16	~0.07

The electrodes generated using h-SiNT-15 showed a 1st cycle specific discharge and charge capacity of ~ 3275 mAh g^{-1} and ~2720 mAh g^{-1} with a FIR loss of ~17-18% at a discharge/charge rate of 300 mA g^{-1} in Li/Li$^+$ system (**Figure 33a, Table 7**) and a coulombic efficiency ~99% after the 1st cycle. The 1st cycle discharge/charge capacities of h-SiNT-10 [216] and h-SiNT-20 are comparable to those of h-SiNT-15. However, h-SiNT-15 and h-SiNT-20 show a higher fade rate (~0.31% loss cycle^{-1} for h-SiNT-15 and ~0.42% loss cycle^{-1} for h-SiNT-20) as compared to h-SiNT-10 (0.067% loss cycle^{-1}) as indicated in **Table 7**. The first cycle irreversible (FIR) loss of the h-SiNTs showed a decrease from ~25% to ~15% with the increase in the wall thickness from ~40 nm (~10 min) to ~75 nm (~20 min) as indicated in **Table 7 and Figure 32e**. This decrease in FIR loss of h-SiNTs correlates with the decrease in the specific surface area (**Figure 32e**), thus, indicating that the major contributing factor for the FIR loss is the decomposition of the electrolyte on the exposed surface of Si and consumption of Li during the process of formation of the solid electrolyte interphase (SEI) layer owing to the higher surface area of the exposed nanotube. A major reduction in FIR loss is obtained by increasing the time of deposition from 10 min (~40 nm wall thickness) to 15 min (~60 nm wall thickness) (~25% in h-SiNT-10 to ~17% in h-SiNT-15).

The higher fade rate of h-SiNT-15 and h-SiNT-20 can be related to the thicker walls observed in these nanostructures which results in likely lowering of the hoop stresses but poor strain relaxation due to the volumetric changes occurring during the lithiation and delithiation reactions with *a-Si*. Post cycled SEM analysis (**Figure 34**) of the h-SiNTs electrodes after the 50th electrochemical cycle showed morphological changes albeit evidence of mechanical stability of h-SiNTs during repeated cycling is observed. The straight tubular hollow microstructure of silicon nanotubes of h-SiNT-15 (~60 nm wall thickness) was retained upon repeated lithiation and delithiation cycles as shown in **Figure 34a** even though the nanotubes showed a fade in capacity. However, the h-SiNT-20 (~75 nm wall thickness) (**Figure 34b**) showed a change in morphology such as bending, twisting and deformation of the tubular structures upon cycling to accommodate the volume changes and relieve the stresses generated in the system due to the thicker walls. This result clearly suggests that the optimum wall thickness of h-SiNTs showing stable structural/morphological changes during lithiation/delithiation is below ~75 nm, a notable aspect deduced from the present study. The stability of these hollow Si structures is also governed by the competing nature of lithium diffusion from the surface of the h-SiNTs and vacancy migration from the interior of the nanotube to the surface (both interior and exterior surfaces) during the volume expansion.[231-232] Lower wall thickness allows for more rapid vacancy migration along with lithium diffusion thus, minimizing the nucleation and growth of pores in the interior of nanotube, thus, explaining the structural stability of h-SiNT-15 while bending and deformation is observed in h-SiNT-20.[231-232]

A study of the differential capacity plots (**Figure 33b**, dQ dV^{-1} *vs.* V) shows various reactions and phases formed during the lithiation and delithiation of the h-SiNT-15 electrodes during the electrochemical processes. The observed reactions peaks during 1st cycle lithiation (~0.15 V, and ~0.08 V) and delithiation (~0.32 V and ~0.48 V) for h-SiNTs are similar to those reported previously for *a*-Si.[186] The first lithiation reaction peak (~0.15 V) is observed due to the reaction of lithium with silicon to form Li-30at% Si phase (Φ_1).[206] The subsequent alloying reaction of Li with Φ_1 phase occurs at lower voltage of ~0.08 V to form Li – 24at%Si (Φ_2). Two distinct peaks are observed at ~0.32 V and ~0.48 V in the first charge cycle (dealloying process) during which phase Φ_1 is formed from Φ_2 at ~0.32 V, which subsequently dealloys at ~0.48 V to from the *a*-Si phase. The reaction peaks occurring during the second lithiation cycle (~0.28 V, ~0.24 V and ~0.08 V) and delithiation cycle (~0.32 V and ~0.48 V) are characteristic peaks for the alloying and dealloying of lithium with amorphous Si. [31, 205-207, 215, 229]

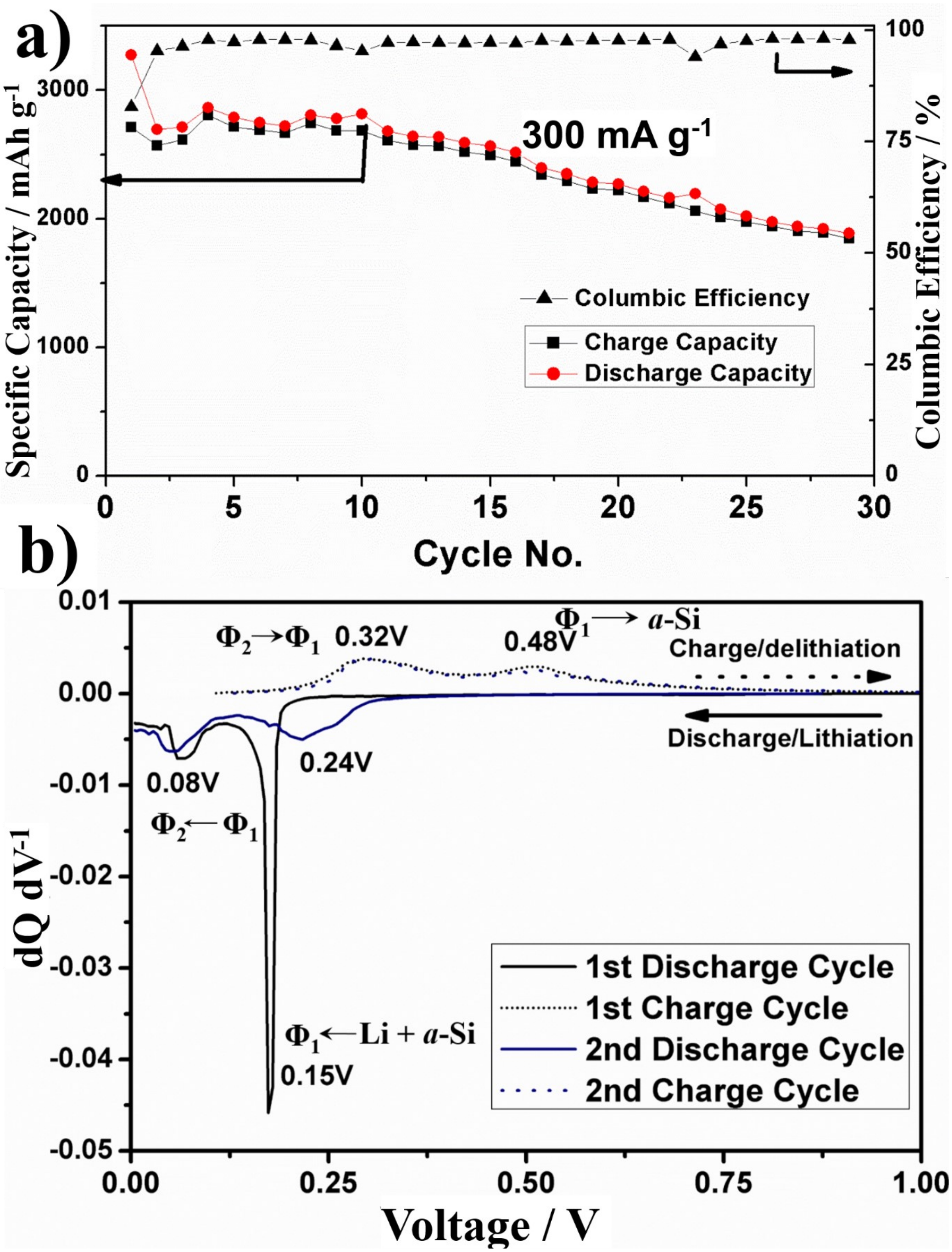

Figure 33: (a) Electrochemical cycling plot showing specific charge/discharge capacity and columbic efficiency of h-SiNT-15 and (b) First and second cycle differential capacity plots for h-SiNT-15 showing various lithiation and delithiation reactions during electrochemical cycling

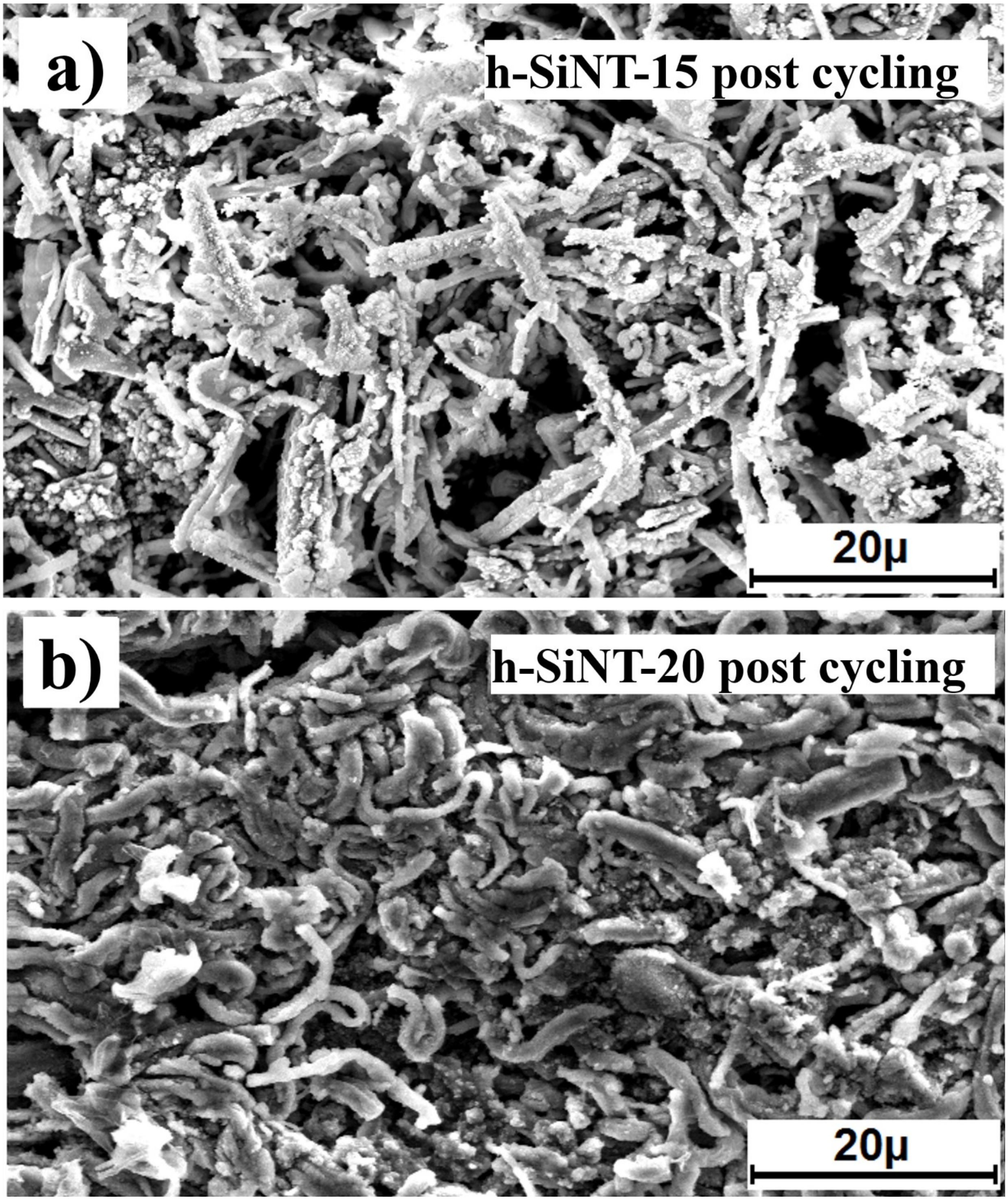

Figure 34: SEM images of a) h-SiNT-15 and b) h-SiNT-20 electrodes after 50th cycle of electrochemical testing in lithium ion battery

3.2.3 Core-Shell Hollow C@Si@C Nanotubes (h-SiNT-15/C)

To improve the long-term cycling stability of h-SiNTs and to further reduce the 1st cycle irreversible loss (FIR), the surface of the h-SiNTs has been coated with carbon to generate core-shell C@Si@C hollow nanotubes. Owing to the better structural and microstructural stability **(Figure 34)**, higher specific capacity (**Table 7**) and low fade rate (**Table 7**) of h-SiNT-15 in comparison to h-SiNT-20, the h-SiNT-15 nanotubular structures were coated with carbon instead of h-SiNT-20 even though the latter had lower FIR loss of 15%.

Although h-SiNT-10 show structural stability on volume expansion and contraction, they possess higher surface area which translates into higher FIR loss. Hence, coating h-SiNT-10 with carbon would lead to higher weight of carbon in the active material (h-SiNT-10/C) due to higher specific surface area and hence, lead to lower specific capacities during cycling. On the other hand, h-SiNT-20 are characterized with lower surface area which translates into lower FIR loss during electrochemical testing in lithium ion battery. However, the h-SiNT-20 show bending and twisting of these nanotubular structures as observed in the post cycling SEM (**Figure 34b**). This inherent deformation behavior during the lithiation and delithiation reactions make h-SiNT-20 less suitable for use even after coating them with carbon (h-SiNT-20/C). Hence, the h-SiNT-15 obtained with deposition time of 15min provides optimal properties of specific surface area and FIR loss without any structural deformation during cycling, for the synthesis of coreshell h-SiNT-15/C nanostructures by carbon coating with minimal decrease in specific capacity due to presence of carbon.

The carbon coating on the h-SiNT-15 has been performed by the thermal decomposition of propylene gas at 700 °C in a CVD tube furnace on the surface of h-SiNT-15 as discussed in the experimental section. The XRD pattern of the carbon coated h-SiNT-15 (**Figure 30b**, h-SiNT-

15/C) shows peaks corresponding to crystalline Si indicating the crystallization of *a*-Si during the thermal deposition of carbon at 700°C which is in the onset temperature range (650 °C - 700 °C) known for inducing crystallization of amorphous silicon.[225] Raman analysis was performed to further confirm the crystalline nature of Si in h-SiNT-15/C as indicated by the XRD pattern. The Raman Spectra of h-SiNT-15/C (**Figure 31f,** h-SiNT-15/C) showed a distinct peak at ~ (515 cm^{-1} - 517 cm^{-1}) corresponding to crystalline silicon consistent with the results obtained in the XRD which shows crystalline peaks for silicon in the core-shell h-SiNT-15/C. The temperature used during carbon deposition (700°C) provides thermal energy for the activation of localized ordered regions to form nucleation sites for crystalline transformation in amorphous h-SiNTs. The rearrangement of Si atoms due to thermally induced diffusion of Si atoms at the interface of these nucleation sites with surrounding amorphous Si, *a*-Si leads to growth of crystalline Si phase and conversion of *a*-Si in h-SiNTs into crystalline silicon phase in h-SiNT-15/C.[225]

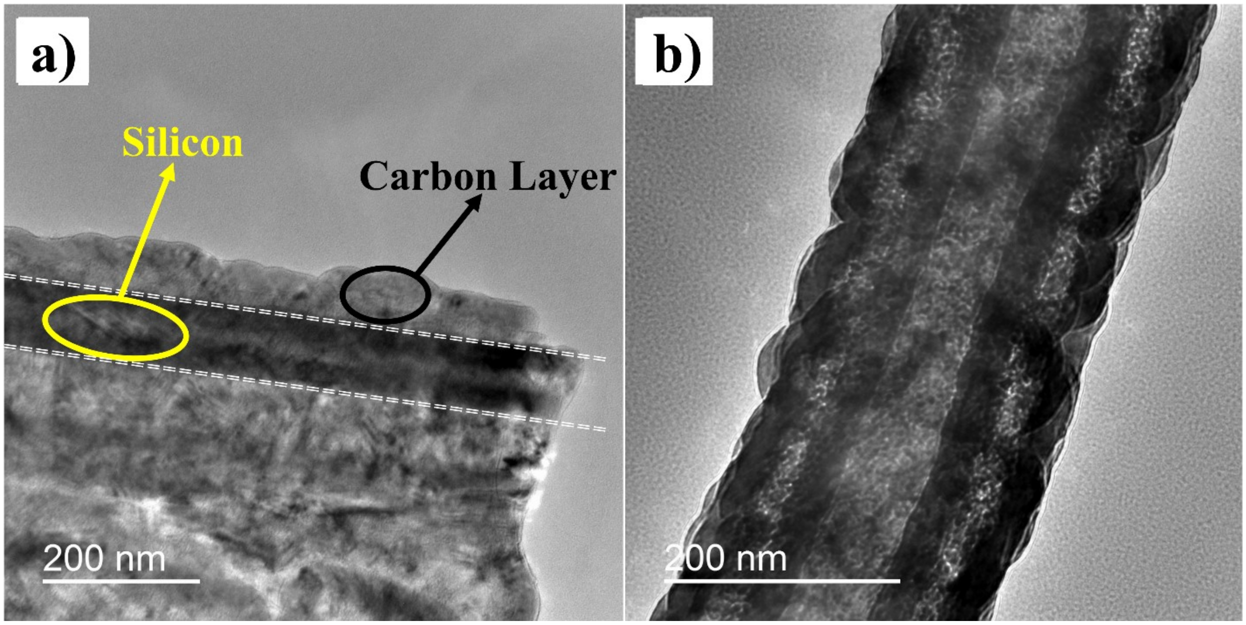

Figure 35: TEM images of core-shell h-SiNT-15/C showing the presence of carbon layer (~50nm) on the interior and exterior surface of the hollow silicon tubes

The SEM analysis of core-shell h-SiNT-15/C (**Figure 31d**) shows that the carbon layer deposition (indicated by rougher surface feature) occurred with the retention of the hollow tubular structure and without inducing any change in morphology or causing fracture of the tubular structures during the pyrolytic carbon deposition process from propene or propylene gas at 700 °C. The presence of silicon and carbon was confirmed by EDAX analysis following scanning electron microscopy. The TEM images (**Figure 35**) show a thin layer of carbon (~50 nm) both on the interior and exterior surface of the h-SiNT-15/C formed because of the gaseous decomposition process thus, confirming the core-shell structure with hollow silicon nanotube as the core and carbon as the shell. The specific surface area of the h-SiNT-15/C is ~ 87 $m^2\ g^{-1}$ as measured by BET analysis which is lower than that of h-SiNT-15 (~110 $m^2\ g^{-1}$ in **Figure 32e and Table 7**) and h-SiNT-20 (~94 $m^2\ g^{-1}$ in **Figure 32e and Table 7**).

The electrochemical performance of the core-shell h-SiNT-15/C architecture showed a 1st cycle discharge and charge capacity of ~1780 mAh g^{-1} and ~1565 mAh g^{-1}, respectively when cycled at a discharge/charge rate of ~300 mA g^{-1}, thus showing a FIR loss of ~13% - 14% (**Figure 36a**). The specific capacity of the composite, h-SiNT-15/C is lower than that of h-SiNT-15 (**Table 7**) due to the presence of the additional C layer which reduces the FIR loss due to a decrease in the specific surface area following the C coating (**Table 7**). To calculate the weight percent of carbon in h-SiNT-15/C, the h-SiNT-15/C were oxidized in a furnace at 1100 °C in oxygen to completely burn off the carbon and form silicon dioxide and the corresponding weight change was used to calculate the carbon content. The weight percent of carbon calculated by this method was ~25-30 wt.%. This result confirms the decrease in the initial charge capacity of as h-SiNTs after carbon coating from ~2770 mAh g^{-1} (h-SiNT-15 in **Figure 33a**) to ~1780 mAh g^{-1} (core-shell h-SiNT-15/C in **Figure 36a**) due to the 25-30 wt.% additional weight of carbon contained in the nanotubes.

It should also be noted that when tested at the higher charge/discharge rate of 1 A g^{-1}, the core-shell h-SiNT-15/C showed a stable discharge capacity of 975 mAh g^{-1} at the end of 120 cycles with a fade of ~0.072% loss cycle^{-1} (**Figure 36a**).

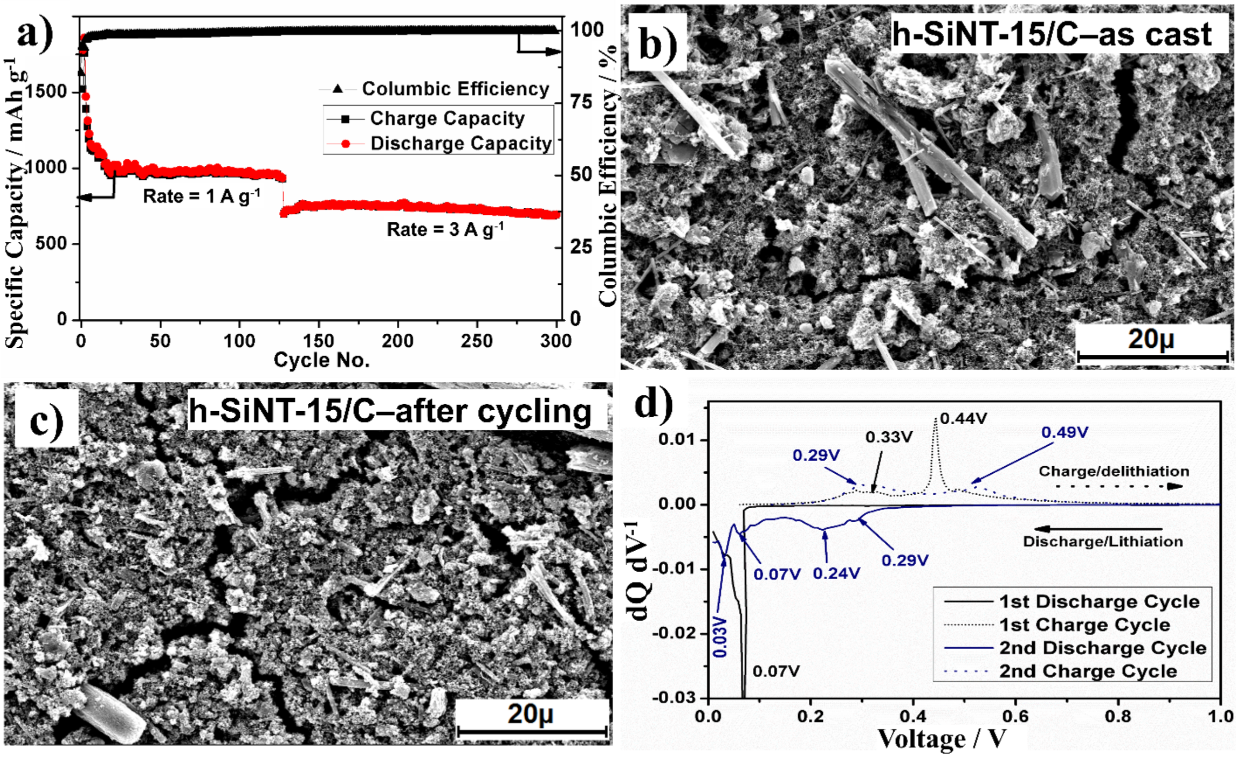

Figure 36 (a) Electrochemical cycling showing long term stability of core-shell h-SiNT-15/C at 300 mA g-1 for first 3 cycles, followed by current rates of 1 A g-1 and 3 A g-1. SEM images showing b) slurry cast core-shell h-SiNT-15/C and c) cycled core-shell h-SiNT-15/C electrodes after electrochemical testing in lithium ion battery, and (d) First and second cycle differential capacity plots for carbon coated core-shell h-SiNT-15/C showing different lithiation and delithiation reactions during electrochemical cycling

Additionally, at a higher discharge/charge rate of 3 A g^{-1}, the h-SiNT-15/C showed a discharge capacity of ~700 mAh g^{-1} at the end of 300 cycles with a columbic efficiency of ~ 99.90 – 99.95% and stable cycling with a fade rate of 0.022% loss cycle^{-1} indicative of improved reversibility of lithiation and delithiation of the electrode during cycling. Post cycled SEM analysis (**Figure 36b, Figure 36c**) of the h-SiNT/C electrodes also showed that the electrodes remain stable without displaying any evidence of catastrophic pulverization of both the electrodes and the silicon nanostructures upon long term cycling of over 300 cycles. Although the carbon coating decreases the gravimetric specific capacity of h-SiNTs, however, the layer of carbon improves the surface conductivity and provides mechanical reinforcement of these tubular nanostructures, thus decreasing the FIR loss and fade rate of the h-SiNT-15/C coreshell nanostructure.

The alloying and de alloying reactions mechanism occurring in the core-shell h-SiNT-15/C nanocomposite during the first charge and discharge cycle (dQ dV^{-1} *vs.* V plot in **Figure 36d**) are different from that observed in h-SiNT-15 (**Figure 36b**) owing to the increased crystalline nature of Si as well as carbon present in the nanotubes. The differential capacity plots for the core-shell h-SiNT-15/C (**Figure 36d**) show an onset of lithiation reaction for the formation of amorphous Li-Si phase (*a*-Li_xSi) at ~0.07 V during the first discharge cycle.[206] Subsequently, during the first charge cycle the dealloying reaction of *a*-Li_xSi phase formed is characterized by a broad peak at ~0.33 V followed by a sharp peak at ~0.44 V, the latter indicating the formation of the delithiated phase from the higher lithiated *a*-Li_xSi phase. On further progress of this dealloying reaction during the end of the charge cycle, a completely amorphous Si phase is formed indicating completion of the conversion reaction of crystalline silicon to amorphous Si during the first discharge/charge cycle. This results in different reaction potentials of the lithiation reaction during the second discharge cycle which shows characteristic peaks observed in *a*-Si system for the reaction of lithium with amorphous silicon, similar to the plots observed in the case of h-SiNT-15 (**Figure 33b**). There also appears to be a small reaction peak corresponding to the formation of *a*-Li_xSi phase from *c*-Si phase at ~0.03 V during the second discharge cycle however, the absence of the sharp reaction peak at ~0.44 V in the second charge cycle confirms the complete conversion of crystalline Si into amorphous Si in the core-shell h-SiNT-15/C within the first two discharge/charge cycles. The stable specific charge/discharge capacities of the core-shell h-SiNT-

15/C configuration clearly indicates that the hollow nanotube structure along with the carbon coating provides a stable geometry to relieve the strains generated during this phase transformation and hence, improve the electrochemical performance of the Si system as an anode in lithium ion battery (LIB).

The rate capability of the core-shell h-SiNT-15/C (**Figure 37a**) show good retention of specific capacity even at high current rates of 5 A g^{-1} when tested at different current rates ranging from 0.25 A g^{-1} (R1) to 5.0 A g^{-1} (R9). The core-shell h-SiNT-15/C show average specific discharge capacities of ~1865 mAh g^{-1}, ~1570 mAh g^{-1}, ~1230 mAh g^{-1}, ~960 mAh g^{-1}, ~861 mAh g^{-1}, ~740 mAh g^{-1}, ~710 mAh g^{-1}, ~595 mAh g^{-1} and ~470 mAh g^{-1} at current rates of 0.25 A g^{-1} (R1), 0.5 A g^{-1} (R2), 1.0 A g^{-1} (R3), 1.5 A g^{-1} (R4), 2.0 A g^{-1} (R5), 2.5 A g^{-1} (R6), 3.0 A g^{-1} (R7), 4.0A g^{-1} (R8), and 5.0 A g^{-1} (R9), respectively under stable cycling. The electrode showed a capacity of ~1250 mAhg^{-1} when subjected to kinetically induced stresses by decreasing the current rate to 1A g^{-1} from 5A g^{-1} indicating stable capacity retention of h-SiNT-15/C despite being exposed to drastic change in current rate.

The electrochemical performance of coreshell C@Si@C hollow nanotubes are comparable to that of Si nanowires (SiNW, ~80nm diameter) coated with ~50nm thick nitrogen doped graphitic layers[221] (SCN1) which show a specific charge capacity of ~2140 mAh g^{-1} during first cycle and ~1260 mAh g^{-1} at the end of 45 cycles at a current rate of 0.6Ag^{-1} reported by Jae Cho and co-workers. In the same study, core-shell SiNW with 50nm carbon layer (SC1) are reported to show a specific charge capacity of ~1040 mAh g^{-1} at the end of 45 cycles.[221] This capacity falls between the current rates of 1Ag^{-1} and 1.5Ag^{-1} for h-SiNT-15/C which is approximately twice the current rate of 0.6Ag^{-1} reported for SC1. The reduction in the Li^+ diffusion distances due to the hollow structure of the h-SiNT-15/C (thickness ~60nm, diffusion distance ~30nm) results in the improved performance as compared to SC1 which have a diffusion distance of ~40nm (radius of SiNW). Additionally, core-shell h-SiNT-15/C show better stability as compared to SC1/SCN1 due to complete amorphization of the silicon within first two charge – discharge cycles and the structural stability offered by the nanotube structure. The performance is also comparable with those obtained for double walled Si nanotubes (DWSiNTs, ~30nm thickness), reported by Wu and co-workers, which show a specific capacity of ~1,200 mAh g^{-1} at a current rate of 1C (~1.2A/g).[211]

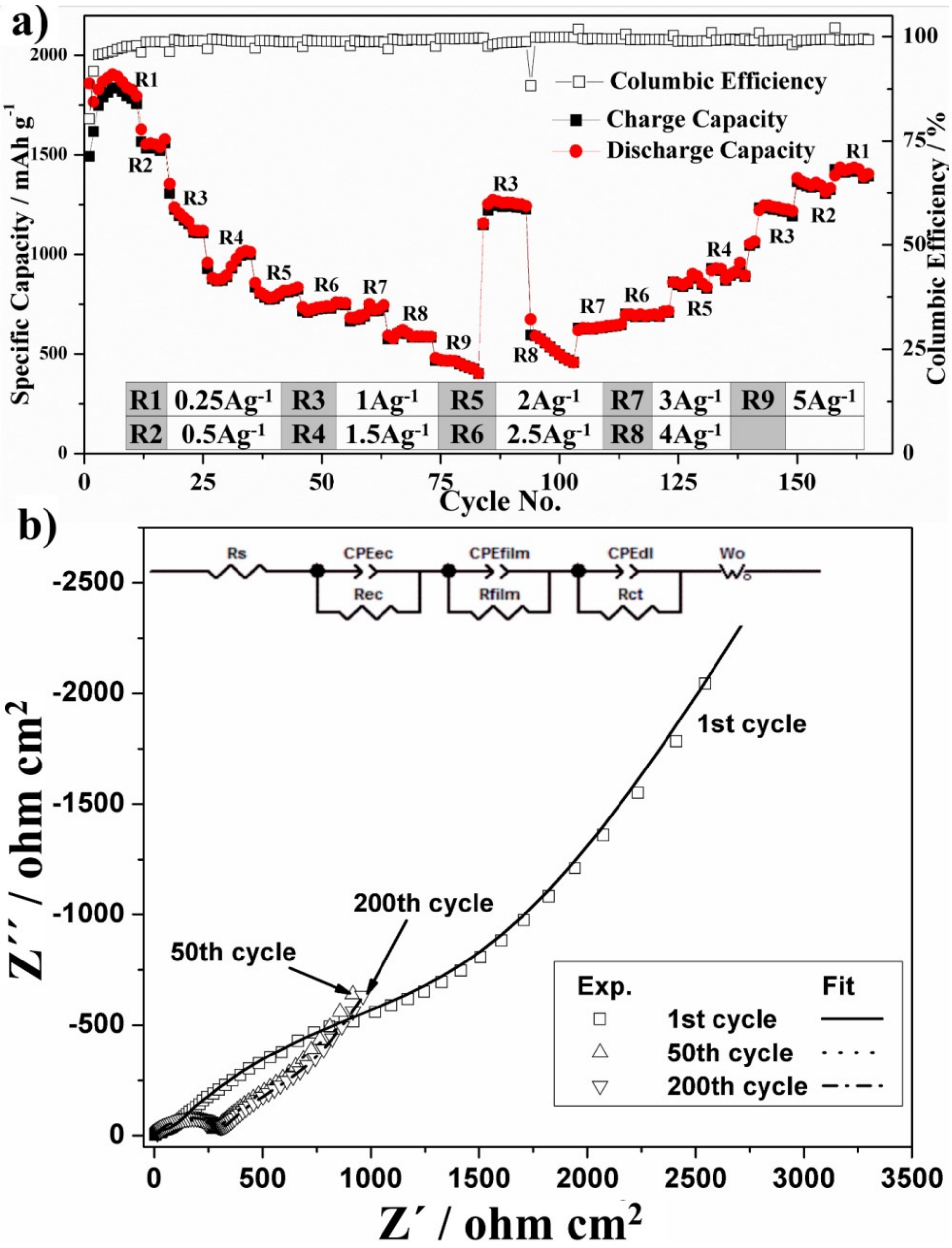

Figure 37 a) Rate capability performance of core-shell hollow nanotubes h-SiNT-15/C at different current rates ranging from 0.25A·g^{-1} to 5Ag^{-1} in lithium ion system. The inset table shows values of different current rates used. b) Impedance spectra of the core-shell h-SiNT-15/C obtained on as assembled coin cell, after 1st, 50th and 200th cycle. The current density applied for lithiation – delithiation cycle was 1 A·g^{-1} in a voltage range of 0.01 V – 1.2 V vs. Li+/Li. The inset shows equivalent circuit with the respective elements used to interpret the impedance response. The lines indicate the resulting fitting response obtained using CNLS simulation

Electrochemical impedance analysis was performed to understand the charge transfer kinetics and the stability exhibited by the carbon coated core-shell hollow silicon nanotube structures (h-SiNT-15/C). The Nyquist spectra were obtained from the assembled coin cells at different stages: after the 1st cycle, 50th cycle and 200th cycle, the results of which are shown in the Nyquist plots in **Figure 37b and Table 8**. The charge-storage behavior of the core-shell h-SiNT-15/C configuration shows characteristic, partially overlapping semicircular regions corresponding to those of the electrode resistance (observed at the electrode-active material interface-R_{ec}, CPE_{ec}), film resistance (related to surface films such as solid electrolyte interphase (SEI), electrode-active material interface-R_{film}, CPE_{film}), electron transfer process (double layer capacitance, CPE_{dl} and charge-transfer resistance, R_{ct}) and the low-frequency Warburg element (W_o, to account for mass-transfer effects.[233-235] The inset in **Figure 37b** depicts the 3-RC elements in series with the solution resistance (R_s) and the Warburg element. The modeling results developed by employing the complex non-linear least square (CNLS) method on this equivalent circuit are in good agreement ($\chi^2 \sim 10^{-4}$) with the Nyquist plots of the experimental results (**Figure 37b**). Upon long term cycling, there is no major difference in the Nyquist plots at the end of the 50th cycle and 200th cycle indicating the stability of the SEI layer and charge transfer characteristics at the electrolyte-electrode interface during the extended cycling of h-SiNT-15/C. There is only a minor change in the charge transfer resistance (~0.037 ohm m^2 to 0.046 ohm m^2) and film resistance (~0.011 ohm m^2 to 0.021 ohm m^2) of the electrode upon repeated lithiation and de-lithiation from the 50th cycle to 200th cycle.

Thus, based on the results presented here, h-SiNTs synthesized by the convenient MgO nanowire template method coupled with the carbon coating of these h-SiNTs to form the core-shell h-SiNT-15/C architectures provide a viable approach to the generation of novel Si nanostructures (core-shell C@Si@C hollow nanotubes) which act as stable composite anode materials for use in lithium ion batteries with high specific charge/discharge capacities (~700 mAh·g^{-1} @ current rate of 3 A·g^{-1} at the end of 300 cycles), low first cycle irreversible loss (~13%-14%, higher areal loading density (~1.7 mg cm^{-2}) and high columbic efficiency (~99.90-99.95%).

Table 8 Values of the circuit elements obtained after modeling the equivalent circuit using a complex non-linear least square (CNLS) method for EIS spectra of carbon coated Si nanotubes (core-shell h-SiNT-15/C)

Cycle	**R_s / Ω m^2**	**R_{ec} / Ω m^2**	**R_{film} / Ω m^2**	**R_{ct} / Ω m^2**
1st	2.38±0.038	0.0025±0.00017	0.0035±0.00014	0.159±0.0021
50th	3.81±0.061	0.00059±0.00004	0.0108±0.00026	0.0368±0.00093
200th	6.23±0.084	0.0093±0.00021	0.0206±0.00039	0.046±0.00073

3.3 Conclusions

In the present study, a hollow amorphous silicon nanotube structures (h-SiNTs) of different wall thicknesses (~40 nm-~75 nm) has been synthesized by using a low pressure chemical vapor deposition (LPCVD) of silicon on sacrificial MgO nanowire template generated by a simple approach followed by acid etching of the MgO template to obtain the hollow Si nanotubes, h-SiNTs. The wall thickness of h-SiNTs has been varied by controlling the deposition time (~10min, ~15min and ~20min) of LPCVD of Si on MgO nanowires template. The wall thickness of the h-SiNTs increases with concomitant consolidation occurring with the increase in time of deposition (~45 nm, ~60 nm, and 75 nm at ~10 min, ~15 min and ~20 min, respectively) which causes the reduction in specific surface area and improvement in the areal loading density of the h-SiNTs.

The first cycle irreversible loss (FIR) loss was reduced from ~25% (10min deposition time) to ~15% (20min deposition time). However, the long term cyclability of h-SiNT-15 (fade rate ~0.31% loss cycle^{-1}) and h-SiNT-20 (~0.42% loss cycle^{-1}) is inferior compared to that of h-SiNT-10 due to the larger wall thickness of the nanotubes. Morphology assessment after long term cycling shows that an optimum wall thickness (~60nm) is needed to exhibit no morphological damage to the nanotubes during the lithiation and de-lithiation processes. Improvements in cycling stability of the optimized h-SiNTs were achieved by coating the h-SiNTs generated following 15 min deposition, h-SiNTs-15 with carbon following pyrolysis of propylene gas.

The core-shell C@Si@C hollow nanotube (h-SiNT-15/C) exhibits a first discharge capacity of ~1780 mAh·g^{-1} and a charge capacity of ~1565 mAh·g^{-1} at a current density of 300 mA·g^{-1}, with ~13.2% first cycle irreversible loss and a very low fade rate of ~ 0.072% loss cycle^{-1} matching the fade rate of the pristine h-SiNTs reported earlier albeit better FIR and loading density. The excellent cyclability of these core-shell h-SiNTs (h-SiNT-15/C) electrodes was further validated by SEM analysis of the post-cycled electrodes which showed the retention of these hollow tubular morphology after repeated cycling. The decrease in surface area after carbon coating leads to the reduction in FIR loss and the carbon layer also improves the cycling stability of the hollow tubular structures thus, leading to better performance of core-shell C@Si@C hollow nanotubes (h-SiNT-15/C) when compared to the uncoated h-SiNTs.

4.0 Water-Soluble Template Derived Nanoscale Silicon Nano-flakes and Nano-rods Morphologies: Stable Architectures for Lithium-ion Anodes

4.1 Introduction

Rock-salt (NaCl) is commercially abundant, cheap and environmentally clean material which when used as a template provides a positive edge over traditional templates such as silica, anodized alumina oxide (AAO), MgO and ZnO by avoiding the use of harsh reagents and temperature conditions (HF, NaOH, HCl) to leach the template. Use of NaCl as a template has been restricted to largely, generation of nanostructures of oxides such as silica, titania[236], SnO_2 [237] and molybdenum oxides [238] or to create porous carbon based composite structures [239].

In the current study, high energy mechanical milling (HEMM) of commercial NaCl is used to develop a water-soluble template/substrate of different particle sizes combined with low pressure thermal chemical vapor deposition (LPCVD) of silicon to generate Si nanoflakes/platelets and Si nanorods. These Si nanostructures not only assume different morphologies but also exhibit nanocrystalline and amorphous structure. The obtained nanostructures response evaluated in light of their specific capacity, cycling stability, rate capability and morphological stability for lithium-ion batteries provide salient attribute of the two different morphologies. This study also gives an initial insight into the processing parameters of NaCl template, influence on the growth mechanism of Si and formation of Si nanostructures during LPCVD and finally, the study reveals the utilization and response of these nanostructures as alternative anode materials for high performance lithium-ion batteries.

4.2 Experimental

4.2.1 Synthesis of Water-Soluble Sacrificial Template

High-energy mechanical milling (HEMM) of commercial sodium chloride (Fisher Scientific, 200-500 μm particle size) resulted in reduction of the particle sizes. 2 gms of NaCl and 20 gms of stainless steel balls (7 mm diameter) were charged into a stainless steel vial and mechanical milling was carried out in a mixer mill (Spex) for 2 hours (thereafter denoted as NaCl-2h) and 20 hours (thereafter denoted as NaCl–20h) to obtain randomly oriented NaCl particles of reduced sizes. The milled NaCl particles dispersed in n-hexane, sonicated for 10 min and then subsequently dried overnight in a vacuum oven at 80°C served as the template for developing the two different Si nanostructures described in the subsequent section.

4.2.2 Synthesis of Silicon Nanostructures

Low-pressure thermal chemical vapor deposition (LPCVD) was used to decompose 5% silane (SiH_4) diluted in argon gas at 500 °C on NaCl–2h and NaCl–20h for 20 min to obtain silicon deposited on these templates. The mass of NaCl template used in Si - LPCVD was maintained constant for all the experiments. The Si coated NaCl-2h and NaCl-20h particles (thereafter denoted as Si/NaCl–2h and Si/NaCl–20h) were then dispersed in deionized water (Millipore), homogenized in a bath sonicator for 10 min and then heated to 80°C to dissolve the NaCl template following which the Si particles were centrifuged. This warm washing process was repeated twice with DI water followed by a final room temperature wash with ethanol. Finally, the obtained silicon was then dried overnight in a drying oven at 100 °C to remove any remaining solvent.

4.2.3 Characterization Techniques

X-ray diffraction studies were performed using Philips X'Pert Pro system with Cu Kα, λ = 0.15406 nm radiation. Scanning electron microscopy (SEM, Philips XL 30) was conducted to study the morphological and compositional analysis. Raman spectroscopy was performed using a Renishaw in-via Raman microscope equipped with a 633 nm red laser to evaluate the vibrational and rotational modes of silicon nanostructures and to determine the composition of the different phases of Si. High-resolution transmission electron microscopy (HRTEM) analyses executed on JEOL JEM-2100F microscope helped to acquire high-resolution TEM images and selected area electron diffraction (SAED) patterns for the various Si nanostructures. Specific surface area (SSA) of the Si nanostructures were measured using the Brunauer–Emmett–Teller (BET) method performed on a Micromeritics ASAP 2020 instrument employing the N_2 adsorption-desorption isotherms.

4.2.4 Electrochemical Testing in Lithium-ion Battery

Slurries were prepared by mixing 60 wt% of active material (Si_{NF} or Si_{NR}) with 30 wt% binder (sodium alginate, MP Biomedicals) and 10 wt% Super-P (MTI Corp) in DI water for atleast 8 hours to ensure good dispersion of the nanoscale morphologies. The slurries were degassed for few minutes before being cast onto copper foils. The foils were later dried in air for 4 hours followed by overnight drying in vacuum at 100°C. An electrode loading in the range of 1.25 -1.7 mg cm^{-2} was achieved on the cut copper foils for the obtained Si nanostructures. The CR 2025 coin cells (MTI Corp) were used for conducting electrochemical cycling studies in which Li metal and Celgard 2250 served as the cathode and separator, respectively. A1 M $LiPF_6$ in ethylene carbonate/diethyl carbonate/fluoroethylene carbonate (45: 45: 10, BASF) was used as the electrolyte in all the studies. Electrochemical cycling testing conducted within the voltage range 0.01–1.2 V vs. Li^+/Li in a galvanostatic current mode provided insights into the cycling response of the two different nanoscale morphologies. The positive potential used as lower cutoff in the voltage window (0.01V) prevents the plating of lithium on the copper substrate while the upper cutoff potential (1.2V) ensures complete delithiation of the charged electrode to Si along with preventing any kind of reaction between the Cu substrate with lithium.

4.3 Results and Discussions

4.3.1 Materials Characterization

The XRD patterns of commercially obtained NaCl of particle size (~200-500 μm, Fisher Scientific), NaCl-2h and NaCl-20h (**Figure 38b**) show no major difference in the x-ray diffraction profiles. However, there was a change in the relative peak intensities (I_{220}/I_{200}, I denoted as intensity) with increasing milling time (**Figure 38b**). Commercial NaCl owing to its preferred orientation (texture) along (200) plane and large particle size (~200-500μm), showed a lower relative peak intensity of (I_{220}/I_{200}) with respect to the standard pattern of random oriented NaCl crystal (JCPDS-5-0628, I_{220}/I_{200}=0.55). With increasing milling time, the particle size decreases as expected due to comminution of the NaCl particles and correspondingly, there is an increase in the random orientation of NaCl crystal. As a result, the relative peak intensities (I_{220}/I_{200}) increases. The SEM analysis of commercial NaCl (**Figure 39a**) shows a particle size in the range of hundreds of microns (~200-500 μm) which on milling for 2h (NaCl–2h, **Figure 39b**) leads to a reduction in particle size in the broad size range of 5μm – 20μm. On further HEMM processing of NaCl for 20h (NaCl-20h, **Figure 39c**), the particle size further reduces to less than 3 μm.

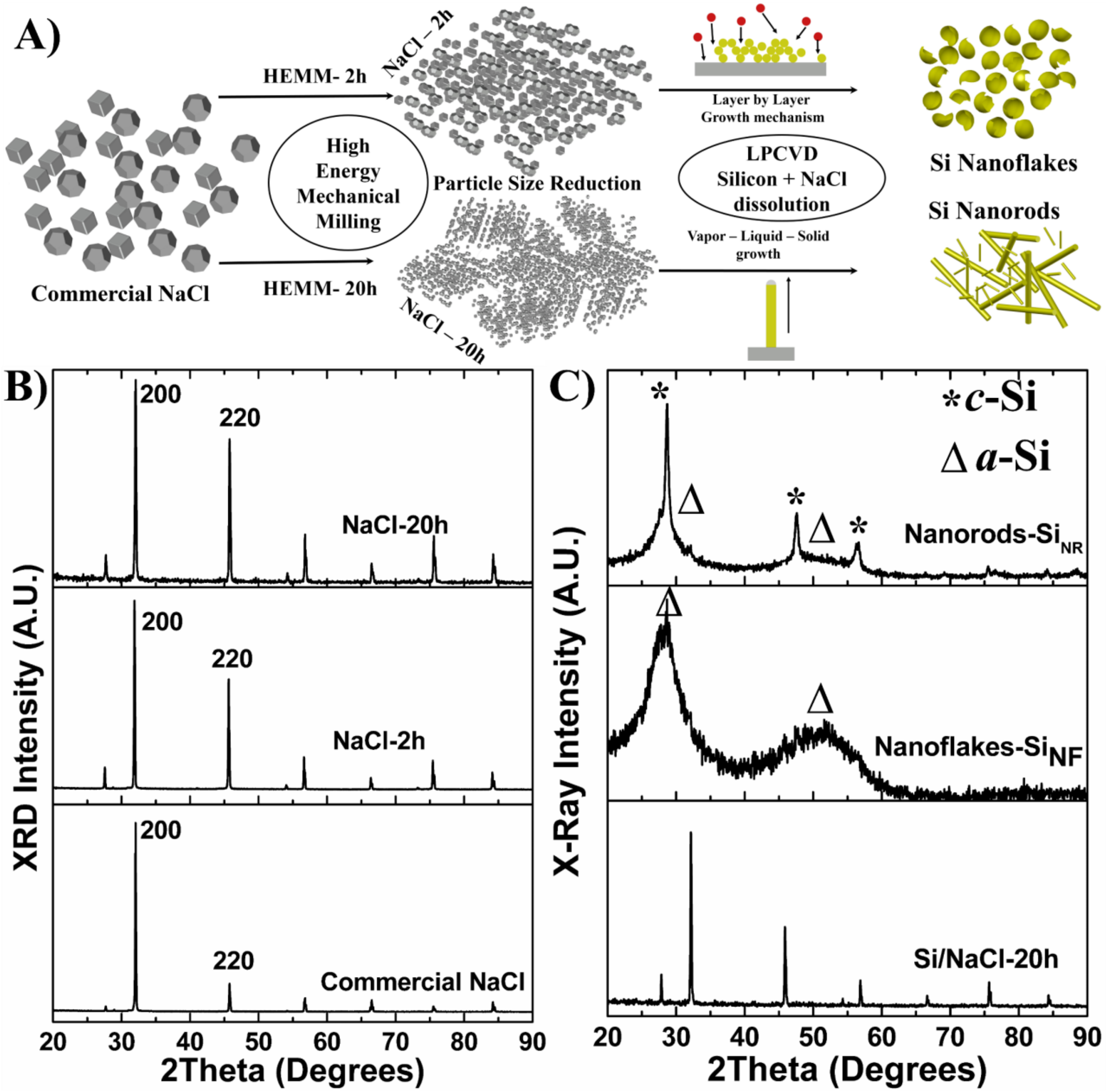

Figure 38 a) Schematic of synthesis process for generation of Si nanostructures from NaCl template. b) XRD patterns of commercial NaCl, milled NaCl for 2h (NaCl-2h) and 20h (NaCl-20h). c) XRD pattern of Si/NaCl and Si nanoflakes and nanorods after dissolution of NaCl template

The XRD patterns of Si deposited on NaCl, (**Figure 38c** for Si/NaCl-20), show the presence of NaCl peaks only. The presence of Si peaks in the XRD pattern were undetectable due to the low intensity with respect to NaCl peaks and amorphous/nanocrystalline nature of Si. On dissolution of the NaCl-2h template from the Si/NaCl-2h, the XRD pattern exhibits two broad peaks indicative of the presence of amorphous silicon (*a*-Si). However, it should be noted that presence of nanocrystalline (*nc*-Si) cannot be discounted since Raman analysis indicated the presence of low volume fraction nanocrystalline Si (*nc*-Si), which will be discussed later. On the other hand, after the dissolution of NaCl-20h template from the NaCl-20h/Si, the XRD pattern shows crystalline peaks of Si (*c*-Si) along with two broad shoulder peaks corresponding to *a*-Si (**Figure 38c**). The final weight of Si obtained after dissolution of underlying NaCl from Si/NaCl-2h and Si/NaCl-20h was ~0.41gm and ~0.53g, respectively for 2gm of NaCl template used for LPCVD process with a daily output of ~1.4g – 1.6g of Si nanostructures on a lab scale from a 1.5" ID x 1" length hot deposition zone. For industrial generation of these NaCl templates the HEMM process can be carried out in liquid hydrocarbons (hexane/decane) to generate well dispersed NaCl template or flame spray pyrolysis of brine solution can also be used.[240-241]

4.3.2 Morphology Assessment

The SEM of Si nanostructures obtained from Si/NaCl-2h (**Figure 39d,e**) and Si/NaCl-20h (**Figure 39f,g**) show very different morphological features with the former showing nanoflakes morphology of silicon (denoted as Si_{NF}) with a thickness in the range of ~40-60nm and the latter showing silicon nanorods (denoted as Si_{NR}) along with low volume fraction of silicon nanoparticles.

The low magnification TEM analysis of Si_{NF} (**Figure 40a**) shows nanoflake morphology formed due to incomplete coverage of Si layer on NaCl – 2h microparticles (5µm – 20µm) during the LPCVD process or due to disintegration of continuous Si layer on dissolution of underlying NaCl particle. The flakes consist of nanoparticles of Si formed as result of silane decomposition sintered together during the growth of the layer. The electron diffraction pattern of Si_{NF} in HRTEM (**Figure 40b**) shows diffused ring pattern confirming the presence of highly disordered Si regions corresponding to *a*-Si present in the nanoflakes.

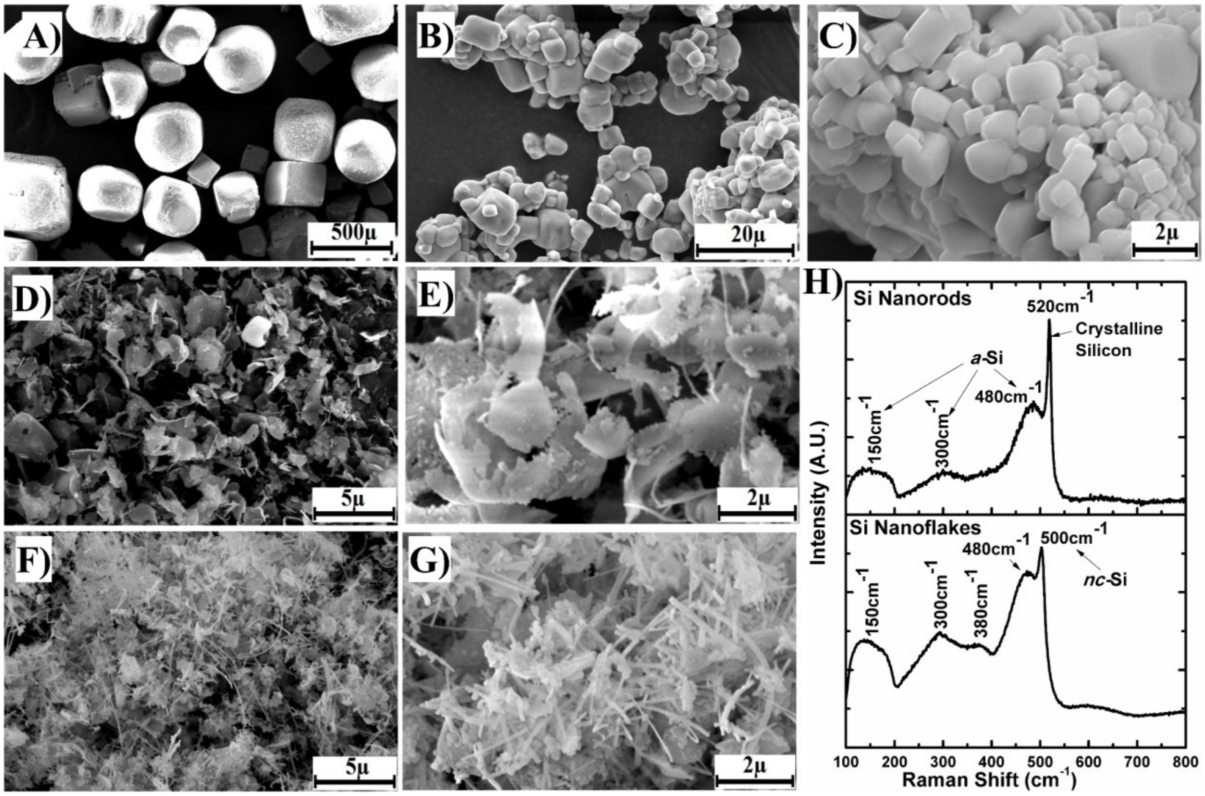

Figure 39 SEM images of a) Commercial NaCl, b) NaCl-2h, c) NaCl-20h, d) and e) Si nanoflakes, f) and g) Si nanorods. h) Raman spectra of silicon nanoflakes (SiNF) and Si nanorods (SiNR)

The TEM analysis of Si_{NR} (**Figure 40c**) shows Si nanorods of 50nm-200nm diameter and few microns in length. Additionally, the TEM analysis (**Figure 40d**) confirms the formation silicon nanoparticle with a particle size ~100nm generated from the surface of NaCl-20h template. The SAED pattern of Si_{NR} shows bright spots confirming the single crystal nature of silicon nanorod

(**Figure 40e, Figure 40f).** The nanorod tends to grow along the (111) plane in [110] direction as indicated by the planes in the SAED pattern. The measured distance between the bright spots ($2/d_{hkl} \sim 6.48$ nm^{-1}) shown in the SAED pattern corresponds to the distance between the planes in the reciprocal lattice ($d_{hkl} \sim 3.09$ Å) which closely matches with the interplanar distance of (111) planes ($d_{111} \sim 3.12$Å) in silicon.

4.3.3 Structural Assessment and Morphology Mechanisms

To evaluate and confirm the amorphous and crystalline nature of silicon in Si_{NF} and Si_{NR}, Raman analysis was conducted on both Si_{NF} and Si_{NR} (**Figure 39h**). The Raman spectra of Si_{NF} (**Figure 39h**) shows a broad peak at 480 cm^{-1} corresponding to amorphous Si and a sharp peak at 500 cm^{-1} corresponding to nanocrystalline Si instead of micro-crystalline Si peak (520cm^{-1}) [31, 226-230, 242] indicating a mixture of amorphous (*a*-Si) and nanocrystalline (*nc*-Si) nature of Si in Si_{NF}. The small peak obtained at ~300 cm^{-1} is signature of the longitudinal acoustic phonon mode for amorphous silicon. However, Si_{NR} obtained after dissolution of the NaCl-20h template from NaCl-20h/Si showed a high intensity distinct peak at 520 cm^{-1} confirming the highly crystalline nature of Si in Si_{NR} (**Figure 39h**). In addition, a broad peak at 480 cm^{-1} corresponding to *a*-Si arises from nanoparticle silicon confirming the presence of crystalline (*c*-Si) and amorphous (*a*-Si) as identified in the XRD pattern of **Figure 38c**.

The above results clearly show that the difference in the particle size of NaCl influence/trigger different growth mechanisms of silicon during low pressure chemical vapor deposition (LPCVD) of silicon on the surface of NaCl particles and hence, result in different morphologies of silicon nanostructures. Bulk and micron size NaCl particles (NaCl-2h) provide ample surfaces for nucleation and preferential 3D growth of Si layer on the surface. The lower temperature used for Si deposition restricts the thermal activation for the surface and consequently, bulk diffusion of Si atoms preventing the formation of crystalline Si. Instead, the adjacent highly disordered Si nucleation and growth centers join and hence, result in a flake-type morphology with the thickness of flakes restricted to ~40-60nm for the 2h milled NaCl (NaCl-2h).

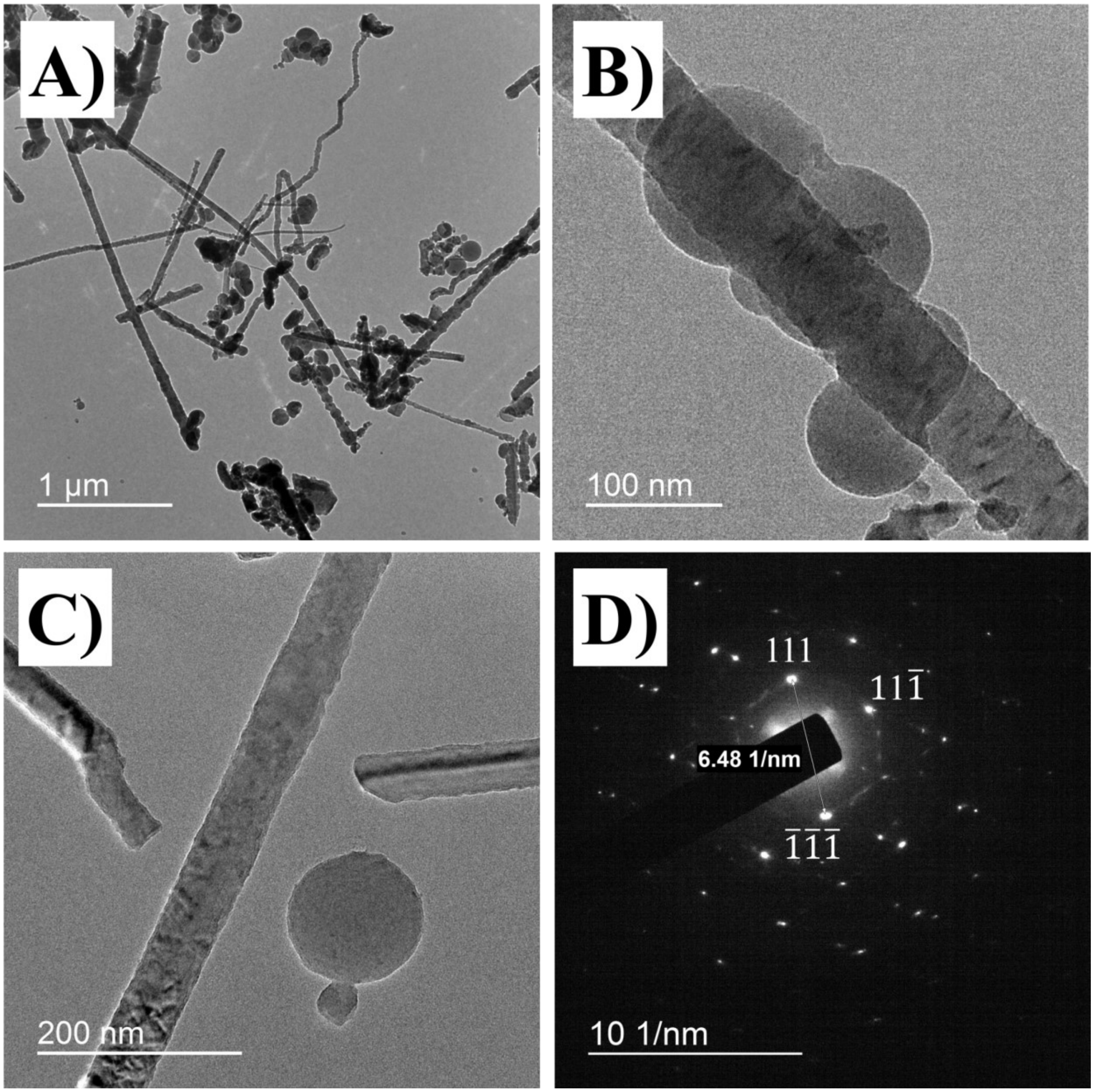

Figure 40 TEM images of a) SiNR (low magnification), b) growth of silicon clusters on SiNR, c) SiNR (high magnification) and d) corresponding SAED pattern of Si nanorod showing bright spots corresponding to (111) planes

On the other hand, longer milling times induces multiple fracture of NaCl particles along the (111) cleavage planes, and surface defects along with reduction in the particle size. There are also reports indicating that the NaCl nanoclusters generated by multi-collision induced disassociation results in lowering of the melting point of NaCl with corresponding decrease in particle size and increasing presence of defects.[243-244] Alkali halide particles also tend to exhibit heterogeneous melting in which liquid phase exists on the surface of the nanoparticles. [245] The expected decrease in the melting point of the NaCl-20h particles due to reduction in particle size causes localized melting on the surface of the NaCl-20h. This is also owing to the presence of surface defects/dislocations, which together culminates in the growth of Si nanorods via the vapor – liquid – solid (VLS) phase mechanism during the low-pressure thermal chemical vapor deposition of silane. [246]

The crystal structure of NaCl is Fm3m (face centered cubic structure) with lattice parameter of ~5.64Å while silicon takes a diamond cubic structure with a lattice parameter of ~5.431Å. The closest packed plane in NaCl is (111) with an interatomic spacing of ~3.23Å which is very similar to that of close packed (111) plane in Si with an interatomic spacing of ~3.12Å which is also the preferred plane for growth of Si crystal. Hence, the lattice mismatch is minimal between the closet packed direction of both NaCl and Si which further assists in preferential 1D growth of Si nanorods along (111) plane on the surface of NaCl – 20h particles by VLS mechanism. The nanorod grow in [110] direction instead of dominantly observed [111] direction which is influenced by the Si/vacuum/molten NaCl interfacial energy, partial pressure of silane, temperature of deposition, crystallization of Si atoms from NaCl – Si eutectic melt and minor presence of oxide impurities[247-249]. The formation of few Si nanoparticles in the Si_{NR} system is due to 3D growth of Si (similar to NaCl – 2h template) on the surface of micron size NaCl particles present in NaCl – 20h, instead of following the VLS mechanism, resulting in highly disordered a-Si phase observed in XRD pattern, Raman spectra and further confirmed by the diffuse ring SAED pattern in **Figure 60**.

Hence, the NaCl–20h template results in the formation of nanorod morphology ($\mathrm{Si_{NR}}$) while the NaCl–2h template results in nanoflake morphology after the dissolution of template. The change in the deposition mechanism from layer by layer to vapor – liquid – solid also explains the highly crystalline nature of silicon in $\mathrm{Si_{NR}}$ when compared to the amorphous nature of silicon in $\mathrm{Si_{NF}}$ obtained from NaCl–20h and NaCl–2h template, respectively. The presence of low volume fraction amorphous silicon in $\mathrm{Si_{NR}}$ is due to the growth of silicon on the micron-sized rod shaped particles present in NaCl–20h and growth of Si on the surface of the nanorods formed. [250]

4.3.4 Electrochemical Performance of Si nanoflakes

The obtained $\mathrm{Si_{NF}}$ and $\mathrm{Si_{NR}}$ were electrochemically cycled under constant current to evaluate their potential as promising anode materials for Lithium ion batteries. The $\mathrm{Si_{NF}}$ showed a first cycle discharge and charge capacities of ~ 2830 $\mathrm{mAh \cdot g^{-1}}$ and 2175 $\mathrm{mAh \cdot g^{-1}}$, respectively, at a current rate of 50 $\mathrm{mA \cdot g^{-1}}$ with a first cycle irreversible loss (FIR loss) of ~ 15-20% (**Figure 41a**). The long term cycling response of the electrodes was also evaluated by testing the electrodes at a current rate of 0.3 $\mathrm{A \cdot g^{-1}}$ for first 5 cycles followed by 1 $\mathrm{A \cdot g^{-1}}$ during the rest of the cycling period (**Figure 41c**). $\mathrm{Si_{NF}}$ showed a high specific discharge capacity of ~1870 $\mathrm{mAh \cdot g^{-1}}$ and ~1150 $\mathrm{mAh \cdot g^{-1}}$ at current rates of 0.3 $\mathrm{A \cdot g^{-1}}$ and 1 $\mathrm{A \cdot g^{-1}}$ during the first and 6th cycle, respectively. Additionally, the $\mathrm{Si_{NF}}$ electrodes showed a stable discharge capacity of ~810 $\mathrm{mAh \cdot g^{-1}}$ at the end of 250 cycles with a columbic efficiency of 99.95-99.97% and a fade rate of ~ 0.11% loss per cycle at a discharge/charge rate of 1 $\mathrm{A \cdot g^{-1}}$.

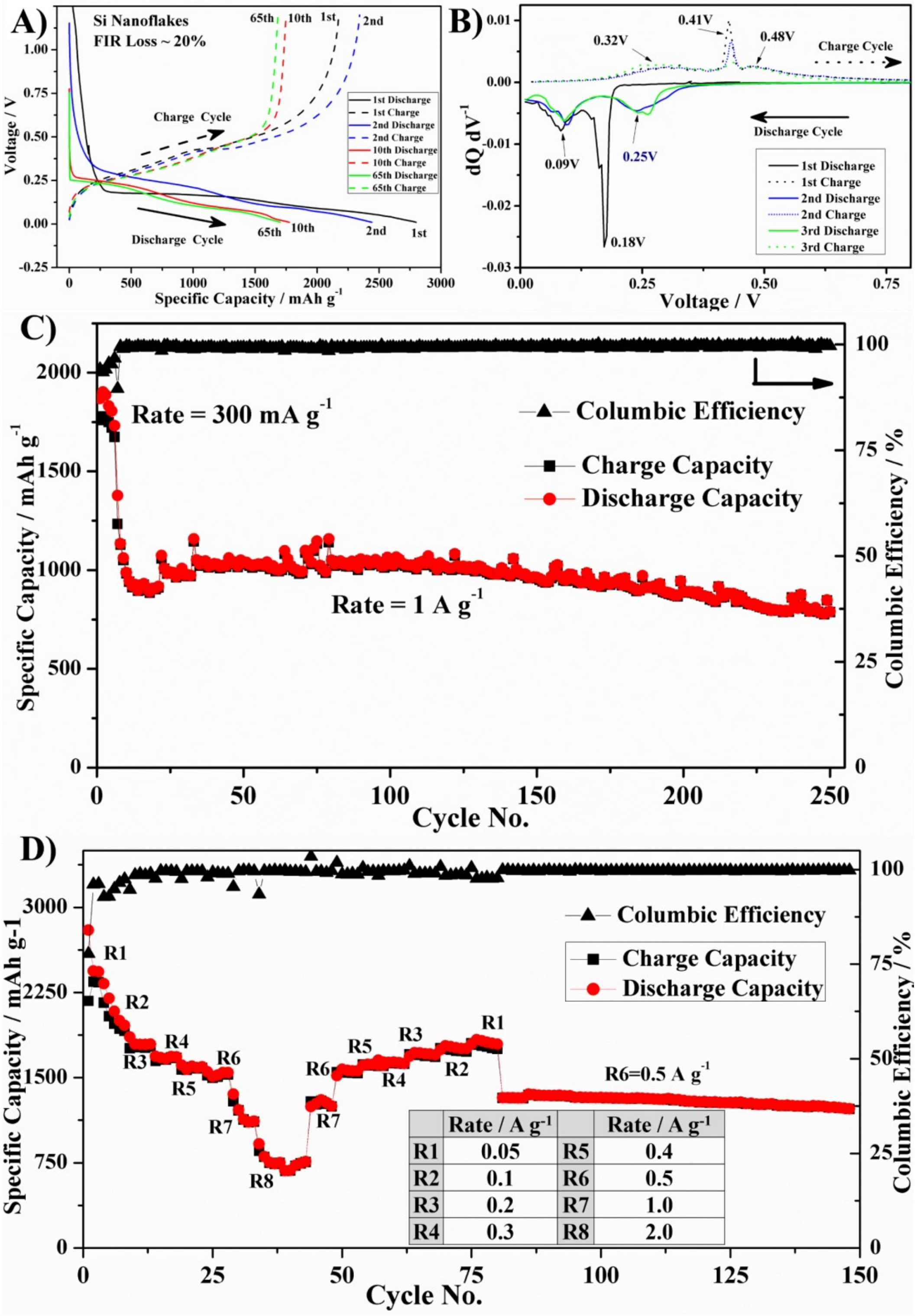

Figure 41 a) Initial charge – discharge curves and b) differential capacity vs voltage profiles of SiNF in Li/Li+ system. c) Long term cycling performance at 0.3A/g for 6 cycles followed by 1A/g for rest of the cycles and d) rate capability test at different current rates (inset table) of SiNF in Li/Li+ system

The differential capacity vs voltage plot (**Figure 41b**) for the Si nanoflakes show two peaks at ~0.18V and ~0.09V respectively, during the first discharge cycle corresponding to the formation of different Li_xSi and Li_ySi (0.18V for amorphous Si and 0.09V for crystalline Si) alloys due to the first cycle lithiation induced alloying process. [5, 31, 205, 208, 215, 229, 251-252]. Subsequent to these two major peaks, there also appears to be a small peak at ~0.03V corresponding to the formation of crystalline $Li_{15}Si_4$ phase from the Li_ySi phase. In the first charge cycle correspondingly, the plot shows two broad peaks at ~0.32V and 0.48V corresponding to the delithiation of Li_xSi phase to form amorphous silicon. The existence of the sharp peak at ~0.41V indicates the transformation of the lithiated Si phase to form amorphous Si through a coexisting two phase $Li_{15}Si_4$ and Li_xSi mechanism.[205] The intensity of this peak however, expectedly decreases upon subsequent cycling leading to formation of completely amorphous silicon within the first 3 discharge – charge cycles. The reduction in intensity of this peak at ~0.41 thus, improves the initial stability of the Si nanoflakes.

The current carrying strength of the electrodes were also tested by evaluating the rate capability potential of the electrodes to study the performance of Si_{NF} at different current rates ranging from 0.05 $A\cdot g^{-1}$ to 2 $A\cdot g^{-1}$, the results of which are displayed in **Figure 41d**. Accordingly, the silicon nanoflakes (Si_{NF}) exhibit stable reversible capacities of ~1800 $mAh\cdot g^{-1}$, 1760 $mAh\cdot g^{-1}$, 1700 $mAh\cdot g^{-1}$, 1625 $mAh\cdot g^{-1}$, 1610 $mAh\cdot g^{-1}$,1560 $mAh\cdot g^{-1}$, 1250 $mAh\cdot g^{-1}$, and 765 $mAh\cdot g^{-1}$. These capacities are obtained when cycled at the following current rates of 0.05 $A\cdot g^{-1}$, 0.1 $A\cdot g^{-1}$, 0.2 $A\cdot g^{-1}$, 0.3 $A\cdot g^{-1}$, 0.4 $A\cdot g^{-1}$, 0.5 $A\cdot g^{-1}$, 1 $A\cdot g^{-1}$ and 2 $A\cdot g^{-1}$, respectively. The results thus demonstrate a good retention of capacity the Si_{NF} electrodes even at high current rates of 1 $A\cdot g^{-1}$ and 2 $A\cdot g^{-1}$. The electrode was given a drastic change in current rate from 0.05 $A\cdot g^{-1}$ to 0.5 $A\cdot g^{-1}$ and subsequent cycling was conducted to evaluate the material for instability in cycling. Si nanoflakes showed stable performance at a current rate of 0.5 A·g^{-1} displaying a specific discharge capacity of ~1225 mAh·g^{-1} at the end of 150 cycles after this drastic change in current rate indicating no instabilities arising from the known catastrophic cracking of electrodes characteristic of silicon systems.

4.3.5 Electrochemical Performance of Si Nanorods

The silicon nanorods (Si$_{NR}$) were also evaluated for their electrochemical response by cycling the electrodes under constant current. The electrodes correspondingly showed a first cycle discharge and charge capacities of ~ 2980 mAh·g^{-1} and ~2500 mAh·g^{-1}, respectively at a current rate of 50 mA·g^{-1} with a first cycle irreversible loss (FIR loss) of ~ 12-15%, putatively displaying a second cycle discharge capacity of ~2740 mAh·g^{-1} (**Figure 42a**).

The long-term cycling response of Si$_{NR}$ was evaluated by the cycling the electrodes at a current rate of 0.3 A·g^{-1} for the first 10 cycles and 1 A·g^{-1} for the remainder of the cycles. Si nanorods (Si$_{NR}$) accordingly, showed a high specific discharge capacity of ~2380 mAh·g^{-1} and ~1710 mAh·g^{-1} at a current rate of 0.3 A·g^{-1} and 1 A·g^{-1} during the first and 11th cycle, respectively. Upon longer cycling at a current rate of 1 A·g^{-1}, the Si nanorods showed discharge capacity of ~740 mAh·g^{-1} at the end of 250cycles with a columbic efficiency of 99.95-99.97% and a fade rate of ~ 0.23% loss per cycle.

Silicon nanorods show a differential capacity vs voltage plot (**Figure 42b**) very similar to the Si nanoflakes (**Figure 41b**) in the first discharge cycle. However, a dominant broad peak at both ~0.09V and ~0.03V indicates the formation of a higher fraction of crystalline Li_ySi and $Li_{15}Si_4$ phase from c-Si during the initial lithiation induced alloying reaction.[205, 253] The first cycle differential capacity charge plots of the silicon nanorods is differentiated from that of the silicon nanoflakes by the existence of a more dominant sharp peak at ~0.41V due to the higher volume fraction of the crystalline $Li_{15}Si_4$ phase. The relative intensity of the two broad peaks (~0.32V and ~0.48V) in contrast with the peak at ~0.41V is clearly an indication of the variation in relative ratios of the amorphous and crystalline phases at the end of the previous lithiation cycle.

The higher peak intensity at ~0.41V compared to peaks at ~0.32 and ~0.48V in the case of nanorods as compared to that of the nanoflakes indicates the higher presence of crystalline phase in the nanorods. Hence, correspondingly a number of cycles are needed for the eventual amorphization of the initially generated crystalline silicon.[253]

Similarly, during the second discharge – charge cycle, the higher intensity of the peak at ~0.41V is indicative of the preferential delithiation of nanorods through crystalline $Li_{15}Si_4$ phase. Higher fraction of crystalline silicon and the presence of highly crystalline silicon in the initially generated Si_{NR} clearly impedes the formation of amorphous Si during cycling. The conversion of crystalline Si into amorphous Si does not reach completion even at the end of 10th charge – discharge cycle. However, there is an increase in the relative intensity of the broad peaks (0.32V and 0.48V) indicating a reduction in the crystalline fraction undergoing the crystalline $Li_{15}Si_4$ to amorphous phase transformation.

The rate capability propensity of the Si nanorods was also evaluated. Accordingly, the Si nanorods nanorods exhibit stable reversible capacities of ~1675 $mAh\cdot g^{-1}$, 1660 $mAh\cdot g^{-1}$, 1600 $mAh\cdot g^{-1}$, 1510 $mAh\cdot g^{-1}$, 1460 $mAh\cdot g^{-1}$, 1380 $mAh\cdot g^{-1}$, 850 $mAh\cdot g^{-1}$ and 470 $mAh\cdot g^{-1}$. These capacities were obtained when the electrodes were cycled at current rates of 0.05 $A\cdot g^{-1}$, 0.1 $A\cdot g^{-1}$, 0.2 $A\cdot g^{-1}$, 0.3 $A\cdot g^{-1}$, 0.4 $A\cdot g^{-1}$, 0.5 $A\cdot g^{-1}$, 1 $A\cdot g^{-1}$ and 2 $A\cdot g^{-1}$, respectively.

The results indeed demonstrate good retention of capacity of the nanorod system when tested at current rates to 0.5 $A\cdot g^{-1}$. The Si nanorods in fact, showed stable performance at a current rate of 0.5 $A \cdot g^{-1}$ with a specific discharge capacity of ~950 $mAh \cdot g^{-1}$ at the end of 150 cycles following the initial aggressive change in current rate without exhibiting any obvious signs of failure that is characteristic of the normal hitherto Si anode systems.

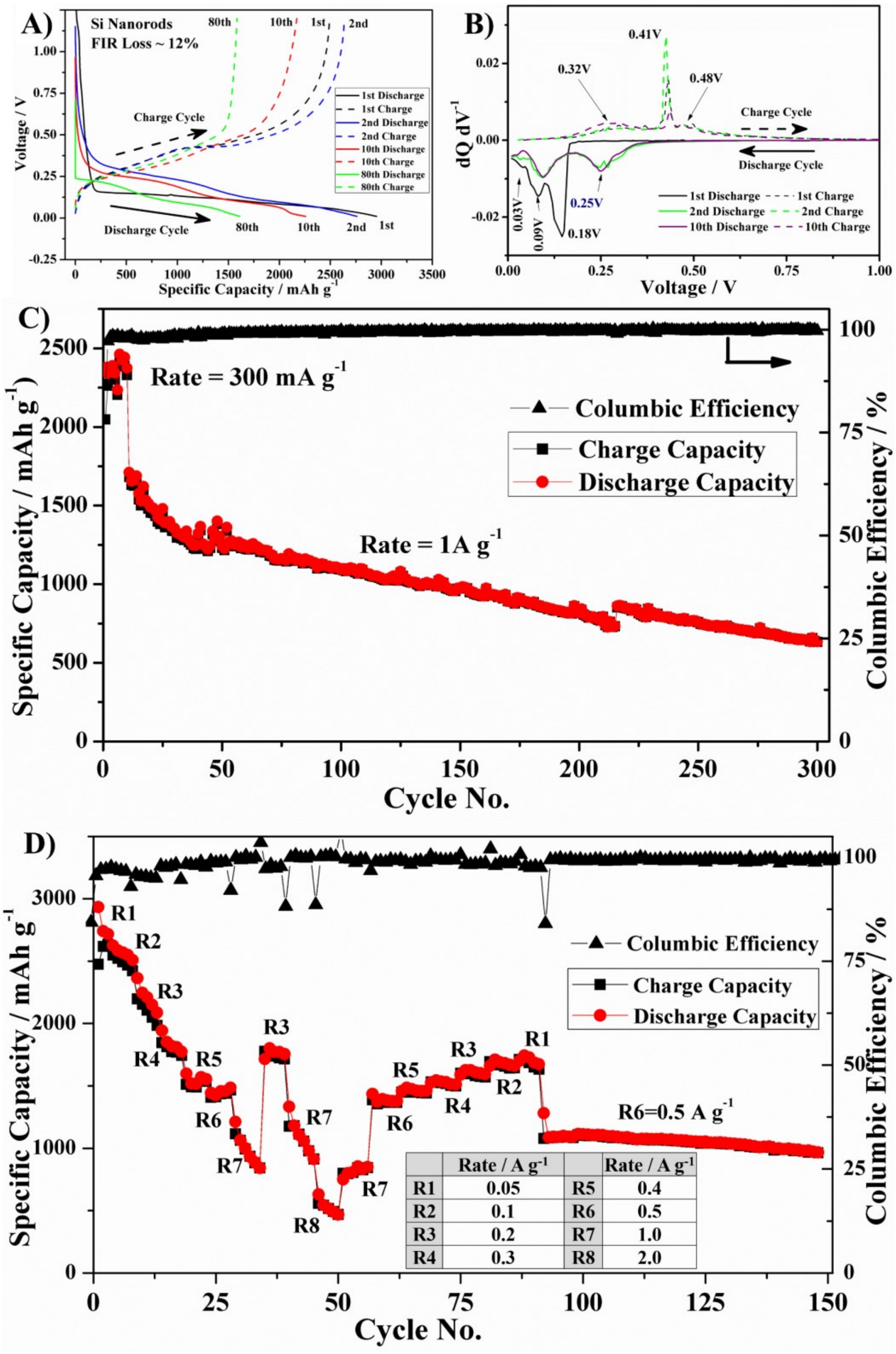

	Rate / A g-1		Rate / A g-1
R1	0.05	R5	0.4
R2	0.1	R6	0.5
R3	0.2	R7	1.0
R4	0.3	R8	2.0

Figure 42 a) Initial charge – discharge curves and b) differential capacity vs voltage profiles of SiNR in Li/Li+ system. c) Long term cycling performance at 0.3A/g for 10 cycles followed by 1A/g for rest of the cycles and d) rate capability test at different current rates (inset table) of SiNR in Li/Li+ system

4.3.6 Comparison of the Cycling Response of Silicon Nanoflakes and Silicon Nanorods

Based on the above discussion of the results, the major difference in the performance of Si_{NF} and Si_{NR} can be attributed to the variation in the content of the different phases of silicon (*a*-Si, *nc*-Si and *c*-Si), coupled with the morphological features and the various nanoscale structures of the respective system. Si_{NF} are composed of a mixture of *a*-Si and *nc*-Si with higher percentage of amorphous silicon phase. However, Si_{NR} consist of higher percentage of highly crystalline Si (*c*-Si) phase in the nanorods combined with a smaller fraction of the *a*-Si formed as result of silicon deposition on the surface of the micron/sub-micron size NaCl particles. Thus, nanorods undergo amorphous Si transformation occurring through the crystalline $Li_{15}Si_4$ pathway (characterized by peak at ~0.41V in **Figure 42b**) which results in an inferior performance and higher capacity loss when compared to the Si_{NF}, during the initial discharge - charge cycles. Si_{NF} consist of a mixture of ~85-87% a-Si with the other phase being *nc*-Si phase while Si_{NR} consist of ~18-20% *a*-Si with the rest comprising crystalline *c*-Si phase of higher crystallinity (**Table 11**, Raman spectra fitting shown in **Figure 62** and **Figure 63**).

Si_{NF} consists of micron-sized nanoflakes formed because of growth/sintering of individual Si particles. However, the thickness (t) of the nanoflakes is restricted to ~40-60nm when compared to Si_{NR} which consist of micron length nanorods with diameters ranging from 50nm – 200nm. The restriction of the thickness in Si_{NF} not only provides a bi-axial pathway for relaxation of strain developed during volume expansion but also allows for easy diffusion of Li^+ ion due to the reduced diffusion lengths (L_d=t/2). This thus, results in Si_{NF} showing a much lower fade rate (0.11% loss per cycle) under long-term cycling conditions as compared to Si_{NR} (0.23% loss per cycle).

These effects of the structural dimensions on Li^+ diffusion distances and their combined influence on the electrochemical response is perceived in the organized plot summarizing the electrochemical responses shown in **Figure 43a.** The plot shows the specific discharge capacity vs. current rate in the stable cycling region of both nanoflakes and nanorods obtained from the rate capability tests. The normalized specific capacity (with respect to the discharge capacity at 50 $mA \cdot g^{-1}$) vs. current rate is also displayed to provide a realistic comparison of the performance of Si_{NF} and Si_{NR}. Silicon nanoflakes show a higher capacity than the nanorod morphology at all the current rates under stable cycling conditions and the specific and normalized capacity of the nanorods in fact, drops at higher currents. The superior performance of Si_{NF} morphologies observed when compared to Si_{NR} during the current rate tests is clearly due to the lower diffusion distances available for Li^+ diffusion.

Post cycled SEM analysis of the electrodes (**Figure 43**) was also carried out to characterize the behavior of electrodes and Si nanostructures during long term cycling. The post-cycled SEM micrograph of Si_{NF} (**Figure 43c**) show the bending and folding of the nanoflakes structures to accommodate the stresses developed during the lithiation and delithiation process. However, it should be noted that there is no structural disintegration of the nanoflakes. In the case of Si_{NR} the post-cycled SEM analysis (**Figure 43e**) shows fracture of nanorods particularly, along the cross section leading to shorter lengths. In addition, the nanorod morphology appears to have collapsed or altered and modified after cycling thus, indicating the formation of particles because of coalescence and disintegration process leading to the instability of the nanorods (**Figure 63**). Hence, it can be construed based on the above data and analyses presented that the nanoflakes morphology indeed show lower fade rate and better capacity retention during long term cycling (**Table 11**) as compared to nanorods by preserving the mechanical integrity of the nanostructures. The minor difference in the FIR loss of SiNF (FIR ~ 17%-20%) and SiNR (FIR ~ 12%-15%) is a result of higher specific surface area of nanoflakes which results in the loss of lithium due to higher surface available for SEI formation during the initial charge – discharge cycle. [254-255] In conclusion, the Si nanoflakes act as superior active material for anode fabrication in lithium ion batteries compared to Si nanorods owing to higher content of amorphous Si, smaller diffusion distances and morphological stability thus, resulting in better electrochemical performance (lower fade rate, good rate capability and higher stable specific capacities) on long term cycling.

The stable capacities of these bare Si nanoflakes is better than magnesiothermic nano-Si and nano Si@C and comparable to that of Si@PCM which show a stable capacity of ~1250mAhg^{-1} @ 0.5Ag^{-1} at the end of 100 cycles, reported by Wu. L et.al. [256] Furthermore, similar capacities and rate performance were observed in carbon sheet anode comprising core-shell Si/C nanosphere bubbles (anode system morphologically similar/analogous to Si nanoflakes) which showed stable capacities of ~1110 mAhg^{-1} during rate capability test and ~1018 mAhg^{-1} at the end of 200cyles @ 1Ag^{-1}, reported by Li. W et. al. [257] The performance of the bare Si_{NF} is also comparable to carbon/CNT based silicon nanoparticle composites derived from rice husk which show a capacity of ~1031mAhg^{-1} @0.5Ag^{-1} at the end of 100cycles with an FIR loss of ~28%, reported by Zhang.Y. et. al. [258] The Si_{NF} system shows promise as stable active material to be incorporated into a lithium battery composite anode system with lower relative weight of porous carbon, graphite [255] or polymer gel matrices by commercial process such as electrospraying [259], spray drying[260], electrospinning [261] or carbon pyrolysis [254] to further enhance the performance, decrease the fade rate/FIR Loss and further improve the stable specific capacity under long term cycling.

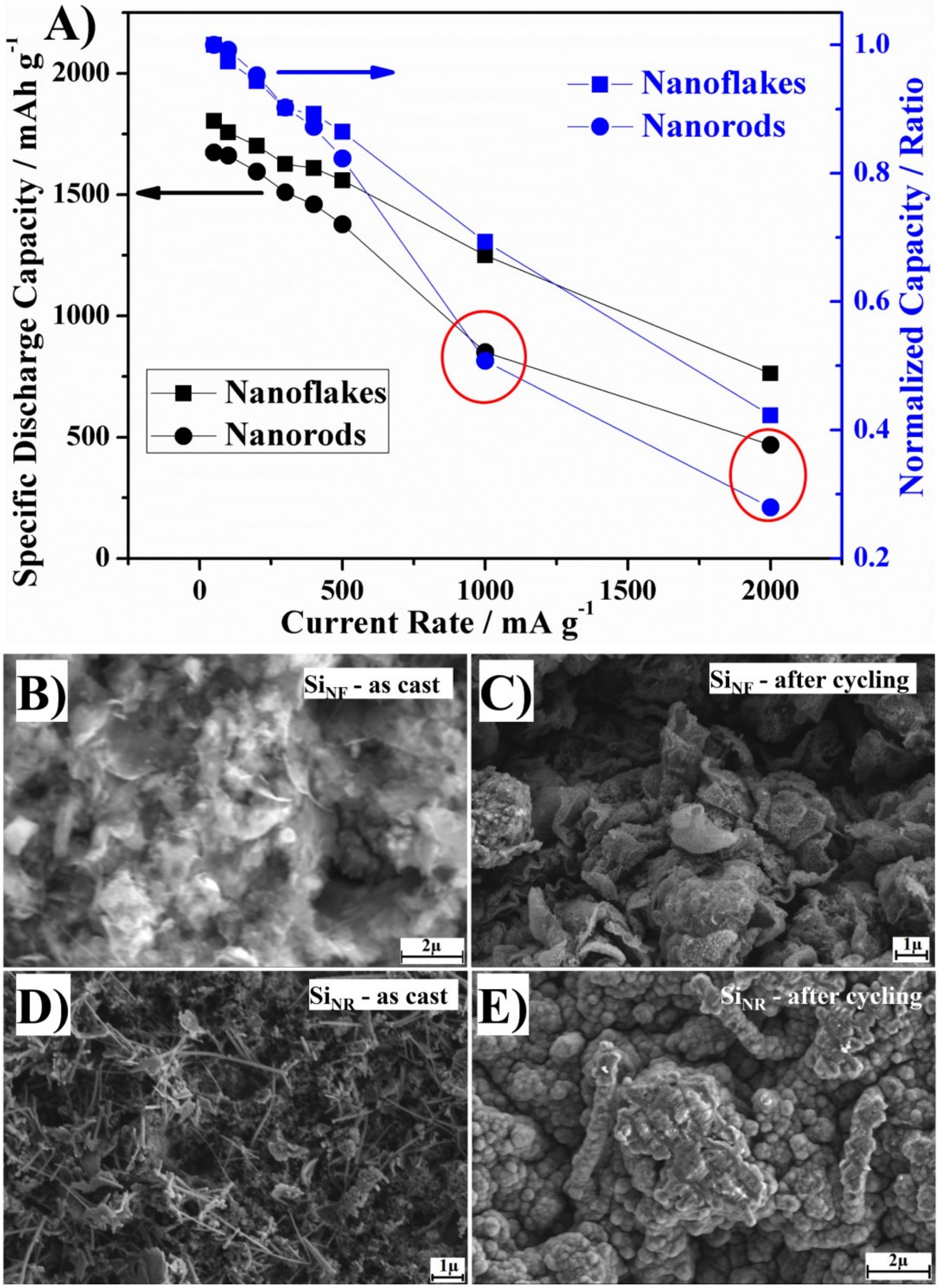

Figure 43 a) Specific discharge capacity / normalized capacity vs current rate in the stable cycling region of Si nanoflakes and Si nanorods. Red circles indicate drop in performance of nanorods at higher current rates. SEM of b) and c) SiNF electrode before and after, d) and e) SiNR electrode before and after 300 cycles during long term testing, respectively

4.4 Conclusions

Silicon nanostructures with different morphology and different crystalline structure (crystalline, nanocrystalline and amorphous) were generated using a facile, high throughput and scalable process involving abundant, cheap, green, completely recyclable water soluble sodium chloride template approach. Silicon was deposited using low-pressure chemical vapor deposition (LPCVD) of silane on different NaCl particle sized templates, derived using high energy mechanical milling (HEMM) to develop Si nanoflakes (Si_{NF}) and nanorods (Si_{NR}). These Si nanostructures serve as high performance anode materials in lithium ion batteries. Both Si nanoflakes and nanorods show high specific charge discharge capacities. However, owing to the structural dimensions, higher content of *a*-Si and presence of *nc*-Si instead of crystalline silicon (*c*-Si) of higher crystallinity, nanoflakes show superior performance as compared to nanorods. Silicon nanorods on the other hand, showed a first cycle discharge and charge capacities of ~ 2980 $mAh\cdot g^{-1}$ and ~2500 $mAh\cdot g^{-1}$, respectively at a current rate of 50 $mA\cdot g^{-1}$ with a first cycle irreversible loss (FIR loss) of ~ 12-15%. Upon longer cycling at a current rate of 1 $A\cdot g^{-1}$ Si nanorods displayed a discharge capacity of ~740 $mAh\cdot g^{-1}$ at the end of 250 cycles with a columbic efficiency of 99.95-99.97% and a fade rate of ~ 0.23% loss per cycle. Silicon nanoflakes on the other hand, showed a first cycle discharge and charge capacities of ~ 2830 $mAh\cdot g^{-1}$ and 2175 $mAh\cdot g^{-1}$, respectively at a current rate of 50 $mA\cdot g^{-1}$ with a first cycle irreversible loss (FIR loss) of ~ 15-20%. Upon longer cycling at a current rate of 1 $A\cdot g^{-1}$, the Si nanoflakes showed a stable discharge capacity of ~810 $mAh\cdot g^{-1}$ at the end of 250 cycles with a columbic efficiency of 99.95-99.97% and a fade rate of ~ 0.11% loss per cycle demonstrating the superior electrochemical response.

5.0 Pulsed Current Electrodeposition of Silicon Thin Films Anodes for Lithium Ion Battery Applications

5.1 Introduction

Electrodeposition or electroplating is a relatively simple, easy, robust, easily scalable, and economically viable electrochemical technique for large area generation of active systems. It is very widely used in industries to synthesize coatings and thin films of various metals, alloys, and particulate composites to enhance the tribological and corrosion resistance properties of materials. Recently, electrodeposition of amorphous silicon (*a*-Si) from non-aqueous electrolytes has been used to deposit thin films and nanostructures of *a*-Si by potentiostatic (constant potential) and galvanostatic (constant current) methods on different substrates—such as nickel foams, nickel coated tobacco mosaic virus (TMV), and copper foil—and their electrochemical properties are studied for LIBs [31, 262-269]. However, there is no reported study on the evolution and modification of the morphology of *a*-Si thin films during the electrodeposition process and the systems suffer from poor areal loading density, low areal capacities, and low overall specific capacity of the anode due to the type of substrates employed.

In this regard, pulse electrodeposition is a well-known modification of traditional electrodeposition process and has been studied for varying the morphology, mechanical properties and composition of different types of metallic, composite, and nano coatings [270-273]. The pulse power electrodeposition approach offers an economical and easy way to change the grain size and morphology of the deposits, thus enhancing the density of coatings and their mechanical strength and corrosion properties [274-277].

In the current work pulsed current electrodeposition (PED) technique was employed to develop Si thin films on Cu foil. PED at various frequencies of the pulsing cycle was used to obtain different morphologies of *a*-Si thin film deposits on Cu foil and their performance in LIB was studied. PED, which is a simple extension of electrodeposition technique, provides an economical way to modify the properties of the thin films by providing modulated voltage/current input into the electrodeposition cell instead of direct current or voltage. The composition and morphology of the thin films are thereby altered with the change in the frequency which correspondingly, influences their performance in the lithium ion batteries.

5.2 Experimental

5.2.1 Pulse Electrodeposition of Silicon on Cu Substrates

Propylene carbonate (PC, 99.9% anhydrous), tetrabutylammonium chloride (TBACL, >97%), silicon tetrachloride ($SiCl_4$, 99.99%), and acetone (99.9%, anhydrous) used for deposition studies were purchased from Sigma–Aldrich (St. Louis, MO, USA) and were used without further purification. Propylene carbonate was selected as the solvent due to its high dielectric constant ($k = 64$) which makes it a good medium for dissolving silicon tetrachloride. For the supporting electrolyte, tetrabutylammonium chloride (TBACL, >97%) was dried overnight in vacuum and added to propylene carbonate to improve the conductivity of the electrolyte.

A solution of 0.5 M $SiCl_4$ and 0.1 M TBACL prepared by dissolving 1.12 g TBACL and 2.3 mL $SiCl_4$ in 37.7 mL PC under regulated atmosphere ($O_2 < 0.1$ ppm and $H_2O < 0.1$ ppm) in a glove box was used as the electrolyte for the PED. EC epsilon (Bioanalytical system, West

Lafayette, IN, USA) was used to conduct linear sweep voltammetry (LSV) of the electrolyte in a cylindrical three electrode cell made of glass and sealed with teflon gaskets at both the ends. For the pulsed electrodeposition study, bare Cu foil was used as the working electrode while platinum wire (diameter = 0.5 mm, 99.95%, Alfa Aesar, Tewksbury, MA, USA, 1 mm distance from working electrode) and platinum foil (0.5 cm L × 0.5 cm B × 0.1 mm thick, 99.9%, Aldrich, St. Louis, MO, USA) served as the reference and counter electrodes, respectively.

Dynatronix pulse power supply (Dynatronix, Amery, WI, USA) was used for the pulsed current electrodeposition of Si films under an argon atmosphere by converting the three-electrode cell into a two - electrode cell. The Cu electrodes were sonicated in ethanol and acetone for 5 min and dried in air before use and 20 ml of the above electrolyte solution was used for the deposition immediately after preparation. The peak current density of the pulsing cycle was 1 $mA\cdot cm^{-2}$ with a duty cycle of 50%, total charge density of 60 $mA\text{-}min\cdot cm^{-2}$ and the frequency of the cycle was maintained at 0 (galvanostatic), 500, 1000, 2000, 3000, 4000, and 5000 Hz. To remove any traces of electrolyte, salts, and impurities, the copper foils electrodeposited with silicon were first rinsed in PC followed by anhydrous acetone under an argon atmosphere. The foils were then allowed to dry in an argon filled glove box approximately for 1 h before further characterization.

5.2.2 Material and Electrochemical Characterization

The pulse electrodeposited samples were always sealed in the glove box under an argon atmosphere before transferring them out of the glove box for further studies. Scanning electron microscopy (SEM, Philips XL 30, FEI, Hillsboro, OR, USA) was used to study the morphological characteristics of the thin films and subsequently, attached Energy Dispersive X-ray Spectroscopy (EDAX, AMETEK, Mahwah, NJ, USA) operated at 10 kV was used along with the GENESIS software for conducting qualitative compositional analysis [278]. Raman spectroscopy was performed using a Renishaw inVia Raman microscope (Renishaw, Gloucestershire, UK) equipped with a 633 nm red laser to evaluate the vibrational and rotational modes of the deposited films. PANalytical Empyrean XRD diffractometer (PANalytical, Almelo, Netherlands) was used for performing Glancing angle X-ray diffraction (GAXRD) on the electrodeposited Si thin films. The Cu foil electrodeposited with Si were assembled under argon atmosphere in a half cell (2025 coin cell) using lithium foil as the counter electrode and 1M $LiPF_6$ in ethylene carbonate (EC), diethylene carbonate (DEC), and fluoroethylene carbonate (FEC) with EC:DEC:FEC = 45:45:10 by volume as electrolyte. The assembled coin cell was tested in the potential window of 0.01V–1.2V with respect to Li/Li^+, at a current rate of 0.3 $A \cdot g^{-1}$ to study their performance as anode material.

5.3 Results and Discussions

5.3.1 Pulsed Current Electrodeposition of Si on Cu Foils

The pictorial diagram of the two - electrode electrodeposition cell along with the polarity of the electrical connections has been shown in **Figure 44a**. The general parameters of operation of the pulsed current electrodeposition are forward peak current density, forward ON TIME, forward OFF TIME, reverse peak current density, reverse ON TIME, reverse OFF TIME, and the total amount of charge supplied (**Figure 44b**). The reduction and deposition of Si^{4+} ions occurs during the ON TIME of the forward cycle (positive cycle) while during the ON TIME of the reverse cycle, the deposited Si is stripped in the form of Si^{4+} and enters the electrolyte solution.

During the OFF TIME also, there is no current passing through the cell and hence, there is no reduction/oxidation taking place at the electrodes. However, during the OFF TIME, since there is no deposition occurring, there is diffusion of Si^{4+} ions from the bulk of the electrolyte towards the ionically depleted region formed at the electrode–electrolyte interface. A typical input cycle of pulse current electrodeposition with both deposition and stripping cycle is as shown in **Figure 44b**. In the current study however, to prevent the complications arising from the oxidation of Cu from the substrate into the electrolyte during the reverse cycle, we have employed only the forward deposition cycle as shown in **Figure 44c**. The percentage ratio of ON TIME (AB) to forward TIME (AB+CD) in the pulsing cycle is termed as the DUTY CYCLE and is kept constant at 50%. The different pulsed current electrodeposition parameters used in the study have been listed in **Table 9**.

Table 9 Pulse current electrodeposition parameters used in the study.

Sample ID	Peak Current Density ($mA\cdot cm^{-2}$)	ON TIME (AB) (ms)	OFF TIME (CD) (ms)	Duty Cycle (%)	Frequency $(AB+CD)^{-1}$ (Hz)	Charge ($mA\text{-}min\cdot cm^{-2}$)
PEDSi-0	1.00	1	0	100	0	60
PEDSi-500	1.00	1	1	50	500	60
PEDSi-1000	1.00	0.5	0.5	50	1000	60
PEDSi-2000	1.00	0.25	0.25	50	2000	60
PEDSi-3000	1.00	0.17	0.17	50	2941	60
PEDSi-4000	1.00	0.13	0.12	52	4000	60
PEDSi-5000	1.00	0.1	0.1	50	5000	60

The linear sweep voltammetry (**Figure 44d**) of the supporting electrolyte TBACL in propylene carbonate solvent showed stable electrolyte window of (−) 0.5 V to (−) 1.9 V without any deposition peak for the current electrochemical setup. With the addition of $SiCl_4$, the LSV shows a cathodic peak corresponding to the reduction of Si^{4+} ions and deposition of Si at around (−) 1.58 V. The pulse electrodeposited films showed yellowish color after they were washed in propylene carbonate followed by anhydrous acetone in the glove box atmosphere. However, upon exposure to ambient atmosphere, the silicon reacts with air/moisture and immediately undergoes oxidation to form silicon dioxide thus turning into a white deposit in due course of time. Hence, the electrodeposited samples were sealed in the glove box under argon atmosphere and then transferred for Raman analysis and into the scanning electron microscopy chamber for further analyses.

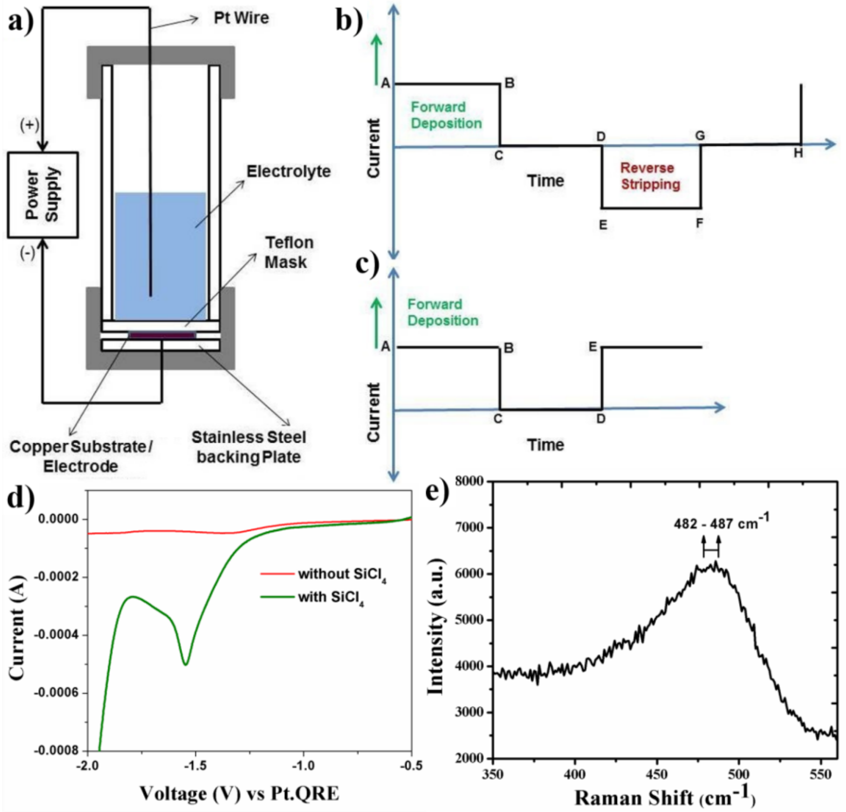

Figure 44 (a) Pictorial representation of the pulse electrodeposition setup; (b) standard input current cycle during pulse electrodeposition; (c) input current cycle for pulse current electrodeposition in the current study; (d) linear sweep voltammogram of electrolyte with and without SiCl4 showing the reduction of Si4+ ion and (e) Raman spectral shift of the pulse current electrodeposited silicon films

The Raman analysis of all the pulse current electrodeposited films was carried within 15 min after exposure to ambient atmosphere. The Raman spectra showed a broad peak (**Figure 44e**), approximately 483–487 cm^{-1} for all the pulse electrodeposited samples. For crystalline silicon, a sharp peak corresponding to transverse optical vibrational mode is reported [226-228] at around 520

cm^{-1}. However, the broad peak obtained in the Raman spectra suggests the presence of amorphous silicon in the thin film which is caused due to the disruption of long-range order as compared to crystalline silicon.

5.3.2 Morphological and Compositional Characterization

SEM analysis was conducted to observe the morphology of the electrodeposited films. For the SEM and EDAX analysis (**Figure 45**), the samples were transferred into the SEM chamber within 5 min of opening the seal to prevent the oxidation of silicon due to prolonged exposure to the oxygen and moisture in the room atmosphere. The EDAX analysis of the samples showed the presence of silicon, oxygen, copper, and carbon (**Figure 45a**). The copper peak (CuL_{α} ~0.93 KeV) arises from the substrate on which the electrodeposition has been carried out while the presence of oxygen is attributed to the partial oxidation of silicon (SiK_{α} ~1.739 KeV) in the brief time the samples are exposed to the room atmosphere while transferring into the SEM chamber. The presence of carbon (CK_{α} ~0.277 KeV) may be attributed to the presence of residual solvent or contamination from the SEM chamber. Another reason for the presence of carbon and oxygen (OK_{α} ~0.525 KeV) can be attributed to the decomposition of electrolyte along with the reduction of silicon due to the localized over potential developed on the growth sites during the electrodeposition process, thus forming a Si–O–C composite system [279-282]. The glancing angle XRD pattern (**Figure 45b**) shows only Cu peaks (2θ ~43.7°, 50.8°) arising from the underlying substrate devoid of any peaks corresponding to crystalline silicon (high intensity peak at 2θ ~28.4°). The zoomed up inset pattern obtained from smoothening of the curves (inset of **Figure 45b**) shows a low intensity broad peak between $27° < 2\theta < 30°$ which confirms the amorphous nature of electrodeposited silicon thin film validating the Raman analysis. Due to the amorphous nature of the silicon in the electrodeposited thin film, the intensity of the Cu peaks dominates the spectra obtained from the glancing angle XRD and the low intensity broad peak of *a*-Si could be noticed only by analyzing the obtained spectra in the 20° < 2θ < 35° region.

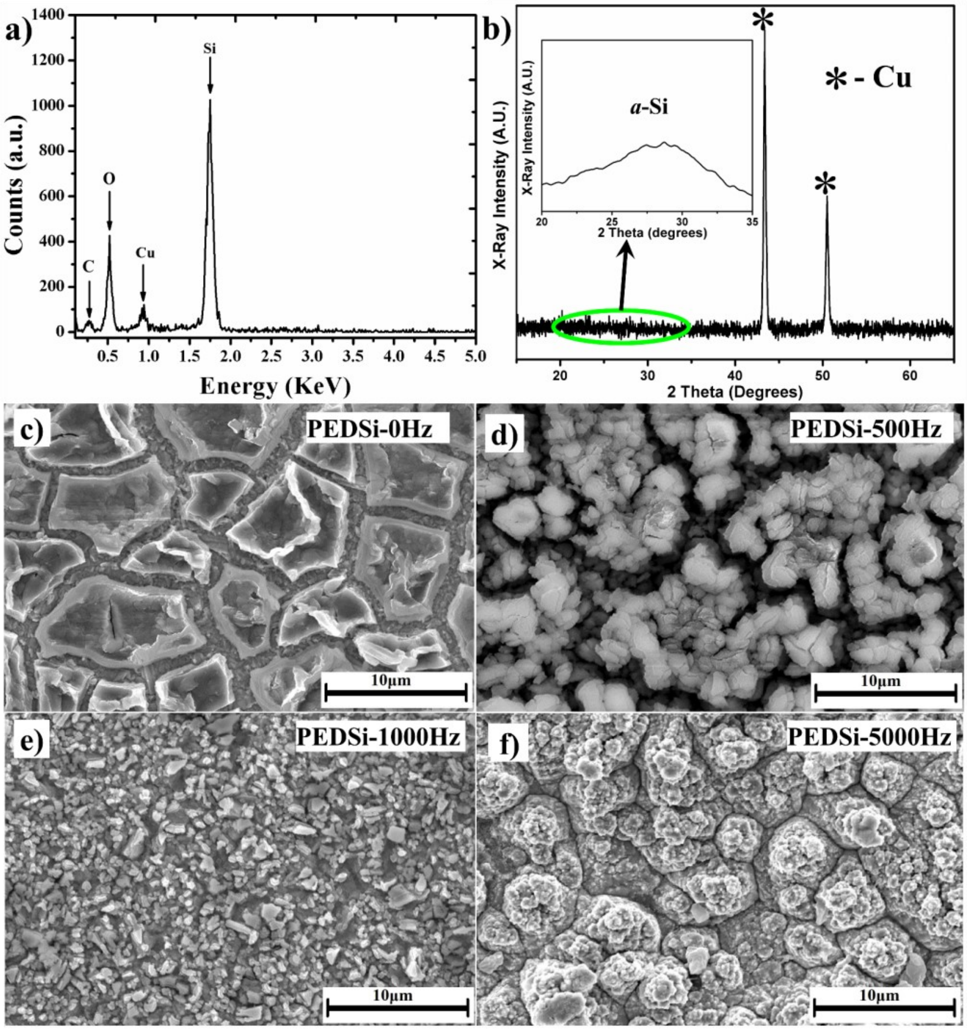

Figure 45 (a) Energy dispersive spectra (EDAX) and (b) XRD pattern of pulse current electrodeposited thin films. The inset shows the smoothened XRD curve between 20° < 2θ < 35°. SEM images of (c) PEDSi-0, (d) PEDSi-500, (e) PEDSi-1000 and (f) PEDSi-5000 Hz

The SEM analysis (**Figure 45**) of the samples shows a drastic change in morphology between the films deposited at 0 (galvanostatic, PEDSi-0), 500 (PEDSi-500) and 1000 Hz (PEDSi-1000). PEDSi-0 (**Figure 45c**) which corresponds to the constant current electrodeposition showed islands of silicon approximately 5–10 μm wide simulating dried mud cracks, which is in good agreement with previous study reported [37]. PEDSi-500 (**Figure 45d**) which corresponds to pulse current frequency of 500 Hz, showed a cracked morphology very similar to PEDSi-0, however, the solid islands of Si were replaced by discrete particulate deposits. At a frequency of 1000 Hz, the island morphology was completely replaced with a thin continuous layer comprising of 1 μm–2 μm silicon particles seen in the SEM analysis of PEDSi-1000 (**Figure 45e**). At higher frequency of 5000 Hz, the deposits retained the thin film morphology as observed in PEDSi-1000 however; the size of the particles comprising the film decreases to less than 1 μm observed in PEDSi-5000 (**Figure 45f**). This change in morphology occurs due to the change in the nucleation and growth kinetics of the film followed by the variation in thickness of the depletion layer at the electrode–electrolyte interface and the decrease in the concentration of ions in the bulk of the solution. The difference in the morphologies can be explained by two different reason depending on the frequencies used during pulse electrodeposition.

At lower frequencies (PEDSi-0 Hz, PEDSi-500 Hz, and PEDSi-1000 Hz), the competitive behavior between the time scale for Si^{4+} diffusion and reduction results in the formation of different morphology of the thin films. During longer ON TIME, the timescale for reduction is more favorable than that for diffusion of Si^{4+} hence, giving a low-density deposition with large grains as in case of PEDSi-0 and PEDSi-500. However, the Si^{4+} diffusion is favored upon decreasing the ON TIME allowing the ions to penetrate into the diffusion structure giving more uniform and denser thin films (PEDSi-1000 Hz) thus, improving the mechanical strength of the Si thin film as well as that of the Si –Cu interface [283-284]. At higher pulse frequencies (PEDSi-1000 Hz to PEDSi-5000 Hz), the pulses are much shorter, i.e., both ON TIME and OFF TIME are of short duration during which the double layer does not have sufficient time to fully charge during

ON TIME and to discharge during the OFF TIME. The completion of one pulse cycle is immediately followed by the next pulse which results in thin pulse diffusion layers. This phenomenon hinders the transport process and makes the diffusion of the migrating Si^{4+} ions from the solution to the cathode surface difficult [284-286]. This rapid change in the pulsing process leads to the formation of thin film by enhanced nucleation rate and limited growth rate resulting in a dense Si film as seen in **Figure 45e,f** similar to pulse electrodeposition of silver alloys [287]. A similar change in morphology has been reported for Sn thin films with the change in frequency of deposition wherein the morphology of Sn thin films change from porous large non-uniform grains to dense structures by increasing the pulse frequency [270].

5.3.3 Electrochemical Characterization of PEDSi on Cu

Electrodeposition driven by controlled atomistic reduction of Si^{4+} ions, results in direct growth of *a*-Si thin film on the Cu surface instead of generating discrete loose particles leading to good mechanical and electrical contact at Cu/Si interface due to the likely strong interface adhesion forces. Hence, the pulse electrodeposited Si electrodes were directly assembled in a 2025 coin cell without addition of any binder or Super P and tested with lithium as counter/reference electrode in the voltage window of 0.01–1.2 V. A significant peak is observed close to ~0.15 V during the first discharge cycle in the differential capacity plot (**Figure 46a**) indicating the alloying reaction of lithium with *a*-Si and presence of partially alloyed (*a*-Li_ySi) and unalloyed (*a*-Si) two phase region as reported in the literature [208, 216, 229]. The presence of a potential peak at ~0.08 V indicates various stages of alloying reactions and complete formation of *a*-Li_xSi during the end of the first discharge cycle. The charge cycle shows reaction peaks at ~0.32 V and ~0.48 V corresponding to the extraction of lithium from electrode which is commonly observed for the de-alloying reaction from the amorphous Li_xSi alloy. The columbic efficiency varied from 94 to 98% from the second to fifth cycle, after which it further improved and remained close to 99.7% for the rest of the cycles.

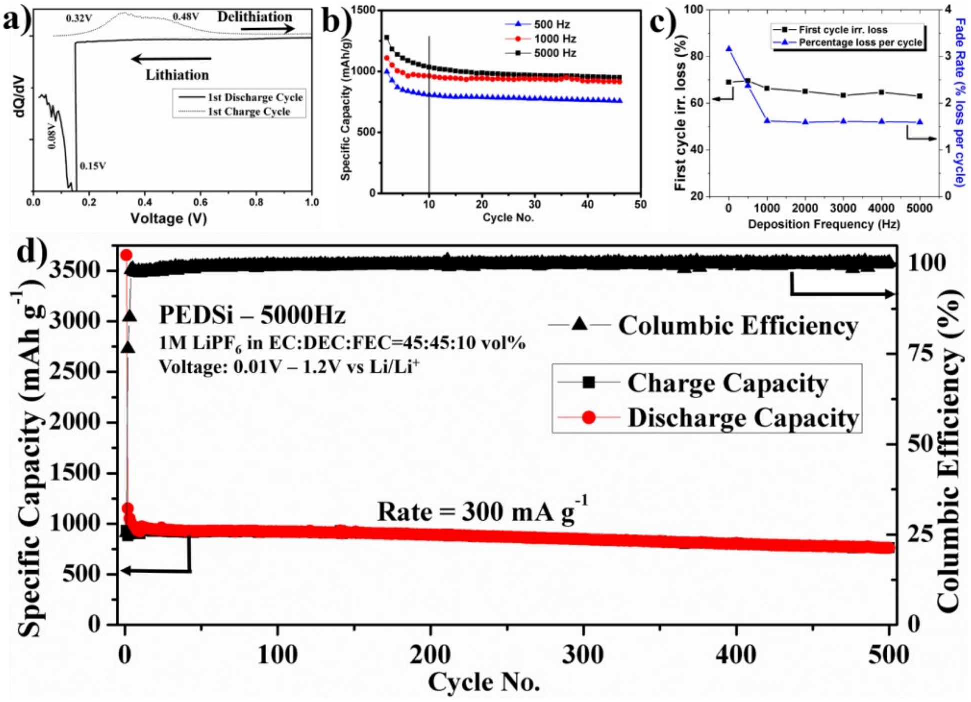

Figure 46 (a) Differential capacity vs Voltage curves of electrodeposited Si film; (b) specific discharge capacity of electrodeposited thin films under different pulse current conditions (from 2nd cycle); (c) Performance of electrodeposited Si films with frequency of deposition. Fade rate (the percentage loss per cycle for first 10 cycles) and first cycle irreversible vs frequency of deposition; (d) Long-term cycling plot of PEDSi-5000 Hz tested in Li/Li+ system

The electrochemical reduction of Si^{4+} during electrodeposition is accompanied solvent decomposition and reduction of tetrabutylammonium ion (TBA^+) leading to formation of carbon and oxygen in the thin film. To calculate the gravimetric capacity of the deposited silicon films, an efficiency parameter for Si^{4+} reduction is introduced into the Faraday's law to calculate the actual number of moles of silicon reduced. An efficiency parameter of 35% efficiency is used in the current work, based on previously reported work using similar electrolyte and deposition conditions [31]. The theoretically calculated areal loading density of Si is ~0.1 $mg \cdot cm^{-2}$ while the experimentally measured loading density of Si is ~0.24–0.28 mg·cm^{-2}. The additional loading density is expected to arise due to the presence of carbon and oxygen in the thin films formed by the reductive decomposition of the solvent and TBACL.

Figure 46b shows the specific capacity plots of pulse electrodeposited silicon films at different frequencies, when tested in lithium ion battery at a current density of 300 mA·g^{-1}. Discharge capacities of 900–1250 mAh·g^{-1} were obtained with a first cycle irreversible (FIR) loss of ~60–70% for these films. Electrodeposited silicon is often associated with high FIR loss due to the formation of Si–O–C films instead of pure silicon and presence of chlorine in the films. This occurs due to the reductive decomposition of the propylene carbonate or TBA^{+}, the local over potential on the surface of the electrolyte leading to localized decomposition, presence of minute traces of water in electrolyte, poor ionic conductivity of the electrolyte, and poor electronic conductivity of electrodeposited Si film. The cycling plot also shows a major loss in capacity during the first 10 cycles after which the specific capacity of the Si thin films stabilizes with lower fade rate.

The pulse current deposited conditions showed very minor reduction in FIR with increase in frequency of deposition (**Figure 46c**) as compared to higher FIR loss exhibited by films deposited under direct current conditions. However, the fade rate in the first 10 cycles showed significant reduction from ~3.15% loss per cycle for films deposited under DC conditions to ~1.5% loss per cycle for PEDSi-5000 Hz. Upon long term cycling at a current rate of 0.3 A·g^{-1} (**Figure 46d**), the PEDSi-5000 Hz thin film showed a gravimetric specific discharge capacity of ~810 mAh·g^{-1} at the end of 500 cycles with a very low fade rate of ~0.056% capacity loss per cycle.

Post cycled SEM analysis of the films for DC conditions showed retention of the island morphology (or cracked film morphology) after 50 charge–discharge cycles which is consistent with the results reported in previous study [31]. PEDSi-500 Hz showed transformation of morphology to cracked thin film morphology during the initial 10 cycles and no further change in the morphology upon further testing till 50 cycles (**Figure 47a–c**). Continuous thin films deposited under PEDSi-1000 Hz (**Figure 47d–f**) and PEDSi-5000 Hz (**Figure 47g–i**), showed development of cracks during the initial 10 cycles of testing after which the films showed no major change in morphology upon further testing, thus indicating the stability of the films due to the improvement in mechanical properties. Electrodeposition being a controlled method involving atomistic adsorption, diffusion and reduction of ions followed by crystallization of atoms, improves the adhesion of thin film to the Cu substrate contributing to mechanical stability of the films. Hence, the electrodeposited films show better performance and stable cycling as compared to sputtered silicon films which fail due to delamination of the films at the substrate–silicon interface [288-289].

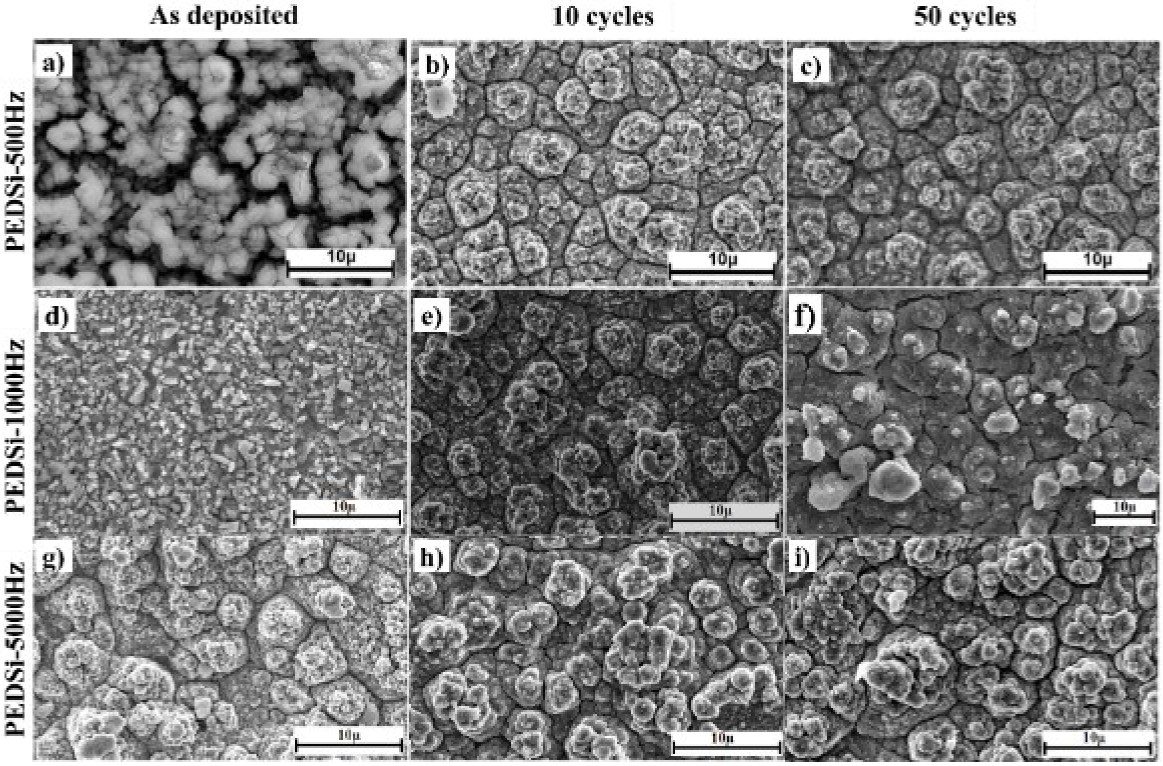

Figure 47 SEM images of (a,b,c) PEDSi-500 Hz, (d,e,f) PEDSi-1000Hz and (g,h,i) PEDSi-5000 Hz, before, after 10 and after 50 electrochemical testing cycles in lithium ion battery

A summary of XPS composition analysis of the Si thin films deposited at different frequencies along with depth profiling (increase in etching time) of the thin film and the calculated FIR loss as per the reversible reaction of Si to form metastable $Li_{3.75}Si$ [253, 290] and the irreversible reaction of Li with oxygen to form Li_2O as shown in **Figure 48** is given below.

$$3.75\ \mathrm{Li} + \mathrm{Si} \Leftrightarrow \mathrm{Li}_{3.75}\mathrm{Si}$$

$$4\ \mathrm{Li} + \mathrm{O}_2 \Rightarrow 2\mathrm{Li}_2\mathrm{O}$$

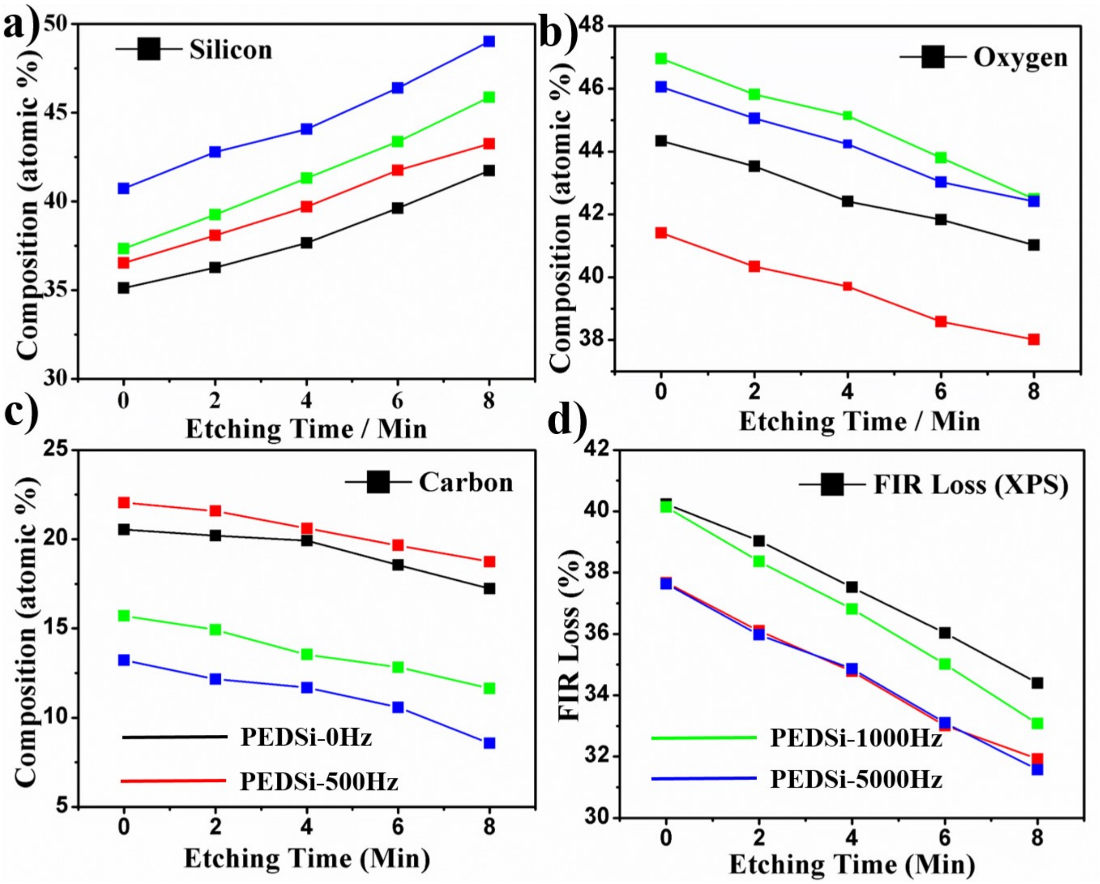

Figure 48 Depth profile of (a) silicon, (b) oxygen and (c) carbon obtained from XPS compositional analysis. (d) The first cycle irreversible loss calculated from the composition of silicon and oxygen in the thin films at various depths. Black, red, green and blue lines indicate the data for PEDSi-0 Hz, PEDSi-500 Hz, PEDSi-1000 Hz and PEDSi-5000 Hz, respectively

The amount of silicon and the ratio of silicon to oxygen increases with depth profiling. Considering that the electrodeposition was conducted under inert conditions and minimal exposure of the films to ambient atmosphere and following earlier reports [281-282], it is likely that increase in oxygen content in the film is probably due to enhanced decomposition of the electrolyte with increase in the thickness of the electrodeposited film and the time of deposition. A similar trend is observed in the calculated FIR loss arising from lithium irreversibly reacting with oxygen indicating that thinner films would show lower FIR loss as compared to thicker films due to the likely reduction in the oxygen content of the electrodeposited thin films following XPS analysis.

The amount of Si content in the film increases with the increase in the frequency of the pulse electrodeposition due to minimal diffusion into the bulk. However, the oxygen content in the film decreases from PEDSi-0 Hz to PEDSi-500 Hz and then increases from PEDSi-500 Hz to PEDSi-5000 Hz. As explained previously at lower frequencies, the growth of Si thin films is guided by relative timescales available for diffusion and reduction of Si^{4+} ions [283-284]. Due to the enhanced diffusion of Si^{4+} ions during the OFF TIME the Si content increases, and the oxygen content decreases from PEDSi-0 Hz to PEDSi-500 Hz. However, at higher frequencies the deposition is governed by enhanced nucleation combined with electrolyte decomposition with limited growth rate [285-287] due to which the content of both silicon and oxygen increases from PEDSi-500 Hz and PEDSi-5000 Hz.

The calculated FIR loss from the XPS composition shows lower FIR loss for PEDSi-500 Hz and PEDSi-5000 Hz when compared to PEDSi-0Hz and PEDSi-1000 Hz. The general drop in the FIR loss with depth is to be expected with the reduction in the surface oxygen in line with **Figure 48b**. Further, the calculated FIR loss is in the range of 28–37% for the pulse electrodeposited films while the experimentally observed values are in the range of 60–70%. The deviation of calculated FIR loss (from XPS compositional analysis) from that observed in electrochemical testing indicates that the FIR loss in these thin films is a combined effect of the loss of lithium due to the oxygen content in the film primarily arising due to electrolyte decomposition and the initial frequency independent disintegration of the thin film during the first cycle discharge. The post-cycled SEM study (**Figure 47**) which shows change in morphology of thin films during the first 10 cycles also confirms the contribution of material loss due to morphological/microstructural disintegration contributing to the FIR loss. More work is clearly warranted to unequivocally ascertain these inferences. The results nevertheless show the influence of frequency of pulsed current electrodeposition on the evolution of morphology and composition (Si, O, C) of the *a*-Si thin films with their subsequent influence on the electrochemical cycling response. Further studies could likely lead to improvements in obtaining high capacity as well as lowering the FIR with improved cycling stability, further attesting to the promise of electrodeposition as a viable approach for generating large scale silicon electrodes for lithium-ion applications.

5.4 Conclusions

Morphology of amorphous silicon was modified by using frequency-dependent pulse current electrodeposition technique. Under galvanostatic conditions, films show mud crack morphology; while at higher frequencies (>1000 Hz) growth of thin continuous film due to the coalescence of electrodeposited particles is observed. Films electrodeposited at 500 Hz show islands of micron size particles forming discontinuous or continuous films under pulse current conditions decreasing in size with increase in frequency. Difference in the morphology is likely due to change in the nucleation and growth mechanisms of thin films formed at the different frequencies studied. The films show an improvement in performance when tested in LIBs with the increase in frequency due to enhanced stability under pulsed current electrodeposition conditions. Consequently, the fade rate (% loss per cycle) reduced from ~3.15% under DC electrodeposition to ~1.6% for pulsed current frequencies greater than 1000 Hz. The films also showed a major change in morphology during the first 10 cycles of electrochemical testing which supports the high fade rate during initial electrochemical cycling. There was minor reduction in first cycle irreversible (FIR) loss with frequency and the pulse electrodeposited films showed a capacity of ~1000–1250 $\mathrm{mAh \cdot g^{-1}}$ with a columbic efficiency of ~99.7% at the end of ~47 cycles. Upon long term cycling at a current rate of 0.3 $\mathrm{A \cdot g^{-1}}$, the thin films deposited at a 5000 Hz frequency showed a capacity of ~805 $\mathrm{mAh \cdot g^{-1}}$ at the end of 500 cycles with a fade rate of ~0.056% capacity loss per cycle demonstrating very good stability and effects of frequency. The loss of lithium due to the presence of oxygen and the change in mechanical integrity due to volumetric expansion during the initial discharge–charge cycle is the major reason for the high FIR loss.

6.0 Nanostructured Si@MWCNT on Copper Substrates: Binderless High Performance Anode System for Lithium - ion Battery

6.1 Introduction

Electrodeposition or electroplating is a relatively simple, effortless, robust, easily scalable and economically viable electrochemical technique. It is very widely used in industries to synthesize coatings and thin films of metals, alloys and particulate composites to enhance the tribological and corrosion resistance properties of materials. Electrodeposition has been used to deposit amorphous silicon (*a*–Si) from non – aqueous electrolytes with thin films and nanostructures of *a*–Si obtained by potentiostatic (constant potential), galvanostatic (constant current) and pulse current methods on different substrates such as nickel foams, nickel coated TMV, copper foil and their electrochemical properties studied for LIBs. [31, 262-269] Si/CNT hybrid nanostructures generated by CVD of Si from silane precursors exhibit good capacity and stable cycling. However, all these systems suffer from poor areal loading density, low areal capacities (Si/CNT structures) and low overall specific capacity of the anode (corrected for the weight of the substrate material) due to the type of substrates (Ni and Ni plated TMV). The deposition of thin film silicon by electrodeposition is associated with formation of Si – O – C composites along with pure silicon due to which all the these thin films show high irreversible loss due to formation of Li_2O and the disintegration of Si thin films during the initial lithiations and delithiation cycles. The increase in thickness of these electrodeposited films reduces the efficiency of Si electrodeposition due to decrease in electronic conductivity of the films which further raises the undesirable FIR loss in lithium ion batteries.

The mitigation of high fade rate during initial cycles associated with Si thin films directly electrodeposited on Cu foils requires a support matrix for the stabilization of Si. Carbon nanotubes (CNTs) form a stable support structure, however, electrodeposition of Si on these CNTs require the electrode design to have electronic continuity. Vertically aligned CNTs (VACNTs) directly adhered to a conducting substrate without barrier / interface coating form thus, form an ideal structure with continuous electrical continuity for Si electrodeposition.

In the current work, a combination of electroless deposition (ELD)[291] , chemical vapor deposition (CVD)[31, 292] and pulsed current electrodeposition (PED) techniques[270-273, 293] were employed to develop Si/CNT nanostructures directly on Cu foil. PED which is a simple extension of electrodeposition technique provides an economical way to modify the properties of the thin films by providing modulated voltage/current input into the electrodeposition cell instead of direct current or voltage. Electroless nickel plated copper was coated with carbon nanotubes (CNTs) using floating catalyst chemical vapor deposition (FCCVD) and subsequently a-Si was electrodeposited using the pulse current frequency on CNT/Cu substrate to obtain a binderless *a*-Si/CNT nanostructured Cu electrode. The first cycle irreversible (FIR) loss in LIBs was reduced by controlling the electrodeposition parameters along with the nature of the electrodeposited Si.

More recently, research has been focused to stabilize Li plating for lithium metal batteries using various substrates such as Au, Ag, Si etc however, the transition from lithium alloying and lithium plating has not been electrochemically characterized in a full cell.[294] Hence, a-Si/CNT electrodes were tested for their electrochemical performance in half cell configuration followed by full cell testing with LiNMC111 at critical condition of low N/P ratio (Negative / positive areal capacity ≤1) under constant current and constant voltage mode to study and analyze the system at different current densities. Efforts have been made to distinguish the electrochemical signal generated from Li plating on Li active materials (for example silicon) to deconvolute nucleation and growth behavior of Li plating from Li alloying with the material (**Appendix A.3**).

6.2 Experimental

6.2.1 Electroless Ni Plating on Cu Substrate

The sensitization of Cu foil was carried out by immersing it in 0.1% $SnCl_2$ solution for 3 min followed by subsequent activation in 0.01% $PdCl_2$ solution for 30sec with the Cu foils washed thoroughly with DI water after each pretreatment step. The mechanism behind this two-step pretreatment method is that, first the Sn^{+2} ions are adsorbed on the surface of substrate during the sensitization treatment which subsequently get displaced by the Pd^{+2} ions on activation. The Pd particles, eventually formed on the surface, serve as the catalytic sites for the electroless deposition of Ni on the Cu substrate. It is to be noted that many other commercial electroless nickel plating methods exist which avoid the use of $PdCl_2$ during the activation treatment. However, for laboratory synthesis the activation of Cu substrate was carried out using $PdCl_2$ solution.

The electroless plating bath consisted of source of nickel ions ($NiSO_4{\cdot}6H_2O$, 30 g l^{-1}), complexing agent ($Na_3C_6H_5O_7$, 100 g l^{-1}), reducing agent ($NaH_2PO_2{\cdot}H_2O$, 20 g l^{-1}), stabilizers ($(NH_4)_2SO_4$ and NH_4Cl, 25 g l^{-1} each) and ammonia solution to maintain the pH value of the electroless bath solution at 9.0.[295-296]

The selective area pretreated Cu foil was immersed in 200 cm^3 of electroless Ni plating solution at a temperature of 85 - 95°C for 5 minutes. The resulting nickel coated Cu foil was washed thoroughly with DI water and dried at 60 °C. The reactions occurring on the catalytically active surface of Cu leading to the electroless coating of Ni can be described by below reactions:

$$Ni^{2+} + H_2PO_2{}^{-} + H_2O \longrightarrow Ni + 2H^{+} + H(HPO_3)^{-} \quad \ldots\ldots\ldots\ldots\ldots (1)$$

$$HPO_2{}^{-} + H_2O \longrightarrow H(HPO_3)^{-} + \frac{1}{2}H_2 \quad \ldots\ldots\ldots\ldots\ldots\ldots\ldots\ldots\ldots\ldots. (2)$$

6.2.2 MWCNT on Ni Plated Cu Substrate (MWCNT/Ni-Cu)

Multiwall carbon nanotubes (MWCNTs) were grown on Ni coated Cu foil in a horizontal quartz tube furnace maintained at 770 °C for a 30 minute deposition time using a floating catalyst method to obtain MWCNT/Cu. Ferrocene was dissolved at 0.1 g ml^{-1} concentration in m-xylene, wherein the iron nanoparticles derived from ferrocene aided the growth of the vertically aligned carbon nanotubes, whereas m-xylene served as the carbon source. The catalyst-carbon source solution was continuously fed at a rate of 0.05 ml min^{-1} into a stainless-steel gas bubbler maintained at 200 °C before allowing it to enter the CVD reactor. Argon and hydrogen were used as the carrier gases flowing at 85 sccm and 15 sccm, respectively. The weight of MWCNT deposited on the surface was approximately 5-10wt% of the nickel-plated Cu substrate which is considerably negligible. For the efficient deposition and high-density growth of CNT a minimum of 10% wt. of Ni in/on the Cu foil is required.

6.2.3 Pulse Electrodeposition of Silicon on Cu and MWCNT/Ni-Cu Substrates

Propylene carbonate (PC, 99.9% anhydrous), tetrabutylammonium chloride (TBACL, >97%), silicon tetrachloride ($SiCl_4$, 99.99%) and acetone (99.9%, anhydrous) used for deposition studies were purchased from Sigma–Aldrich (St. Louis, MO) and were used without further purification.

A solution of 0.5 M $SiCl_4$ and 0.1 M TBACL (degassed for 24h under vacuum at room temperature) prepared by dissolving 1.12g TBACL and 2.3ml $SiCl_4$ in 37.7ml PC under regulated atmosphere ($O_2 < 0.1$ ppm and $H_2O < 0.1$ ppm) in a glove box was used as the electrolyte for the PED. For the electrodeposition study, bare Cu or MWCNT/Ni-Cu foils were used as the working electrode while platinum wire (diameter = 0.5 mm, 99.95%, Alfa Aesar, 1mm distance from working electrode) and platinum foil (0.5cm L × 0.5cm B x 0.1mm thk, 99.9%, Aldrich) served as the reference and counter electrodes, respectively, in a cylindrical three electrode cell made of glass and sealed with teflon gaskets at both the ends (**Appendix A.3**, **Figure 64a)**.

Dynatronics pulse power supply was used for the pulsed current electrodeposition of Si films under argon atmosphere by converting the three-electrode cell into a two-electrode cell. The MWCNT/Ni-Cu electrodes were washed in ethanol and acetone for 5 min and dried in air, following which they were wetted in PC under vacuum for 15min. The above electrolyte solution (20ml) was used for the deposition immediately after preparation and the deposition process was repeated by replenishing the electrolyte to increase the areal loading density of Si. The peak current density of the pulsing cycle was $0.2 \text{ mA} \cdot \text{cm}^{-2}$ with a duty cycle of 20%, total charge density of $30 - 180 \text{ mA·min·cm}^{-2}$ and the frequency of the cycle was 500 Hz. For increasing the amount of silicon in the electrode the above process was repeated by replenishing the electrolyte till the desired loading was achieved (charge density of $60 - 600 \text{ mA·min·cm}^{-2}$). To remove any traces of electrolyte, salts and impurities, the deposited substrates were first rinsed in PC followed by anhydrous acetone in argon atmosphere. The obtained EDSi-MWCNT/Ni-Cu foils were then allowed to dry in an argon filled glove box approximately for 1 h before further characterization/processing.

Furthermore, the obtained EDSi-MWCNT/Ni-Cu were sealed in capped Swagelok fitting and heat treated under argon atmosphere at 500°C for 1hr to obtain *a*-Si-MWCNT/Ni-Cu electrodes. For full cell cycling the first cycle irreversible loss of *a*-Si-MWCNT/Ni-Cu electrodes was adjusted to 0% by the addition of calculated amount of lithium particle dispersion on the top of electrode followed by drying in vacuum for 24hour.

6.2.4 Material Characterization

The samples (EDSi/Cu and EDSi-MWCNT/Ni-Cu) were always sealed in the glove box under argon atmosphere before transferring them out of the glove box for further studies. Scanning electron microscopy (SEM, Philips XL 30 or Zeiss) was used to study the morphological and compositional analysis. Raman spectroscopy was performed using a Renishaw in-via Raman microscope equipped with a 633 nm red laser to evaluate the vibrational and rotational modes of the deposited films.

6.2.5 Electrochemical Characterization

Half Cell Testing: The Cu and CNT/Cu electrodes electrodeposited with Si (EDSi-MWCNT/Ni-Cu and *a*-Si-MWCNT/Ni-Cu) were assembled under argon atmosphere in a half cell (2025 coin cell) using lithium foil as the counter electrode and 1M $LiPF_6$ in ethylene carbonate (EC), diethylene carbonate(DEC) and fluoroethylene carbonate (FEC) with EC:DEC:FEC = 45 : 45 : 10 by volume as electrolyte. The assembled coin cells were tested at a different current rate in the potential window of 0.01V – 1.2V with respect to Li/Li+ to study their performance as anode material under constant current (CC-current rate, CC-50 $mA\cdot g^{-1}$ to CC-4000 $mA\cdot g^{-1}$ etc) followed by constant voltage (CV-voltage, CV-0.01 and CV-1.2) mode.

Full cell Testing: LiNMC111 powder (MTI XTL Corp.) was dispersed in Super P and PVDF (LiNMC111 : SuperP : PVDF=90:5:5 %wt.) using NMP solvent and the slurry was coated on aluminum current collector to obtain areal loadings of ~15 – 20 $mg\cdot cm^{-2}$ (theoretical stable capacity ~ 140-150$mA\cdot h\cdot g^{-1}$ – LiNMC111 @C/10 current rate) corresponding to an areal capacity of ~2-3$mAh\cdot cm^{-2}$. Subsequently, modified CR2025 coin cell (**Appendix A.3, Figure 64d**) were assembled using *a*-Si-MWCNT/Ni-Cu as the anode and LiNMC111 cathode (electrode diameter = 10mm each) and tested at different current rate using CC-CV mode (CC-15 $mA\cdot g^{-1}$ to CC-150 $mA\cdot g^{-1}$, CV-2.7 and CV-4.2) in the potential window of 2.7V – 4.2V to study their electrochemical performance.

6.3 RESULTS AND DISCUSSIONS

6.3.1 MWCNT on Electroless Ni Coated Cu Foil

The SEM analysis (**Figure 49e**) and EDAX elemental mapping (**Appendix A.3**, **Figure 65**) of the Cu foil after electroless plating indicates a distinct layer of Ni (<1micron) thickness well adhered to the Cu foil formed because of the Ni^{2+} reduction by the hypophosphite in the solution. Electroless plating of Ni is independent of the nature of the surface unlike electroplating process and hence, provides a more uniform coating on the Cu foil along with selective deposition of Nickel on the surface.

Subsequently, multiwalled carbon nanotubes were grown on the Ni-Cu foils at 770°C – 850°C by the injection of ferrocene/xylene vapor mixture in the presence of Ar/H_2 atmosphere. The decomposition of ferrocene generates Fe nanoparticles which assist the growth of vertically aligned carbon nanotubes due to the catalytic decomposition of the xylene which acts as the carbon precursor. The SEM analysis of the vertically aligned MWCNT/Ni-Cu foils shows a distinct layer of highly dense vertically aligned CNTs well adhered to the Ni-Cu foil without delamination under bending forces (**Figure 49f, g, Appendix A.3 Figure 66**). The length of the CNTs were approximately 40-150 micron and can be tailored by changing the time and temperature of the deposition. The elemental EDAX mapping of the cross section shows a well-defined carbon elemental mapping with a distinct boundary from the Ni – Cu substrate. However, the mapping of Ni and Cu show solid state inter diffusion due to their similar atomic radii, electronegativity and crystal structures (face centered cubic/ lattice parameters) thus, forming a solid solution of Ni – Cu alloy triggered by the high temperatures involved during the CVD growth of the CNTs.

The presence of Ni activates the Cu surface for the growth of the CNTs along with improving the adhesion of the CNTs to the substrate without the use of barrier coatings such as chromium or titanium[297]. A study on the VACNT growth by CVD on different loadings of electroless Ni on Cu indicated that a minimum of 10-15 % at. of Ni in Cu was essential for complete uniform coverage of high density VACNT on the substrate along with good adhesion to the substrate. Additionally, the Cu – Ni contains minor quantities of phosphorus (from electroless plating) which drastically improves the corrosion resistance of the foils which is essential during the electrodeposition of silicon from highly acidic chloride electrolytes over long deposition times.

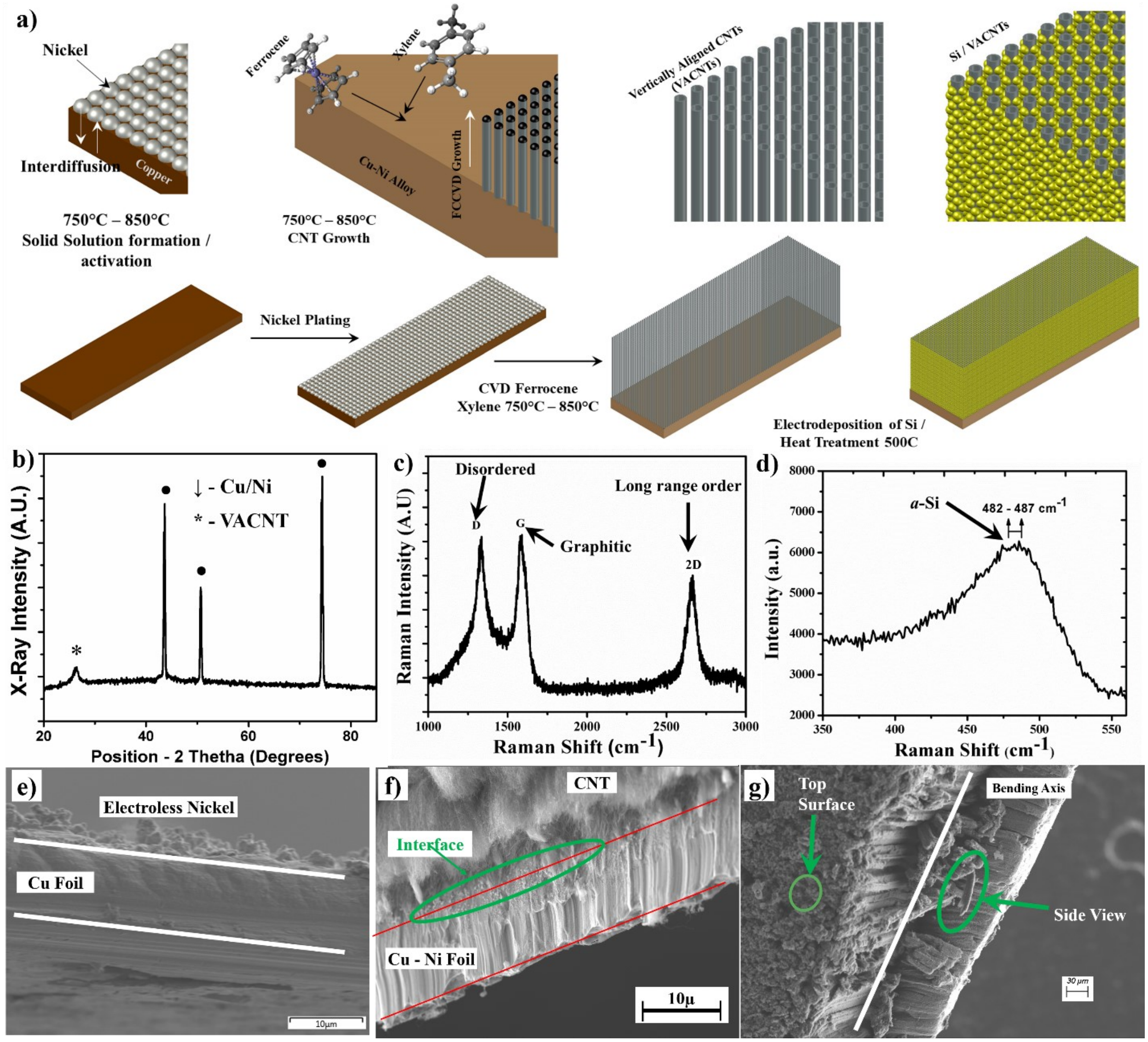

Figure 49 a) Schematic showing different steps and phenomenon during synthesis of Si-MWCNT/Cu-Ni electrodes, b) XRD pattern of MWCNT/Cu-Ni substrates, c) and d) Raman spectra of MWCNT in MWCNT/Cu-Ni and Si in EDSi-MWCNT/Cu-Ni, respectively, SEM analysis e) electroless Ni plated Cu, f) MWCNT/Cu-Ni cross sections and g) MWCNT/Cu-Ni under deformation

The XRD analysis of the Ni-Cu foils shows overlapping peaks corresponding to that of Cu and Ni due to their similar crystal structures. The Ni-Cu foils after the CVD process showed additional peak at 2theta = 26.5 degrees indicating the growth of vertically aligned carbon nanotubes in MWCNT/Ni-Cu foils. Raman spectroscopy was conducted to analyze the quality of the CNTs generated by the decomposition of xylene during the CVD process. The Raman spectra (**Figure 49c**) shows two peaks at ~1350 cm^{-1} (D-band disorder-induced phonon mode), ~1590 cm^{-1} (G-band in-plane vibrational mode) and ~2680 cm^{-1} (2D-band) corresponding to the disordered, graphitic carbon and long-range order observed in the CNTs [298-299]. The ratio of I_D/I_G was ~0.90-0.93 indicating that the CNTs are highly graphitic and the 2D/G ratio was ~0.85 indicating the growth of multiwalled CNTs.

6.3.2 Electrodeposition of Si on MWCNT/Ni-Cu Foils (EDSi-MWCNT/Ni-Cu)

The pictorial diagram of the two-electrode electrodeposition cell along with the polarity of the electrical connections (**Appendix A.3 Figure 64**) and the description of the parameters has been provided in Appendix A.3. The study of frequency dependent effects on pulse current electrodeposited Si thin films indicate minor variation in FIR loss and decrease in the fade rate of the thin films during electrochemical lithiation and delithiation.[293]

The Raman analysis of EDSi-MWCNT/Ni-Cu was carried within 15mins after exposure to ambient atmosphere. The Raman spectra showed a broad peak (**Figure 49d, Figure 50a**), approximately between 483 cm^{-1} – 487 cm^{-1} indicating amorphous nature of silicon in the electrode (crystallite size < 1.5nm) which is caused due to the disruption of long-range order as compared to crystalline silicon (520 cm^{-1}). The subsequent heat treatment of EDSi-MWCNT/Ni-Cu at 500°C for 1h shows complete evolution of the peaks at ~380cm^{-1} and ~301cm^{-1} indicating the conversion of Si – O – C structure into amorphous/nanocrystalline Si and SiO_x (x~2). The evolution of broad peak at ~870 – 920 cm^{-1} and increase in its intensity represents the formation of Si – O – Si bonds indicating the formation of SiO_x structure due to the heat treatment process.

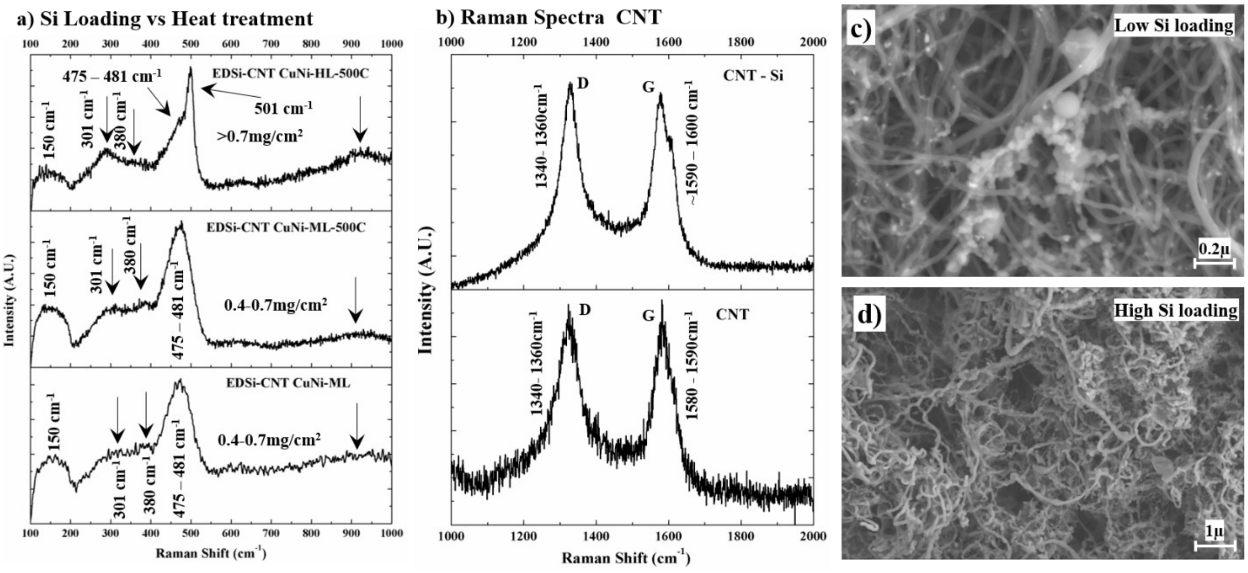

Figure 50 a) Raman Spectroscopic analysis of a) electrodeposited Si on CNT under different loadings and heat treatment conditions, b) VACNT before and after electrodeposition of silicon. SEM analysis of Si/VACNT under c) low and d) high loadings silicon (increased time of deposition)

Heat treatment of Si/CNTs with increased areal loading show evolution of amorphous-nanocrystalline silicon characterized by the peak at ~495 cm^{-1}. The reduced diffusion distances of Si due to agglomerated deposition triggers the partial conversion of highly disordered amorphous silicon into more ordered amorphous/nanocrystalline silicon in the electrodeposited silicon under high loading, however with the crystallite size in the nano crystalline silicon still remaining ~3.5nm – 5nm. Raman spectroscopy study of CNTs after electrodeposition show development of D’ peak which are ascribed to atomic vibrations along the circumference of the CNT due to the deposition of silicon on the CNTs. The development of this D’ band signifies the splitting of the CNT bundles into individual carbon nanotubes during electrodeposition.[300-301]

For the SEM and EDAX analysis, the samples were transferred into the SEM chamber within 5 mins of opening the seal to prevent the oxidation of silicon due to prolonged exposure to the oxygen and moisture in the room atmosphere (**Figure 50c, Figure 50d**). The EDAX analysis of the samples showed the presence of silicon, oxygen, copper, nickel and carbon. Silicon electrodeposited for shorter times (lower Si content) showed the Si nanoparticles on CNT while those deposited for longer times showed coalescence of the silicon growth sites to form continuous thin film on the CNTs. The coalescence of these growth sites to form thin film of Si on CNTs further reinforces the formation of nanocrystalline Si on heat treatment observed during Raman spectroscopy analysis. Additionally, the CNT bundle growth obtained during the CVD process is absent showing individual carbon nanotubes in agreement with the development of D’ band in the Raman analysis.

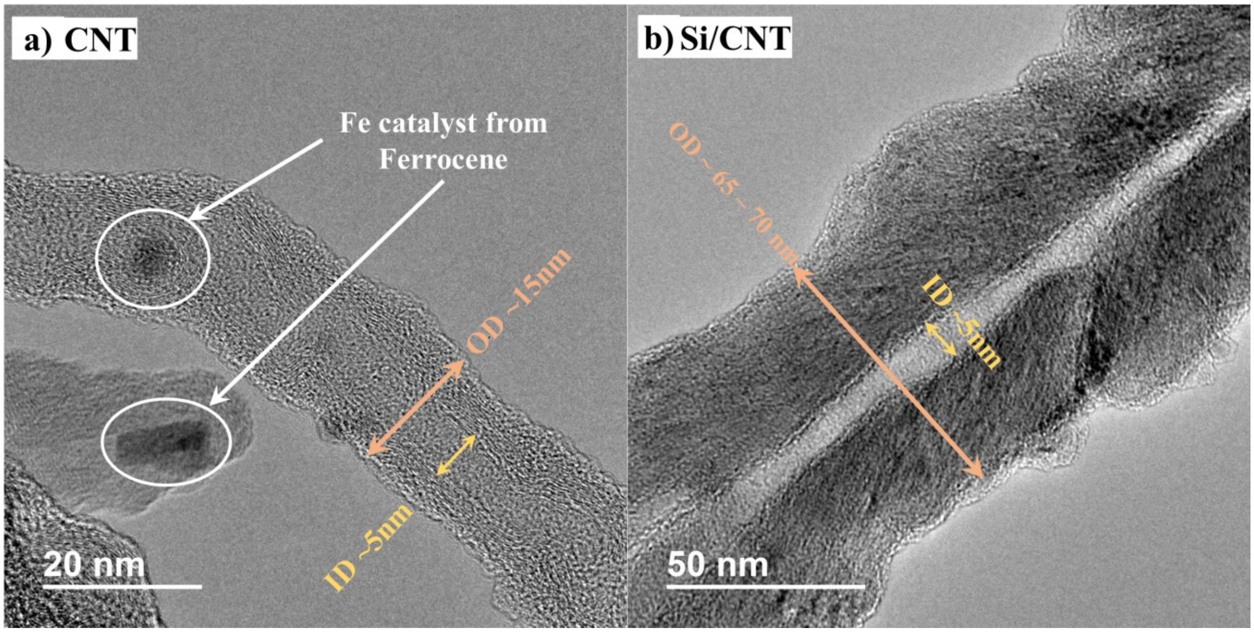

Figure 51 TEM analysis of a) CNT grown by floating catalyst chemical vapor deposition method and b) Si/CNT obtained after electrodepostion of Si on VACNT/Ni-Cu electrodes

The TEM analysis of the CNTs (**Figure 51a**) indicates the growth of CNTs assisted by the Fe nanocatalyst formed by the decomposition of ferrocene. These CNTs have an outer diameter of ~14 – 16nm and an inner diameter of ~5 nm, thus, giving rise to a wall thickness of ~5 nm which corresponds to ~10 – 14 layers of graphene in the CNT walls confirming the multi walled nature of the CNTs observed in the raman spectroscopic analysis (**Figure 49c**). The TEM analysis of Si/CNT indicate an outer diameter of ~65 – 70nm indicating the formation of silicon layer on the

CNTs with a thickness of ~25 – 30nm. Additionally, the lack of clear demarcation of silicon – carbon interface further confirms the development of the D' band which describes the defects in the sidewall of multiwalled carbon nanotubes.

6.3.3 Electrochemical Characterization of EDSi-MWCNT/Ni-Cu

Electrochemical testing of electrodeposition silicon on MWCNT/Ni-Cu showed a reduction in FIR loss to ~35-50% as compared to thin films of electrodeposited Si on copper which show a first cycle irreversible loss of ~ 60-75% due the presence of oxygen and mechanical decrepitation of the films during the initial cycles[293]. The analysis of the differential capacity vs voltage indicates a significant peak close to ∼0.15 V during the first discharge cycle (**Figure 52a**) due to the alloying reaction of lithium with *a*-Si and presence of partially alloyed (Li_xSi) and unalloyed (*a*-Si) two phase region. The presence of a potential peak at ~0.08V suggests various stages of alloying reactions and formation of intermediate Li_xSi at different stages during the discharge cycle. The charge cycle shows reaction peaks at ∼0.33 V and ∼0.46 V corresponding to the extraction of lithium from lithiated amorphous silicon which is commonly observed for the de-alloying reaction from the amorphous alloys of Li_xSi.[293, 302-303] The columbic efficiency varied from 97 to 98% from the 2nd to 5th cycle, after which it further improved and remained > 99.7% for the rest of the cycles. EDSi-MWCNT/Ni-Cu showed a capacity of ~2100-2150 $mA\cdot h\cdot g^{-1}$ during the 2nd – 5th cycles after which the charge discharge capacities stabilized at ~1950-2000 $mA\cdot h\cdot g^{-1}$ at a current rate of ~300 $mA\cdot g^{-1}$.

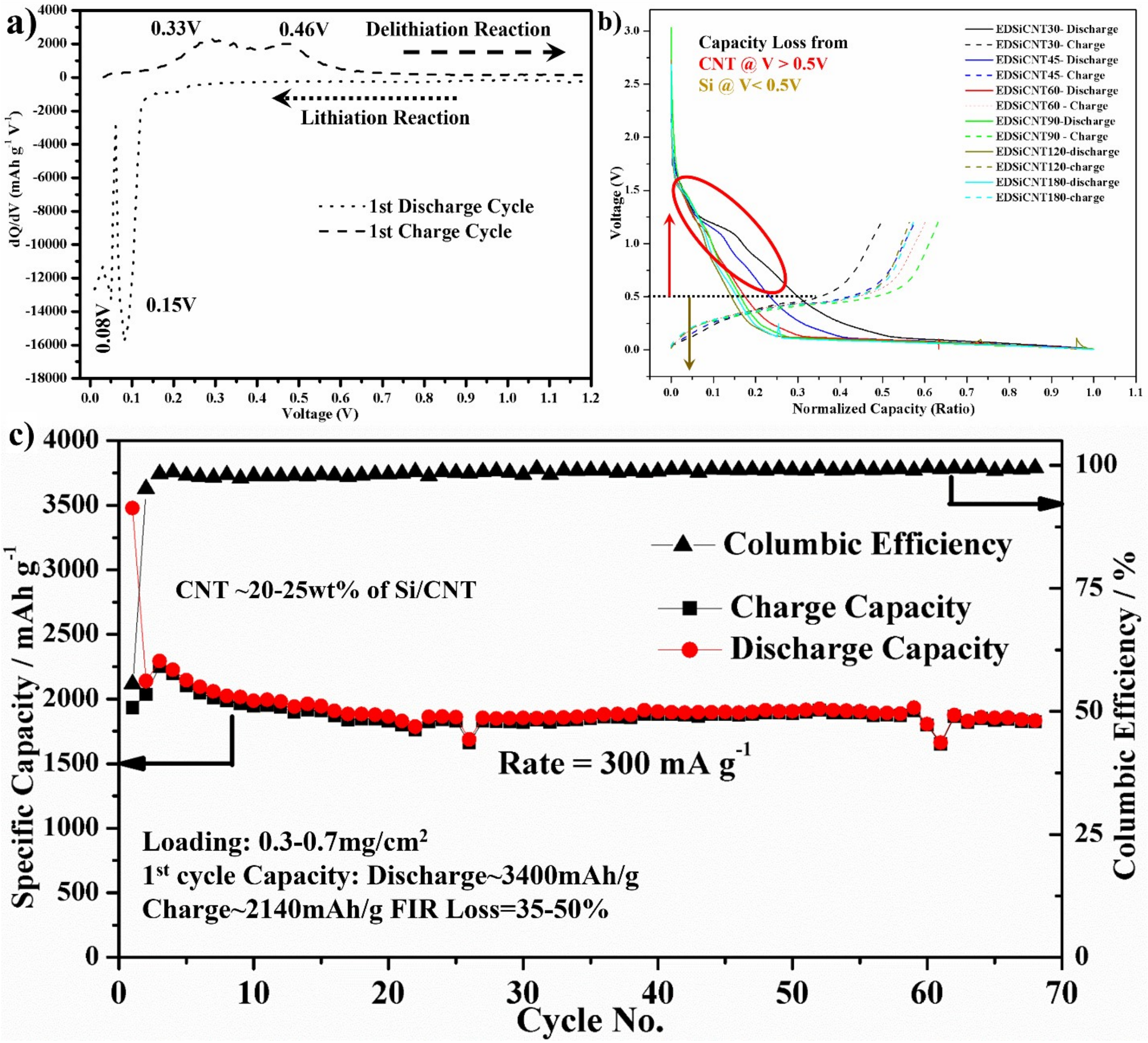

Figure 52 a) Differential capacity vs voltage plot of EDSi-MWCNT/Cu-Ni electrode indicating the electrochemical reaction potentials of lithium with silicon, b) Voltage capacity plots of EDSi-CNT at different deposition times c) Cycling performance of EDSi-MWCNT/Cu-Ni in Li/Li+ system

The voltage vs capacity plots of EDSi/CNT system were studied for different charge of Si electrodeposition ranging from 30 mAh·cm^{-2} - 180 mAh·cm^{-2} (indicated as EDSiCNT30 to EDSiCNT180) at a electrodeposition current density of 0.2 mA · cm^{-2} and a duty cycle of 20% on MWCNT/Cu-Ni electrodes (**Figure 52b**). The contribution to the capacity in the first discharge cycle can be spearated in two regions at 0.5V. The major contribution of capacity in the voltage range of OCV – 0.5V is due to Li interaction with CNT/SEI layer formation and from 0.5V – 0.01V is that with silicon. During the low deposition times the major contribution to FIR loss is from CNTs (~35% for first discharge capacity of EDSiCNT30) which decreases to ~15-20% with the increase in time of deposition (>60 mAh·cm^{-2}, EDSiCNT60). Increase in time of deposition reduces the FIR loss to ~35 – 40% for EDSiCNT90 with the loss arising from CNT matrix/surface area and silicon in approximately equal proportions (~15-20% from each component).

However, as the time of deposition further increases the FIR loss increases to ~40 – 50% with the silicon contribution increasing to ~30 – 35% indicating the formation of Si – O – C composite. The increase in surface area is directly proportional to the radius of the nanostructure and the rate of increase of surface area decreases with the increase in the area. From a geometric perspective,

$$\frac{\Delta A}{A} = \left(\frac{R_O}{R_i} - 1\right) \qquad \frac{\Delta V}{V} = \frac{\Delta M}{M} = \left(\frac{R_O^2}{R_i^2} - 1\right) \qquad \text{..................(6-1)}$$

where A = surface area of a cylinder, V is the volume of cyclinder, M = mass of cylinder, Δ = change in the unit, R_O and R_i are outer and inner radius, respectively. Hence, the change in area follows y = x – 1 while that of volume and mass follows $y = x^2 - 1$ trend with the latter dominating as the value of x increases (at higher deposition times).

Hence, the effect of surface area (V>0.5V) on FIR loss is negligible between EDSiCNT60 to EDSiCNT180. However, the Si electrodeposition was increased and subsequent, heat treat treatment was employed to convert the Si – O – C composite to Si thus, enabling improvement in the areal capacity of the electrode.

6.3.4 Electrochemical Characterization of a-Si-MWCNT/Ni-Cu

Subsequently, *EDSi-MWCNT/Ni-Cu* were heat treated at 500°C for 1hr in argon atmosphere to convert the electrodeposited Si – O – C into *a/nc*-Si and SiO_x to form *a-Si-MWCNT/Ni-Cu* which were tested in coin cells with Li. *a-Si-MWCNT/Ni-Cu* show a reduced FIR loss of ~20 – 35% with an initial charge/discharge capacity of ~2200-2250 $mA \cdot h \cdot g^{-1}$ at a current rate of 50 $mA \cdot g^{-1}$ indicating the effect of breakdown of Si-O-C composite structure in the system. Subsequent rate capability testing under CC – CV mode till 200 $mA \cdot g^{-1}$ and 100% depth of charge/discharge showed capacities of ~1475-1550 $mA \cdot h \cdot g^{-1}$ at the end of 50 cycles with a fade rate of ~0.35% loss per cycle which is an accurate analysis for practical application in full cell lithium ion batteries. A study on the voltage vs capacity plots of *a-Si-MWCNT/Ni-Cu* (**Figure 53c**) system indicates a tendency to bypass the lithiation of silicon and enter into a lithium plating regime under high current densities.

The system shows discharge capacities of ~1975 $mA \cdot h \cdot g^{-1}$, 1675 $mA \cdot h \cdot g^{-1}$, 1550 $mA \cdot h \cdot g^{-1}$, 1025 $mA \cdot h \cdot g^{-1}$ under CV mode at current densities of 200 $mA \cdot g^{-1}$ (~0.25 $mA \cdot cm^{-2}$), 500 $mA \cdot g^{-1}$ (~0.6 $mA \cdot cm^{-2}$), 1000 $mA \cdot g^{-1}$ (~1.2 $mA \cdot cm^{-2}$) and 2000 $mA \cdot g^{-1}$ (~2.4 $mA \cdot cm^{-2}$), respectively. At high current rates of 4000 $mA \cdot g^{-1}$ (~4.8 $mA \cdot cm^{-2}$) the system shows a capacity of ~ 250 $mA \cdot h \cdot g^{-1}$ in the constant current mode and ~1430 $mA \cdot h \cdot g^{-1}$ under the CV-0.01V mode indicating the tendency to bypass the Si lithiation and shift towards plating of lithium. The study of the differential capacity vs voltage plots indicate two broad peaks corresponding to the lithiation of silicon at lower current densities (CC-50 $mA \cdot g^{-1}$, CC-200 $mA \cdot g^{-1}$, CC-500 $mA \cdot g^{-1}$ and CC-1000 $mA \cdot g^{-1}$) however, at higher current densities of (CC-2000 $mA \cdot g^{-1}$) indicate the first lithiation peak drifting towards low potential and incomplete lithiation under CC mode and at CC-4000 $mA \cdot g^{-1}$ the peak is completely absent indicating suppression of lithiation reaction.

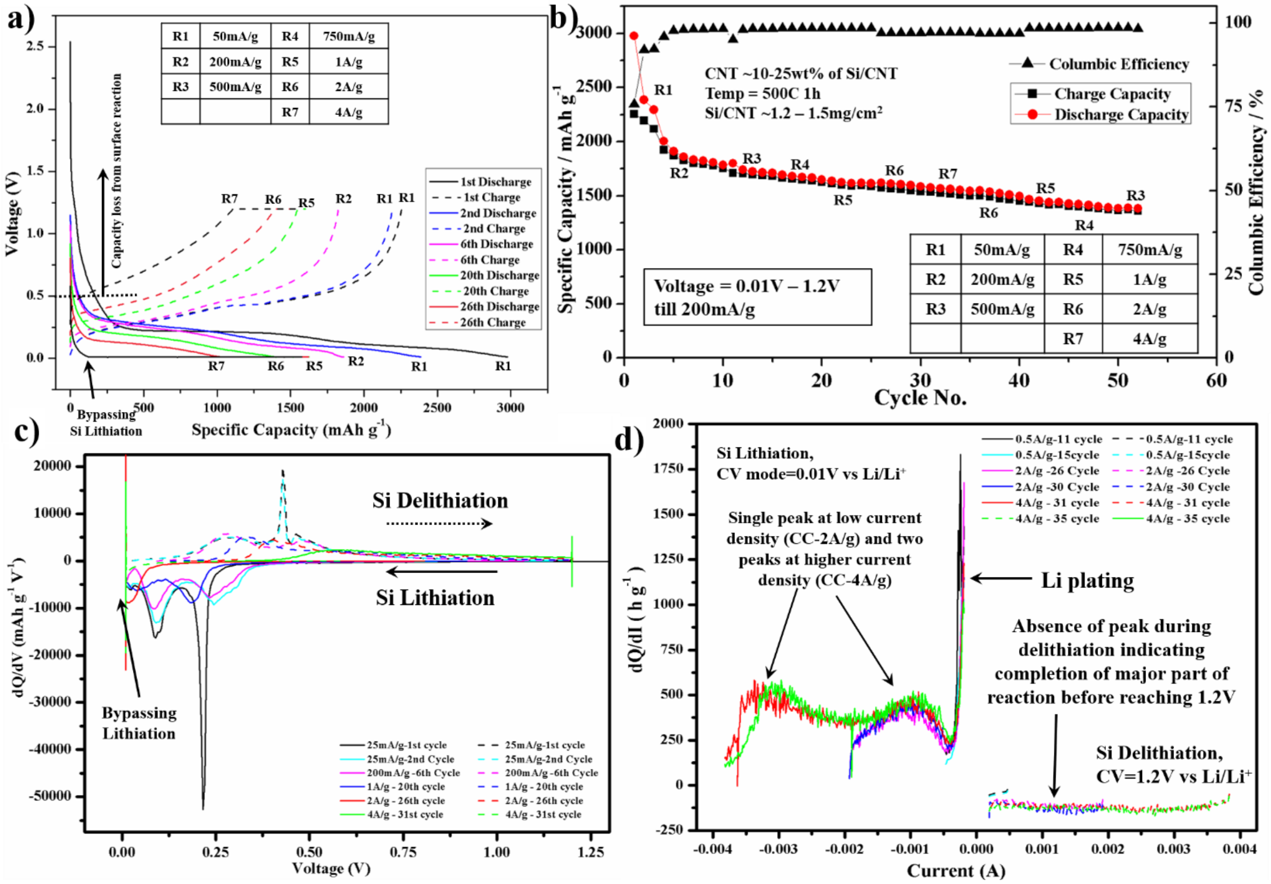

Figure 53 a) Differential capacity vs voltage plot of EDSi-MWCNT/Cu-Ni electrode indicating the electrochemical reaction potentials of lithium with silicon b) Cycling performance of EDSi-MWCNT/Cu-Ni in Li/Li+ system c) Voltage vs capacity plots of a-Si-MWCNT/Cu-Ni indicating at different current rates followed by constant voltage mode. d) Cycling performance of a-Si-MWCNT/Cu-Ni in Li/Li+ system under CC-CV mode at different current densities. e) Differential capacity vs voltage plot of a-Si-MWCNT/Cu-Ni electrode indicating the electrochemical reaction potentials of lithium with silicon at different current densities under CC-CV mode of testing. f) differential capacity vs current indicating the different reactions occurring under CV-0.01V and CV-1.2V mode at different current densities for a-Si-MWCNT/Cu-Ni

During the initial delithiation cycle an additional sharp peak is obtained (~0.402V) along with two broad peaks (0.315V and 0.485V) at a current density of 50 mA·g^{-1} which is due to the active diffusion of lithium along the 111 planes during lithiation at low ionic flux. This phenomenon is well observed in crystalline silicon and the signal disappears primarily due to breakdown of the atomic structure of Si as a part of amorphization process and possibly at higher current rates with increased Li^+ flux suppressing the preferential motion of Li along the 111 planes.

Hence, the differential capacity vs current analysis was done in the CV mode region of the electrochemical plating. The study of the electrochemical signal during the de-lithiation under CV-1.2V mode is devoid of any peaks indicating the completion of major part of lithiation reaction in CC mode at all current densities before entering the CV mode which can also be observed in the voltage vs capacity plots. However, in the discharge cycle under CV-0.01V mode peaks corresponding to the lithiation of silicon can be observed at higher current densities of CC-2000 $mA\cdot g^{-1}$ and CC-4000 $mA\cdot g^{-1}$ indicating the completion of Si lithiation under CV mode. The system when subjected to CC-2000 $mA\cdot g^{-1}$ current density showed single broad peak and when subjected to CC-4000 $mA\cdot g^{-1}$ current density showed two broad peaks corresponding to lithiation of silicon very similar to the differential voltage vs capacity plots at lower current rates. Hence, at higher current rates the system has the tendency to exhibit a combination of Si lithiation and Li plating especially under uncontrolled voltage conditions. Additionally, a sharp peak is observed at the end of CV-0.01V mode possibly due to the system drifting towards Li plating at very low potentials.

Further interpretation of the high current density data analysis concludes that the nucleation potential which is often used to analyze lithium plating (under two electrode conditions) may be a combination of Si lithiation signal which may suppress the signal from actual nucleation potential of Li plating, especially during the initial plating/deplating cycles when Si or other Li-active material based systems are used for characterizing lithium plating resulting in scientific misinterpretation of the data [**Appendix A.3 Figure 69**].

6.3.5 Electrochemical Characterization of a-Si-MWCNT/Ni-Cu and LiNMC111 System

The *a-Si-MWCNT/Ni-Cu* electrodes were tested with LiNMC111 electrodes (in an insulated coincell with matching diameter of both electrodes) with LiNMC111 loading >15 mg·cm^{-2} targeted at an areal charge density >2 mAh·cm^{-2} very close to that of *a-Si-MWCNT/Ni-Cu* (~2.25 mAh·cm^{-2} @ 200 mA·g^{-1}, 1.2 mg·cm^{-2}, 1900 mA·h·g^{-1} capacity) to capture and study the effect of competing phenomenon of silicon lithiation and Li plating (**Figure 54**). The FIR loss of *a-Si-MWCNT/Ni-Cu* was adjusted to 0% by addition of lithium dispersion into the electrodes as per the capacity loss observed in the half cell testing of *a-Si-MWCNT/Ni-Cu* with lithium (~700 mA·h·g^{-1} loss in the first 3 cycles corresponds to ~0.19g of Li per gram of *a-Si-MWCNT*).

The rate capability testing (**Figure 54 a, b)** of the full cell configuration shows a FIR loss of ~15% with respect to LiNMC111 matching that of commercial LiNMC111 (**Appendix A.3 Figure 67**) indicating the reduction in FIR loss of *a-Si-MWCNT/Ni-Cu* to ~0% by the addition of lithium dispersion. On further cycling at different current densities under CC – CV conditions and 100% depth of charge – discharge till 15 mA·g^{-1}, the system shows a fade rate of ~0.743% loss per cycle in the low current rate testing conditions (less than CC-75 mA·g^{-1}). This fade rate is a combination of that of LiNMC111 (~0.12-0.19% loss per cycle) and that of *a-Si-MWCNT/Ni-Cu* (~0.35% loss per cycle) observed in the individual cells along with the possible fade caused by electrolyte degradation under high loading conditions.

However, at higher current densities (>75 mA·g^{-1}-LiNMC, 1000 mA·g^{-1}-anode, 1.2 mA · cm^{-2} areal current density) the fade rate increases in the system which can be observed in between 35th – 40th cycle (150 mA·g^{-1} – LiNMC, 2000 mA·g^{-1} – anode, 2.4 mA · cm^{-2} areal current density). A study of the voltage vs capacity (**Figure 54a)** plots indicate a specific capacity of ~110 mA·h·g^{-1} and 65 mA·h·g^{-1} with respect to LiNMC111 under CC-75 mA·g^{-1} and CC-150 mA·g^{-1}

corresponding to an areal capacity of ~1.76 mAh·cm^{-2} and 1.05 mAh·cm^{-2} and lithiation capacity of ~1470 mA·h·g^{-1} and ~900 mA·h·g^{-1} with respect to *a-Si-MWCNT/Ni-Cu*.

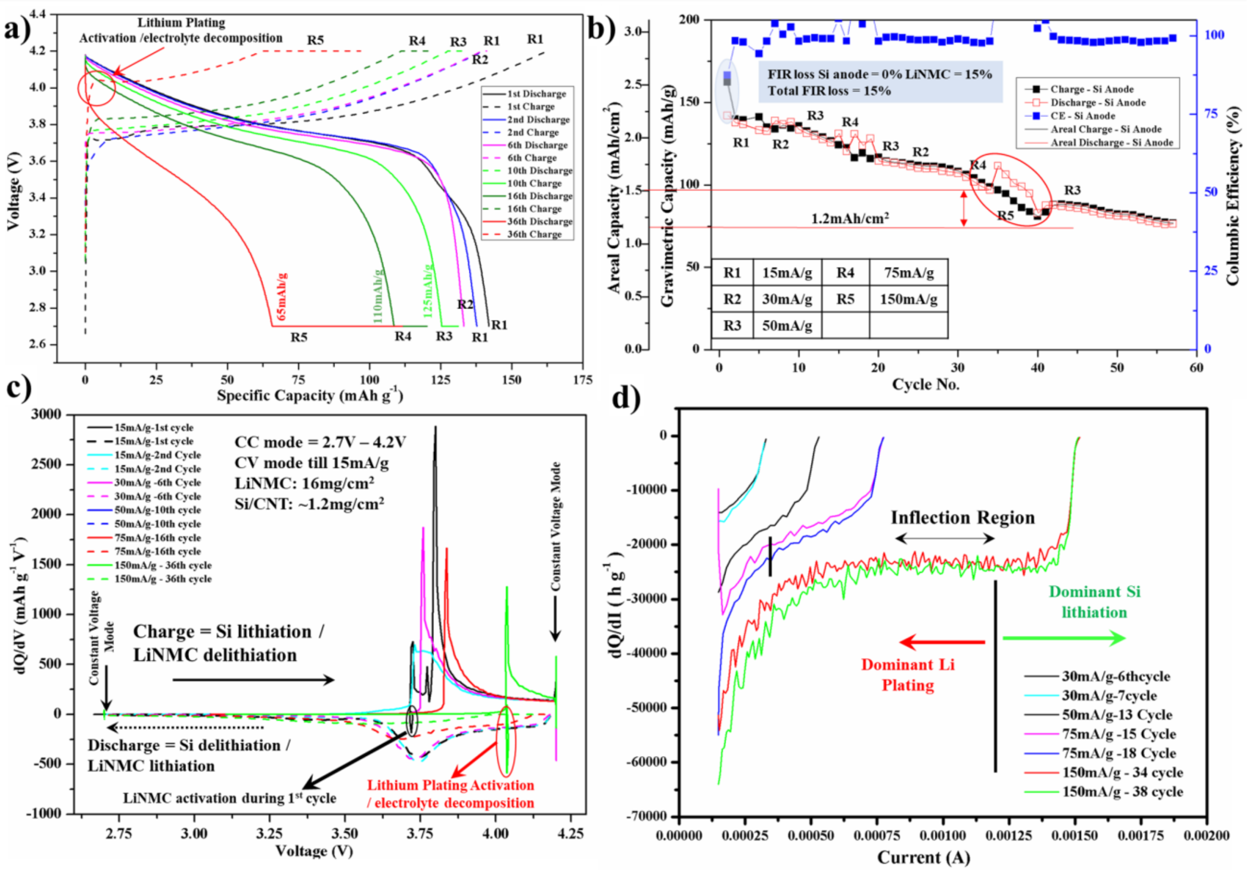

Figure 54 a) Voltage – capacity plots, b) electrochemical cycling performance, c) differential capacity vs voltage and d) differential capacity vs current of a-Si-MWCNT/Ni-Cu with LiNMC111 (critical loading) full cell testing under constant current – current voltage mode testing conditions. Kindly refer to Table 15 for current rates

The specific capacity of *a-Si-MWCNT/Ni-Cu* at this current density (CC-2000 mA·g^{-1}) under constant current mode is ~1000 mA·h·g^{-1} which corresponds to an areal charge capacity of ~1.1 – 1.2 mAh·cm^{-2}. This capacity limitation triggers Li plating due to lack of voltage control in the full cell which reflects in the high fade rate observed in this region due to unstable lithium plating. A study of differential capacity vs voltage plot (**Figure 54c)** under CC mode shows two overlapping peaks of high intensity and broad distribution during the charging cycle which is a combination of delithiation of LiNMC111 and lithiation of *a-Si-MWCNT/Ni-Cu*, respectively. The first charge cycle shows a negative reaction peak which is a characteristic overpotential of de-intercalation observed in LiNMC111 which is absent during the subsequent cycling at current densities of 15 mA·g^{-1}, 30 mA·g^{-1}, 50 mA·g^{-1} and 75 mA·g^{-1} which confirms the lithiation of *a-Si-MWCNT/Ni-Cu* instead of plating at these current densities. However, at higher current density of 150 mA·g^{-1} the negative peak appears during the charging cycle at voltage > 4.05V corresponding to the overpotential associated with Li plating or electrolyte decomposition suggesting initiation of parallel parasitic process. This negative peak is also observed in LiNMC111 – Li coin cells (Appendix A.3 **Figure 67d**) even at low current densities with reaction voltages < 4.05V confirming that this peak represents initiation of Li plating (nucleation region) compared to electrolyte decomposition.

Analysis of differential capacity vs current (**Figure 54d)** under CV-4.2V during the charge cycle indicates a minor peak indicating the completion of reaction when subjected to CC-30 mA·g^{-1} and a tendency to drift towards Li plating as the current density increases. At high current density (CC-150 mA·g^{-1}) a dominant Li plating regime can be observed overlapping the single lithiation peak of *a-Si-MWCNT/Ni-Cu* which is observed in similar analysis in half cell testing of the anode (**Figure 54f**, 2A · g). The fade rate of the system under CC-150 mA·g^{-1} is ~2.654% loss per cycle with the unstable CE at this current rate arising from the Li plating behavior (>100%). [294]

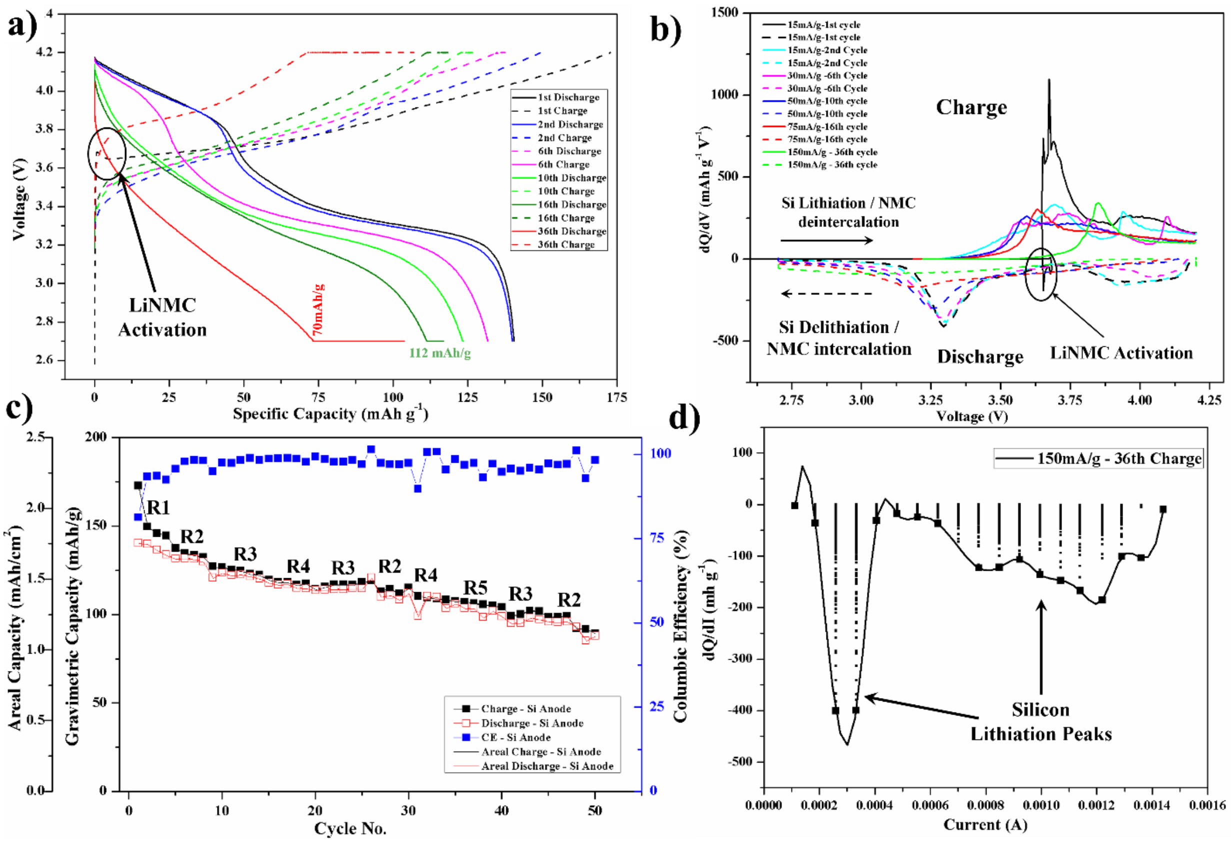

Figure 55 a) Voltage – capacity plots, b) differential capacity vs voltage, c) electrochemical cycling performance and d) differential capacity vs current in CV mode indicating Si lithiation peaks of *a-Si-MWCNT/Ni-Cu* with LiNMC111 (lower loading) full cell under constant current – current voltage mode testing conditions. Kindly refer to Table 15 for current rates

A similar study conducted with lower loading of LiNMC (< 12 mg · cm^2) shows dominant reaction peaks of lithium reacting with silicon in the electrochemical signal of differential capacity vs voltage plots (**Figure 55a**). The charge cycle is associated with the splitting of LiNMC peak into two broad peaks corresponding to that of Si lithiation and similar electrochemical signal is obtained during the discharge cycle. The negative peak in the charge cycle at higher current rates (**Figure 54a - 150mA/g**) is absent in this system indicating lack of Li plating behavior. Additionally, the onset of the reaction occurs at ~3.4V with dominant peaks at ~3.72V and ~3.85V during charge cycle while during the discharge cycle the dominant reactions occur at ~3.9V and

~3.35V. The fade rate of the system is devoid any fluctuations at higher current densities of 75mA/g and 150mA/g indicating stability of the system due lithiation of silicon and absence of lithium plating. The CE of the system at higher current rates under lower LiNMC loadings is much more stable than that with critical LiNMC loadings due to the absence of Li plating. The differential charge vs current under CV – 4.2 @ 150 mA · g^{-1} (**Figure 55d**) for low loading LiNMC111 shows a different signal corresponding to the reaction peaks of lithiation of silicon instead of a convolution of Li plating and Si lithiation as observed in high loading LiNMC (**Figure 54d**). The capacity contribution under CV – 2.7 and CV – 4.2 condition @ 150 mA · g^{-1}, is ~35 - 40 mAh · g^{-1} and this capacity originates from the lithiation of silicon observed from the dQ/dI plots.

The cycled coincell (full cell LiNMC - EDSi-MWCNT/Cu-Ni) was disassembled followed by testing each of the electrodes in half cell configurations to estimate the amount of electrochemical degradation suffered by the cathode and anode systems. The LiNMC cathode showed a specific capacity of ~80 – 95 mAh/g at a current density of 15 mA/g while EDSi-MWCNT/Cu-Ni electrode showed a specific capacity of ~1000 - 1200mAh/g at the end of 50 cycles indicating that both the systems have undergone equivalent electrochemical degradation similar to half-cell testing probably due to instability of electrolyte component, direct decomposition of electrolyte at higher current rates and accelerated degradation at voltages beyond 4V.

6.3.6 Electrochemical Impedance Spectroscopy (EIS) of a-Si-MWCNT/Ni-Cu

EIS analysis was conducted to analyze the evolution of different phenomenon occurring in the half cell / full cell configuration and study their respective contribution to the degradation of the system at different cycles (**Figure 56**). The high frequency intercept (R_S), relates to the ohmic portion of the electrode impedance and includes contributions from the electronic conductivity of the electrodes and ionic conductivity of the electrolyte solution, as well as any electronic contact resistances associated with the cell hardware, current collectors, and electrode materials. The interfacial impedance due to solid – electrolyte interphase (R_{SEI}) formation and the interphase electronic contacts between the current collector is represented by high frequency depressed semicircles (100 kHz – 20 kHz). The depressed semicircle in the low to medium frequency region represents the charge-transfer resistance (R_{CT}) while the low-frequency (> 200 mHz) Warburg impedance tail (W_0) describes diffusion-related phenomena in the device.[304]

Table 10 Values of the circuit elements obtained after modeling the equivalent circuit using a complex non-linear least square (CNLS) method for EIS spectra of a-Si-MWCNT/Ni-Cu with Li & LiNMC111

<table>
<tr><th colspan="5"><i>a-Si-MWCNT/Ni-Cu</i> in half-cell configuration with Li</th></tr>
<tr><th>Cycle</th><th>R_s / Ω cm^{-2}</th><th>R_{SEI} / Ω cm^{-2}</th><th>R_{Film} / Ω cm^{-2}</th><th>R_{CT} / Ω cm^{-2}</th></tr>
<tr><td>3rd</td><td>1.051378</td><td>16.23062</td><td>-NA-</td><td>11.258621</td></tr>
<tr><td>50th</td><td>1.059335</td><td>22.63502</td><td>-NA-</td><td>56.627329</td></tr>
<tr><td>100th</td><td>1.291383</td><td>41.95324</td><td>-NA-</td><td>284.50538</td></tr>
<tr><th colspan="5"><i>a-Si-MWCNT/Ni-Cu</i> full cell configuration with critical LiNMC111 loading</th></tr>
<tr><th>Cycle</th><th>R_s / Ω cm^{-2}</th><th>R_{SEI} / Ω cm^{-2}</th><th>R_{Film} / Ω cm^{-2}</th><th>R_{CT} / Ω cm^{-2}</th></tr>
<tr><td>3rd</td><td>7.562893</td><td>10.7783</td><td>5.007862</td><td>8.477987</td></tr>
<tr><td>10th</td><td>10.5456</td><td>13.97642</td><td>6.426101</td><td>15.41352</td></tr>
<tr><td>20th</td><td>10.55346</td><td>16.90252</td><td>8.710692</td><td>16.28774</td></tr>
<tr><td>60th</td><td>10.55975</td><td>31.72956</td><td>32.51572</td><td>21.24214</td></tr>
<tr><th colspan="5"><i>a-Si-MWCNT/Ni-Cu</i> full cell configuration with lower LiNMC111 loading</th></tr>
<tr><th>Cycle</th><th>R_s / Ω cm^{-2}</th><th>R_{SEI} / Ω cm^{-2}</th><th>R_{Film} / Ω cm^{-2}</th><th>R_{CT} / Ω cm^{-2}</th></tr>
<tr><td>3rd</td><td>7.703</td><td>8.938142</td><td>0.607017</td><td>0.002651</td></tr>
<tr><td>10th</td><td>11.42</td><td>11.03899</td><td>0.757259</td><td>5.847353</td></tr>
<tr><td>50th</td><td>15.01</td><td>25.99</td><td>1.879938</td><td>12.75468</td></tr>
</table>

a-Si-MWCNT/Ni-Cu in half cell system indicate the evolution of SEI (R_{SEI}) and charge transfer resistance (R_{CT}) with the increase in number of cycles with accelerated degradation of the system upon repeated cycling (**Figure 56a**). There is a minor increase in the impedance due to SEI layer (16.2 $\Omega \cdot cm^{-2}$ to 41.9 $\Omega \cdot cm^{-2}$) between 3rd cycle to 100th cycle indicating minimal degradation of the Si electrode. However, the charge transfer resistance merges with the Warburg phenomenon indicating drastic increase in the diffusion related impedance most probably due to dynamic detrimental nature of Li plating and deplating (on the reference electrode) at high current densities and charge densities impeding the diffusion kinetics on the Li electrode in half cell. This is marked by drastic increase in the charge transfer resistance from 11.25 $\Omega \cdot cm^{-2}$ to 284.5 $\Omega \cdot cm^{-2}$ between the 3rd and 100th cycle. Li plating is often associated with the formation of high surface area lithium, globular deposition and dendritic growth which create resistance to the motion of Li^+ in the electrolyte by changing the Li electrode structure.

a-Si-MWCNT/Ni-Cu with critical LiNMC111 loading (**Figure 56b**) shows formation of depressed semicircles in the high frequency region and evolution of a new semicircle convoluted with the SEI layer formation. This depressed semicircle inbetween the SEI layer and charge transfer region is described by the film resistance (R_{Film}) indicating the formation of Li+ impermeable layer due to critical LiNMC111 loadings used greater than the areal capacity of *a-Si-MWCNT/Ni-Cu*. The R_{SEI} shows a gradual increasing trend along with R_{CT} however, the film resistance (R_{Film}) increases drastically between 20th cycle to 50th cycle from 8.71 $\Omega \cdot cm^{-2}$ to 32.51 $\Omega \cdot cm^{-2}$ indicating the damage done by the irreversible nature of unstable Li plating on *a-Si-MWCNT/Ni-Cu* electrode. The increase in film resistance is minimal between 3rd to 20th cycle from 5.00 $\Omega \cdot cm^{-2}$ to 8.71 $\Omega \cdot cm^{-2}$ indicating that the there is no or minimal Li plating on *a-Si-MWCNT/Ni-Cu* at lower gravimetric and areal current densities.

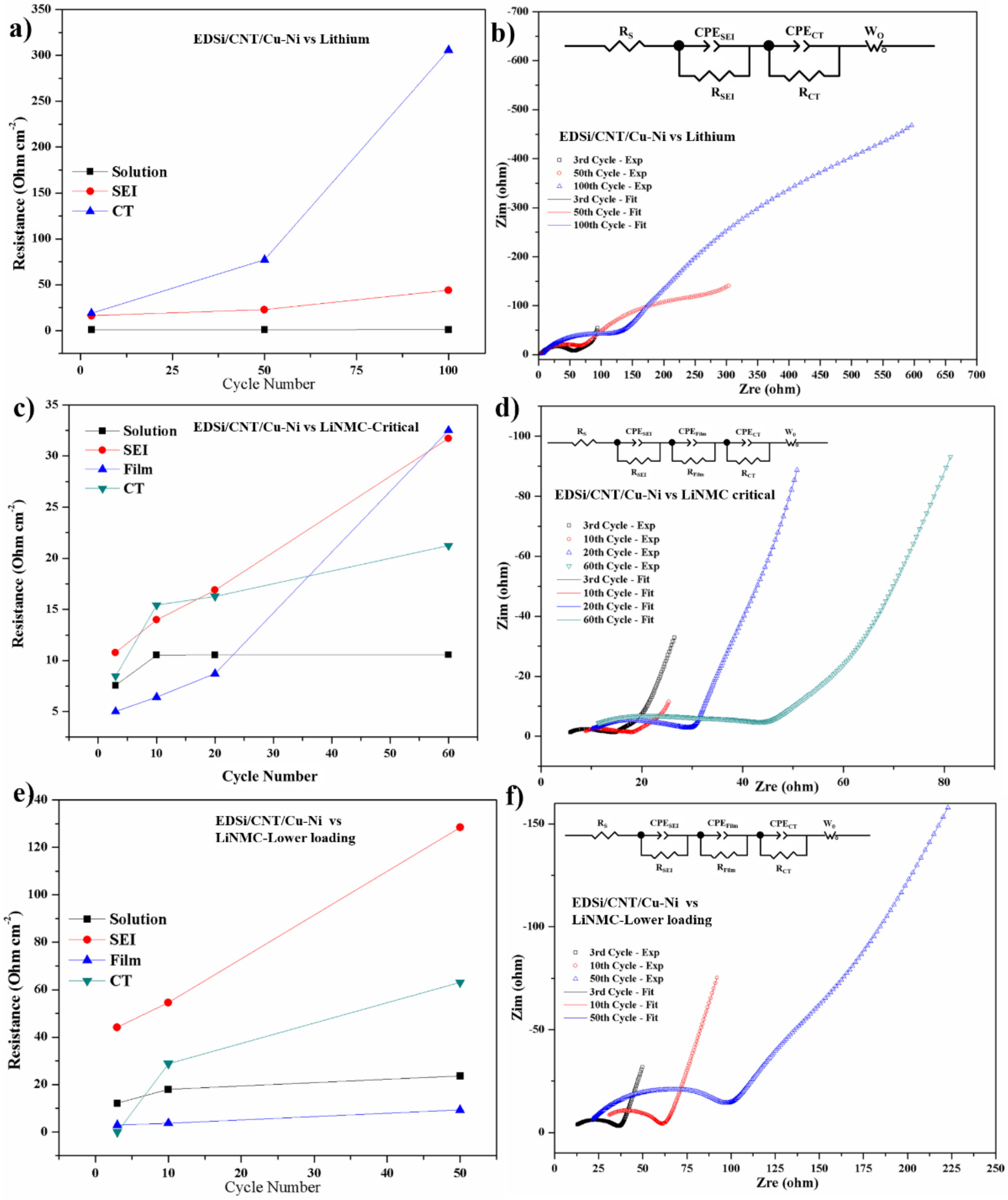

Figure 56 a), c), e) Resistance vs cycle number and b), d), f) Nyquist plots of a-Si-MWCNT/Ni-Cu in half-cell configuration with Li, full cell configuration with critical LiNMC111 loading and low loading LiNMC, respectively. (Inset: Circuit diagram used for fitting the EIS spectra). Kindly refer to Table 12, Table 13 and Table 14 for fitting parameters

On the other hand, *a-Si-MWCNT/Ni-Cu* with lower loading of LiNMC111 record higher values of Rs, R_{SEI} and R_{CT} as compared to that with critical LiNMC111 loading. However, the there is no major contribution to the overall impedance from film resistance nor there is a dramatic change in R_{Film} between 10th and 50th cycle indicating absence of Li plating behavior. Hence, the electrochemical performance is much more stable even at higher current densities when compared to the systems tested with higher / critical LiNMC111 loadings.

6.3.7 Concept and Evolution of Electrode Design

Electrodeposited silicon is often associated with high first cycle irreversible loss due to the formation of Si – O – C films instead of pure silicon and presence of chlorine in the films. This occurs due to the reductive decomposition of the propylene carbonate or TBA+, local over potential on the surface of the electrolyte leading to localized decomposition, presence of minute traces of water in electrolyte, poor ionic conductivity of the electrolyte and poor electronic conductivity of electrodeposited Si film.[279, 305-308]

$$4.4\,Li + Si \longrightarrow Li_{4.4}Si \longrightarrow 4.4\,Li + Si \quad \dots\dots\dots\dots\dots (3)$$

$$4\,Li + O_2 \longrightarrow 2Li_2O \;\dots\dots\dots\dots\dots (4)$$

The content of silicon and the ratio of silicon to oxygen content increases with the increase in depth of the thin film indicating preferential decomposition of the propylene carbonate with the increase in the thickness of the electrodeposited film. The electronic conductivity of Si is lower than that of Cu and hence, after the formation of a layer of silicon the electronic conductivity of the substrate decreases which restricts the electron transfer from growth front to the underlying substrate. The efficiency of Si plating is influenced by the electron transfer from the active plating/electrolyte interface to the substrate and the decrease in the electronic conductivity of the substrate facilitates the decomposition of electrolyte. Hence, the thin films during Si electrodeposition show regions of ~60-80nm (near to the substrate) with higher silicon content followed by drastic increase in the content of carbon and oxygen which reflects in high irreversible loss of electrodeposited Si thin films.[265] Vertically aligned CNTs on Cu-Ni substrates form an ideal support structure for developing nanostructures with high silicon content and lower carbon – oxygen content by depositing Si layers of ~50-70nm on the CNTs. This is expected to decrease the FIR loss as compared to Si thin films which are affected by higher oxygen content and the mechanical disintegration during the initial cycles.

However, the EDSi – MWCNT structures have higher surface area which contribute to the FIR loss (~250 – 400 $mA\cdot h\cdot g^{-1}$ or ~15-20% FIR loss) between voltage range of OCV – 0.5V during the first discharge cycle. Additionally, the FIR loss contribution from 0.5V – 0.01V is (~450 – 500 $mA\cdot h\cdot g^{-1}$ or another 20 - 30% FIR loss) is contributed by the electrochemically active silicon in the electrode due to the presence of oxygen in electrodeposited Si – O – C along with Si film on CNTs. The impetus of the electrode design is to achieve higher areal capacities and hence, by increasing the Si content in the system the contribution of surface area to the FIR loss is reduced to ~150-200 $mA\cdot h\cdot g^{-1}$ (~15-20% FIR loss between OCV – 0.5V) in conjunction with increasing the gravimetric/areal capacities. Subsequently, EDSi-MWCNT/Ni-Cu were heat treated at 500°C for 1h to facilitate the complete conversion of Si – O – C into active Si and inactive SiO_x (x~2) thus, rendering the oxygen inactive for the electrochemical process and reducing the FIR loss contribution from electrochemically active Si to ~300-350 $mA\cdot h\cdot g^{-1}$ (~10-20% FIR loss). The temperature of heat treatment is fixed to ~500 °C – 550 °C to prevent rearrangement and complete crystallization of *a*-Si triggered by thermo activated diffusion of Si atoms. Hence, *a*-Si-MWCNT/Ni-Cu show and FIR loss of ~20-30% (~600-700 $mA\cdot h\cdot g^{-1}$) and a stable capacity of ~2200-2300 $mA\cdot h\cdot g^{-1}$ @50 $mA\cdot g^{-1}$. During the full cell testing of *a*-Si-MWCNT/Ni-Cu with LiNMC111, dispersed lithium was added to the Si anode to match the first cycle capacity loss of ~700 $mA\cdot h\cdot g^{-1}$ (~ Li/ *a*-Si-MWCNT = 0.2 weight ratio). The full cell system shows good electrochemical performance at lower current rates (50mA·g-LiNMC, <2mA·h·cm^2) however, noticeable higher capacity fade rates are observed at higher current rates. The study of charge – discharge curves and the reaction plots indicate that at higher current rates the contribution of lithiation of silicon decreases and the system develops a tendency for Li plating and electrolyte decomposition. Hence, the stability of the system decreases due to the low columbic efficiency associated with Li plating and hence, the fade rate increases at higher areal and gravimetric current rates. This effect is unrecognized during the half cell testing of anodes due to voltage window being restricted to 0.01V to 1.2V hence preventing the lithium plating.

Carbon has low solubility in copper which restricts the interface adhesion of CNTs when directly grown on copper substrate. Additionally, copper and iron are devoid of any solid solution or intermetallic phases which restricts / prevents the growth of CNTs on copper using FCCVD method and hence, the need to activate the copper surface for the growth of vertically aligned CNTs. Nickel accommodates higher carbon in the form of solid solution as compared to Cu along with the formation of austenitic Fe – Ni phase at T > 400°C which makes it an ideal element for the activation of copper surface for VACNT growth. Additionally, Ni has the ability to form solid solution with Cu which reduces the lattice mismatch during the heating and cooling from the high temperatures involved during the growth of CNTs. Hence, Ni diffuses into Cu due to solid state diffusion at high temperatures involved in the growth of CNTs increasing the strength of the Cu substrate along with preventing warping due to thermal stresses in thin Cu foils. Additionally, the improvement in carbon solubility in the Ni enhances the adhesion of CNTs on the substrate as observed in **Figure 49g** which retain the adhesion even under folding / bending.[309-317]

6.4 Conclusions

1.Activation of Cu surface for the growth of vertically aligned CNTs has been achieved by the deposition of a thin film of nickel using electroless plating. Subsequently, silicon was electrodeposited on these VACNT/Cu-Ni nanostructures to obtain EDSi-VACNT/Cu-Ni electrodes which were electrochemically characterized for lithium ion batteries especially for FIR loss.

2.High surface area resulting from carbon (CNTs) and the formation of Si – O – C composite structure are major contributions for the FIR loss and by increasing the amount of electrodeposited silicon the contribution of FIR loss from the high surface area region or carbon (OCV – 0.5V) reduces and that from the lithiation of silicon increases indicating the increase in amount of Si – O – C in the electrodeposited silicon. The FIR loss in EDSi/MWCNT-Cu-Ni decreases to 35-50% as compared to silicon thin films directly electrodeposited on Cu foils which show an FIR loss of 60 – 70% with the FIR loss arising from a combination of high surface area of the nanostructures and oxygen content in the electrodeposited silicon.

3.Heat treatment of EDSi/MWCNT-Cu-Ni electrodes at 500°C showed reduction in FIR loss to 20%-35% due to the decomposition of Si – O – C composite structure into *a/nc*-Si and SiO_x (x~2).

4.Rate capability electrochemical testing analysis and study of these electrodes in half cell configuration using constant current – constant voltage mode indicated the tendency for Li plating and bypassing the lithiation of silicon at higher current densities of CC-2000 $mA\cdot g^{-1}$ and CC-4000 $mA\cdot g^{-1}$ even at positive potentials close to 0V.

5.The FIR loss was adjusted by addition of lithium dispersion and subsequently, full cell electrochemical testing analysis was carried out with high loading LiNMC111 electrodes to analyze and study the effect of various current densities. The system tends to develop a tendency towards Li plating and at higher current rates even under constant voltage conditions during the charging cycle leading to an increase in the fade rate. Differential capacity vs current plots have been used to analyze the constant voltage region and study the electrochemical response pattern to identify the Li plating behavior in the system at critical LiNMC111 loadings.

6.Analysis of full cell testing of LiNMC111 under critical loadings with *a*-Si-MWCNT/Ni-Cu indicate the evolution of Li plating phenomenon along with silicon lithiation at high gravimetric / areal current densities. The differential capacity vs current plots in the constant voltage region indicate peaks corresponding to both silicon lithiation and Li plating.

7.On the other hand, analysis of full cell testing of LiNMC111 under lower loadings with *a*-Si-MWCNT/Ni-Cu indicate only silicon lithiation behavior and the electrochemical signal devoid of any Li plating even at high current densities with stable cycling behavior when compared to critical loading LiNMC.

8.New electrochemical analysis technique (differential capacity vs current) in constant voltage mode condition has been developed and the electrochemical signal was analyzed to identify the Li plating and silicon lithiation phenomenon.

9.The presence of film resistance in between the high frequency (SEI layer) and medium frequency (charge transfer) for critical loading LiNMC11 in the EIS analysis confirms the Li plating phenomenon leading to the failure of *a*-Si-MWCNT/Ni-Cu vs critical loading LiNMC111.

7.0 Overall Conclusions and Summary

Hollow amorphous silicon nanotube structures (h-SiNTs) of different wall thicknesses (~40 nm-~75 nm) has been synthesized by using a low pressure chemical vapor deposition (LPCVD) of silicon on sacrificial MgO nanowire template generated by a simple approach followed by acid etching of the MgO template to obtain the hollow Si nanotubes, h-SiNTs. The wall thickness of h-SiNTs has been varied by controlling the deposition time (~10min, ~15min and ~20min) of LPCVD of Si on MgO nanowires template. The wall thickness of the h-SiNTs increases with concomitant consolidation occurring with the increase in time of deposition (~45 nm, ~60 nm, and 75 nm at ~10 min, ~15 min and ~20 min, respectively) which causes the reduction in specific surface area and improvement in the areal loading density of the h-SiNTs.

The first cycle irreversible loss (FIR) loss was reduced from ~25% (10min deposition time) to ~15% (20min deposition time). However, the long term cyclability of h-SiNT-15 (fade rate ~0.31% loss cycle^{-1}) and h-SiNT-20 (~0.42% loss cycle^{-1}) is inferior compared to that of h-SiNT-10 due to the larger wall thickness of the nanotubes. Morphology assessment after long term cycling shows that an optimum wall thickness (~60nm) is needed to exhibit no morphological damage to the nanotubes during the lithiation and de-lithiation processes. Improvements in cycling stability of the optimized h-SiNTs were achieved by coating the optimized h-SiNTs obtained from 15 min of Si deposition (h-SiNTs-15) with carbon by pyrolysis of propylene gas.

The core-shell C@Si@C hollow nanotube (h-SiNT-15/C) exhibits a first discharge capacity of ~1780 mAh·g^{-1} and a charge capacity of ~1565 mAh·g^{-1} at a current density of 300 mA·g^{-1}, with ~13.2% first cycle irreversible loss and a very low fade rate of ~ 0.072% loss cycle^{-1} matching the fade rate of the pristine h-SiNTs reported earlier albeit better FIR and areal loading density. The excellent cyclability of these core-shell h-SiNTs (h-SiNT-15/C) electrodes was further validated by SEM analysis of the post-cycled electrodes which showed the retention of these hollow tubular morphology after repeated cycling. The decrease in surface area after carbon coating leads to the reduction in FIR loss and the carbon layer also improves the cycling stability of the hollow tubular structures, thus, leading to better performance of core-shell C@Si@C hollow nanotubes (h-SiNT-15/C) when compared to the uncoated h-SiNTs.

Silicon nanostructures with different morphology and different crystalline structure (crystalline, nanocrystalline and amorphous) were generated using a facile, high throughput and scalable process involving abundant, cheap, green, completely recyclable water soluble sodium chloride template approach. Silicon was deposited using low-pressure chemical vapor deposition (LPCVD) of silane on different NaCl particle sized templates, derived using high energy mechanical milling (HEMM) to develop Si nanoflakes (Si_{NF}) and nanorods (Si_{NR}). These Si nanostructures serve as high performance anode materials in lithium ion batteries. Both Si nanoflakes and nanorods show high specific charge discharge capacities. However, owing to the structural dimensions, higher content of *a*-Si and presence of *nc*-Si instead of crystalline silicon (*c*-Si) of higher crystallinity, nanoflakes show superior performance as compared to nanorods. Silicon nanorods on the other hand, showed a first cycle discharge and charge capacities of ~ 2980 $mAh\cdot g^{-1}$ and ~2500 $mAh\cdot g^{-1}$, respectively at a current rate of 50 $mA\cdot g^{-1}$ with a first cycle irreversible loss (FIR loss) of ~ 12-15%. Upon longer cycling at a current rate of 1 $A\cdot g^{-1}$ Si nanorods displayed a discharge capacity of ~740 $mAh\cdot g^{-1}$ at the end of 250 cycles with a columbic efficiency of 99.95-99.97% and a fade rate of ~ 0.23% loss per cycle. Silicon nanoflakes on the other hand, showed a first cycle discharge and charge capacities of ~ 2830 $mAh\cdot g^{-1}$ and 2175 $mAh\cdot g^{-1}$, respectively at a current rate of 50 $mA\cdot g^{-1}$ with a first cycle irreversible loss (FIR loss) of ~ 15-20%. Upon longer cycling at a current rate of 1 A·g^{-1}, the Si nanoflakes showed a stable discharge capacity of ~810 mAh·g^{-1} at the end of 250 cycles with a columbic efficiency of 99.95-99.97% and a fade rate of ~ 0.11% loss per cycle demonstrating the superior electrochemical response.

Morphology of amorphous silicon was modified by using frequency-dependent pulse current electrodeposition technique. Under galvanostatic conditions, films show mud crack morphology; while at higher frequencies (>1000 Hz) growth of thin continuous film due to the coalescence of electrodeposited particles is observed. Films electrodeposited at 500 Hz show islands of micron size particles forming discontinuous or continuous films under pulse current conditions with decreasing particle size due to increase in frequency. Difference in the morphology is likely due to change in the nucleation and growth mechanisms of thin films formed at the different frequencies studied. The films show an improvement in performance when tested in LIBs with the increase in frequency due to enhanced stability under pulsed current electrodeposition conditions. Consequently, the fade rate (% loss per cycle) reduced from ~3.15% under DC electrodeposition to ~1.6% for pulsed current frequencies greater than 1000 Hz. The films also showed a major change in morphology during the first 10 cycles of electrochemical testing which supports the high fade rate during initial electrochemical cycling. There was minor reduction in first cycle irreversible (FIR) loss with frequency and the pulse electrodeposited films showed a capacity of ~1000–1250 mAh·g^{-1} with a columbic efficiency of ~99.7% at the end of ~47 cycles. Upon long term cycling at a current rate of 0.3 A·g^{-1}, the thin films deposited at a 5000 Hz frequency showed a capacity of ~805 mAh·g^{-1} at the end of 500 cycles with a fade rate of ~0.056% capacity loss per cycle demonstrating very good stability and effects of frequency. The loss of lithium due to the presence of oxygen and the change in mechanical integrity due to volumetric expansion during the initial discharge–charge cycle is the major reason for the high FIR loss. Hence, to stabilize the initial mechanical disintegration the development was focused on CNTs to act as a support structure. However, to enable the electrodeposition of silicon on CNTs requires electrical continuity of the CNTs and hence, VACNT directly adhered to conducting substrate form an attractive substrate for Si electrodeposition.

Activation of Cu surface for the growth of vertically aligned CNTs has been achieved by the deposition of a thin film of nickel using electroless plating. Subsequently, silicon was electrodeposited on these VACNT/Cu-Ni nanostructures to obtain EDSi-VACNT/Cu-Ni electrodes which were electrochemically characterized for lithium ion batteries especially for FIR loss. High surface area and the formation of Si – O – C composite structure are major contributions for the FIR loss and by increasing the amount of electrodeposited silicon the contribution of FIR loss from the high surface area region (OCV – 0.5V) reduces and that from the lithiation of silicon increases indicating the increase in amount of Si – O – C in the electrodeposited silicon. The FIR loss in EDSi/MWCNT-Cu-Ni decreases to 35-50% as compared to silicon thin films directly electrodeposited on Cu foils which show an FIR loss of 60-70% with the FIR loss arising from a combination of high surface area of the nanostructures and oxygen content in the electrodeposited silicon. Heat treatment of EDSi/MWCNT-Cu-Ni electrodes at 500°C showed reduction in FIR loss to 20%-35% due to the decomposition of Si – O – C composite structure into a/nc-Si and SiO_x (x~2). Rate capability electrochemical testing analysis and study of these electrodes in half cell configuration using constant current – constant voltage mode indicated the tendency for Li plating and bypassing the lithiation of silicon at higher current densities of CC-2000 $mA\cdot g^{-1}$ and CC-4000 $mA\cdot g^{-1}$ even at positive potentials close to 0V. The FIR loss was adjusted by addition of lithium dispersion and subsequently full cell electrochemical testing analysis was carried out with high loading LiNMC111 electrodes to analyze and study the effect of various current densities. The system tends to develop a tendency towards Li plating and at higher current rates even under constant voltage conditions during the charging cycle leading to an increase in the fade rate. Differential capacity vs current plots have been used to analyze the constant voltage region and study the electrochemical response pattern to identify the Li plating behavior in the system at critical LiNMC111 loadings. Analysis of full cell testing of LiNMC111 under critical loadings with *a*-Si-MWCNT/Ni-Cu indicate the evolution of Li plating phenomenon along with silicon lithiation at high gravimetric / areal current densities. The differential capacity vs current plots in the constant voltage region indicate peaks corresponding to both silicon lithiation and Li plating. On the other hand, analysis of full cell testing of LiNMC111 under lower loadings with *a*-Si-MWCNT/Ni-Cu indicate only silicon lithiation behavior and the electrochemical signal devoid of any Li plating even at high current densities with stable cycling behavior when compared to critical loading LiNMC. New electrochemical analysis technique (differential capacity vs current) in constant voltage mode condition has been developed and the electrochemical signal was analyzed to identify the Li plating and silicon lithiation phenomenon. The presence of film resistance in between the high frequency (SEI layer) and medium frequency (charge transfer) for critical loading LiNMC11 in the EIS analysis confirms the Li plating phenomenon leading to the failure of *a*-Si-MWCNT/Ni-Cu vs critical loading LiNMC111.

Appendix A Supplementary Information

Appendix A.1 Supplementary Information: Silicon−Carbon Core−Shell Hollow Nanotubular Configuration

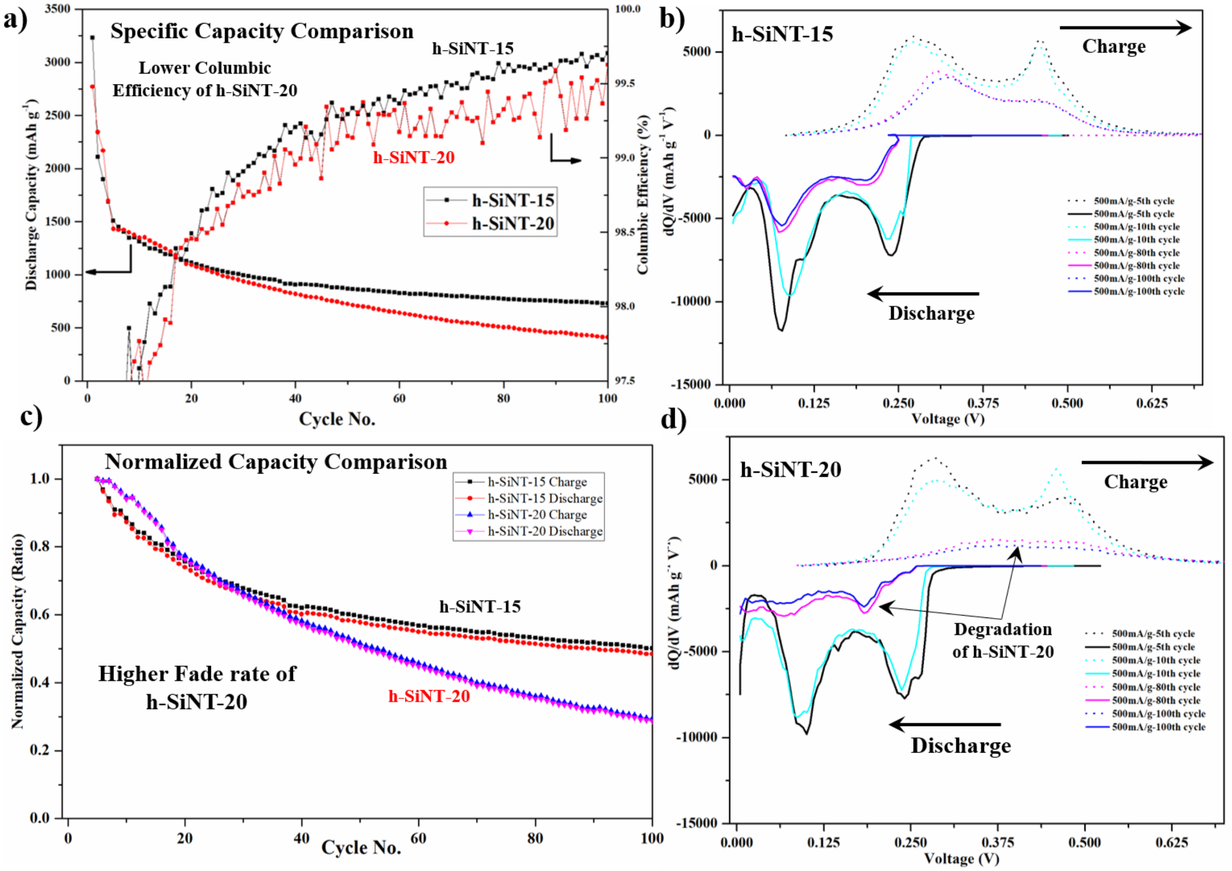

Figure 57 Comparison of a) specific discharge capacity and coulombic efficiency, c) normalized capacity of h-SiNT-15 and h-SiNT-20, differential capacity vs voltage plots of b) h-SiNT-15 and d) h-SiNT-20

A comparison of h-SiNT-15 and h-SiNT-20 has been provided in this section when tested in a half cell coin cell configuration with respect to Li metal. During long term cycling h-SiNT-20 are marked by higher degradation rates and lower coulombic efficiency (**Figure 57 a, b**) when compared to h-SiNT-15. The differential capacity plots (**Figure 57 b, d)** indicate major suppression in the intensity of reaction peaks during both lithiation and de-lithiation from 10th cycle to 80th cycle for h-SINT-20 as compared to h-SiNT-15 confirming the higher degradation the nanotubes due larger wall thickness and bending and twisting.

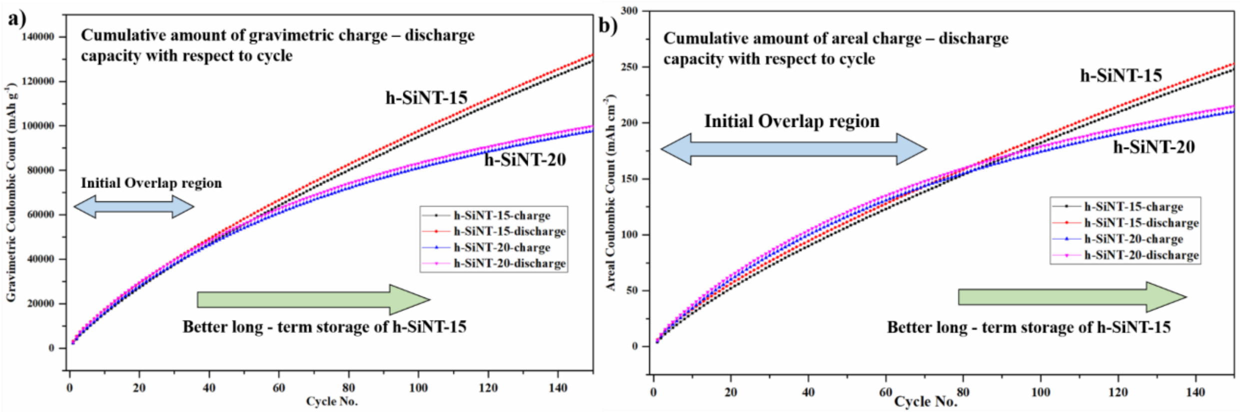

Figure 58 Cumulative a) gravimetric and b) areal capacity of h-SiNT-15 and h-SiNT-20 during long term cycling

The cumulative plot of gravimetric/areal capacities (**Figure 58**) over 150 cycles indicate the ability of h-SiNT-15 to accommodate higher amount of charge and discharge when compared to h-SiNT-20. This performance can be related to the structural degradation of h-SiNT-20 which is observed in post cycling scanning electron microscopy. (**Figure 34, Figure 59**)

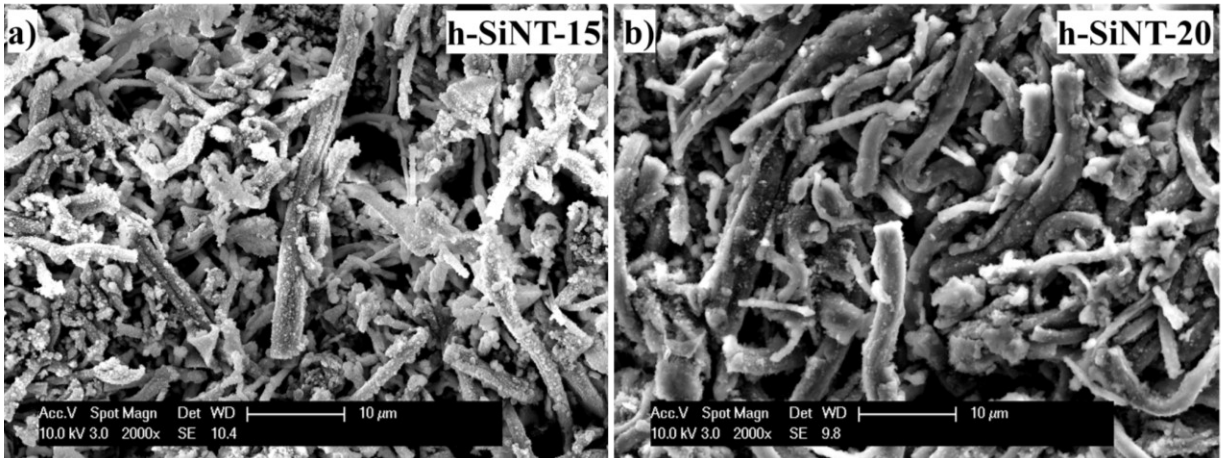

Figure 59 High magnification post cycling SEM analysis of a) h – SiNT – 15 and b) h – SiNT – 20

Appendix A.2 Supplementary Information: Water-Soluble Template Derived Nanoscale Silicon Nano-Flakes and Nano-Rods Morphologies: Stable Architectures for Lithium Ion Anodes

Table 11 Summary of processing, characterization and electrochemical performance in Li/Li$^+$ system of Si$_{NF}$ and Si$_{NR}$

		Si$_{NF}$	**Si$_{NR}$**
NaCl Template	**HEMM**	2 hour	20 hour
	Particle Size	>20μ	>2μ
CVD Mechanism		Layer by layer	VLS growth
Morphology		Flakes, 40-60nm thk	Nanorods, 50-200nm dia
Phases (Raman)		~85% *a*-Si, *nc*-Si	~18%*a*-Si, *c*-Si
Capacity / mAh·g^{-1}	**1st Discharge**	~2830	~2980
	1st Charge	~2175	~2500
	250th Discharge @ 1 A·g^{-1}	~810	~740
FIR Loss / %		~17-20	~12-15
Fade Rate / % loss cycle^{-1}		0.11	0.23
Amorphization Cycles		3	>10

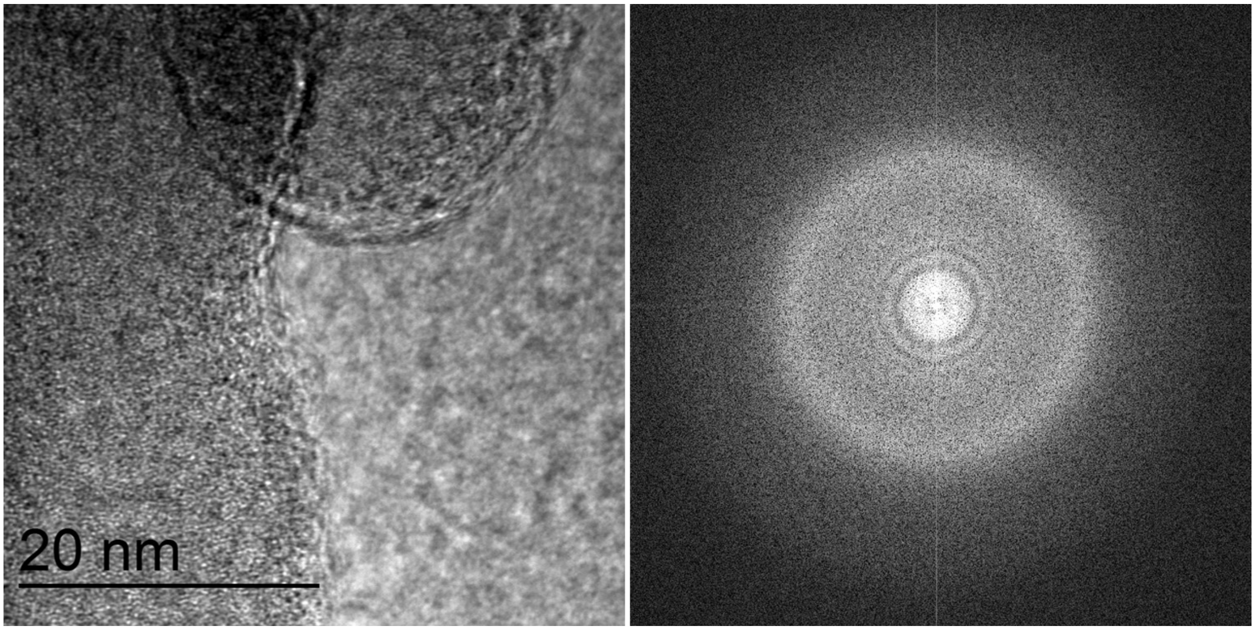

Figure 60 a) HRTEM image and b) corresponding SAED pattern showing diffused rings of Si nanoparticles in SiNR system indicating highly disordered a-Si

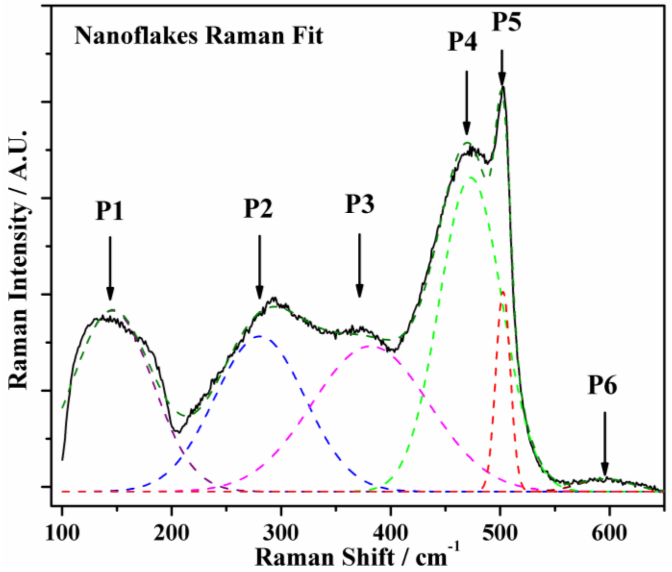

Figure 61 Deconvolution and fitting of Raman spectra of nanoflakes. Solid line indicates experimental data and dotted lines indicate the fitted Gaussian distribution curves. Light green and red curves indicate the amorphous and nanocrystalline phases corresponding to P4 and P5 peaks, respectively

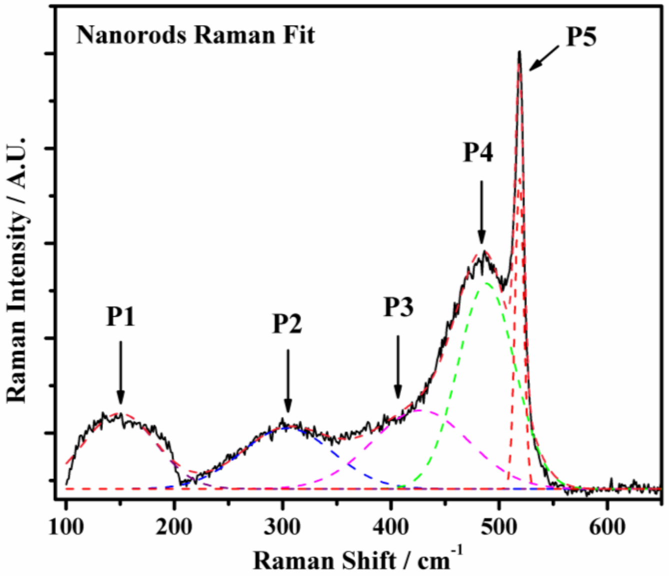

Figure 62 Deconvolution and fitting of Raman spectra of nanoflakes. Solid line indicates experimental data and dotted lines indicate the fitted Gaussian distribution curves. Light green and red curves indicate the amorphous and crystalline phases corresponding to P4 and P5 peaks, respectively

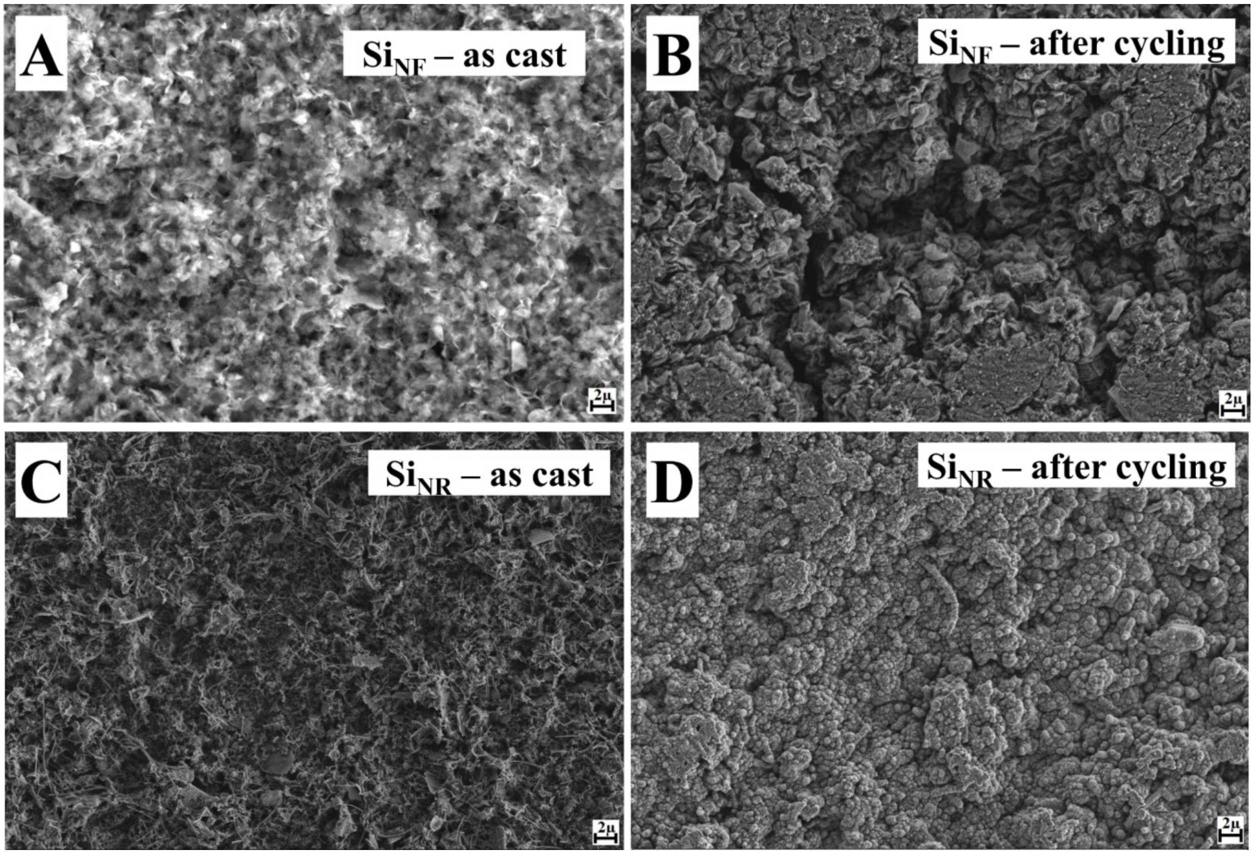

Figure 63 Post cycling SEM analysis (low magnification) of SiNF and SiNR. a) and c) SEM images of as cast electrodes, b) and d) SEM images of electrodes after 300 cycles, of SiNF and SiNR, respectively

Appendix A.3 Supplementary Information: Nanostructured Si@MWCNT on Copper Substrates: Binderless High Performance Anode System for Lithium-ion Battery

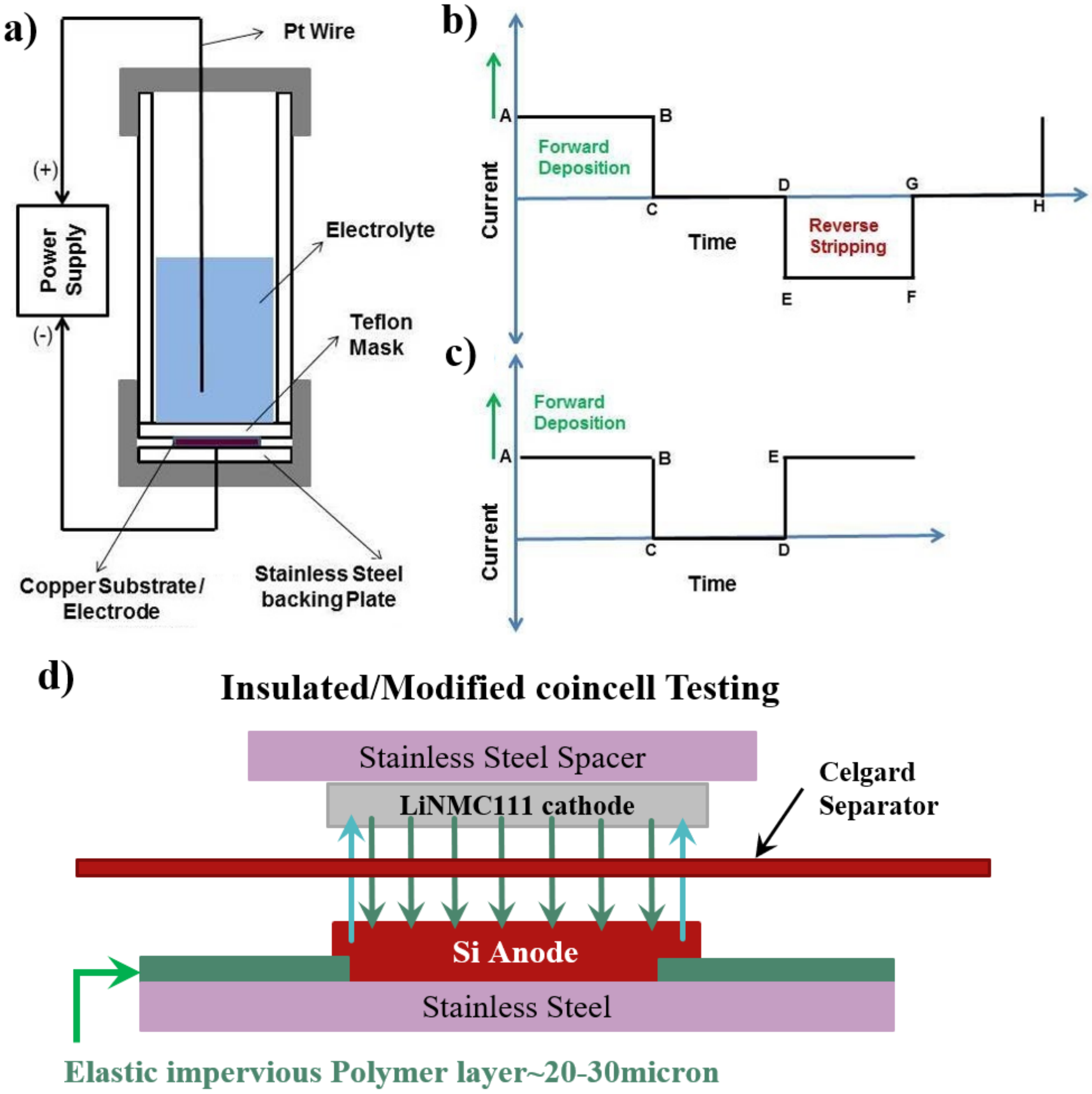

Figure 64 Pictorial representation of a) pulse electrodeposition setup, b) standard input current cycle during pulse electrodeposition, c) input current cycle for pulse current electrodeposition in the current study, d) Insulated / modified coincell testing for full cell testing

The general parameters of operation of pulsed current electrodeposition are forward peak current density, forward ON TIME, forward OFF TIME, reverse peak current density, reverse ON TIME, reverse OFF TIME and the total amount of charge supplied. The reduction and deposition of Si^{4+} ions take place during the ON TIME of the forward cycle (positive cycle) while during the ON TIME of the reverse cycle the deposited Si is stripped in the form of Si^{4+} and enters the electrolyte solution. During the OFF TIME there is no current introduced through the cell and there is no reduction/oxidation taking place at the electrodes. However, during the OFF TIME there is diffusion of Si^{4+} ions from the bulk of the electrolyte towards the ionically depleted region formed at the electrode – electrolyte interface. A typical input cycle of pulse current electrodeposition is as shown in **Figure 64b**. In the current study, to prevent the complications arising from the oxidation of Cu from the substrate into the electrolyte during reverse cycle, we have employed only the forward deposition cycle as shown in **Figure 64c**. The percentage ratio of ON TIME (AB) to forward TIME (AB+CD) in the pulsing cycle is termed as the DUTY CYCLE and is kept constant at 20%.

The insulated coin cell testing (**Figure 64d**) was developed to study the Li plating behavior and provides a way to restrict the Li flux on the negative electrode and prevent the spread of Li plating. The soft elastic impervious layer on the SS backing plate in coin cells provide a way to maintain the electrical contact/continuity as well as restrict the plating on the stainless-steel backing in the coin cell. This provides an easy accurate method to match the electrode area along whilst enabling the use of smaller electrodes for testing materials during initial development stage to record accurate behavior of materials close to full cell pouch cell systems where the areal mismatch of negative and positive electrode is less than 1%. Kindly note that the positive electrode is devoid of this insulation since the plating phenomenon is absent at such high potentials.

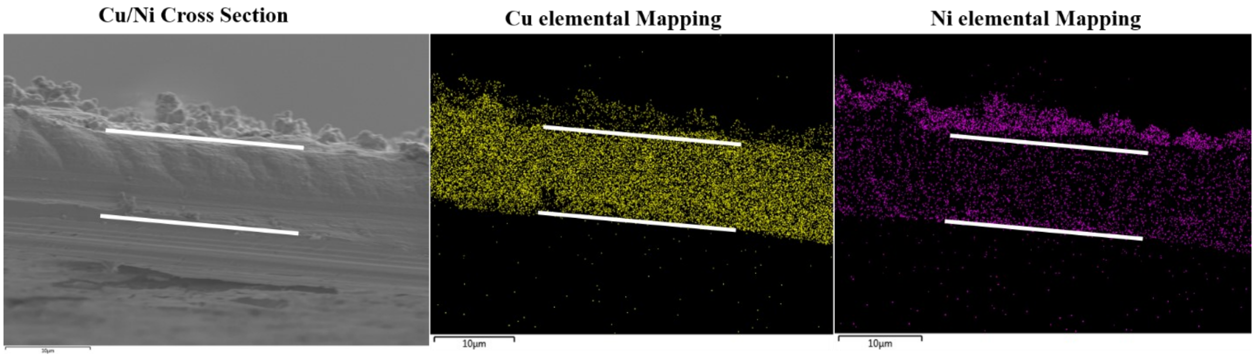

Figure 65 EDAX elemental mapping of electroless Ni plated Copper foils showing Ni deposition on Copper

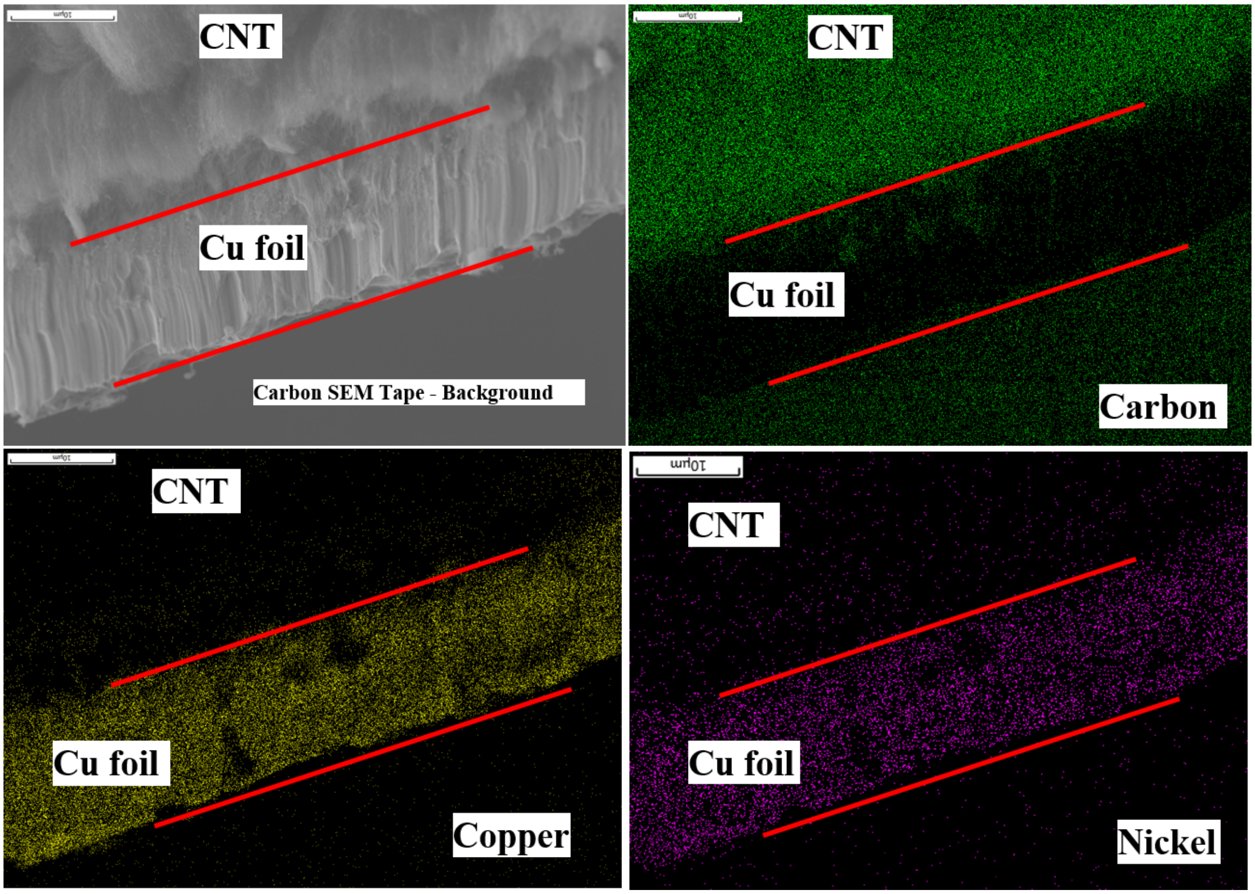

Figure 66 EDAX elemental mapping of Vertically aligned carbon nanotubes grown on electroless Ni plated Copper foils showing distinct growth of CNTs on Cu – Ni foil

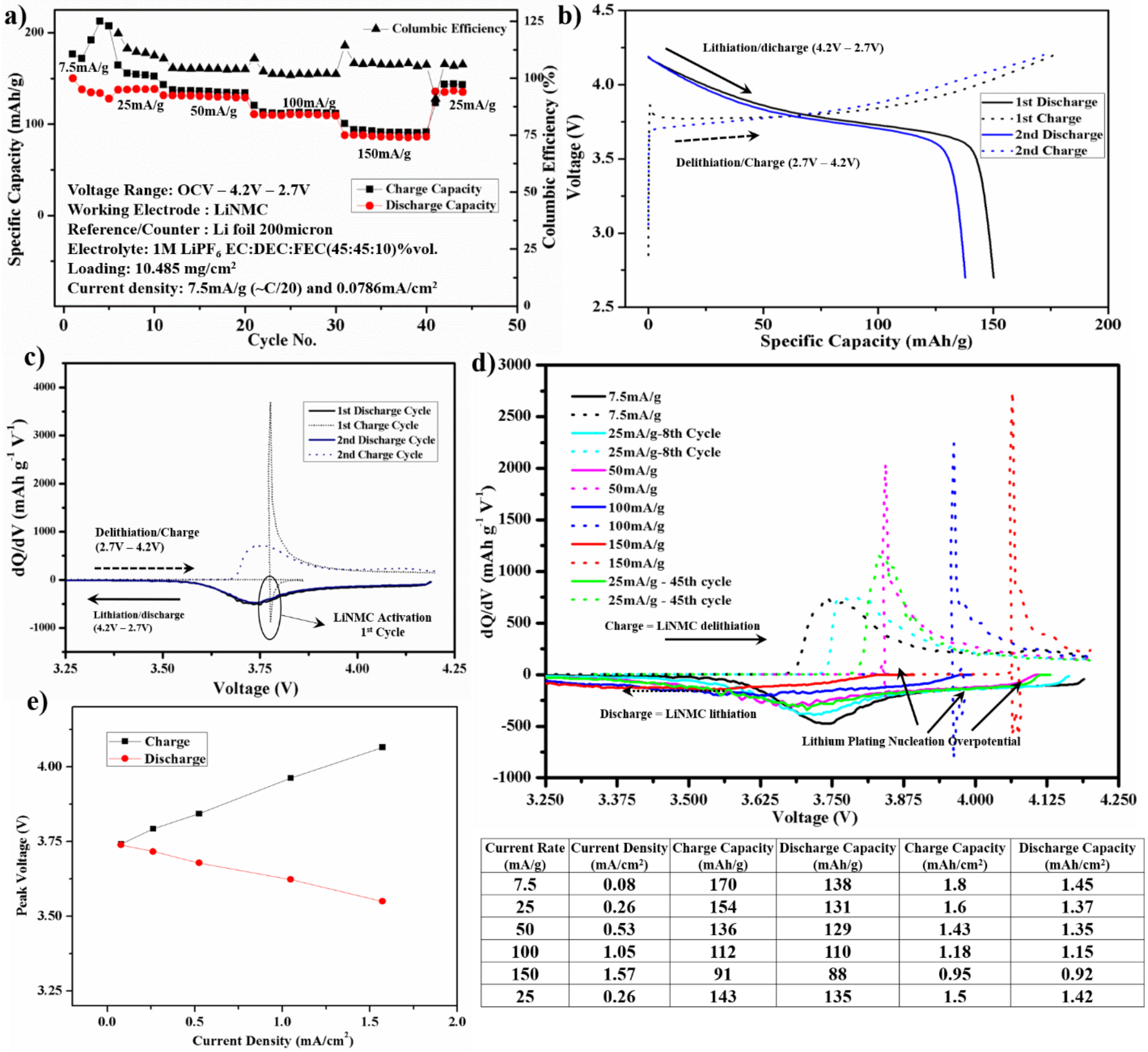

Current Rate (mA/g)	Current Density (mA/cm²)	Charge Capacity (mAh/g)	Discharge Capacity (mAh/g)	Charge Capacity (mAh/cm²)	Discharge Capacity (mAh/cm²)
7.5	0.08	170	138	1.8	1.45
25	0.26	154	131	1.6	1.37
50	0.53	136	129	1.43	1.35
100	1.05	112	110	1.18	1.15
150	1.57	91	88	0.95	0.92
25	0.26	143	135	1.5	1.42

Figure 67 Electrochemical characterization of LiNMC111 in Li/Li+ system. a) rate capability testing at different current densities, b) voltage vs specific capacity plots during the initial charge discharge cycles, c) differential capacity vs voltage plots indicating the reaction peaks, d) differential capacity vs voltage plots at different current densities and different cycles of the rate capability testing, e) reaction peak voltages vs areal current density

LiNMC111 cathode during the half cell testing at moderate areal loading shows a minor activation peak during the first cycle (**Figure 67b**) which reflects as negative peak in the differential capacity vs voltage plots (**Figure 67c**). This peak is absent in the second cycle at the same current density (**Figure 67c**) which further confirms that the peak is from activation of LiNMC111 and the system activation is complete in the first cycle. However, with the change in gravimetric current rate / areal current density, this negative peak still exists in the differential capacity vs voltage plots (**Figure 67d**). However, this phenomenon / signal arises from the nucleation potential of Li plating on the Li metal with the modulus/absolute value of the intensity of this peak increasing with the increase in current density. Hence, the existence of this negative peak on subsequent cycling indicates the initiation of plating phenomenon.

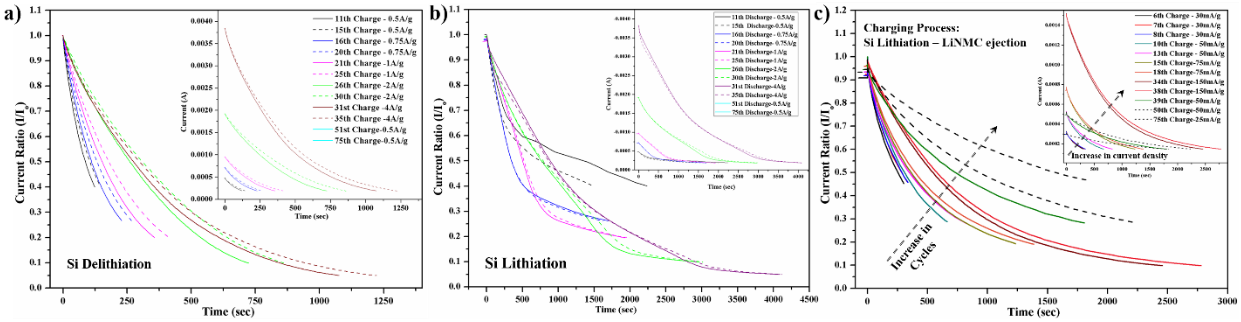

Figure 68 Relaxation behavior of system under CV mode subjected to different CC mode current rate. All insets indicate the actual current vs time response. Current ratio vs time responses of a-Si-MWCNT/Cu-Ni during a) Deithiation, b) Lithiation in half cell configuration and c) that of full cell testing of LiNMC111 with a-Si-MWCNT/Cu-Ni system. The differential capacity vs current plots are derived by analyzing these responses.

At higher current rate the system shows negative potential indicating Li plating profile (**Figure 69**) under unrestricted lower voltage with the equilibrium voltage of plateau at ~ (-)0.1V. However, under relaxation conditions the OCP of the system jumps back to ~0.15 – 0.2V indicating that the system undergoes Li plating and Li reaction simultaneously. Hence, the nucleation potential recorded under constant current conditions for Li plating on Li active materials has an overlapping signal arising from the Li reaction. However, when discharged under low current rates (C/20) to 0.01V (~80-90% of specific discharge capacity) and then subjected to high current the actual nucleation potential for Li plating is recorded.

This suppresses the signal from silicon lithiation and the nucleation and growth of Li plating on silicon can be analyzed distinguishing the capacity contribution of Li reaction from Li plating on the Li active system/substrate/electrode. It should be noted that the system after plating (orange profile) tends to stabilize at ~0.002-0.005V which indicates that the sharp peak obtained at low voltages in differential charge vs current in CV mode (**Figure 54d**) is probably due to Li plating.

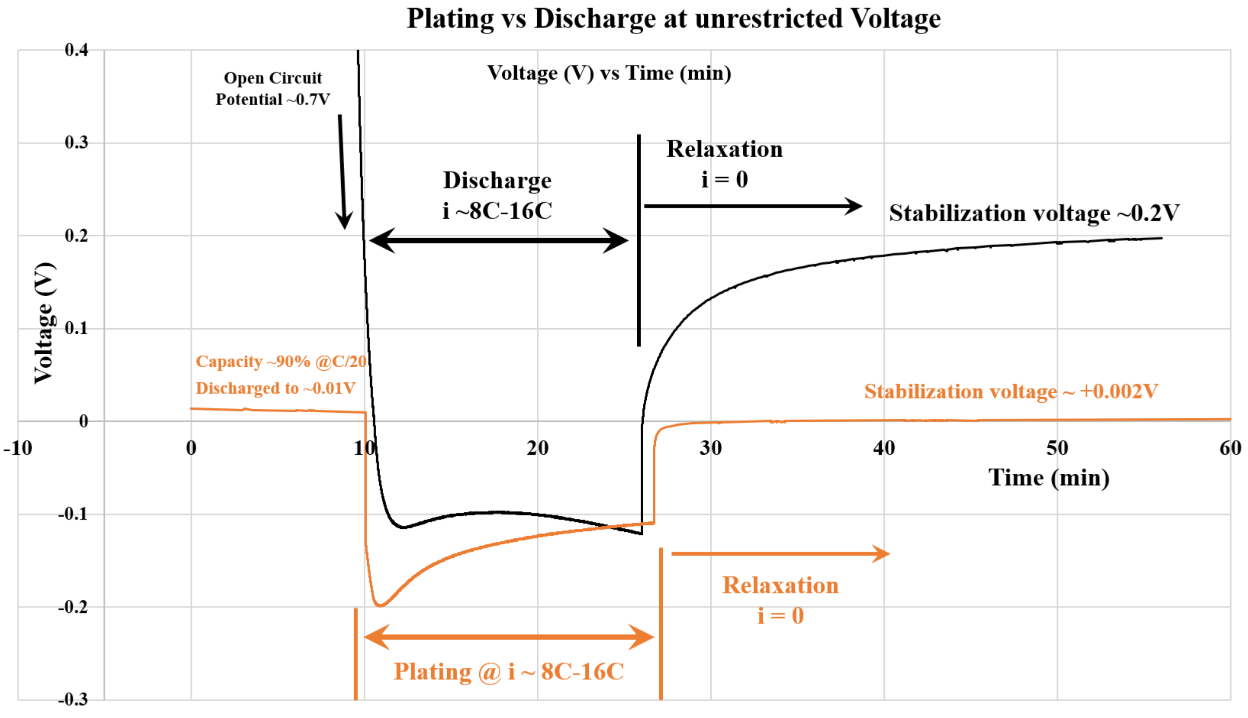

Figure 69 Voltage vs time curves of EDSi-MWCNT/Cu – Ni system under unrestricted potential indicating the difference in electrochemical data response

Below are the recommendations for scientific study related to Li plating on Li active materials.

1.Discharge the system to ~0.01V @ C/20 current rate till it attains ~80 - 90% of the lithiation discharge capacity.

2.Subject the system to plating at a current rate >C/2 (10 times the current density in the discharge cycle).

3.To analyze the stability of lithium plating restrict the deplating voltage cutoff to ~80% of the lowest lithiation stabilization voltage (for example ~0.08V is the lowest stabilization voltage for silicon)

4.In case the voltage cutoff is off the limits of the cycler, it is recommended to plate at least 10 times capacity of lithium reaction with active system in that voltage cutoff range.

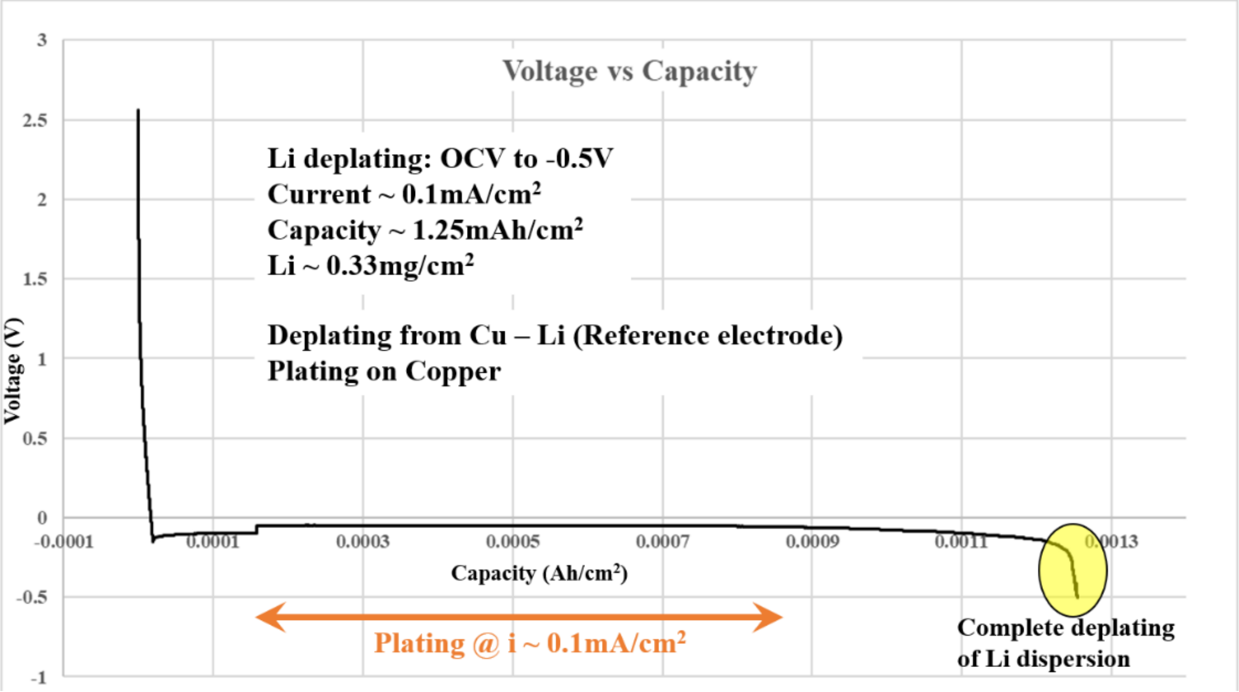

Figure 70 Voltage vs capacity of Li deplating till complete removal of Li from Cu – Li electrode and plating on Cu electrode

Deplating of lithium from Cu – Li system and plating on to Cu electrode indicating Li loading of ~0.33mg/cm^2 on copper by addition of Li dispersion. The voltage decreases to -0.5V indicating the complete removal of Li in the electrochemical system.

Table 12 Fitting results using a complex non-linear least square (CNLS) method for EIS spectra of a-Si-MWCNT/Ni-Cu with Li in half cell configuration using Zview

Cycle No		**3**	**50**	**100**
R_s	**(ohm·cm^{-2})**	1.02973	1.04215	1.27069
CPE_{SEI}	**T**	4.50E-05	0.0001	7.87E-05
	P	0.70499	0.62387	0.6138
R_{SEI}	**(ohm·cm^{-2})**	16.1701	22.6828	44.0223
CPE_{CT}	**T**	0.01	0.00185	0.00064
	P	0.56	0.75363	0.79683
R_{CT}	**(ohm·cm^{-2})**	19.0063	77.1901	305.8
W_o	**R**	0.92115	0.94768	24.21
	T	0.03571	0.00516	0.18
	P	0.51704	0.40046	0.70811

Table 13 Fitting results using a complex non-linear least square (CNLS) method for EIS spectra of a-Si-MWCNT/Ni-Cu with critical loading LiNMC in full cell configuration using Zview

Cycle		**3**	**10**	**20**	**60**
R_s	**(ohm·cm^{-2})**	7.56289	10.5456	10.5535	10.5597
CPE_{SEI}	**T**	3.03E-05	9.64E-05	1.15E-05	2.64E-05
	P	0.70784	0.57588	0.87982	0.61969
R_{SEI}	**(ohm·cm^{-2})**	10.7783	13.9764	16.9025	31.7296
CPE_{Film}	**T**	0.0012	0.00072	0.00068	0.00086
	P	0.66698	0.80423	0.51943	0.51444
R_{Film}	**(ohm·cm^{-2})**	5.00786	6.426	8.71069	32.5157
CPE_{CT}	**T**	0.01553	0.01701	0.01702	0.01228
	P	0.75189	0.66324	0.86279	0.81121
R_{CT}	**(ohm·cm^{-2})**	8.47799	15.4135	16.2877	21.2421
Wo	**T**	1.41E-07	6.72E-08	9.29E-08	1.81E-07
	P	1.95E-10	9.60E-10	2.46E-10	7.15E-11
	R	0.43705	0.48973	0.47768	0.42753

Table 14 Fitting results using a complex non-linear least square (CNLS) method for EIS spectra of a-Si-MWCNT/Ni-Cu with lower loading LiNMC in full cell configuration using Zview

Cycle		3	8	50
R_s	**$(\text{ohm}\cdot\text{cm}^{-2})$**	7.703	11.42	15.01
CPE_{SEI}	**T**	1.68E-04	0.00127	8.37E-05
	P	0.49715	0.28187	0.55034
R_{SEI}	**$(\text{ohm}\cdot\text{cm}^{-2})$**	8.93814	11.039	25.99
CPE_{Film}	**T**	2.22E-04	3.23E-05	5.05E-05
	P	0.91463	1.139	1.093
R_{Film}	**$(\text{ohm}\cdot\text{cm}^{-2})$**	0.60702	0.75726	1.87994
CPE_{CT}	**T**	6.12E-10	1.90E-05	0.00389
	P	1.953	0.78355	0.84652
R_{CT}	**$(\text{ohm}\cdot\text{cm}^{-2})$**	0.00265	5.84735	12.7547
Wo	**T**	5.41E-07	1.43E-05	0.00025
	P	8.18E-12	1.24E-09	2.11E-09
	R	0.37512	0.39086	0.33965

Table 15 Gravimetric and areal current density of full cell testing of a-Si-MWCNT/Cu – Ni with LiNMC111 (critical loading > 16 mg · cm2 and lower loading < 12 mg · cm2)

Critical High Loading LiNMC111 vs *a-Si-MWCNT/Cu - Ni*		**mA/g**	**A/g**	**Areal current Density mA/cm2**	**Lower Loading LiNMC111 vs *a-Si-MWCNT/Cu - Ni***		**mA/g**	**A/g**	**Areal current Density mA/cm2**
		LiNMC	**Si**				**LiNMC**	**Si**	
	R1	**15**	**0.194575**	**0.233491**		**R1**	**15**	**0.15566**	**0.186792**
	R2	**30**	**0.389151**	**0.466981**		**R2**	**30**	**0.311321**	**0.373585**
	R3	**50**	**0.648585**	**0.778302**		**R3**	**50**	**0.518868**	**0.622642**
	R4	**75**	**0.972877**	**1.167453**		**R4**	**75**	**0.778302**	**0.933962**
	R5	**150**	**1.945755**	**2.334906**		**R5**	**150**	**1.556604**	**1.867925**

Appendix B Development of Other Lithium Battery Based Systems

Appendix B.1 Supplementary Information: Carbon Based Electrodes for Lithium Plating and De-plating

Appendix B.1.1 Experimental Method

Carbon Nanofiber (CNF) by Electrospinning Process (Figure 71):

Synthesis of Polyacrylonitrile Fibers:

Polyacrylonitrile (Sigma Aldrich): 0.8g – 1g

N, N Dimethyl Formamide (Sigma Aldrich): 15ml

Distance from Rotary Drum to tip of needle = 14 – 16cm

Applied Voltage = 13KV – 15KV

Stabilization / Oxidation Temperature: 240 C for 4 hour in air / oxygen atmosphere

Carbonization temperature: 750C – 1000C for 1 hour in Argon atmosphere in ramp rate of 1 – 2 C/min followed by ambient cooling.

PDMS curing Process (Sylgard 184):

Mixing of PDMS:

Sylgard 184 is packaged in lot matched kits with the base and curing agent in separate containers. Mix the two components thoroughly using a weight or volume ratio of 10:1. Note: The pot life is 2 hours for catalyzed Sylgard 184 at room temperature.

It is recommended to vacuum de-air, with a residual pressure of 10-20 mm mercury, which, when applied for applied for 30 minutes, will sufficiently de-air the material.

Curing of PDMS:

Cure using one of the following recommended schedules:

15 minutes at 150°C, 1 hour at 100°C, 4 hours at 65°C, 24 hours at 23°C

Synthesis of CNF / PDMS structure: (Figure 71)

Coat the PDMS (~30micron) on cleaned Cu foil substrate (30 mins acetone / ethanol / isoproponal and dried in ambient conditions) using doctor blade technique. Place the CNF on the PDMS coated copper foil and apply a uniaxial force of ~30T in MTI Corp uniaxial press for 24 hours. If possible, keep checking every 30 mins to see the decrease in hydraulic pressure and keep increasing it to 30T. Remove the pressure and place the CNF – PDMS – Copper in oven at 120°C for another 12hours. There are chances that sometimes the curing may not happen due to the impurities and behavior of PDMS.

Characterization

The electrochemical testing of CNF was conducted in a coincell in the voltage range of ~0.001V to 1.2V at a current rate of ~25 $mA \cdot g^{-1}$ and areal current densities of 0.1 $mA \cdot cm^{-2}$ and 4 $mA \cdot cm^{-2}$ to record the lithiation and de-lithiation behavior and performance of fibers. The Sands time experiment was conducted in a flooded electrolyte two electrode cell at different current densities ranging from 1mA/cm^{-2} to 5 $mA \cdot cm^{-2}$ after subjecting the electrode to ~25$mA \cdot g^{-1}$ current density in the positive cycle till ~0.001V. Subsequently, the electrodes were tested in modified coin cell using PDMS as the blocking agent to prevent irregular lithium plating in the coincell and focus the flux of lithium ions to the electrode. Scanning electron microscopy (SEM, Philips XL 30 or Zeiss) was used to study the morphological and electrode structure. Raman spectroscopy, if applicable was performed using a Renishaw in-via Raman microscope equipped with a 633 nm red laser.

Appendix B.1.2 Characterization and Electrochemical Results

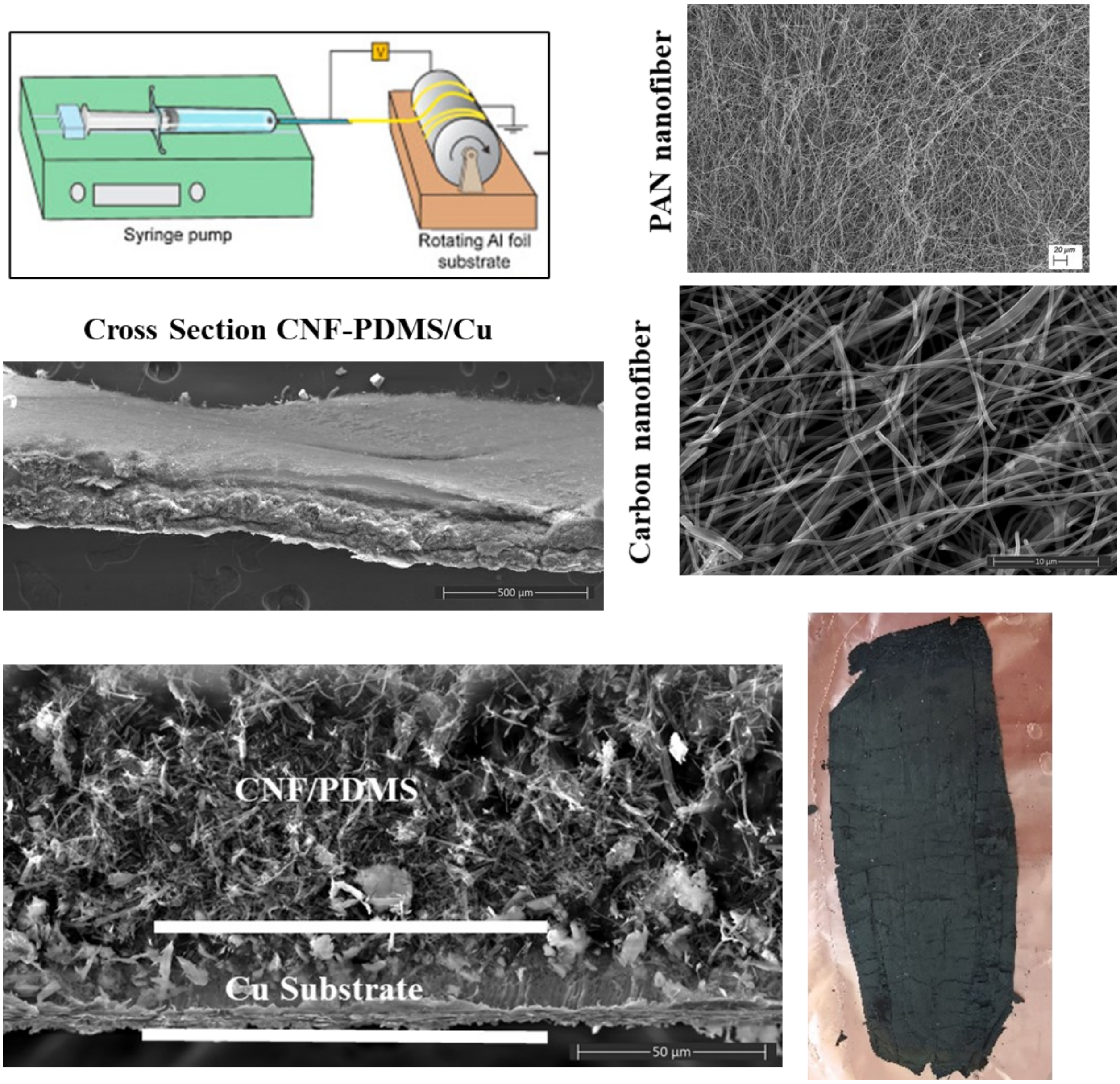

Figure 71 Pictorial Representation of electrospinning set up, SEM images of polyacrylonitrile, carbon nanofiber and cross section of CNF/PDMS/Cu substrate

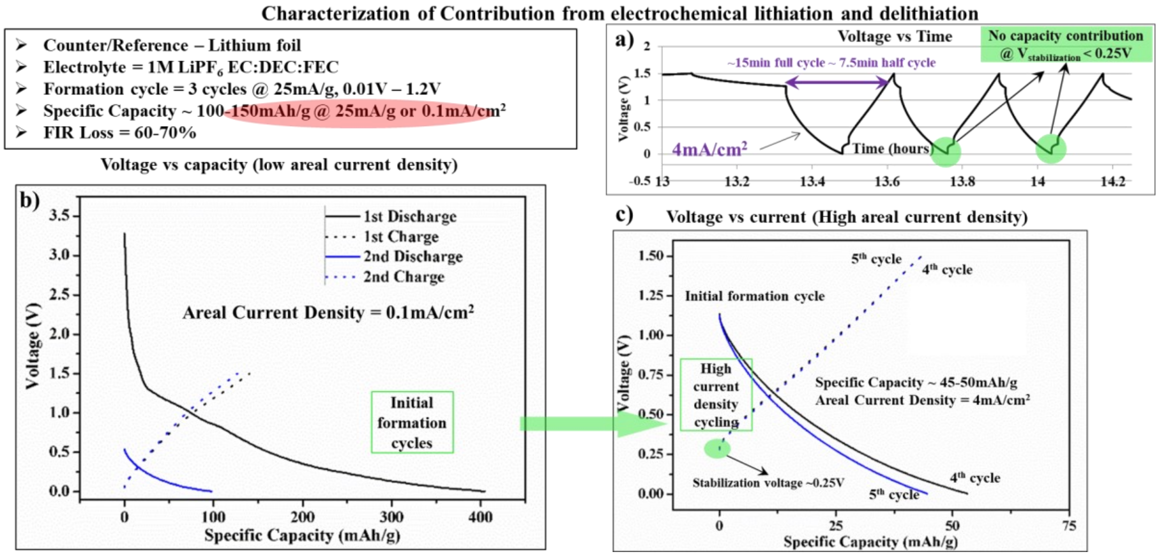

Figure 72 Electrochemical cycling of carbon nanofiber under lithiation and delithiation conditions along with a)stabilization voltage, b) and c) voltage – capacity plots at different current rates

The FIR loss in CNF system ~250-300mAh/g with very low capacities ~100-150mAh/g and ~40-50mAh/g at low and high current rates, respectively (**Figure 72**). The contribution of Li intercalation reaction is very low, and CNF show low capacity to intercalation. The stabilization voltage on intercalation is ~0.25V which is equilibrium potential for Li – carbon reaction.

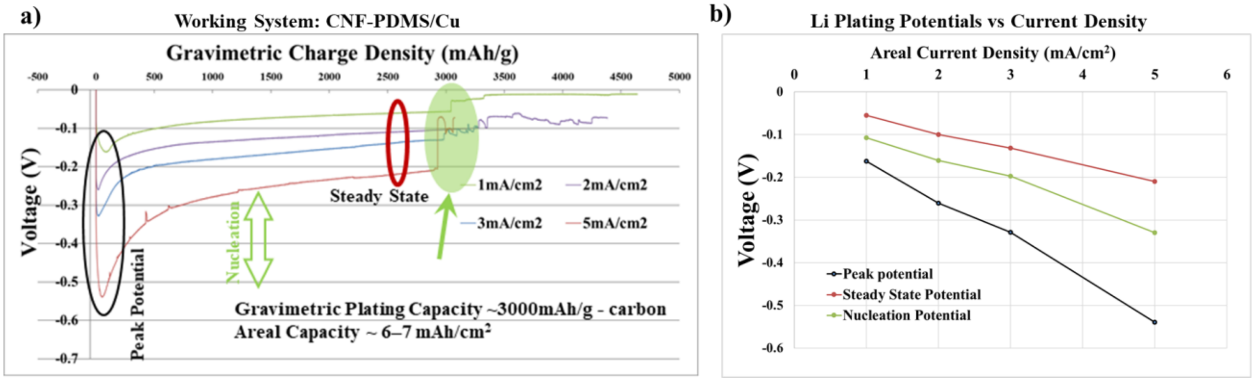

Figure 73 a) Stable regime of plating (Sands time experiment) and b) Different Li plating potentials with respect to current density

The stable plating regime shows minimal fluctuations before hitting the undesired mossy or fractal Li growth. (**Figure 73**) This region indicates stable reversible Li plating with the formation of hemispherical growth sites and coalescence of these structures on CNF. Hence, these CNF based systems are expected to show high CE within this region of plating and deplating. The possible capacity of these CNF based architectures is ~3000mAh/g w.r.t CNF competing with that of silicon - based anode systems at a gravimetric current rate of ~2A/g. The systems suffer from an irreversible loss of ~300-350mAh/g (~10-20%) due to the initial formation /intercalation reaction followed by initial CE fluctuations.

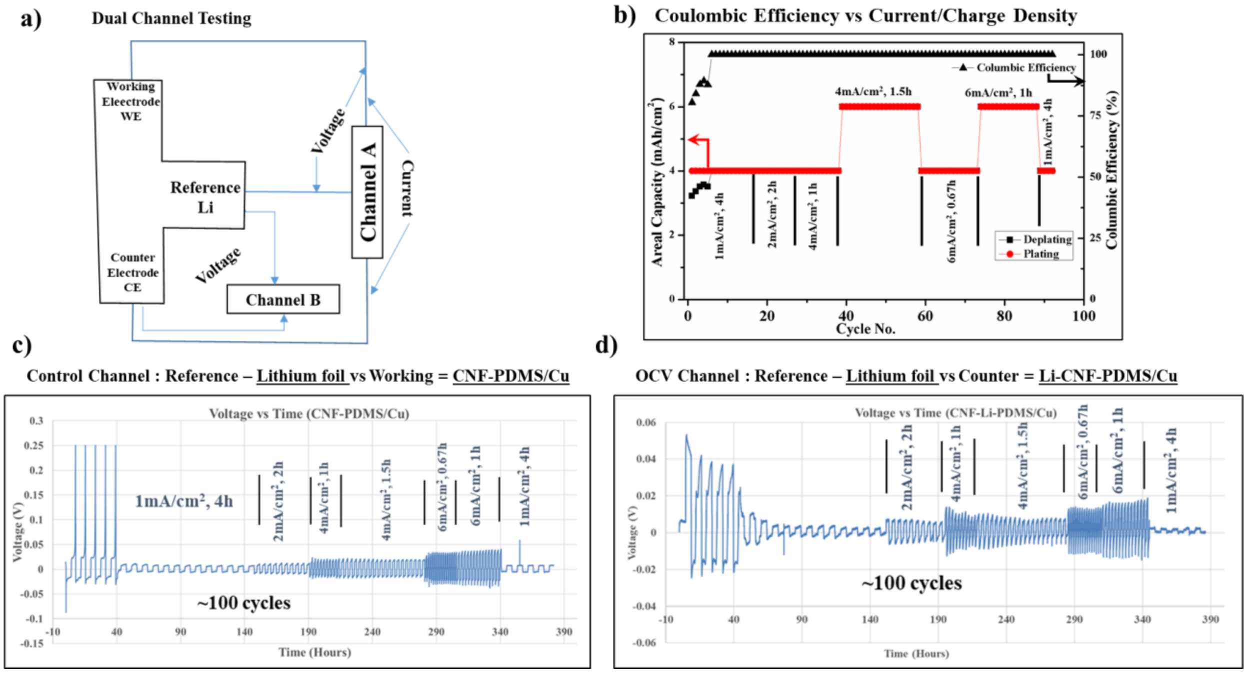

Figure 74 a) Pictorial representation of dual channel set up, b) rate capability and columbic efficiency study of CNF/PDMS-Cu working electrode, c) voltage profile of working electrode in control channel A and d) voltage profile of counter electrode in Channel B

Channel A is used to control and set the parameters for plating and deplating study for the working electrode CNF-PDMS/Cu. Channel B is used to monitor the voltage of Counter electrode with respect to the reference Lithium. (**Figure 74**) The counter electrode was replaced with Li-CNF-PDMS/Cu instead of plain Li foil to simultaneously check for voltage profile of plating / deplating when Li is melted into CNF-PDMS/Cu. The voltage profile of CNF-PDMS/Cu (working electrode) and Li/CNF composite (Counter electrode) with respect to reference Li shows minimal fluctuations and stable plating and deplating. This test confirms the stability of Li plating / deplating before moving into coincell testing.

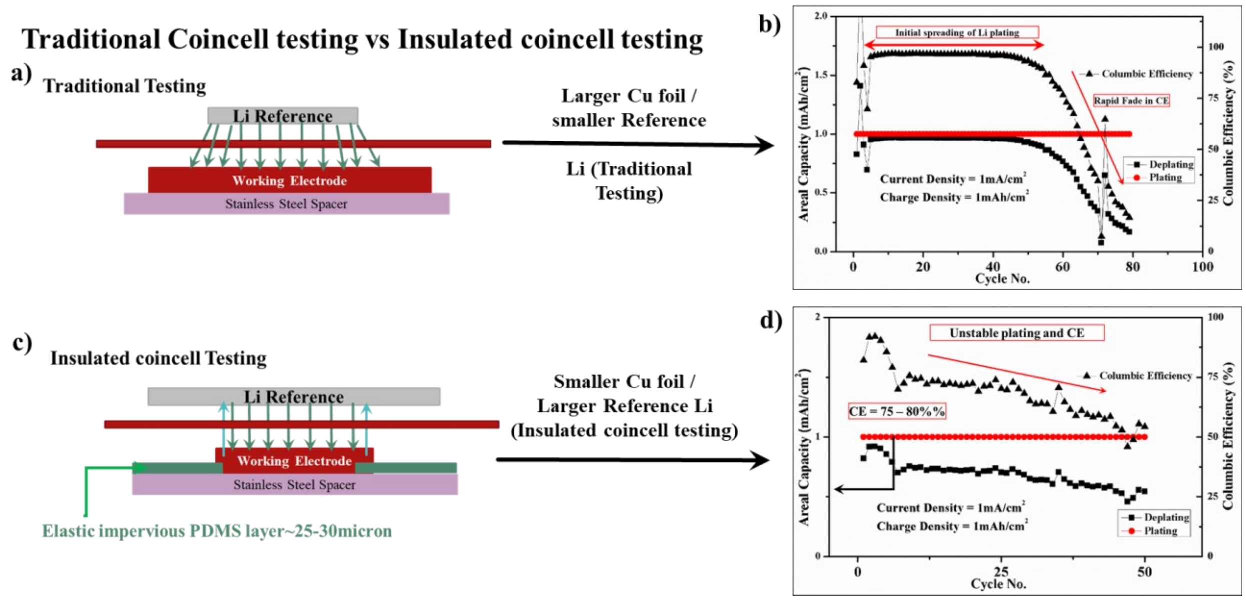

Figure 75 a) and c) Traditional testing and insulated coin cell testing in coincell with their respective electrochemical responses b) and d) for bare copper electrode

The traditional coin cell testing employed shows stabilized CE region during initial plating which is due to the spread of Li plating on the working electrode. (**Figure 75**) The insulated coincell testing focuses the Li flux to the working electrode and hence, the true performance of the system is recorded.

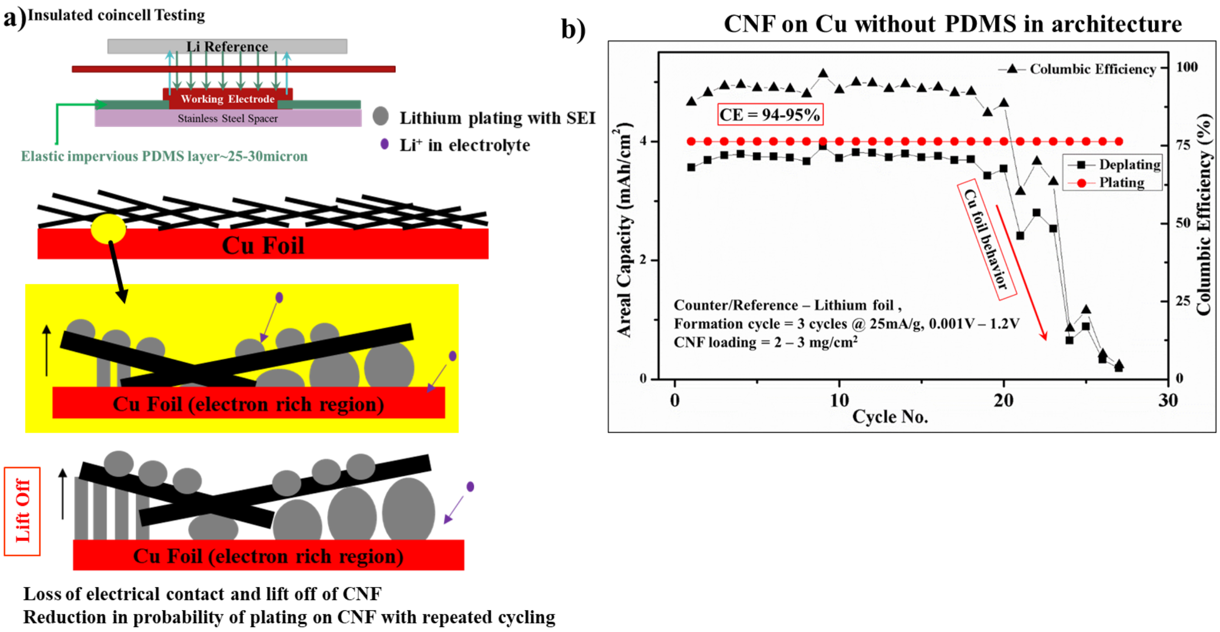

Figure 76 a) Schematic of the expected plating behavior in the CNF on Cu without architecture and b) the electrochemical response of CNF without the electrode architecture

Li plating is associated with porous insulating SEI formation and probability of plating is higher in electron rich region. (**Figure 76**) Without the PDMS architecture CNF/Cu shows improved performance as compared to Cu foil due to distribution on lithium plating on Cu and CNF. However, CNF/Cu approaches Cu foil behavior due to loss of electrical contact between Cu foil and CNF (formation of SEI layer / liftoff of CNF) and preferential plating of Li on Cu foil due to high electron density on Cu foil.

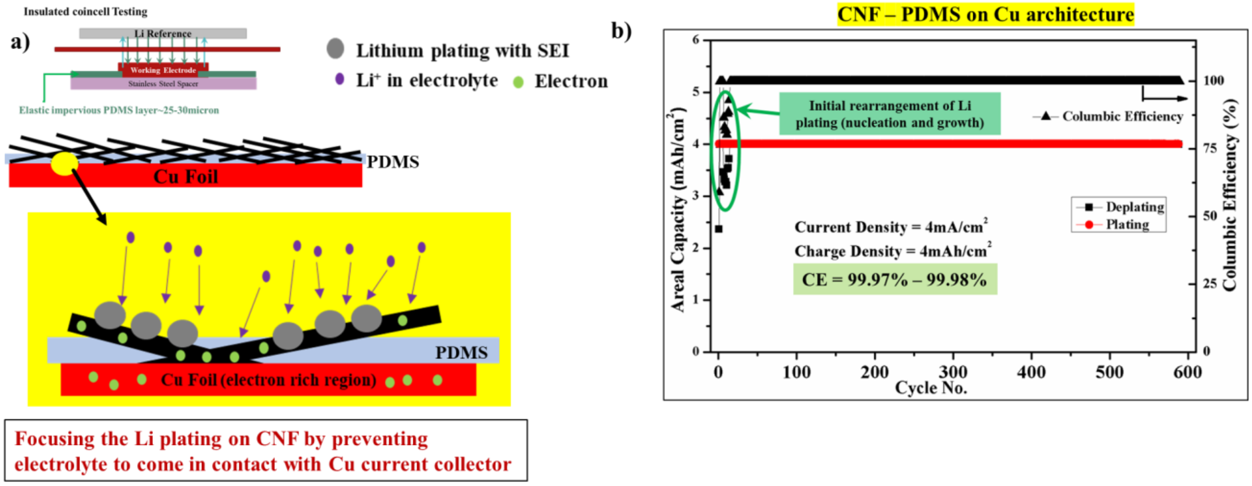

Figure 77 a) Schematic of the expected plating behavior in the CNF/PDMS-Cu and b) the electrochemical response of CNF with the electrode architecture

The architecture provides no loss of electrical contact and prevents the lift of CNF from copper substrate. (**Figure 77**) Replacing the Cu foil with CNF may effects/adds to the impedance in full cell system depending on the electronic conductivity of the CNF. Hence, CNF-PDMS/Cu architecture provides improved performance and better design.

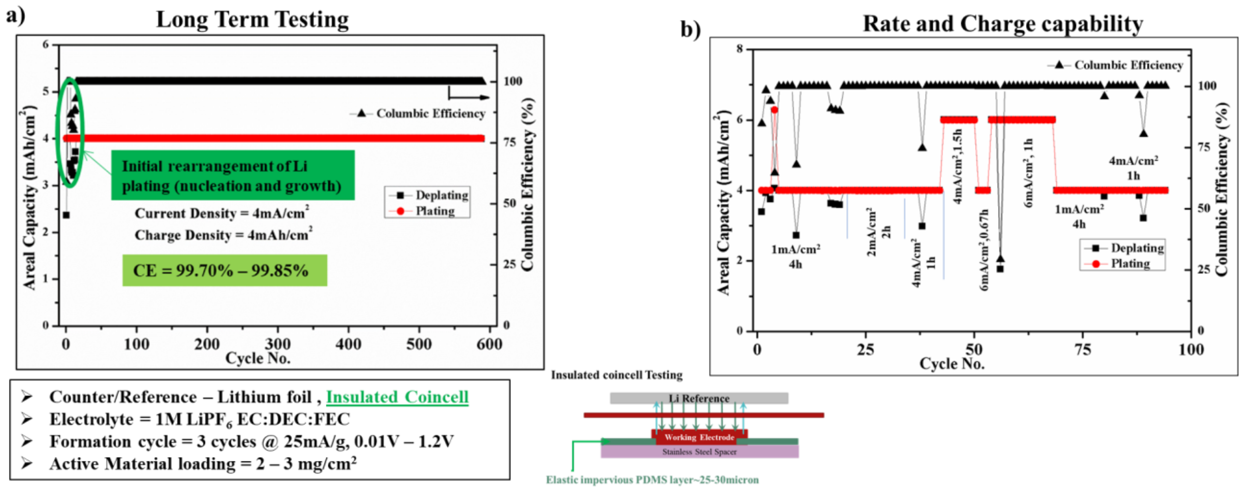

Figure 78 a) Long Term testing of CNF-PDMS-Cu and b) rate capability electrochemical testing in insulated coin cell testing

CNF based architecture shows a high columbic efficiency of ~99.70 – 99.85% for over 600 cycles. The rate capability study shows stable plating efficiency from areal current rates of 1mA/cm^2 to 6mA/cm^2 and charge density of 4mAh/cm^2 to 6mAh/cm^2. (**Figure 78**) The gravimetric specific capacity of the CNF based systems for plating is ~2000-2500mAh/g based on the areal charge density of plating.

Appendix B.2 Supplementary Information: Flexible Nano Silicon Based Carbon Nanofiber Composite: Versatile Anode for Li-Ion Batteries

Appendix B.2.1 Experimental Method

Si - Carbon Nanofiber (Si/CNF) by Electrospinning Process:(Figure 79)

Synthesis of Si / Polyacrylonitrile Fibers:

Polyacrylonitrile (Sigma Aldrich): 0.8g – 1g (polymer)

Nano silicon (MTIXTL) = Variable depending on loading in final CNF (0.3 g and 0.5 g)

N, N Dimethyl Formamide (Sigma Aldrich): 15ml

Distance from Rotary Drum to tip of needle = 14 – 16cm

Applied Voltage = 13KV – 15KV

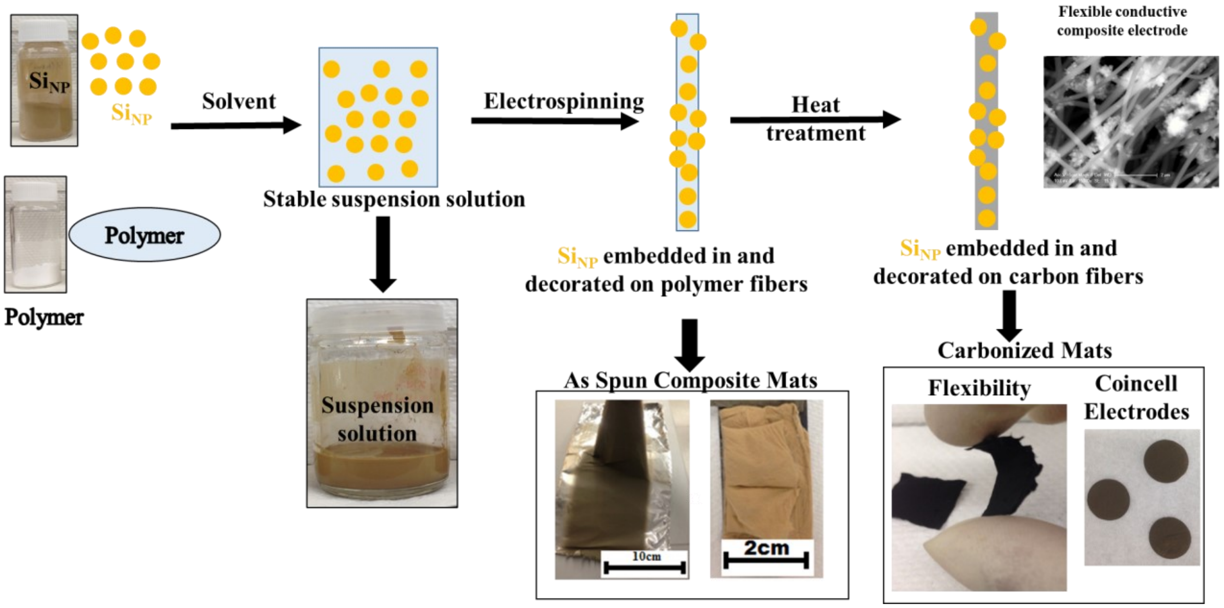

Figure 79 Schematic showing the different stages of the synthesis process along with macro images

Stabilization / Oxidation Temperature (iHT): 180 - 240 C for 4 hour in air / oxygen atmosphere

Carbonization temperature: 500C – 700C for 1 hour in Argon atmosphere in ramp rate of 1 - 2 C/min followed by ambient cooling. HT1 = 500C and HT2 = 700C

Subsequently, the Si-CNF electrodes were dipped in 2 wt.% solution of sodium salt of alginic acid in DI water and dried.

Characterization:

Raman spectroscopy was performed using a Renishaw inVia Raman microscope (Renishaw, Gloucestershire, UK) equipped with a 633 nm red laser to evaluate the vibrational and rotational modes of the deposited films. PANalytical Empyrean XRD diffractometer (PANalytical, Almelo, Netherlands) was used for collecting the XRD spectrum of the system. The electrodes were assembled under argon atmosphere in a half cell (2025 coin cell) using lithium foil as the counter electrode and 1M $LiPF_6$ in ethylene carbonate (EC), diethylene carbonate (DEC), and fluoroethylene carbonate (FEC) with EC:DEC:FEC = 45:45:10 by volume as electrolyte. The assembled coin cell was tested in the potential window of 0.01V–1.2V with respect to Li/Li^+, at various current rates to study their performance as anode material.

Appendix B.2.2 Experimental Results

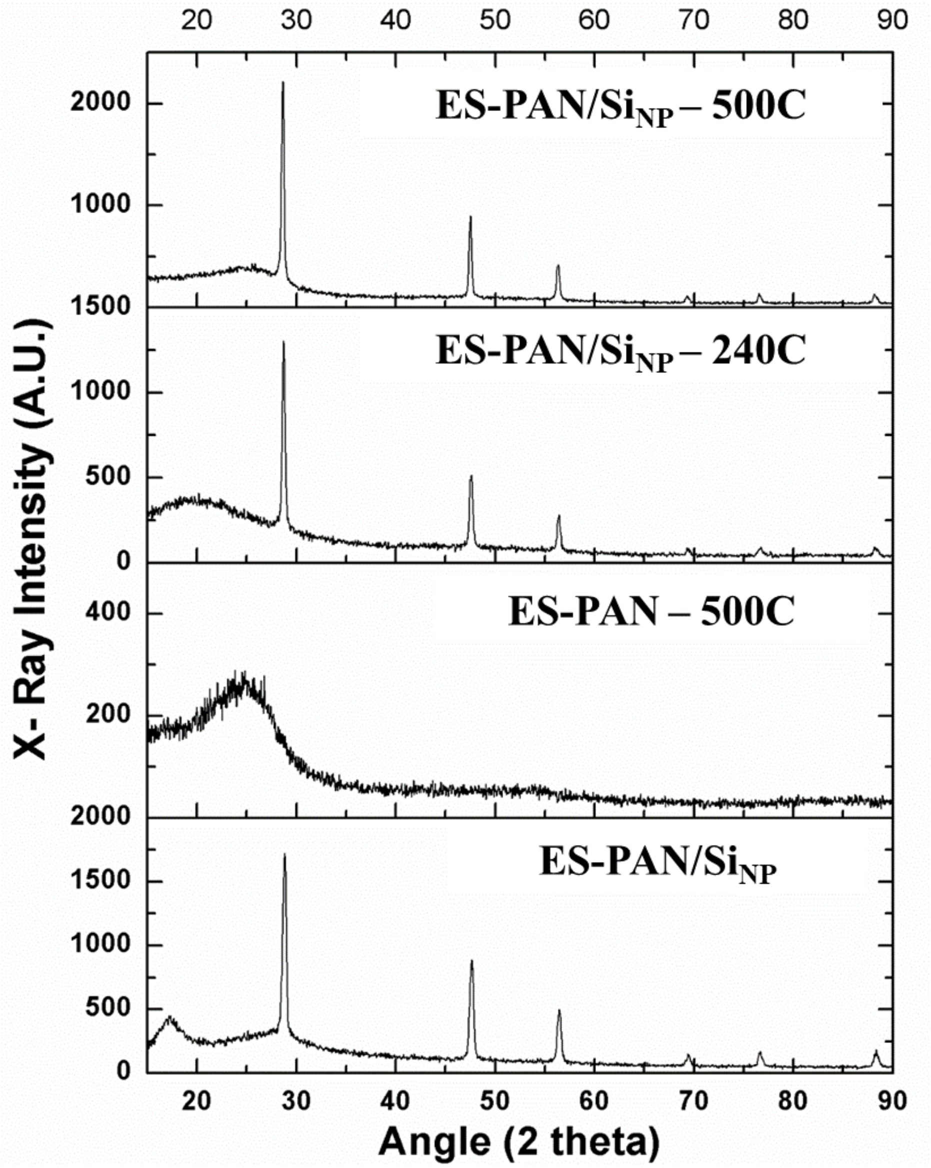

Figure 80 XRD analysis of the electro spun system indicating the phases at different conditions and stages of the synthesis procedure

Electro spun polymer with Si_{NP} show low intensity amorphous peaks and high intensity peaks corresponding to polymer and Si_{NP} respectively (**Figure 80**). Electro spun polymer after carbonization heat treatment retains the amorphous nature. There is no evolution of new peaks in the heat-treated polymer+ Si_{NP} mats. The electrodes formed after heat treating the electro spun mats are, hence, composite in nature. The heat - treated mats show peak at ~515 cm^{-1} corresponding to Si$_{NP}$. The small peak difference from 520cm^{-1} for crystalline Si can be attributed to the small size of the Si$_{NP}$ as compared to bulk crystalline Si. (**Figure 81**) The heat-treated mats show two broad bands at ~1350 cm^{-1} – 1360 cm^{-1} and at ~1585 cm^{-1} – 1590 cm^{-1} corresponding to D and G bands of carbon. By tailoring the heat treatment schedule the ratio of disordered and graphitic carbon can be controlled D/G ratio influences mechanical and electrical properties of the matrix.

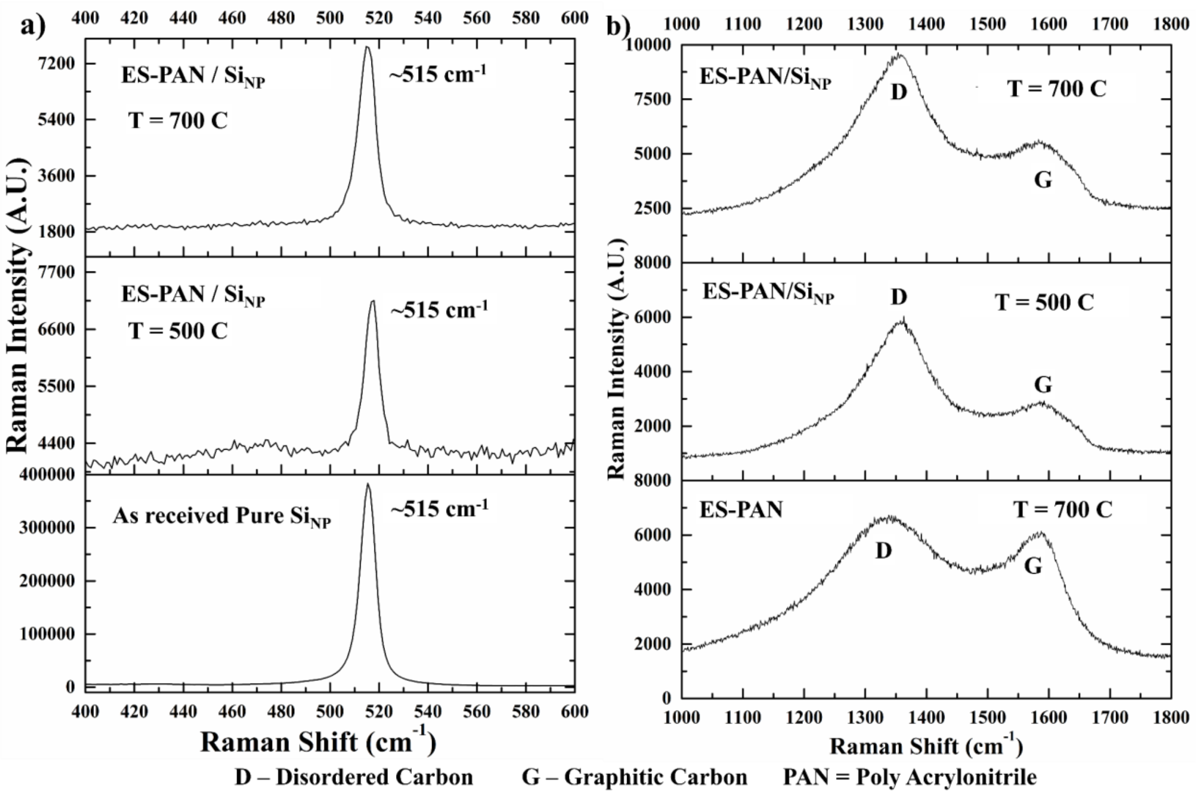

Figure 81 Raman Analysis of silicon and polyacrylonitrile with respect to temperature at various stages of electrode development

As spun pure polymer mats show interconnected nano fibrous structure. The composite polymer – Si$_{NP}$ mats show polymer nanofibers decorated with Si$_{NP}$. The composite nanofiber structure has been retained after carbonization heat treatment and the Si$_{NP}$ are still adherent to/embedded in the nanofibers. The composite mats are porous in nature and allow percolation of electrolyte hence, ensuring uniform, easy and complete wetting as compared to slurry coating method.

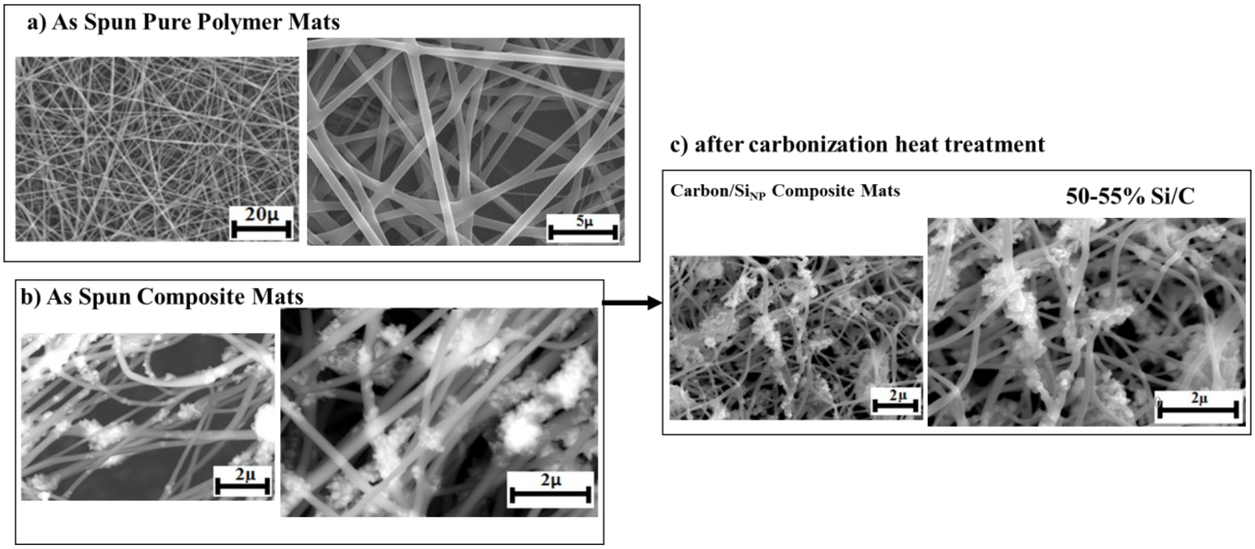

Figure 82 SEM analysis of a) as spun PAN polymer mats, b) as spun composite mats and c) after carbonization heat treatment

As spun pure polymer mats show interconnected nano fibrous structure. (**Figure 82**) The composite polymer – Si_{NP} mats show polymer nanofibers decorated with Si_{NP}. The composite nanofiber structure has been retained after carbonization heat treatment and the Si_{NP} are still adherent to/embedded in the nanofibers. The composite mats are porous in nature and allow percolation of electrolyte hence, ensuring uniform, easy and complete wetting as compared to slurry coating method.

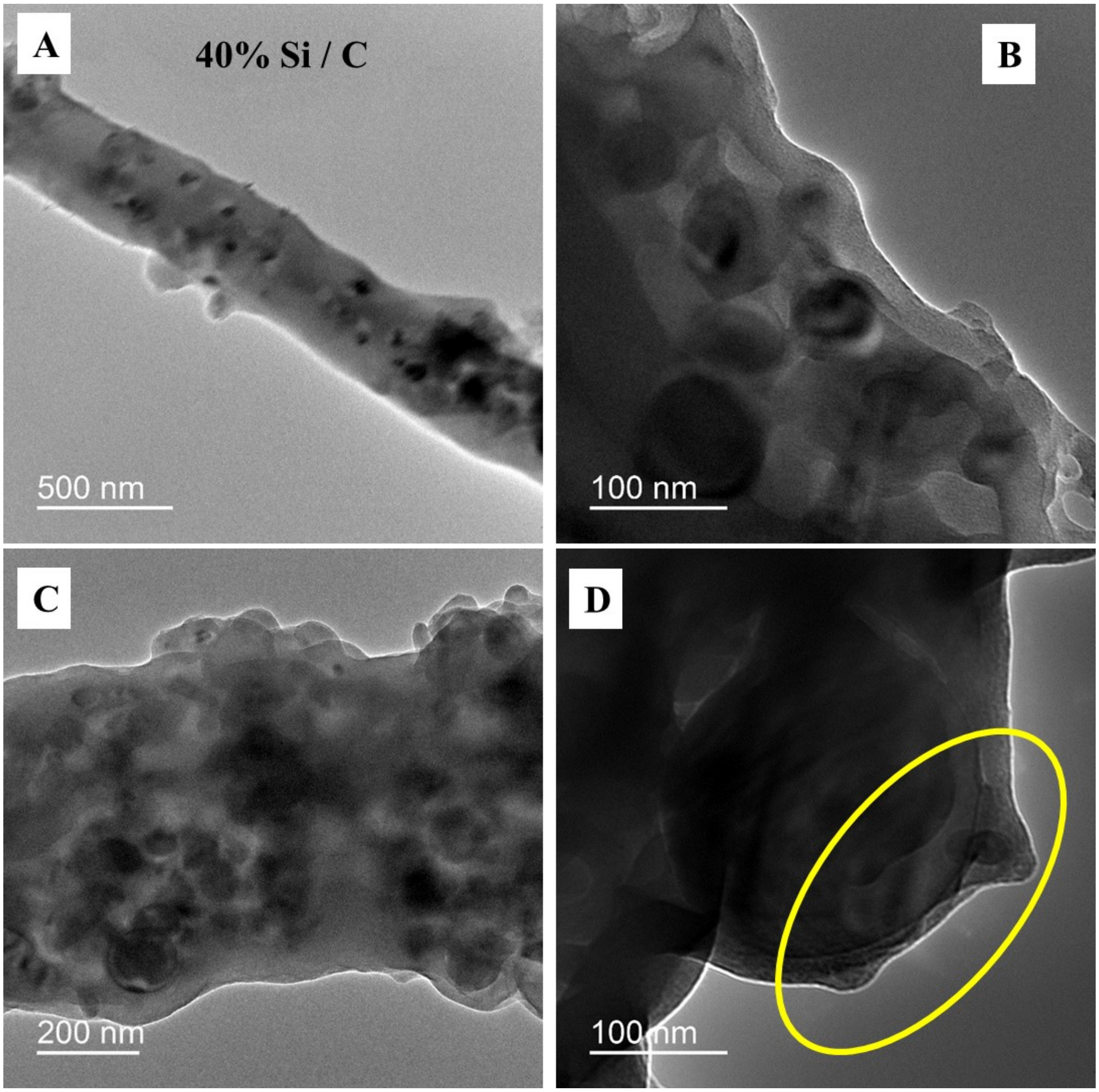

Figure 83 TEM analysis of Si / CNF nanofibers at different magnifications

The diameter of the fibers ~350 – 500 nm. The particles (~100nm) are distributed both inside and on the surface of the carbon fibers. Agglomeration of particles occurs in certain regions. Si_{NP} on the surface are encapsulated by carbon layer. (**Figure 83**)

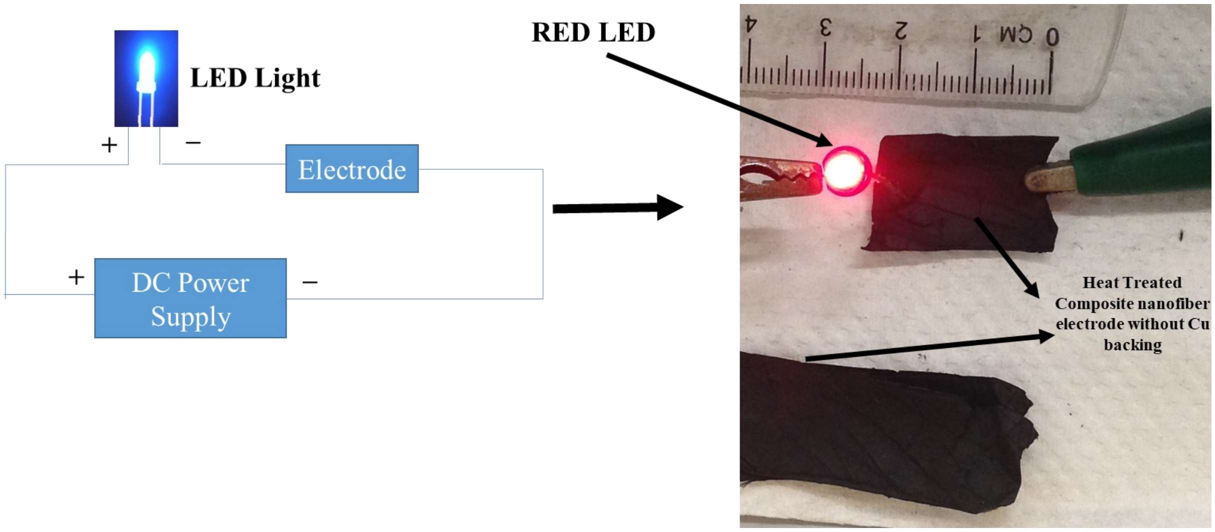

Figure 84 Electrical circuit diagram and corresponding real time image depicting the electrical continuity of the electrode

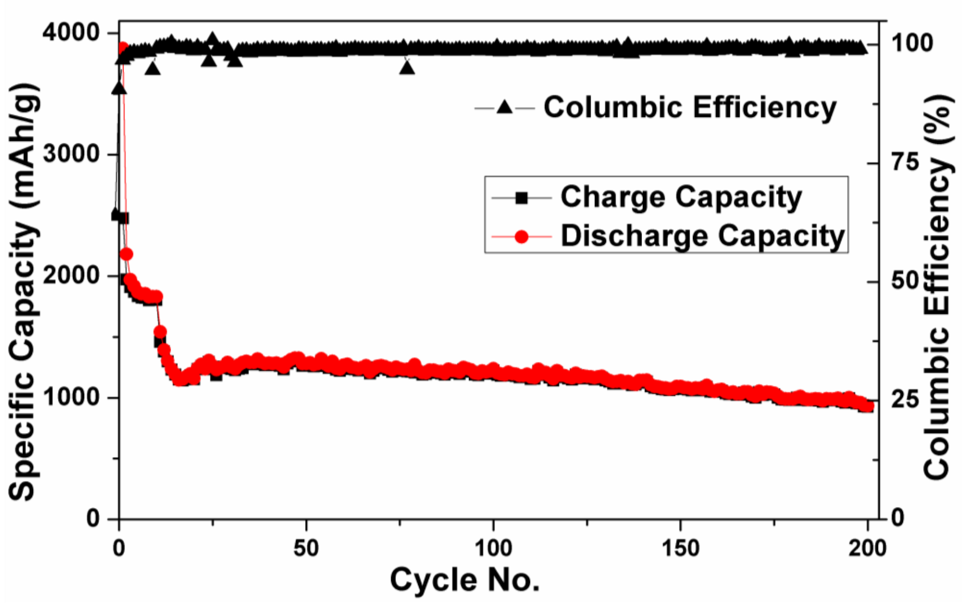

Figure 85 Electrochemical performance of Si/CNF electrode at current rates of 0.2 $A\cdot g^{-1}$ and 0.5 A/g tested in coin cell for Li battery

The electrical continuity of the electrode was measure by using a simple DC powered circuit. The LED light turned on when the two ends of the heat - treated electrode was connected in the circuit. The electrodes are continuous and electrically conducting from end to end. The electrode is used without Cu backing foil. (**Figure 84**) The electrochemical performance of sodium alginate coated Si/CNF mats showed a FIR loss of ~35 – 40% and stable specific capacity of ~1750 – 1850 mAh·g^{-1} at 0.2A/g and ~1200 – 1250 mAh·g^{-1} at 0.5 A/g. (**Figure 85**)

Appendix B.3 Supplementary Information: Hybrid Solid State Electrolytes using ZSM

Problem Statement:

Stabilization of lithium plating (~20-30micron) is critical for the development of high energy density lithium ion batteries (LIBs) involving high voltage cathode and lithium-sulfur systems. Ceramic electrolytes based on cubic and garnet structure have shown good solid-state Li+ conductivity. However, these systems are still far from being commercialized due to mechanical/crystallographic instability and high volumetric mass densities. Hence, garnet-based electrolytes are currently rendered ineffective for immediate application in LIBs. Polymer based electrolytes suffer from extensive deformation due to low elastic modulus and high ductility.

Fundamental Approach:

Solid state Li^+ migration is a compounded effect of bulk and grain boundary diffusion phenomenon which suffer from high activation energy and ionic scattering effect, respectively. However, surface diffusion has the least activation energy and shows promise for exhibiting the highest Li+ conductivity. (**Figure 86**)

The fundamental approach here involves creation of aligned surface diffusion pathways within the grain thus, reducing the activation energy for Li^+ diffusion thus forming a novel hybrid ceramic electrolyte (HCE).

Surface diffusion being the dominant phenomenon in bulk electrolyte and at the anode/electrolyte interface stabilizes Li plating profile by minimizing the mismatch in the Li+ flux occurring in the bulk and at the interface. The electronic conductivity is low marked by the wide band gap > 4 – 6 eV.

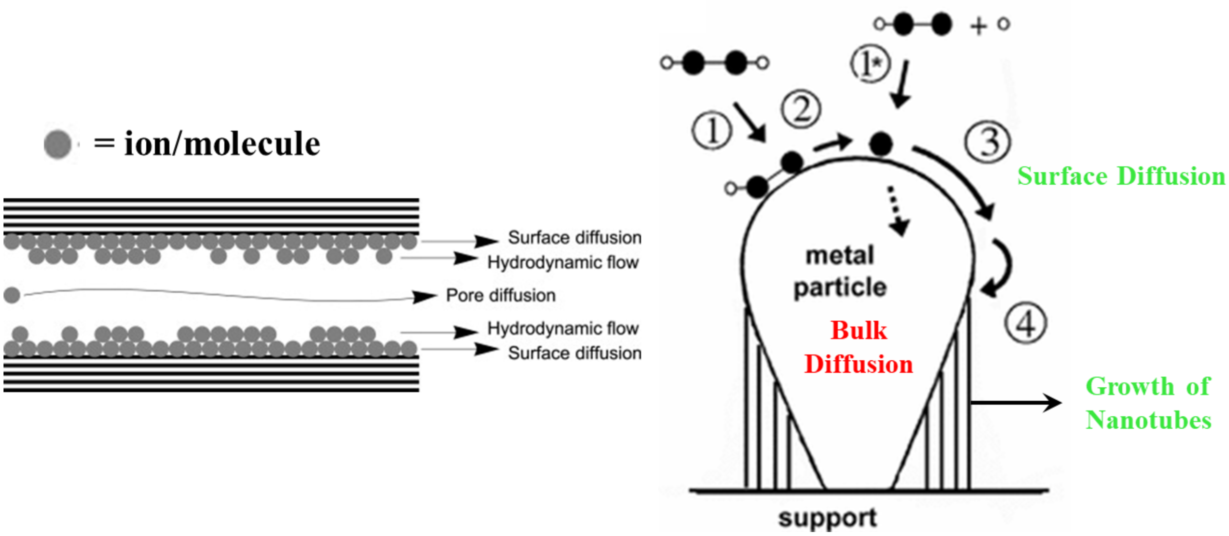

Figure 86 Schematic representation of surface diffusion vs pore diffusion in a particle and the low activation energy of surface diffusion leading to growth of CNT

Experimental Method: (Figure 87)

Weight of ZSM - 5 = 0.95g; Weight of binder (stearic acid) = 0.05g; Solvent = DI water

Pelletizing pressure = 40T (MTI XTL)

Heat treatment temperature = 500 – 600C for 6 hour in air

Ion exchange with $LiPF_6$ EC:DEC:FEC and drying with lithium carried in glove box.

The electrochemical testing was conducted in symmetric Li/HCE/Li configuration.

Novel hybrid ceramic electrolytes (HCE) were developed from ZSM - 5 with enhanced Li^+ diffusion utilizing the low activation energy for surface migration. The crystallographic channels in the inorganic framework provide pathways for efficient transport of Li^+ ions thus making them attractive ceramic electrolyte materials.

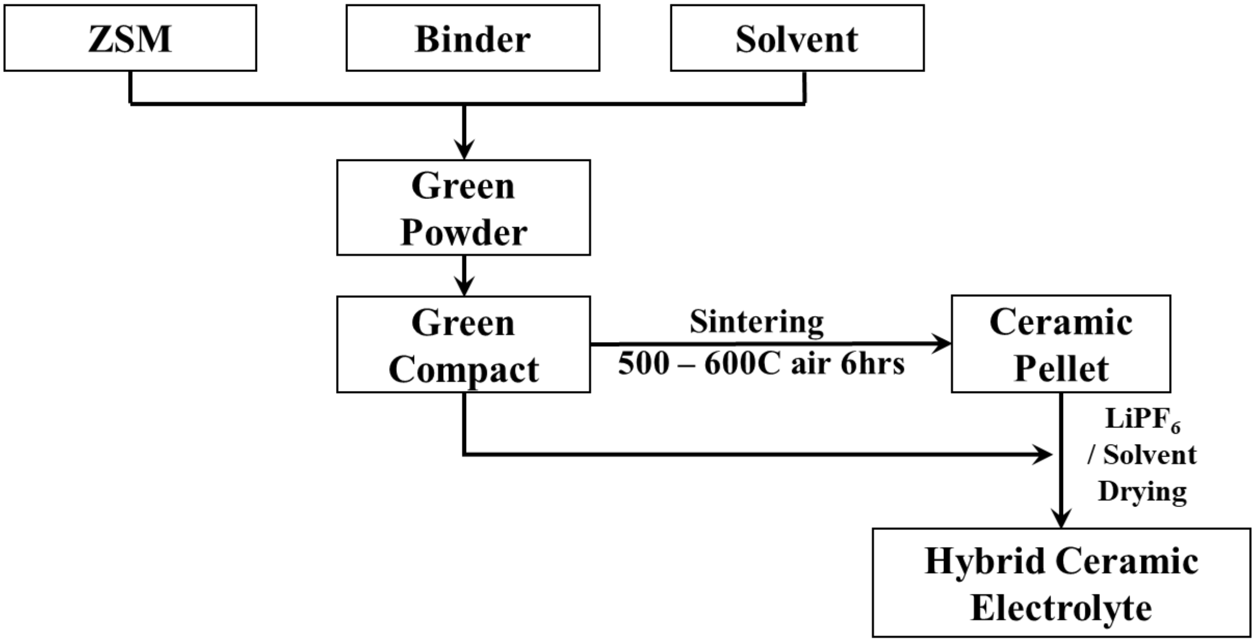

Figure 87 Flow chart representing the steps for the synthesis of hybrid ceramic electrolyte

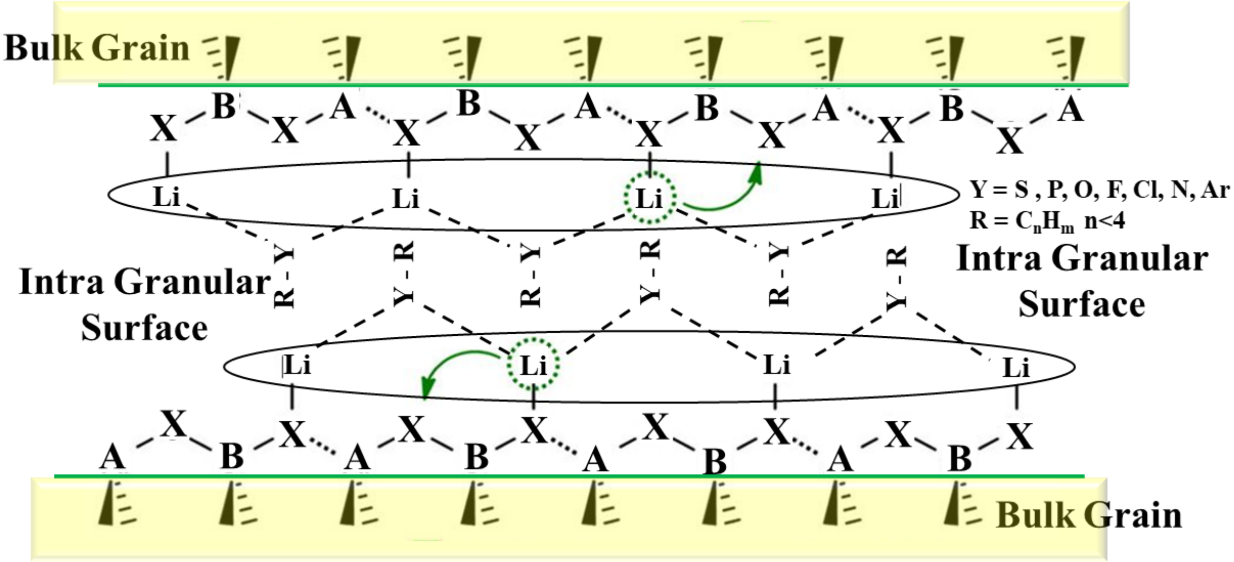

Figure 88 Graphical representation of surface diffusion of Li+ assisted by ZSM-5 surface

Reduction in activation energy due to molecular interaction between Li^+ with surface functional groups in organic molecule and ZSM-5 structure. (**Figure 88**) Surface migration sites provide low activation energy sites as compared to interstitial crystallographic stable atomic sites in traditional solid-state electrolytes.

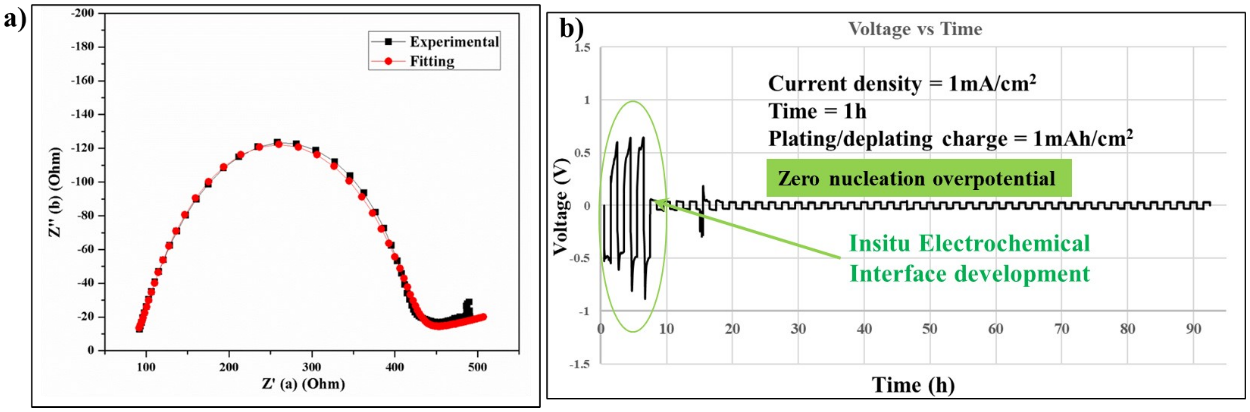

Figure 89 a) EIS spectra of hybrid ceramic electrolyte in Li/Li+ and b) electrochemical performance in symmetric coin cell.

Hybrid Ceramic Electrolytes are developed using ZSM - 5 as electrolyte framework systems. These novel ceramic electrolytes show a Li^+ conductivity of ~ 1.2557 x 10^{-4} S/cm or 0.12557 mS/cm (in the range of 10^{-1} to 10^{-2} mS/cm) at room temperature very close to that of liquid electrolytes (**Figure 89**). The electrolytes show low plating / deplating potentials ranging from 100mV@1mA/cm^2 – 450mV @4mA/cm^2 surpassing garnet / polymer-based electrolytes. Currently, efforts are underway to stabilize the electrolyte architecture, establish repeatability along with overpotential and coulombic efficiency studies on copper substrate/lithium.

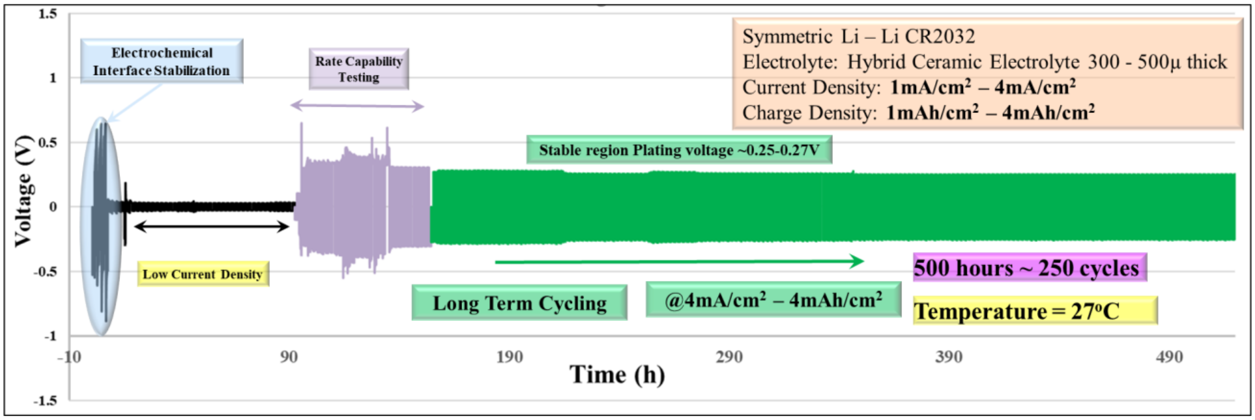

Figure 90 The long - term cycling of Li/ZSM-5/Li system at different current densities over a time of 500h

The initial stages are marked by the development of stable electrochemical interface @Li/HCE interface. The low current density testing indicates stable plating and deplating without any nucleation over potential indicating stable plating at the interface (**Figure 90**). The rate capability testing shows plating potential of ~0.1V to 0.4V for a 300-500µ electrolyte at current density of ~1mA/cm^2 – 4mA/cm^2.

Table 16 Different plating over potentials of Li in hybrid ceramic electrolytes

Current Density (I_D)	1 mA/cm^2	2 mA/cm^2	3 mA/cm^2	4 mA/cm^2
Voltage (V)	0.1 - 0.11	0.3-0.34	0.38-0.39	0.4-0.41

Appendix C Supplementary Information: Standard Operating Procedures for Different Systems

Appendix C.1 Atmospheric Pressure Chemical Vapor Deposition (CNT)

Foreword:

Kindly refer/study the manuals of every component of the system in case it is assembled system. Additionally, study the behavior of precursors (SDS, MSDS, OSHA, GHS, etc.).

Watch/study/assimilate/practice the general operational videos related to operation of quarter turn valve, ball valve, needle valve, switching on vacuum pump, etc. separately (away from the system), before operating the system. Watch the videos from manufacturer if available and contact the manufacturer about the capabilities / compatibility of the equipment before proceeding with the process. Sometimes the manufacturer may relinquish/decline the responsibility of the gases or materials used for the system and suggest upgrading / new system / modifications. The gases are required to be vented into scrubber system installed in operational fume hood. If existing, the vacuum pump and the outlet / inlet to ambient atmosphere are required to be installed in the operational fume hood.

Additionally, please study/read the manual and identify the different parts / components of the reactor system before operating the system. The use of spontaneously pyrophoric gases (silane, etc.) and the use of toxic/poisonous gases (or reactor gases resulting in pyrophoric/toxic/poisonous gases as by products) is not at all recommended for the system at NECST laboratory.

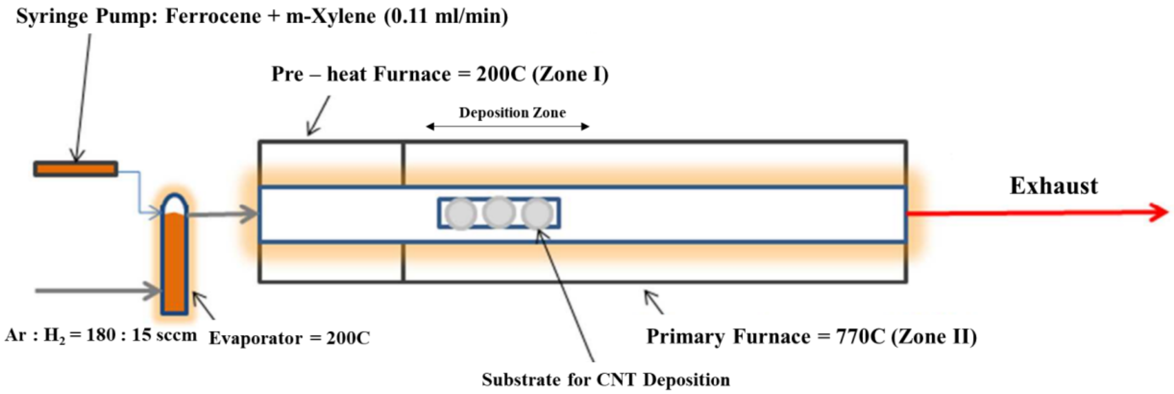

Figure 91 Schematic diagram of CVD setup for CNT deposition

Steps for Atmospheric Pressure Chemical Vapor Deposition (CNT)

1.Clean all the fittings / valves with ethanol along with the piping to remove blockages due to previous usage. If required use high pressure air or vacuum pump to clear the blockages depending on convenience.

2.Load substrate into a quartz tube.

3.Load the quartz tube into CVD system. Adjust the substrate location to match the deposition zone.

4.Seal the interface of the quartz tube and metal connector by tightening the metal nuts / screw fixture at two ends of the quartz tube.

5.Close the furnace.

6.Set furnace temperature Zone 1 to 200°C (Ramp=less than 10°C/min) and Zone 2 to 770°C (Ramp= less than 10°C/min) and switch on the furnace.

7.Set the temperature of evaporator to 200°C and switch on the heating.

8.Switch on the argon gas line on the mass flow controller and set the flow rate to 180 sccm.

9.Switch on the H_2 gas line on the mass flow controller and set the flow rate to 15 sccm. Switch off the mass flow controller after the set point of flow is reached.

10.Allow the system to stabilize at the set temperatures and flow rate of argon (~5 – 7 hour). Keep checking every 30 mins for any fluctuations or malfunction of the furnaces.

11.Switch on the hydrogen gas and allow for the flow to stabilize (~15 – 30 mins)

12.Load freshly prepared mixture of liquid precursor (for CNT deposition 70 mg ferrocene in 10 ml m-xylene stirred for 1hr) in the syringe pump and set the flow rate to 0.1 ml/min to drop into the evaporator

13. After achieving the required time of deposition switch off the syringe pump.

14.Subsequently, switch off the hydrogen gas in the flow meter.

15.Switch off the temperature control of evaporator, followed by the two furnaces (Zone I and Zone II)

16.Allow the system to cool down in argon atmosphere. (takes ~7 – 8 hour or may be more)

17. Switch off the argon flow

Disclaimer: The author of this document / dissertation along with the committee is not responsible for the results and damages to the personnel / equipment / material / assets arising from the use / practice of this operational procedure. Under the circumstances that any such type of incident / event occurs the individual/organization requesting the procedure to be utilized and the laboratory executing the procedure would be liable for any kind of damages incurred. Kindly recommend the user to figure out with a law practicing individual / attorney / legal department of the organization before employing the standard operating procedure.

Parameters for CNT deposition:

Ferrocene = 0.07g, m-Xylene = 10ml, Flow rate of Ferrocene/Xylene = 0.1ml/hour

Argon Flow rate = 180 sccm, hydrogen flow rate = 15sccm

Zone I = 200°C and Zone II = 770°C

Appendix C.2 Low Pressure Thermal Chemical Vapor Deposition

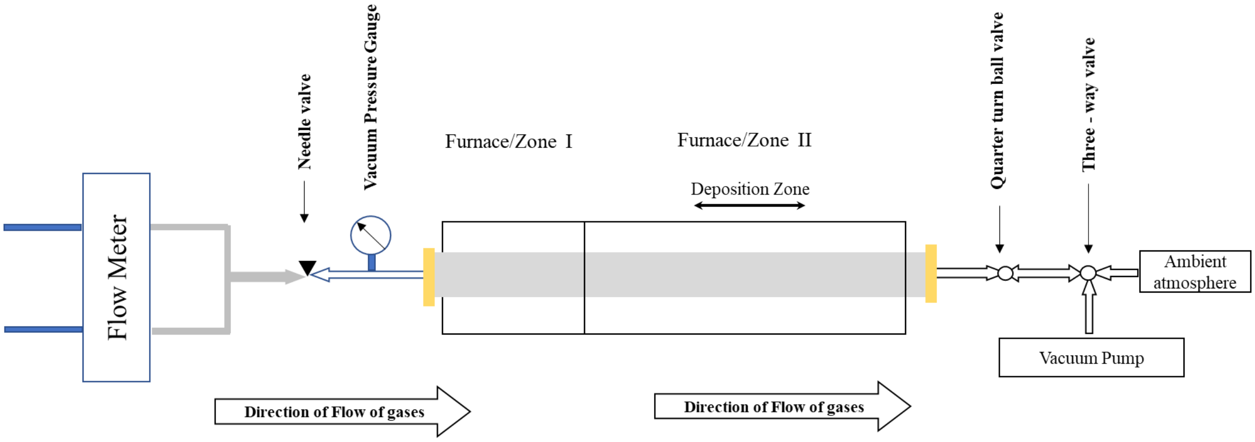

Figure 92 Schematic diagram of low - pressure thermal chemical vapor deposition set up

Foreword:

Kindly refer/study the manuals of every component of the system in case it is assembled system. Additionally, study the behavior of precursors (SDS, MSDS, OSHA, GHS, etc).

Watch/study/assimilate/practice the general operational videos related to operation of quarter turn valve, ball valve, needle valve, switching on vacuum pump, etc. separately (away from the system), before operating the system. Watch the videos from manufacturer if available and contact the manufacturer about the capabilities / compatibility of the equipment before proceeding with the process. Sometimes the manufacturer may relinquish responsibility of the gases or materials used for the system and suggest upgrading / new system / modifications. The gases are required to be vented into scrubber system installed in operational fume hood. The vacuum pump and the outlet / inlet to ambient atmosphere are required to be installed in the operational fume hood.

Additionally, please study/read the manual and identify the different parts / components of the reactor system before operating the system. The use of spontaneously pyrophoric gases (silane, etc.) at flow rates beyond 10sccm is not recommended and the use of toxic/poisonous gases (or reactor gases resulting in pyrophoric/toxic/poisonous gases as by products) is NOT AT ALL recommended for the system at NECST laboratory.

Low Pressure Chemical Vapor Deposition Procedure

1.Clean all the fittings with ethanol along with the piping to remove blockages due to previous usage. If required use high pressure air or vacuum pump to clear the blockages.

2.Close all the valves connected leading in / out to the reactor and mass flow controller before (and after) operation.

3.Load substrate material into a quartz tube.

4.Load the quartz tube into CVD system. Adjust the substrate location to match the deposition zone (center of Zone II).

5.Seal the interface of the quartz tube and metal connector by tightening the metal nuts / screw fixture / fittings at two ends of the quartz tube.

6.Gently close the lids of both the furnaces (Zone 1 and Zone 2).

7.Turn the three - way needle valve to connect/open vacuum pump/line to the quartz tube. Usually it is 90 degrees rotation angle.

8.Switch on the vacuum pump and allow the system to reach stabilization and low pressure (-30 inch vacuum pressure) and wait for 30 min.

Leak Test Procedure 1:

9.Turn off/close the entry line cut off valve (needle valve) and then turn off/close the vacuum line cut off valve (quarter turn ball valve). Switch off the vacuum pump.

10.Allow the system to rest for 5 - 6 hour and check for loss in vacuum or increase in pressure. Keep checking every 30 mins.

Note: If there is an increase in pressure, then the stainless - steel end fittings of quartz tube may have leak. Hence, tighten the screws, check for cracks in O-rings or cracks in quartz tube. There are chances for the valves to be leaking too. Depending on analysis replace the parts or consult with a certified piping / plumbing / reactor expert/professional.

11.If there is no pressure change / loss of vacuum / increase in pressure, switch on the vacuum pump (wait for 5 min)

12.Turn the three - way valve to connect the pump to the reactor (wait for 5 min)

13.Open the quarter turn valve (wait for 5 min)

14.Open the needle valve (wait for 5 min).

Leak Test Procedure 2:

15.Turn off/close the vacuum line cut off valve (quarter turn ball valve) to cut off the vacuum line.

16.Switch off the vacuum pump.

17.Allow the system to rest for 5 - 6 hour and check for loss in vacuum or increase in pressure. Keep checking every 30 mins.

Note: If there is an increase in pressure, then the flow meter to needle valve is having a leak. Depending on analysis replace the parts or consult with a certified piping / plumbing / reactor expert/professional.

18.If there is no pressure change / loss of vacuum / increase in pressure, proceed with the operation.

Operational Procedure:

19. If there is no pressure change / loss of vacuum / increase in pressure, switch on the vacuum pump (wait for 5 min)

20.Turn the three - way valve to connect the pump to the reactor (wait for 5 min)

21.Open the quarter turn valve (wait for 5 min)

22.Turn on / Open the valve of argon gas line leading to reactor mass flow controller.

23.Switch on the argon gas line on the mass flow controller and set the flow rate to required value.

24.Set furnace temperature Zone 2 to required temperature and ramp rate and switch on the furnace.

25.Allow the system to stabilize at the set temperatures and flow rate of argon (~5 – 7 hour). Keep checking every 30 mins for any fluctuations or malfunction of the furnaces and other parts.

26.Turn on / Open the valve of secondary gas line leading to reactor mass flow controller.

27.Switch on the secondary precursor gas line on the mass flow controller with preset flow rate to start the deposition.

NOTE 1: Under the circumstances that there are fumes / fire / residue / blasting / popping sound / odor in the vacuum pump or anywhere in the reactor (for example, when using pyrophoric / spontaneously combustible / poisonous gases) within 1 min of switching “ON” the gas line flowmeter follow the below steps:

a)Cut off the main inlet line of the gas (safest and most easily accessible point)

b)Leave the laboratory premises.

c)E-mail the situation to higher authorities.

d)Raise an alert to EHS.

NOTE 2: There may be detectors installed for gases, etc. However, depending on the behavior of reactants the detectors may be rendered ineffective. A detector in ambient conditions for spontaneously combustible gas may not be effective due to high reactivity of gas to form the respective by products (solid, moisture, etc) resulting in an explosion / catastrophic effect before reaching the detector installed in ambient condition.

28. After achieving the required time of deposition switch off the mass flow controller of secondary precursor gas line. Wait for 30 min for argon purging and cleaning residual precursor gas. If required, increase the argon flow rate to 300 sccm after 15min.

NOTE 1: Longer deposition times may lead to clogging of piping and valves at the outlet.

29.Switch off / shut down the furnace of Zone II with argon flow still ON and wait till temperature reaches to less than 30°C (5 – 7 hours)

30.Close the quarter turn ball valve at the exit and allow the pressure to increase to (-)15mm Hg vacuum.

31.Open the quarter turn ball valve to vacuum the reactor to (-) 30 inch vacuum pressure (for 5 mins).

32.Repeat steps 27 and 28 for 5 times.

33.Reduce the argon flow rate to 200 sccm.

34.Close the quarter turn ball valve at the exit and allow the pressure to increase to (-)15mm to (-) 10mm Hg vacuum.

35.Shut off the argon flow control and then shut off the vacuum pump.

36.Turn the three - way valve slowly to connect the reactor to ambient surrounding (non – vacuum line) to bleed so that the reactor reaches atmospheric pressure.

37.Disassemble the exit stainless steel fitting of the quartz tube and remove the sample/material from the deposition zone.

38.Switch off / turn off / close all the valves / inlets leading to the reactor.

Disclaimer: The author of this document / dissertation along with the committee is not responsible for the results and damages to the personnel / equipment / material / assets arising from the use / practice of this operational procedure. Under the circumstances that any such type of incident / event occurs the individual/organization requesting the procedure to be utilized and the laboratory executing the procedure would be liable for any kind of damages incurred. Kindly recommend the user to figure out with a law practicing individual / attorney / legal department of the organization before employing the standard operating procedure.

Parameters used for Silicon deposition on MgO template:

Argon = 180 sccm, Silane/SiH_4 = 20sccm, Temperature Zone II = 500°C, Time of deposition = 10min, 15min and 20min, weight of MgO template = 0.9 – 1.0g

Parameters used for Silicon deposition on NaCl template:

Argon = 180 sccm, Silane/SiH_4 = 20sccm, Time of deposition = 15min and 20min, weight of NaCl template = 3 grams

Length of deposition zone = 1 inch, center of the Zone II reactor.

Parameters used for CVD Si deposition of CNT (NECST - Super C Inc, E36EA0BA-F43E-4CD5-B5D3-2FFAC4698916):

Argon = 500 sccm, Silane/SiH_4 = 20sccm, Temperature Zone II = 550°C, Time = 20 min, 25 min

Appendix C.3 Plasma Enhanced Low Pressure Chemical Vapor Deposition

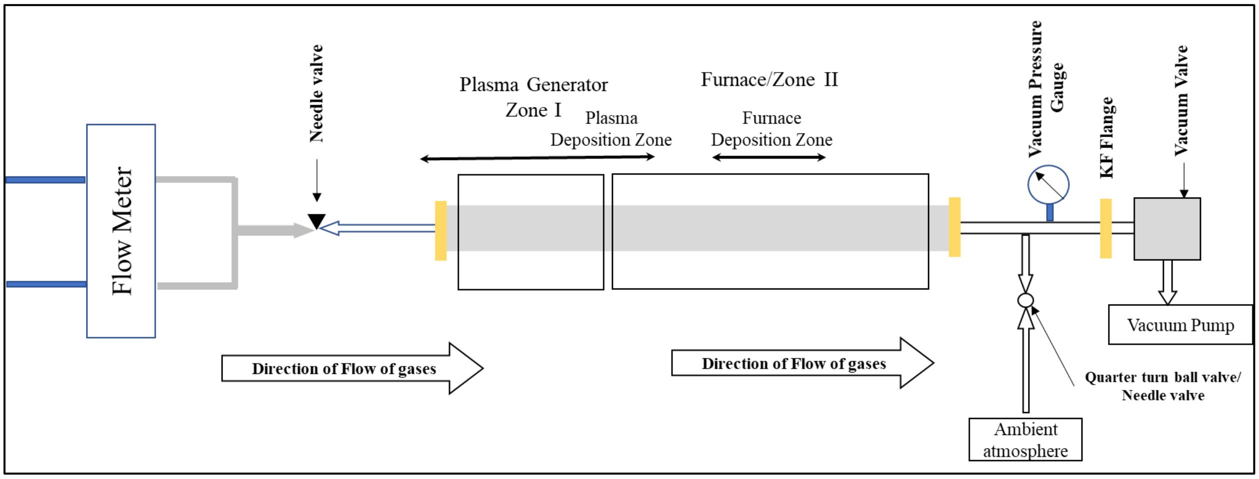

Figure 93 Schematic diagram of low - pressure thermal chemical vapor deposition set up

Foreword:

Kindly refer/study the manuals of every component of the system in case it is assembled system. Additionally, study the behavior of precursors (SDS, MSDS, OSHA, GHS, etc).

Watch/study/assimilate/practice the general operational videos related to operation of quarter turn valve, ball valve, needle valve, switching on vacuum pump, etc. separately (away from the system), before operating the system. Watch the videos from manufacturer if available and contact the manufacturer about the capabilities / compatibility of the equipment before proceeding with the process. Sometimes the manufacturer may relinquish responsibility of the gases or materials used for the system and suggest upgrading / new system / modifications. The gases are required to be vented into scrubber system installed in operational fume hood. The vacuum pump and the outlet / inlet to ambient atmosphere are required to be installed in the operational fume hood.

Additionally, please study/read the manual and identify the different parts / components of the reactor system before operating the system. The use of spontaneously pyrophoric gases (silane, etc.) at flow rates greater than 10sccm is not recommended and the use of toxic/poisonous gases (or reactor gases resulting in pyrophoric/toxic/poisonous gases as by products) is NOT AT ALL recommended for the system at NECST laboratory.

Plasma Enhanced Low Pressure Chemical Vapor Deposition Procedure

1.Clean all the end fittings with ethanol along with dismantlable piping to remove blockages due to previous usage. If required use high pressure air or vacuum pump to clear the blockages.

2.Close all the valves connected leading in / out to the reactor and mass flow controller before (and after) operation.

3.Load substrate material into a quartz tube.

4.Load the quartz tube into CVD system. Adjust the substrate location to match the deposition zone (Zone I).

5.Seal the interface of the quartz tube and metal connector by tightening the metal nuts / screw fixture / fittings at two ends of the quartz tube.

6.Gently close the lids of the furnace (Zone 2).

7.Turn on / open the vacuum valve to connect/open vacuum pump line to the quartz tube.

8.Switch on the vacuum pump and allow the system to reach stabilization and low pressure (5 to 20 mTorr) and wait for 30 min.

Leak Test Procedure 1:

9.Turn off / close the entry line cut off valve (needle valve / quarter turn valve)

10. Then turn off / close the vacuum line cut off valve (vacuum valve). Switch off the vacuum pump.

11.Allow the system to rest for 3 - 4 hour and check for loss in vacuum or increase in pressure (not to exceed 40 mTorr). Keep checking every 30 mins.

Note: If there is an increase in pressure gauge reading, then the stainless - steel end fittings of quartz tube may have leak. Hence, tighten the screws, check for cracks in O-rings or cracks in quartz tube. There are chances for the valves to be leaking too. Depending on analysis replace the parts or consult with a certified piping / plumbing / reactor expert/professional/manufacturer.

12.If there is no pressure change, switch on the vacuum pump (wait for 5 min)

13.Turn on/Open the vacuum valve to connect the pump to the reactor (wait for 5 min)

14.Turn on / Open the quarter turn valve (wait for 5 min)

15.Tun on / Open the needle valve (wait for 5 min).

Leak Test Procedure 2:

16.Turn off / close the vacuum line cut off valve (quarter turn ball valve) to cut off the vacuum line.

17.Switch off the vacuum pump.

18.Allow the system to rest for 3 - 4 hour and check for loss in vacuum or increase in pressure (not to exceed 40mTorr). Keep checking every 30 mins.

Note: If there is an increase in pressure, then the flow meter to needle valve is having a leak. Depending on analysis replace the parts or consult with a certified piping / plumbing / reactor expert/professional/manufacturer.

19.If there is no drop in pressure proceed with the operation.

Operational Procedure:

20. If there is no pressure change, switch on the vacuum pump (wait for 5 min)

21.Turn on / open the vacuum valve to connect the pump to the reactor (wait for 5 min)

22.Turn on / Open the quarter turn valve (wait for 5 min)

23.Turn on / Open the valve of argon gas line leading to reactor mass flow controller.

24.Switch on the argon gas line on the mass flow controller and set the flow rate to required value.

25.If required, set furnace temperature Zone 2 to required temperature and ramp rate and switch on the furnace (only if required). Else skip the step.

26.Allow the system to stabilize at the set temperatures and flow rate of argon (~3 – 5 hour). Keep checking every 30 mins for any fluctuations in pressure gauge or malfunction of the furnaces and other parts.

27.Set the power in RF plasma generator to required level and switch on the RF plasma generator (Zone 1) to generate plasma in the reactor. The color of plasma varies with type of gases and conditions.

Note 1: Recommend maximum power: 80% of the upper rated/value or power threshold of the generator. Additionally, try to ensure maximum decomposition of the precursor gas (when using specialty / pyrophoric gases / poisonous gases) depending on the system.

28.Wait for 10mins for the plasma to stabilize.

Note: If the plasma is fluctuating switch off the RF plasma generator. Email the authorities and if required contact the manufacturer.

29.If the plasma is stable: Turn on / open the valve of secondary gas line leading to reactor mass flow controller.

30.Switch on the secondary precursor gas line on the mass flow controller with preset flow rate to start the deposition.

NOTE 1: If the plasma is fluctuating / absent / noisy after switching on the secondary gas (when using pyrophoric, spontaneously combustible gases, poisonous gases) follow steps below:

a)Cut off the main inlet line of the gas (safest and most easily accessible point)

b)Leave the laboratory premises.

c)E-mail the situation to higher authorities.

d)Raise an alert to EHS.

NOTE 2: Under the circumstances that there are fumes / fire / residue / blasting / popping sound in the vacuum pump or anywhere in the reactor (for example, when using pyrophoric, spontaneously combustible gases / poisonous) within 1 min of switching "ON" the gas line flowmeter follow the below steps:

a)Cut off the main inlet line of the gas (safest and most easily accessible point)

b)Leave the laboratory premises.

c)E-mail the situation to higher authorities.

d)Raise an alert to EHS.

NOTE 3: There may be detectors installed for gases, etc. However, depending on the behavior of reactants the detectors may be rendered ineffective. A detector in ambient conditions for spontaneously combustible gas may not be effective due to high reactivity of gas to form the respective by products (solid, moisture, etc) resulting in an explosion / catastrophic effect before reaching the detector installed in ambient condition.

31. After achieving the required time of deposition / run time switch off the mass flow controller of secondary precursor gas line.

NOTE 1: Longer deposition times may lead to clogging of piping and valves both at the inlet and outlet.

32.Wait for 30 min for argon purging and cleaning residual precursor secondary gas. If required, increase the argon flow rate to 300 sccm after 15min while monitoring the pressure gauge at the outlet.

33.Switch off / shut down the RF generator with argon flow still ON.

34.If the Zone II furnace is used/utilized, switch off the furnace of Zone II with argon flow still ON and wait till temperature reaches to less than 30°C (3-4 hours).

35.Close the vacuum valve at the exit and allow the pressure to increase to 30 torr.

36.Open the vacuum valve to vacuum the reactor to 5 – 20 mTorr vacuum pressure (for 5 mins).

37.Repeat steps 27 and 28 for 5 times.

38.Reduce the argon flow rate to 200 sccm.

39.Close the vacuum valve at the exit and allow the pressure to increase to 100 Torr.

40.Shut off the argon flow control and then shut off the vacuum pump.

41.Turn on / Open the quarter turn valve / needle valve at exit (ambient atmosphere) slowly to connect the reactor to ambient surrounding (non – vacuum line) and to bleed air so that the reactor reaches atmospheric pressure.

42.Disassemble the stainless – steel fittings at the exit of the quartz tube and remove the sample/material from the deposition zone.

43.Switch/turn off/close all the valves / inlets leading to the reactor.

Disclaimer: The author of this document / dissertation along with the committee is not responsible for the results and damages to the personnel / equipment / material / assets arising from the use / practice of this operational procedure. Under the circumstances that any such type of incident / event occurs the individual/organization requesting the procedure to be utilized and the laboratory executing the procedure would be liable for any kind of damages incurred. Kindly recommend the user to figure out with a law practicing individual / attorney / legal department of the organization before employing the standard operating procedure.

Appendix C.4 Dual Target Torus Magnetron Sputtering Machine

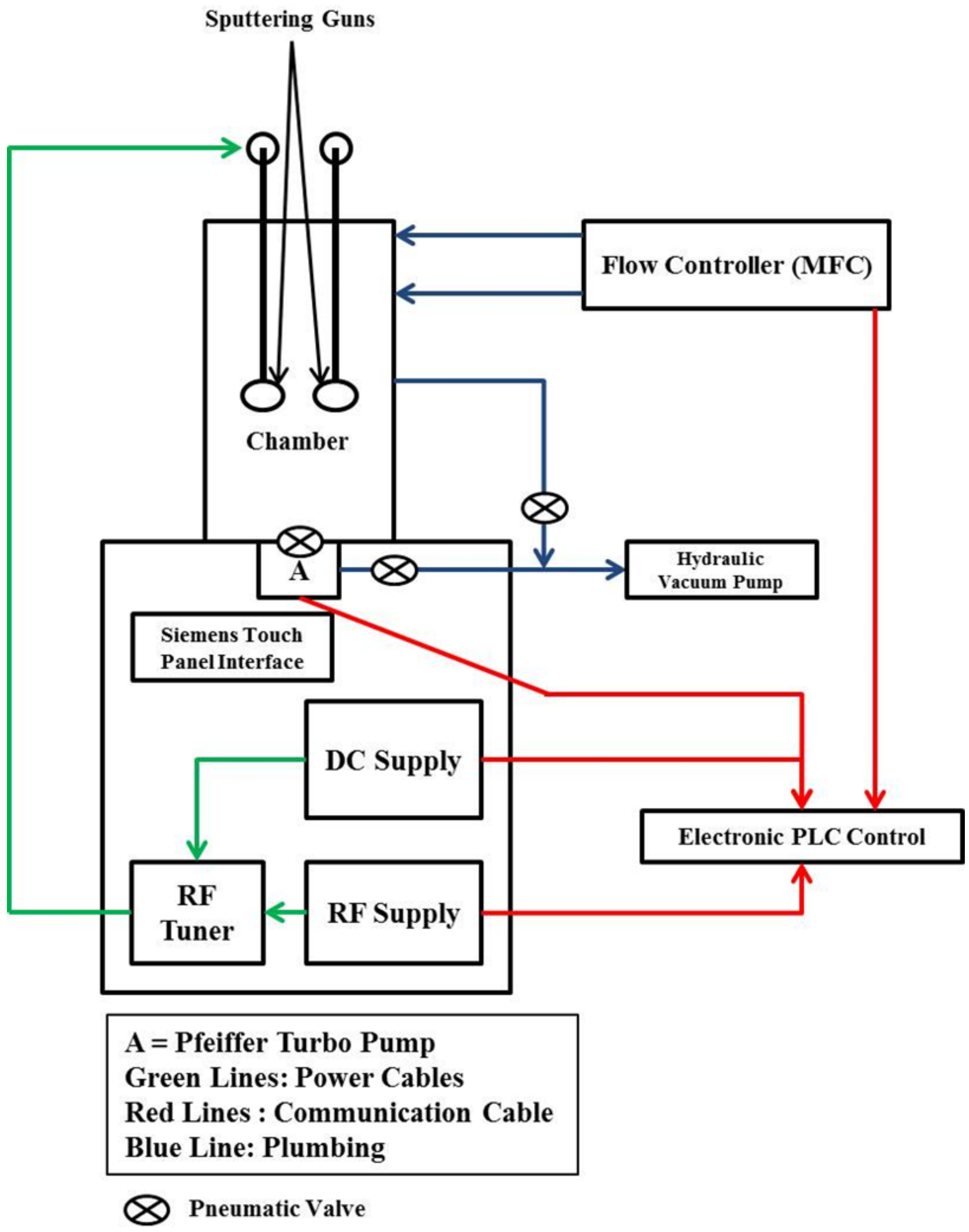

Figure 94 Schematic diagram of Dual Target Torus Magnetron DC/RF Sputtering Machine

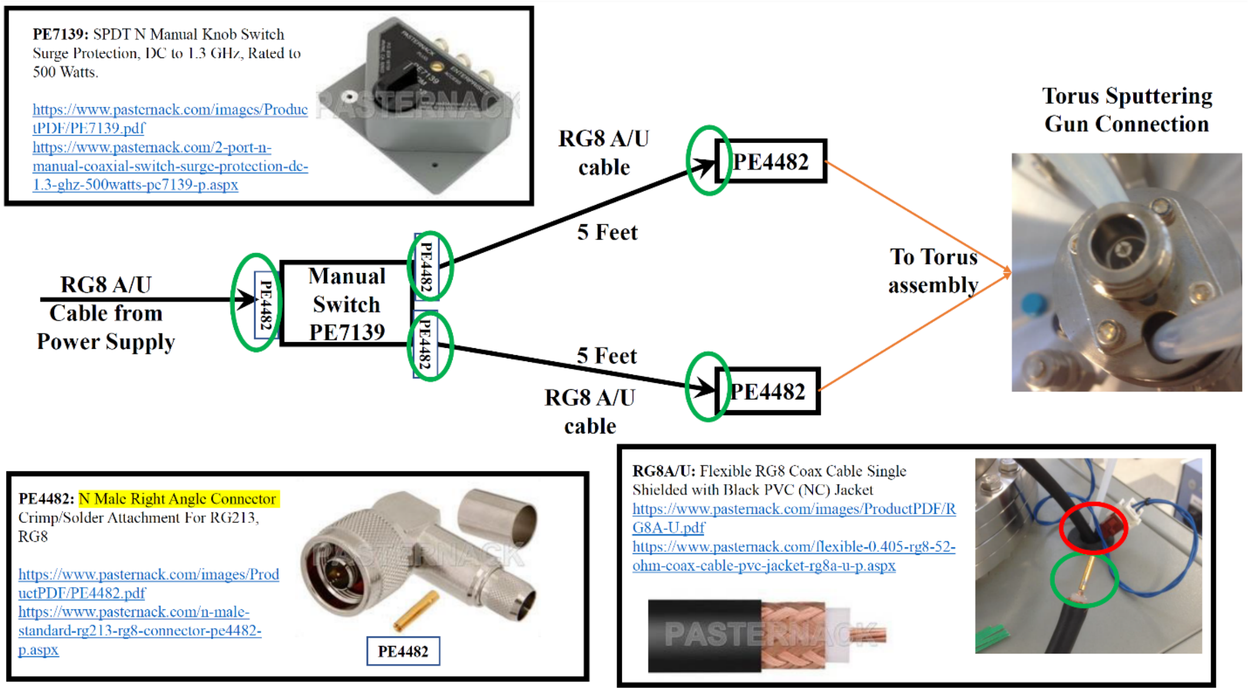

PE7139: SPDT N Manual Knob Switch Surge Protection, DC to 1.3 GHz, Rated to 500 Watts.

https://www.pasternack.com/images/ProductPDF/PE7139.pdf
https://www.pasternack.com/2-port-n-manual-coaxial-switch-surge-protection-dc-1.3-ghz-500watts-pe7139-p.aspx

PE4482: N Male Right Angle Connector Crimp/Solder Attachment For RG213, RG8

https://www.pasternack.com/images/ProductPDF/PE4482.pdf
https://www.pasternack.com/n-male-standard-rg213-rg8-connector-pe4482-p.aspx

RG8A/U: Flexible RG8 Coax Cable Single Shielded with Black PVC (NC) Jacket
https://www.pasternack.com/images/ProductPDF/RG8A-U.pdf
https://www.pasternack.com/flexible-0.405-rg8-52-ohm-coax-cable-pvc-jacket-rg8a-u-p.aspx

Figure 95 Electrical connections and upgradation set up for Dual Target TORUS Magnetron Gun

Foreword:

Kindly refer/study the manuals of every component of the system in case it is assembled system. Additionally, study the behavior of precursors (SDS, MSDS, OSHA, GHS, etc).

Watch/study/assimilate/practice the general operational videos related to operation of quarter turn valve, ball valve, needle valve, switching on vacuum pump, etc. separately (away from the system), before operating the system. Watch the videos from manufacturer if available and contact the manufacturer about the capabilities / compatibility of the equipment before proceeding with the process. Sometimes the manufacturer may relinquish responsibility of the gases or materials used for the system and suggest upgrading / new system / modifications.

Additionally, please study/read the manual and identify the different parts / components of the sputtering system before operating the system. The use of spontaneously flammable/pyrophoric gases/materials (silane, lithium, etc.) and the use of toxic/poisonous/radioactive gases (or gases/materials resulting in flammable/pyrophoric/toxic/poisonous/radioactive gases/materials as by products, especially arsenic, phosphorus, selenium, tellurium, chlorine, bromine, iodine, lanthanide, actinide series, etc. and not limited to mentioned elements) is NOT AT ALL recommended for the system at NECST laboratory.

Standard Operation Procedure: Dual Target Torus DC/RF Magnetron Sputtering

1.Open Gas 1 (Ar-inside sputtering chamber) and Gas 2 (N_2-to open the pneumatic valves, target cover opening), start vacuum pump

2.Turn on GREEN button, Navigate Screen: Menu➔ set system parameters Login: ADMIN, Password: 100

3.Check parameters in all configurations (total 16)

4.Click on: Power button on machine

5.Select Target (open valve for desired target)

6.Remove targets and substrate holder

7.Put both the targets, substrate inside the chamber

Check water level, Switch ON Water (coolant)

Close the door screw

8.Click System Overview➔ Start vacuum

CG-2: Increasing, CG-1: Decreasing via roughing pump (pressure inside chamber)

HV is closed (no vacuuming inside chamber yet)

HV opened➔ Ultra vacuuming on

<u>Leave it for ~ 30 mins</u>

CG-2: Coming/pumping down

When the frequency ~ 1200 Hz➔ Turbo Pump will start (green)

9.Manual: Green i.e. active

10.Select Target 1, check/change time for spluttering, Select DC or RF mode

11.Select the direction of Black Knob on manual Switch direction

12.Stop on Screen (can resume again by clicking Start)

13.Click Vent

14.Open the chamber door screw lock slowly

15.Power Button (red—on the machine—off)

16.Water switch off

17.Gas valves, pump closed

18.Take out substrate

Disclaimer: The author of this document / dissertation along with the committee is not responsible for the results and damages to the personnel / equipment / material / assets arising from the use / practice of this operational procedure. Under the circumstances that any such type of incident / event occurs the individual/organization requesting the procedure to be utilized and the laboratory executing the procedure would be liable for any kind of damages incurred. Kindly recommend the user to figure out with a law practicing individual / attorney / legal department of the organization before employing the standard operating procedure.

Equipment Contact:

1. Anatech USA (PLC, electronics, pneumatics, plumbing, electrical)
2. Kurt J Lesker (Chamber / Torus Magnetron sputtering guns)
3. Bharat Gattu, NECST Lab / Dept. of Chem. & Petroleum Engineering (Upgradation of system, semi – automation, connections, operation, thin film battery, solid state battery)

Bibliography

1.Winter, M.; Brodd, R. J., What Are Batteries, Fuel Cells, and Supercapacitors? *Chem. Rev.* **2004**, *104*, 4245-4269.

2.Council, N. R., *Meeting the Energy Needs of Future Warriors*; The National Academies Press: Washington, DC, 2004, p 136.

3.Chan, C. K.; Peng, H. L.; Liu, G.; McIlwrath, K.; Zhang, X. F.; Huggins, R. A.; Cui, Y., High-Performance Lithium Battery Anodes Using Silicon Nanowires. *Nat. Nanotechnol.* **2008**, *3*, 31-35.

4.Park, M.-H.; Kim, M. G.; Joo, J.; Kim, K.; Kim, J.; Ahn, S.; Cui, Y.; Cho, J., Silicon Nanotube Battery Anodes. *Nano Letters* **2009**, *9*, 3844-3847.

5.Wang, W.; Epur, R.; Kumta, P. N., Vertically Aligned Silicon/Carbon Nanotube (Vascnt) Arrays: Hierarchical Anodes for Lithium-Ion Battery. *Electrochemistry Communications* **2011**, *13*, 429-432.

6.Wang, W.; Kumta, P. N., Nanostructured Hybrid Silicon/Carbon Nanotube Heterostructures: Reversible High-Capacity Lithium-Ion Anodes. *ACS Nano* **2010**, *4*, 2233-2241.

7.Kasavajjula, U.; Wang, C.; Appleby, A. J., Nano- and Bulk-Silicon-Based Insertion Anodes for Lithium-Ion Secondary Cells. *Journal of Power Sources* **2007**, *163*, 1003-1039.

8.Cui, L. F.; Hu, L. B.; Choi, J. W.; Cui, Y., Light-Weight Free-Standing Carbon Nanotube-Silicon Films for Anodes of Lithium Ion Batteries. *Acs Nano* **2010**, *4*, 3671-3678.

9.Cui, L.-F.; Ruffo, R.; Chan, C. K.; Peng, H.; Cui, Y., Crystalline-Amorphous Core−Shell Silicon Nanowires for High Capacity and High Current Battery Electrodes. *Nano Letters* **2008**, *9*, 491-495.

10.Kim, I.; Blomgren, G. E.; Kumta, P. N., Nanostructured Si/Tib2 Composite Anodes for Li-Ion Batteries. *Electrochemical and Solid State Letters* **2003**, *6*, A157-A161.

11.Kim, I.; Kumta, P. N.; Blomgren, G. E., Si/Tin Nanocomposites - Novel Anode Materials for Li-Ion Batteries. *Electrochemical and Solid State Letters* **2000**, *3*, 493-496.

12.Kim, I. S.; Blomgren, G. E.; Kumta, P. N., Si-Sic Nanocomposite Anodes Synthesized Using High-Energy Mechanical Milling. *Journal of Power Sources* **2004**, *130*, 275-280.

13.Park, M. H.; Kim, M. G.; Joo, J.; Kim, K.; Kim, J.; Ahn, S.; Cui, Y.; Cho, J., Silicon Nanotube Battery Anodes. *Nano Letters* **2009**, *9*, 3844-3847.

14.Kim, J. W.; Sung, Y. E.; Oh, S. M., Failure Modes of Silicon Powder Negative Electrode in Lithium Secondary Batteries. *Electrochemical and solid-state letters* **2004**, *7*, A306-A309.

15.Ohara, S.; Suzuki, J. J.; Sekine, K.; Takamura, T., Attainment of High Rate Capability of Si Film as the Anode of Li-Ion Batteries. *Electrochemistry* **2003**, *71*, 1126-1128.

16.Li, X. G.; He, Y. Q.; Swihart, M. T., Surface Functionalization of Silicon Nanoparticles Produced by Laser-Driven Pyrolysis of Silane Followed by Hf-Hno3 Etching. *Langmuir* **2004**, *20*, 4720-4727.

17.Hata, K.; Yoshida, S.; Fujita, M.; Yasuda, S.; Makimura, T.; Murakami, K.; Shigekawa, H., Self-Assembled Monolayer as a Template to Deposit Silicon Nanoparticles Fabricated by Laser Ablation. *Journal of Physical Chemistry B* **2001**, *105*, 10842-10846.

18.Morisaki, H.; Hashimoto, H.; Ping, F. W.; Nozawa, H.; Ono, H., Strong Blue Light Emission from an Oxygen-Containing Si Fine Structure. *Journal of Applied Physics* **1993**, *74*, 2977-2979.

19.Okada, R.; Iijima, S., Oxidation Property of Silicon Small Particles. *Applied Physics Letters* **1991**, *58*, 1662-1663.

20.Won, C. W.; Nersisyan, H. H.; Shin, C. Y.; Lee, J. H., Porous Silicon Microparticles Synthesis by Solid Flame Technique. *Microporous and Mesoporous Materials* **2009**, *126*, 166-170.

21.Song, T., et al., Arrays of Sealed Silicon Nanotubes as Anodes for Lithium Ion Batteries. *Nano Letters* **2010**, *10*, 1710-1716.

22.Wu, H., et al., Stable Cycling of Double-Walled Silicon Nanotube Battery Anodes through Solid-Electrolyte Interphase Control. *Nat. Nanotechnol.* **2012**, *7*, 309-314.

23.Suryanarayana, C., Mechanical Alloying and Milling. *Progress in Materials Science* **2001**, *46*, 1-184.

24.Datta, M. K.; Maranchi, J.; Chung, S. J.; Epur, R.; Kadakia, K.; Jampani, P.; Kumta, P. N., Amorphous Silicon-Carbon Based Nano-Scale Thin Film Anode Materials for Lithium Ion Batteries. *Electrochimica Acta* **2011**, *56*, 4717-4723.

25.Maranchi, J. P.; Hepp, A. F.; Evans, A. G.; Nuhfer, N. T.; Kumta, P. N., Interfacial Properties of the a-Si/Cu:Active--Inactive Thin-Film Anode System for Lithium-Ion Batteries. *Journal of The Electrochemical Society* **2006**, *153*, A1246-A1253.

26.Maranchi, J. P.; Hepp, A. F.; Kumta, P. N., High Capacity, Reversible Silicon Thin-Film Anodes for Lithium-Ion Batteries. *Electrochemical and Solid State Letters* **2003**, *6*, A198-A201.

27.Epur, R.; Ramanathan, M.; Beck, F. R.; Manivannan, A.; Kumta, P. N., Electrodeposition of Amorphous Silicon Anode for Lithium Ion Batteries. *Materials Science and Engineering B-Advanced Functional Solid-State Materials* **2012**, *177*, 1151-1156.

28.Sepahvand, V.; Komai, T.; Momtazi, F.; Shahabi, S., A New Species of the Ghost Shrimp Genus Neocallichirus Sakai, 1988 from Iran, and New Record of N. Manningi Kazmi & Kazmi, 1992 (Decapoda: Axiidea: Callianassidae). *Zootaxa* **2018**, *4527*, 239-254.

29.Meunier, V.; Kephart, J.; Roland, C.; Bernholc, J., Ab Initio Investigations of Lithium Diffusion in Carbon Nanotube Systems. *Physical Review Letters* **2002**, *88*.

30.Yu, M. F.; Files, B. S.; Arepalli, S.; Ruoff, R. S., Tensile Loading of Ropes of Single Wall Carbon Nanotubes and Their Mechanical Properties. *Physical Review Letters* **2000**, *84*, 5552-5555.

31.Epur, R.; Datta, M. K.; Kumta, P. N., Nanoscale Engineered Electrochemically Active Silicon-Cnt Heterostructures-Novel Anodes for Li-Ion Application. *Electrochimica Acta* **2012**, *85*, 680-684.

32.Whittingham, M. S., Electrical Energy Storage and Intercalation Chemistry. *Science* **1976**, *192*, 1126-1127.

33.Yoshio, M.; Brodd, R. J.; Kozawa, A., *Lithium-Ion Batteries: Science and Technologies*; Springer, 2010.

34.Aurbach, D.; Zinigrad, E.; Teller, H.; Dan, P., Factors Which Limit the Cycle Life of Rechargeable Lithium (Metal) Batteries. *Journal of The Electrochemical Society* **2000**, *147*, 1274-1279.

35.Dan, P.; Mengeritsky, E.; Aurbach, D.; Weissman, I.; Zinigrad, E., More Details on the New Limno2 Rechargeable Battery Technology Developed at Tadiran. *Journal of Power Sources* **1997**, *68*, 443-447.

36.Agarwal, R. R., Phase Changes and Diffusivity in the Carbon-Lithium Electrode. *Journal of Power Sources* **1989**, *25*, 151-158.

37.Mizushima, K.; Jones, P. C.; Wiseman, P. J.; Goodenough, J. B., Lixcoo2 (0≪X≪-1): A New Cathode Material for Batteries of High Energy Density. *Materials Research Bulletin* **1980**, *15*, 783-789.

38.Nazri, G.-A. P., Gianfranco, *Lithium Batteries: Science and Technology*, 2004.

39.Peljo, P.; Girault, H. H., Electrochemical Potential Window of Battery Electrolytes: The Homo–Lumo Misconception. *Energy & Environmental Science* **2018**, *11*, 2306-2309.

40.Skare, M. Project Thesis - Coated Silicon Nanoparticles as Anode in Lithium Ion Batteries. 2016.

41.Tarascon, J. M.; Armand, M., Issues and Challenges Facing Rechargeable Lithium Batteries. *Nature* **2001**, *414*, 359-67.

42.http://www.mpoweruk.com/images/pouch.gif.

43.Whittingham, M. S., Electrochemical Characteristics of Vse2 in Lithium Cells. *Materials Research Bulletin* **1978**, *13*, 959-965.

44.Murphy, D. W.; Trumbore, F. A., The Chemistry of Tis3 and Nbse3 Cathodes. *Journal of The Electrochemical Society* **1976**, *123*, 960-964.

45.Trumbore, F. A., Niobium Triselenide - a Unique Rechargeable Positive Electrode Material. *Journal of Power Sources* **1989**, *26*, 65-75.

46.Fenton, D. E.; Parker, J. M.; Wright, P. V., Complexes of Alkali-Metal Ions with Poly(Ethylene Oxide). *Polymer* **1973**, *14*, 589-589.

47.Oradd, G.; Edman, L.; Ferry, A., Diffusion: A Comparison between Liquid and Solid Polymer Litfsi Electrolytes. *Solid State Ionics* **2002**, *152*, 131-136.

48.Hagman, L. O.; Kierkega.P, Crystal Structure of Name2 4(Po4)3 - Me4 =Ge Ti Zr. *Acta Chemica Scandinavica* **1968**, *22*, 1822-&.

49.Aono, H.; Sugimoto, E.; Sadaoka, Y.; Imanaka, N.; Adachi, G.-y., Electrical Property and Sinterability of Liti2(Po4)3 Mixed with Lithium Salt (Li3po4 or Li3bo3). *Solid State Ionics* **1991**, *47*, 257-264.

50.Sloop, S. E.; Pugh, J. K.; Wang, S.; Kerr, J. B.; Kinoshita, K., Chemical Reactivity of Pf5 and Lipf6 in Ethylene Carbonate/Dimethyl Carbonate Solutions. *Electrochemical and Solid State Letters* **2001**, *4*, A42-A44.

51.Vogdanis, L.; Martens, B.; Uchtmann, H.; Hensel, F.; Heitz, W., Synthetic and Thermodynamic Investigations in the Polymerization of Ethylene Carbonate. *Makromolekulare Chemie-Macromolecular Chemistry and Physics* **1990**, *191*, 465-472.

52.Chakraborty, A.; Dixit, M.; Aurbach, D.; Major, D. T., Predicting Accurate Cathode Properties of Layered Oxide Materials Using the Scan Meta-Gga Density Functional. *npj Computational Materials* **2018**, *4*, 60.

53.Shao-Horn, Y.; Croguennec, L.; Delmas, C.; Nelson, E. C.; O'Keefe, M. A., Atomic Resolution of Lithium Ions in Licoo2. *Nature Materials* **2003**, *2*, 464-467.

54.Dahn, J. R.; Vonsacken, U.; Juzkow, M. W.; Aljanaby, H., Rechargeable Linio2 Carbon Cells. *Journal of The Electrochemical Society* **1991**, *138*, 2207-2211.

55.Broussely, M.; Perton, F.; Labat, J.; Staniewicz, R. J.; Romero, A., Li/Lixnio2 and Li/Lixcoo2 Rechargeable Systems - Comparative-Study and Performance of Practical Cells. *Journal of Power Sources* **1993**, *43*, 209-216.

56.Rougier, A.; Gravereau, P.; Delmas, C., Optimization of the Composition of the Li1-Zni1+Zo2 Electrode Materials: Structural, Magnetic, and Electrochemical Studies. *Journal of The Electrochemical Society* **1996**, *143*, 1168-1175.

57.Fan, L.-Z.; Wang, X.-L.; Long, F.; Wang, X., Enhanced Ionic Conductivities in Composite Polymer Electrolytes by Using Succinonitrile as a Plasticizer. *Solid State Ionics* **2008**, *179*, 1772-1775.

58.Itoh, T.; Hirai, K.; Uno, T.; Kubo, M., Solid Polymer Electrolytes Based on Squaric Acid Structure. *Ionics* **2008**, *14*, 1-6.

59.Pitawala, H. M. J. C.; Dissanayake, M. A. K. L.; Seneviratne, V. A.; Mellander, B. E.; Albinson, I., Effect of Plasticizers (Ec or Pc) on the Ionic Conductivity and Thermal Properties of the (Peo)9litf: Al2o3 Nanocomposite Polymer Electrolyte System. *J Solid State Electrochem* **2008**, *12*, 783-789.

60.Raghavan, P.; Zhao, X.; Kim, J.-K.; Manuel, J.; Chauhan, G. S.; Ahn, J.-H.; Nah, C., Ionic Conductivity and Electrochemical Properties of Nanocomposite Polymer Electrolytes Based on Electrospun Poly(Vinylidene Fluoride-Co-Hexafluoropropylene) with Nano-Sized Ceramic Fillers. *Electrochimica Acta* **2008**, *54*, 228-234.

61.Thackeray, M. M.; David, W. I. F.; Bruce, P. G.; Goodenough, J. B., Lithium Insertion into Manganese Spinels. *Materials Research Bulletin* **1983**, *18*, 461-472.

62.Thackeray, M. M.; Johnson, P. J.; Depicciotto, L. A.; Bruce, P. G.; Goodenough, J. B., Electrochemical Extraction of Lithium from Limn2o4. *Materials Research Bulletin* **1984**, *19*, 179-187.

63.Amatucci, G.; Tarascon, J. M., Optimization of Insertion Compounds Such as Limn2o4 for Li-Ion Batteries. *Journal of The Electrochemical Society* **2002**, *149*, K31-K46.

64.Dahn, J. R.; Sleigh, A. K.; Shi, H.; Reimers, J. N.; Zhong, Q.; Way, B. M., Dependence of the Electrochemical Intercalation of Lithium in Carbons on the Crystal-Structure of the Carbon. *Electrochimica Acta* **1993**, *38*, 1179-1191.

65.Gasparou.H, Modification of Magnetic Properties of Graphite by Creation of Rhomboedral Sequences. *Carbon* **1967**, *5*, 441-&.

66.Tran, T.; Kinoshita, K., Lithium Intercalation Deintercalation Behavior of Basal and Edge Planes of Highly Oriented Pyrolytic-Graphite and Graphite Powder. *Journal of Electroanalytical Chemistry* **1995**, *386*, 221-224.

67.Thackeray, M. M., Manganese Oxides for Lithium Batteries. *Progress in Solid State Chemistry* **1997**, *25*, 1-71.

68.Tu, X. Y.; Shu, K. Y., X-Ray Diffraction Study on Phase Transition of Orthorhombic Limno2 in Electrochemical Conversions. *J Solid State Electrochem* **2008**, *12*, 245-249.

69.Yoshio, M.; Xia, Y.; Kumada, N.; Ma, S., Storage and Cycling Performance of Cr-Modified Spinel at Elevated Temperatures. *Journal of Power Sources* **2001**, *101*, 79-85.

70.Li, G. H.; Ikuta, H.; Uchida, T.; Wakihara, M., The Spinel Phases Lim(Y)Mn(2-Y)O(4) (M=Co,Cr,Ni) as the Cathode for Rechargeable Lithium Batteries. *Journal of The Electrochemical Society* **1996**, *143*, 178-182.

71.Robertson, A. D.; Lu, S. H.; Averill, W. F.; Howard, W. F., M3+-Modified Limn2o4 Spinel Intercalation Cathodes .1. Admetal Effects on Morphology and Electrochemical Performance. *Journal of The Electrochemical Society* **1997**, *144*, 3500-3505.

72.Tarascon, J. M.; Wang, E.; Shokoohi, F. K.; McKinnon, W. R.; Colson, S., The Spinel Phase of Limn2o4 as a Cathode in Secondary Lithium Cells. *Journal of The Electrochemical Society* **1991**, *138*, 2859-2864.

73.Xun, S.; Song, X.; Grass, M. E.; Roseguo, D. K.; Liu, Z.; Battaglia, V. S.; Liu, G., Improved Initial Performance of Si Nanoparticles by Surface Oxide Reduction for Lithium-Ion Battery Application. *Electrochemical and Solid State Letters* **2011**, *14*, A61-A63.

74.Hu, Y. S.; Demir-Cakan, R.; Titirici, M. M.; Muller, J. O.; Schlogl, R.; Antonietti, M.; Maier, J., Superior Storage Performance of a Si@Siox/C Nanocomposite as Anode Material for Lithium-Ion Batteries. *Angew. Chem.-Int. Edit.* **2008**, *47*, 1645-1649.

75.Nadimpalli, S. P. V.; Sethuraman, V. A.; Dalavi, S.; Lucht, B.; Chon, M. J.; Shenoy, V. B.; Guduru, P. R., Quantifying Capacity Loss Due to Solid-Electrolyte-Interphase Layer Formation on Silicon Negative Electrodes in Lithium-Ion Batteries. *Journal of Power Sources* **2012**, *215*, 145-151.

76.Zhang, W.-J., A Review of the Electrochemical Performance of Alloy Anodes for Lithium-Ion Batteries. *Journal of Power Sources* **2011**, *196*, 13-24.

77.Yen, Y.-C.; Chao, S.-C.; Wu, H.-C.; Wu, N.-L., Study on Solid-Electrolyte-Interphase of Si and C-Coated Si Electrodes in Lithium Cells. *Journal of The Electrochemical Society* **2009**, *156*, A95-A102.

78.Winter, M.; Besenhard, J. O.; Spahr, M. E.; Novak, P., Insertion Electrode Materials for Rechargeable Lithium Batteries. *Adv Mater* **1998**, *10*, 725-763.

79.Choi, N. S.; Yew, K. H.; Lee, K. Y.; Sung, M.; Kim, H.; Kim, S. S., Effect of Fluoroethylene Carbonate Additive on Interfacial Properties of Silicon Thin-Film Electrode. *Journal of Power Sources* **2006**, *161*, 1254-1259.

80.Dalavi, S.; Guduru, P.; Lucht, B. L., Performance Enhancing Electrolyte Additives for Lithium Ion Batteries with Silicon Anodes. *Journal of The Electrochemical Society* **2012**, *159*, A642-A646.

81.Li, H.; Huang, X.; Chen, L.; Wu, Z.; Liang, Y., A High Capacity Nano - Si Composite Anode Material for Lithium Rechargeable Batteries. *Electrochemical and Solid-state letters* **1999**, *2*, 547-549.

82.Guo, Z. P.; Wang, J. Z.; Liu, H. K.; Dou, S. X., Study of Silicon/Polypyrrole Composite as Anode Materials for Li-Ion Batteries. *Journal of Power Sources* **2005**, *146*, 448-451.

83.Padhi, A. K.; Nanjundaswamy, K. S.; Goodenough, J. B., Phospho-Olivines as Positive-Electrode Materials for Rechargeable Lithium Batteries. *Journal of The Electrochemical Society* **1997**, *144*, 1188-1194.

84.Whittingham, M. S., Lithium Batteries and Cathode Materials. *Chem. Rev.* **2004**, *104*, 4271-4301.

85.Morgan, D.; Van der Ven, A.; Ceder, G., Li Conductivity in Lixmpo4 (M = Mn, Fe, Co, Ni) Olivine Materials. *Electrochemical and Solid State Letters* **2004**, *7*, A30-A32.

86.Funabiki, A.; Inaba, M.; Ogumi, Z., Ac Impedance Analysis of Electrochemical Lithium Intercalation into Highly Oriented Pyrolytic Graphite. *Journal of Power Sources* **1997**, *68*, 227-231.

87.Song, X. Y.; Kinoshita, K.; Tran, T. D., Microstructural Characterization of Lithiated Graphite. *Journal of The Electrochemical Society* **1996**, *143*, L120-L123.

88.Chung, S. Y.; Bloking, J. T.; Chiang, Y. M., Electronically Conductive Phospho-Olivines as Lithium Storage Electrodes. *Nature Materials* **2002**, *1*, 123-128.

89.Fong, R.; von Sacken, U.; Dahn, J. R., Studies of Lithium Intercalation into Carbons Using Nonaqueous Electrochemical Cells. *Journal of The Electrochemical Society* **1990**, *137*, 2009-2013.

90.Dahn, J. R., Phase Diagram of Li_xc_6. *Physical Review B* **1991**, *44*, 9170-9177.

91.Chen, Z. H.; Dahn, J. R., Reducing Carbon in Lifepo4/C Composite Electrodes to Maximize Specific Energy, Volumetric Energy, and Tap Density. *Journal of The Electrochemical Society* **2002**, *149*, A1184-A1189.

92.Besenhard, J. O.; Fritz, H. P., Cathodic Reduction of Graphite in Organic Solutions of Alkali and Nr4+ Salts. *Journal of Electroanalytical Chemistry and Interfacial Electrochemistry* **1974**, *53*, 329-333.

93.Winter, M.; Novák, P.; Monnier, A., Graphites for Lithium-Ion Cells: The Correlation of the First-Cycle Charge Loss with the Brunauer-Emmett-Teller Surface Area. *Journal of The Electrochemical Society* **1998**, *145*, 428-436.

94.Prosini, P. P.; Zane, D.; Pasquali, M., Improved Electrochemical Performance of a Lifepo4-Based Composite Cathode. *Electrochimica Acta* **2001**, *46*, 3517-3523.

95.Kang, B.; Ceder, G., Battery Materials for Ultrafast Charging and Discharging. *Nature* **2009**, *458*, 190-193.

96.Xu, K., Nonaqueous Liquid Electrolytes for Lithium-Based Rechargeable Batteries. *Chem. Rev.* **2004**, *104*, 4303-4417.

97.Huggins, R. A., *Advanced Batteries : Materials Science Aspects*; Springer, 2009.

98.Yao, N. P.; Heredy, L. A.; Saunders, R. C., Emf Measurements of Electrochemically Prepared Lithium-Aluminum Alloy. *Journal of The Electrochemical Society* **1971**, *118*, 1039-&.

99.Martino, F. J.; Vissers, D. R.; Mrazek, F. C.; Shimotake, H., Effects of Metal Additives on Lifetime and Performance of Li-Al-M/Fesx Cells. *Journal of The Electrochemical Society* **1977**, *124*, C274-C274.

100.Foster, M. S.; Croutham.Ce; Wood, S. E., Thermodynamics of Binary Alloys .2. Lithium-Tin System. *Journal of Physical Chemistry* **1966**, *70*, 3042-&.

101.Wen, C. J.; Huggins, R. A., Chemical Diffusion in Intermediate Phases in the Lithium-Tin System. *Journal of Solid State Chemistry* **1980**, *35*, 376-384.

102.Wen, C. J.; Huggins, R. A., Thermodynamic Study of the Lithium-Tin System. *Journal of The Electrochemical Society* **1981**, *128*, 1181-1187.

103.Tedmon, C. S.; Hagel, W. C., Electrochemical Formation of Lithium Alloys from Molten Lithium Fluoride. *Journal of The Electrochemical Society* **1968**, *115*, 151-&.

104.Gleiter, H., Nanocrystalline Materials. *Progress in Materials Science* **1989**, *33*, 223-315.

105.Johnson, C. E.; Foster, M. S., Phase Equilibrium Studies of Lithium Halide-Containing Electrolytes. *Journal of The Electrochemical Society* **1969**, *116*, 1612-&.

106.Jiang, J. W.; Fortier, H.; Reimers, J. N.; Dahn, J. R., Thermal Stability of 18650 Size Li-Ion Cells Containing Libob Electrolyte Salt. *Journal of The Electrochemical Society* **2004**, *151*, A609-A613.

107.Weppner, W.; Huggins, R. A., Determination of Kinetic-Parameters of Mixed-Conducting Electrodes and Application to System Li3sb. *Journal of The Electrochemical Society* **1977**, *124*, 1569-1578.

108.Weppner, W.; Huggins, R. A., Electrochemical Investigation of Chemical Diffusion, Partial Ionic Conductivities, and Other Kinetic-Parameters in Li3sb and Li3bi. *Journal of Solid State Chemistry* **1977**, *22*, 297-308.

109.Xu, K., Nonaqueous Liquid Electrolytes for Lithium-Based Rechargeable Batteries. *Chem. Rev.* **2004**, *104*, 4303-4418.

110.Lai, S. C., Solid Lithium-Silicon Electrode. *Journal of The Electrochemical Society* **1976**, *123*, 1196-1197.

111.Sharma, R. A.; Seefurth, R. N., Thermodynamic Properties of Lithium-Silicon System. *Journal of The Electrochemical Society* **1976**, *123*, 1763-1768.

112.Wen, C. J.; Huggins, R. A., Chemical Diffusion in Intermediate Phases in the Lithium-Silicon System. *Journal of Solid State Chemistry* **1981**, *37*, 271-278.

113.Winter, M.; Besenhard, J. O., Electrochemical Lithiation of Tin and Tin-Based Intermetallics and Composites. *Electrochimica Acta* **1999**, *45*, 31-50.

114.Yang, J.; Winter, M.; Besenhard, J. O., Small Particle Size Multiphase Li-Alloy Anodes for Lithium-Ion-Batteries. *Solid State Ionics* **1996**, *90*, 281-287.

115.Besenhard, J. O.; Yang, J.; Winter, M., Will Advanced Lithium-Alloy Anodes Have a Chance in Lithium-Ion Batteries? *Journal of Power Sources* **1997**, *68*, 87-90.

116.Matsuda, Y.; Nakashima, H.; Morita, M.; Takasu, Y., Behavior of Some Ions in Mixed Organic Electrolytes of High-Energy Density Batteries. *Journal of The Electrochemical Society* **1981**, *128*, 2552-2556.

117.Mao, O.; Turner, R. L.; Courtney, I. A.; Fredericksen, B. D.; Buckett, M. I.; Krause, L. J.; Dahn, J. R., Active/Inactive Nanocomposites as Anodes for Li-Ion Batteries. *Electrochemical and Solid State Letters* **1999**, *2*, 3-5.

118.Mao, O.; Dahn, J. R., Mechanically Alloyed Sn-Fe(-C) Powders as Anode Materials for Li-Ion Batteries - Ii. The Snfe System. *Journal of The Electrochemical Society* **1999**, *146*, 414-422.

119.Mao, O.; Dunlap, R. A.; Courtney, I. A.; Dahn, J. R., In Situ Mossbauer Effect Studies of the Electrochemical Reaction of Lithium with Mechanically Alloyed Sn2fe. *Journal of The Electrochemical Society* **1998**, *145*, 4195-4202.

120.Mao, O.; Dunlap, R. A.; Dahn, J. R., Mechanically Alloyed Sn-Fe(-C) Powders as Anode Materials for Li-Ion Batteries - I. The Sn2fe-C System. *Journal of The Electrochemical Society* **1999**, *146*, 405-413.

121.Mao, O.; Dahn, J. R., Mechanically Alloyed Sn-Fe(-C) Powders as Anode Materials for Li-Ion Batteries - Iii. Sn2fe : Snfe3c Active/Inactive Composites. *Journal of The Electrochemical Society* **1999**, *146*, 423-427.

122.Boukamp, B. A.; Lesh, G. C.; Huggins, R. A., All-Solid Lithium Electrodes with Mixed-Conductor Matrix. *Journal of The Electrochemical Society* **1981**, *128*, 725-729.

123.Aurbach, D.; Gamolsky, K.; Markovsky, B.; Gofer, Y.; Schmidt, M.; Heider, U., On the Use of Vinylene Carbonate (Vc) Electrolyte Solutions for Li-Ion as an Additive to Batteries. *Electrochimica Acta* **2002**, *47*, 1423-1439.

124.Li, J.; Dahn, J. R., An in Situ X-Ray Diffraction Study of the Reaction of Li with Crystalline Si. *Journal of The Electrochemical Society* **2007**, *154*, A156-A161.

125.Ryu, J. H.; Kim, J. W.; Sung, Y. E.; Oh, S. M., Failure Modes of Silicon Powder Negative Electrode in Lithium Secondary Batteries. *Electrochemical and Solid State Letters* **2004**, *7*, A306-A309.

126.Beaulieu, L. Y.; Eberman, K. W.; Turner, R. L.; Krause, L. J.; Dahn, J. R., Colossal Reversible Volume Changes in Lithium Alloys. *Electrochemical and Solid State Letters* **2001**, *4*, A137-A140.

127.Ulus, A.; Rosenberg, Y.; Burstein, L.; Peled, E., Tin Alloy-Graphite Composite Anode for Lithium-Ion Batteries. *Journal of The Electrochemical Society* **2002**, *149*, A635-A643.

128.Atthipalli, G.; Epur, R.; Kumta, P. N.; Allen, B. L.; Tang, Y.; Star, A.; Gray, J. L., The Effect of Temperature on the Growth of Carbon Nanotubes on Copper Foil Using a Nickel Thin Film as Catalyst. *Thin Solid Films* **2011**, *519*, 5371-5375.

129.Atthipalli, G.; Epur, R.; Kumta, P. N.; Yang, M. J.; Lee, J. K.; Gray, J. L., Nickel Catalyst-Assisted Vertical Growth of Dense Carbon Nanotube Forests on Bulk Copper. *Journal of Physical Chemistry C* **2011**, *115*, 3534-3538.

130.Pedrosa, V. A.; Epur, R.; Benton, J.; Overfelt, R. A.; Simonian, A. L., Copper Nanoparticles and Carbon Nanotubes-Based Electrochemical Sensing System for Fast Identification of Tricresyl-Phosphate in Aqueous Samples and Air. *Sensors and Actuators B-Chemical* **2009**, *140*, 92-97.

131.Jampani, P. H.; Kadakia, K.; Hong, D. H.; Epur, R.; Poston, J. A.; Manivannan, A.; Kumta, P. N., Cvd Derived Vanadium Oxide Nano-Sphere-Carbon Nanotube (Cnt) Nano-Composite Hetero-Structures: High Energy Supercapacitors. *Journal of The Electrochemical Society* **2013**, *160*, A1118-A1127.

132.Toyoura, K.; Koyama, Y.; Kuwabara, A.; Oba, F.; Tanaka, I., First-Principles Approach to Chemical Diffusion of Lithium Atoms in a Graphite Intercalation Compound. *Physical Review B* **2008**, *78*, 214303.

133.Telling, R. H.; Heggie, M. I., Stacking Fault and Dislocation Glide on the Basal Plane of Graphite. *Philosophical Magazine Letters* **2003**, *83*, 411-421.

134.Warren, B. E., X-Ray Diffraction Study of Carbon Black. *The Journal of Chemical Physics* **1934**, *2*, 551-555.

135.Besenhard, J. O.; Fritz, H. P., The Electrochemistry of Black Carbons. *Angewandte Chemie International Edition in English* **1983**, *22*, 950-975.

136.Allart, D.; Montaru, M.; Gualous, H., Model of Lithium Intercalation into Graphite by Potentiometric Analysis with Equilibrium and Entropy Change Curves of Graphite Electrode. *Journal of The Electrochemical Society* **2018**, *165*, A380-A387.

137.Kanno, R.; Kawamoto, Y.; Takeda, Y.; Ohashi, S.; Imanishi, N.; Yamamoto, O., Carbon Fiber as a Negative Electrode in Lithium Secondary Cells. *Journal of The Electrochemical Society* **1992**, *139*, 3397-3404.

138.Fong, R.; Vonsacken, U.; Dahn, J. R., Studies of Lithium Intercalation into Carbons Using Nonaqueous Electrochemical-Cells. *Journal of The Electrochemical Society* **1990**, *137*, 2009-2013.

139.Yamada, Y.; Yamada, A., Review—Superconcentrated Electrolytes for Lithium Batteries. *Journal of The Electrochemical Society* **2015**, *162*, A2406-A2423.

140.Idota, Y. 5478671, 1995.

141.Shen, C.; Ge, M.; Luo, L.; Fang, X.; Liu, Y.; Zhang, A.; Rong, J.; Wang, C.; Zhou, C., In Situ and Ex Situ Tem Study of Lithiation Behaviours of Porous Silicon Nanostructures. *Scientific Reports* **2016**, *6*, 31334.

142.Huggins, R. A.; Nix, W. D., Decrepitation Model for Capacity Loss During Cycling of Alloys in Rechargeable Electrochemical Systems. *Ionics* **2000**, *6*, 57-63.

143.Liu, X. H.; Zhong, L.; Huang, S.; Mao, S. X.; Zhu, T.; Huang, J. Y., Size-Dependent Fracture of Silicon Nanoparticles During Lithiation. *Acs Nano* **2012**, *6*, 1522-1531.

144.Mayo, M. J., High and Low Temperature Superplasticity in Nanocrystalline Materials. *Nanostructured Materials* **1997**, *9*, 717-726.

145.Yoshio, M. B., Ralph. J; Kozawa Akiya, *Lithium-Ion Batteries: Science and Technologies*; Springer, 2009, p 452.

146.Lee, J. K.; Oh, C.; Kim, N.; Hwang, J.-Y.; Sun, Y.-K., Rational Design of Silicon-Based Composites for High-Energy Storage Devices. *Journal of Materials Chemistry A* **2016**, *4*, 5366-5384.

147.van der Marel, C.; Vinke, G. J. B.; van der Lugt, W., The Phase Diagram of the System Lithium-Silicon. *Solid State Communications* **1985**, *54*, 917-919.

148.Okamoto, H., Li-Si (Lithium-Silicon). *J. Phase Equilib. Diffus.* **2009**, *30*, 118-119.

149.Radvanyi, E.; Porcher, W.; De Vito, E.; Montani, A.; Franger, S.; Jouanneau Si Larbi, S., Failure Mechanisms of Nano-Silicon Anodes Upon Cycling: An Electrode Porosity Evolution Model. *Physical Chemistry Chemical Physics* **2014**, *16*, 17142-17153.

150.Kim, H.; Seo, M.; Park, M.-H.; Cho, J., A Critical Size of Silicon Nano-Anodes for Lithium Rechargeable Batteries. *Angewandte Chemie International Edition* **2010**, *49*, 2146-2149.

151.Xun, S.; Song, X.; Wang, L.; Grass, M. E.; Liu, Z.; Battaglia, V. S.; Liu, G., The Effects of Native Oxide Surface Layer on the Electrochemical Performance of Si Nanoparticle-Based Electrodes. *Journal of the Electrochemical Society* **2011**, *158*, A1260-A1266.

152.Nadimpalli, S. P. V.; Sethuraman, V. A.; Dalavi, S.; Lucht, B.; Chon, M. J.; Shenoy, V. B.; Guduru, P. R., Quantifying Capacity Loss Due to Solid-Electrolyte-Interphase Layer Formation on Silicon Negative Electrodes in Lithium-Ion Batteries. *Journal of Power Sources* **2012**, *215*, 145-151.

153.Huang, Q.; Loveridge, M. J.; Genieser, R.; Lain, M. J.; Bhagat, R., Electrochemical Evaluation and Phase-Related Impedance Studies on Silicon–Few Layer Graphene (Flg) Composite Electrode Systems. *Scientific Reports* **2018**, *8*, 1386.

154.Chen, L. B.; Wang, K.; Xie, X. H.; Xie, J. Y., Effect of Vinylene Carbonate (Vc) as Electrolyte Additive on Electrochemical Performance of Si Film Anode for Lithium Ion Batteries. *Journal of Power Sources* **2007**, *174*, 538-543.

155.Peled, E., The Electrochemical Behavior of Alkali and Alkaline Earth Metals in Nonaqueous Battery Systems—the Solid Electrolyte Interphase Model. *Journal of The Electrochemical Society* **1979**, *126*, 2047-2051.

156.Peled, E.; Golodnitsky, D.; Ardel, G., Advanced Model for Solid Electrolyte Interphase Electrodes in Liquid and Polymer Electrolytes. *Journal of The Electrochemical Society* **1997**, *144*, L208-L210.

157.Ein-Eli, Y., A New Perspective on the Formation and Structure of the Solid Electrolyte Interface at the Graphite Anode of Li-Ion Cells. *Electrochemical and Solid-State Letters* **1999**, *2*, 212.

158.Kanamura, K.; Tamura, H.; Shiraishi, S.; Takehara, Z. i., Xps Analysis of Lithium Surfaces Following Immersion in Various Solvents Containing Libf4. *Journal of The Electrochemical Society* **1995**, *142*, 340-347.

159.Kanamura, K.; Shiraishi, S.; Takehara, Z. i., Electrochemical Deposition of Very Smooth Lithium Using Nonaqueous Electrolytes Containing Hf. *Journal of The Electrochemical Society* **1996**, *143*, 2187-2197.

160.Ein-Eli, Y.; McDevitt, S. F.; Laura, R., The Superiority of Asymmetric Alkyl Methyl Carbonates. *Journal of The Electrochemical Society* **1998**, *145*, L1-L3.

161.Li, C.; Shi, T.; Li, D.; Yoshitake, H.; Wang, H., Effect of Surface Modification on Electrochemical Performance of Nano-Sized Si as an Anode Material for Li-Ion Batteries. *RSC Advances* **2016**, *6*, 34715-34723.

162.Yang, J.; Winter, M.; Besenhard, J. O., Small Particle Size Multiphase Li-Alloy Anodes for Lithium-Ionbatteries. *Solid State Ionics* **1996**, *90*, 281-287.

163.Yang, J.; Takeda, Y.; Imanishi, N.; Ichikawa, T.; Yamamoto, O., Snsbx-Based Composite Electrodes for Lithium Ion Cells. *Solid State Ionics* **2000**, *135*, 175-180.

164.Fan, Q.; Chupas, P. J.; Whittingham, M. S., Characterization of Amorphous and Crystalline Tin-Cobalt Anodes. *Electrochemical and Solid State Letters* **2007**, *10*, A274-A278.

165.Wilson, A. M.; Reimers, J. N.; Fuller, E. W.; Dahn, J. R., Lithium Insertion in Pyrolyzed Siloxane Polymers. *Solid State Ionics* **1994**, *74*, 249-254.

166.Nagao, Y.; Sakaguchi, H.; Honda, H.; Fukunaga, T.; Esaka, T., Structural Analysis of Pure and Electrochemically Lithiated Sio Using Neutron Elastic Scattering. *Journal of The Electrochemical Society* **2004**, *151*, A1572-A1575.

167.Li, H.; Huang, X. J.; Chen, L. Q.; Zhou, G. W.; Zhang, Z.; Yu, D. P.; Mo, Y. J.; Pei, N., The Crystal Structural Evolution of Nano-Si Anode Caused by Lithium Insertion and Extraction at Room Temperature. *Solid State Ionics* **2000**, *135*, 181-191.

168.Yang, J.; Takeda, Y.; Imanishi, N.; Capiglia, C.; Xie, J. Y.; Yamamoto, O., Siox-Based Anodes for Secondary Lithium Batteries. *Solid State Ionics* **2002**, *152*, 125-129.

169.Datta, M. K.; Kumta, P. N., Silicon and Carbon Based Composite Anodes for Lithium Ion Batteries. *Journal of Power Sources* **2006**, *158*, 557-563.

170.Wilson, A. M.; Zank, G.; Eguchi, K.; Xing, W.; Dahn, J. R., Pyrolysed Silicon-Containing Polymers as High Capacity Anodes for Lithium-Ion Batteries. *Journal of Power Sources* **1997**, *68*, 195-200.

171.Xing, W.; Wilson, A. M.; Zank, G.; Dahn, J. R., Pyrolysed Pitch-Polysilane Blends for Use as Anode Materials in Lithium Ion Batteries. *Solid State Ionics* **1997**, *93*, 239-244.

172.Larcher, D.; Mudalige, C.; George, A. E.; Porter, V.; Gharghouri, M.; Dahn, J. R., Si-Containing Disordered Carbons Prepared by Pyrolysis of Pitch/Polysilane Blends: Effect of Oxygen and Sulfur. *Solid State Ionics* **1999**, *122*, 71-83.

173.Hayes, S. E.; Eckert, H.; Even, W. R.; Guidotti, R., Structural and Electrochemical Characterization of Glassy Carbon Prepared from Silicon-Doped Polymethacrylonitrile/Divinylbenzene Copolymer. *Journal of The Electrochemical Society* **1999**, *146*, 2435-2442.

174.Xue, J. S.; Myrtle, K.; Dahn, J. R., An Epoxy-Silane Approach to Prepare Anode Materials for Rechargeable Lithium Ion Batteries. *Journal of The Electrochemical Society* **1995**, *142*, 2927-2935.

175.Holzapfel, M.; Buqa, H.; Krumeich, F.; Novák, P.; Petrat, F.-M.; Veit, C., Chemical Vapor Deposited Silicon⁄Graphite Compound Material as Negative Electrode for Lithium-Ion Batteries. *Electrochemical and Solid-state letters* **2005**, *8*, A516-A520.

176.Wang, W.; Datta, M. K.; Kumta, P. N., Silicon-Based Composite Anodes for Li-Ion Rechargeable Batteries. *J. Mater. Chem.* **2007**, *17*, 3229-3237.

177.Cui, L. F.; Ruffo, R.; Chan, C. K.; Peng, H. L.; Cui, Y., Crystalline-Amorphous Core-Shell Silicon Nanowires for High Capacity and High Current Battery Electrodes. *Nano Letters* **2009**, *9*, 491-495.

178.Graetz, J.; Ahn, C. C.; Yazami, R.; Fultz, B., Highly Reversible Lithium Storage in Nanostructured Silicon. *Electrochemical and Solid State Letters* **2003**, *6,* A194-A197.

179.Wang, W.; Kumta, P. N., Reversible High Capacity Nanocomposite Anodes of Si/C/Swnts for Rechargeable Li-Ion Batteries. *Journal of Power Sources* **2007**, *172*, 650-658.

180.Huang, R.; Fan, X.; Shen, W. C.; Zhu, J., Carbon-Coated Silicon Nanowire Array Films for High-Performance Lithium-Ion Battery Anodes. *Applied Physics Letters* **2009**, *95*.

181.Chen, H. X.; Xiao, Y.; Wang, L.; Yang, Y., Silicon Nanowires Coated with Copper Layer as Anode Materials for Lithium-Ion Batteries. *Journal of Power Sources* **2011**, *196*, 6657-6662.

182.Thess, A., et al., Crystalline Ropes of Metallic Carbon Nanotubes. *Science* **1996**, *273*, 483-487.

183.Evanoff, K.; Khan, J.; Balandin, A. A.; Magasinski, A.; Ready, W. J.; Fuller, T. F.; Yushin, G., Towards Ultrathick Battery Electrodes: Aligned Carbon Nanotube - Enabled Architecture. *Adv Mater* **2012**, *24*, 533-+.

184.Magasinski, A.; Dixon, P.; Hertzberg, B.; Kvit, A.; Ayala, J.; Yushin, G., High-Performance Lithium-Ion Anodes Using a Hierarchical Bottom-up Approach. *Nature Materials* **2010**, *9*, 353-358.

185.Krishnan, R.; Lu, T. M.; Koratkar, N., Functionally Strain-Graded Nanoscoops for High Power Li-Ion Battery Anodes. *Nano Letters* **2011**, *11*, 377-384.

186.Zhou, S.; Liu, X. H.; Wang, D. W., Si/Tisi2 Heteronanostructures as High-Capacity Anode Material for Li Ion Batteries. *Nano Letters* **2010**, *10*, 860-863.

187.Yao, Y.; Huo, K. F.; Hu, L. B.; Liu, N. A.; Ha, J. J.; McDowell, M. T.; Chu, P. K.; Cui, Y., Highly Conductive, Mechanically Robust, and Electrochemically Inactive Tic/C Nanofiber Scaffold for High-Performance Silicon Anode Batteries. *Acs Nano* **2011**, *5*, 8346-8351.

188.Liu, N.; Wu, H.; McDowell, M. T.; Yao, Y.; Wang, C.; Cui, Y., A Yolk-Shell Design for Stabilized and Scalable Li-Ion Battery Alloy Anodes. *Nano Letters* **2012**, *12*, 3315-3321.

189.Li, W. Z.; Liang, C. H.; Zhou, W. J.; Qiu, J. S.; Zhou, Z. H.; Sun, G. Q.; Xin, Q., Preparation and Characterization of Multiwalled Carbon Nanotube-Supported Platinum for Cathode Catalysts of Direct Methanol Fuel Cells. *Journal of Physical Chemistry B* **2003**, *107*, 6292-6299.

190.Serp, P.; Corrias, M.; Kalck, P., Carbon Nanotubes and Nanofibers in Catalysis. *Applied Catalysis a-General* **2003**, *253*, 337-358.

191.Wildgoose, G. G.; Banks, C. E.; Compton, R. G., Metal Nanopartictes and Related Materials Supported on Carbon Nanotubes: Methods and Applications. *Small* **2006**, *2*, 182-193.

192.Du, C. S.; Pan, N., High Power Density Supercapacitor Electrodes of Carbon Nanotube Films by Electrophoretic Deposition. *Nanotechnology* **2006**, *17*, 5314-5318.

193.Obreja, V. V. N., On the Performance of Supercapacitors with Electrodes Based on Carbon Nanotubes and Carbon Activated Material - a Review. *Physica E-Low-Dimensional Systems & Nanostructures* **2008**, *40*, 2596-2605.

194.Wang, G. X.; Zhang, B. L.; Yu, Z. L.; Qu, M. Z., Manganese Oxide/Mwnts Composite Electrodes for Supercapacitors. *Solid State Ionics* **2005**, *176*, 1169-1174.

195.Evanoff, K.; Khan, J.; Balandin, A. A.; Magasinski, A.; Ready, W. J.; Fuller, T. F.; Yushin, G., Towards Ultrathick Battery Electrodes: Aligned Carbon Nanotube – Enabled Architecture. *Adv Mater* **2012**, *24*, 533-537.

196.Besteman, K.; Lee, J. O.; Wiertz, F. G. M.; Heering, H. A.; Dekker, C., Enzyme-Coated Carbon Nanotubes as Single-Molecule Biosensors. *Nano Letters* **2003**, *3*, 727-730.

197.Kong, J.; Chapline, M. G.; Dai, H. J., Functionalized Carbon Nanotubes for Molecular Hydrogen Sensors. *Adv Mater* **2001**, *13*, 1384-1386.

198.Wang, J., Carbon-Nanotube Based Electrochemical Biosensors: A Review. *Electroanalysis* **2005**, *17*, 7-14.

199.Kumar, M.; Ando, Y., Chemical Vapor Deposition of Carbon Nanotubes: A Review on Growth Mechanism and Mass Production. *Journal of nanoscience and nanotechnology* **2010**, *10*, 3739-3758.

200.Curry, C., *Bloomberg*.

201.Safarabadi, A. M.; Abbaszadeh, S.; Sepahvand, H.; Ebrahimi, F., An Overview of the Important Analgesic Herbs in Iran. *Anaesth Pain Intensi* **2018**, *22*, 522-528.

202.Davarnejad, R.; Pishdad, R.; Sepahvand, S., Dye Adsorption on the Blends of Saffron Petals Powder with Activated Carbon: Response Surface Methodology. *Int J Eng-Iran* **2018**, *31*, 2001-2008.

203.Ev Everywhere Grand Challange. Energy, D. o., Ed. https://www.energy.gov/sites/prod/files/2014/02/f8/eveverywhere_blueprint.pdf, 2013.

204.Chan, C. K.; Peng, H.; Liu, G.; McIlwrath, K.; Zhang, X. F.; Huggins, R. A.; Cui, Y., High-Performance Lithium Battery Anodes Using Silicon Nanowires. *Nat. Nanotechnol.* **2008**, *3*, 31-5.

205.Cui, L.-F.; Ruffo, R.; Chan, C. K.; Peng, H.; Cui, Y., Crystalline-Amorphous Core−Shell Silicon Nanowires for High Capacity and High Current Battery Electrodes. *Nano Letters* **2009**, *9*, 491-495.

206.Datta, M. K.; Kumta, P. N., In Situ Electrochemical Synthesis of Lithiated Silicon–Carbon Based Composites Anode Materials for Lithium Ion Batteries. *Journal of Power Sources* **2009**, *194*, 1043-1052.

207.David, L.; Asok, D.; Singh, G., Synthesis and Extreme Rate Capability of Si–Al–C–N Functionalized Carbon Nanotube Spray-on Coatings as Li-Ion Battery Electrode. *ACS Applied Materials & Interfaces* **2014**, *6*, 16056-16064.

208.Epur, R.; Datta, M. K.; Kumta, P. N., Nanoscale Engineered Electrochemically Active Silicon–Cnt Heterostructures-Novel Anodes for Li-Ion Application. *Electrochimica Acta* **2012**, *85*, 680-684.

209.Evanoff, K.; Benson, J.; Schauer, M.; Kovalenko, I.; Lashmore, D.; Ready, W. J.; Yushin, G., Ultra Strong Silicon-Coated Carbon Nanotube Nonwoven Fabric as a Multifunctional Lithium-Ion Battery Anode. *ACS Nano* **2012**, *6*, 9837-9845.

210.Song, T., et al., Arrays of Sealed Silicon Nanotubes as Anodes for Lithium Ion Batteries. *Nano Letters* **2010**, *10*, 1710-1716.

211.Wu, H., et al., Stable Cycling of Double-Walled Silicon Nanotube Battery Anodes through Solid-Electrolyte Interphase Control. *Nat Nano* **2012**, *7*, 310-315.

212.Yao, Y.; McDowell, M. T.; Ryu, I.; Wu, H.; Liu, N.; Hu, L.; Nix, W. D.; Cui, Y., Interconnected Silicon Hollow Nanospheres for Lithium-Ion Battery Anodes with Long Cycle Life. *Nano Letters* **2011**, *11*, 2949-2954.

213.Chou, S. L.; Zhao, Y.; Wang, J. Z.; Chen, Z. X.; Liu, H. K.; Dou, S. X., Silicon/Single-Walled Carbon Nanotube Composite Paper as a Flexible Anode Material for Lithium Ion Batteries. *Journal of Physical Chemistry C* **2010**, *114*, 15862-15867.

214.Palomino, J.; Varshney, D.; Weiner, B. R.; Morell, G., Study of the Structural Changes Undergone by Hybrid Nanostructured Si-Cnts Employed as an Anode Material in a Rechargeable Lithium-Ion Battery. *Journal of Physical Chemistry C* **2015**, *119*, 21125-21134.

215.Lu, Z.; Wong, T.; Ng, T.-W.; Wang, C., Facile Synthesis of Carbon Decorated Silicon Nanotube Arrays as Anode Material for High-Performance Lithium-Ion Batteries. *RSC Advances* **2014**, *4*, 2440-2446.

216.Epur, R.; Hanumantha, P. J.; Datta, M. K.; Hong, D.; Gattu, B.; Kumta, P. N., A Simple and Scalable Approach to Hollow Silicon Nanotube (H-Sint) Anode Architectures of Superior Electrochemical Stability and Reversible Capacity. *Journal of Materials Chemistry A* **2015**, *3*, 11117-11129.

217.Zhong, Y.; Yue, C.; Chen, B. B.; Sun, S. B.; Zheng, M. S.; Zhao, L. B.; Wu, S. T.; Li, J.; Kang, J. Y.; Lin, L. W., Synthetic Preparation of Novel 3d Si/Tio2-Ti2o3 Composite Nanorod Arrays as Anodes in Lithium Ion Batteries. *Rsc Advances* **2015**, *5*, 37399-37404.

218.Yu, Y. J.; Yue, C.; Sun, S. B.; Lin, W.; Su, H.; Xu, B. B.; Li, J. T.; Wu, S. T.; Li, J.; Kang, J. Y., The Effects of Different Core-Shell Structures on the Electrochemical Performances of Si-Ge Nanorod Arrays as Anodes for Micro-Lithium Ion Batteries. *Acs Applied Materials & Interfaces* **2014**, *6*, 5884-5890.

219.Yue, C.; Yu, Y. J.; Yin, J.; Wong, T. L.; Zang, Y. S.; Li, J.; Kang, J. Y., Fabrication of 3d Hexagonal Bottle-Like Si-Sno2 Core-Shell Nanorod Arrays as Anode Material in on Chip Micro-Lithium-Ion-Batteries. *Journal of Materials Chemistry A* **2013**, *1*, 7896-7904.

220.Kim, S. Y.; Ostadhossein, A.; van Duin, A. C. T.; Xiao, X. C.; Gao, H. J.; Qi, Y., Self-Generated Concentration and Modulus Gradient Coating Design to Protect Si Nano-Wire Electrodes During Lithiation. *Physical Chemistry Chemical Physics* **2016**, *18*, 3706-3715.

221.Cho, Y. J.; Kim, H. S.; Im, H.; Myung, Y.; Jung, G. B.; Lee, C. W.; Park, J.; Park, M. H.; Cho, J.; Kang, H. S., Nitrogen-Doped Graphitic Layers Deposited on Silicon Nanowires for Efficient Lithium-Ion Battery Anodes. *Journal of Physical Chemistry C* **2011**, *115*, 9451-9457.

222.Chowdhury, C.; Karmakar, S.; Datta, A., Capping Black Phosphorene by H-Bn Enhances Performances in Anodes for Li and Na Ion Batteries. *Acs Energy Lett* **2016**, *1*, 253-259.

223.Karmakar, S.; Chowdhury, C.; Datta, A., Two-Dimensional Group Iv Monochalcogenides: Anode Materials for Li-Ion Batteries. *Journal of Physical Chemistry C* **2016**, *120*, 14522-14530.

224.Al-Hazmi, F.; Alnowaiser, F.; Al-Ghamdi, A. A.; Al-Ghamdi, A. A.; Aly, M. M.; Al-Tuwirqi, R. M.; El-Tantawy, F., A New Large – Scale Synthesis of Magnesium Oxide Nanowires: Structural and Antibacterial Properties. *Superlattices and Microstructures* **2012**, *52*, 200-209.

225.S.M.Scholz; J.Dutta; H.Hofmann; H.Hofmeister, Raman Spectroscopic Study of Silicon Nanopowders. *J. Mater. Sci. Technol.* **1997**, *13*, 327-332.

226.Vink, R. L. C.; Barkema, G. T.; van der Weg, W. F., Raman Spectra and Structure of Amorphous Si. *Physical Review B* **2001**, *63*, 115210.

227.Parker, J. H.; Feldman, D. W.; Ashkin, M., Raman Scattering by Silicon and Germanium. *Physical Review* **1967**, *155*, 712-714.

228.Smit, C.; van Swaaij, R. A. C. M. M.; Donker, H.; Petit, A. M. H. N.; Kessels, W. M. M.; van de Sanden, M. C. M., Determining the Material Structure of Microcrystalline Silicon from Raman Spectra. *Journal of Applied Physics* **2003**, *94*, 3582-3588.

229.Datta, M. K.; Maranchi, J.; Chung, S. J.; Epur, R.; Kadakia, K.; Jampani, P.; Kumta, P. N., Amorphous Silicon–Carbon Based Nano-Scale Thin Film Anode Materials for Lithium Ion Batteries. *Electrochimica Acta* **2011**, *56*, 4717-4723.

230.Epur, R.; Minardi, L.; Datta, M. K.; Chung, S. J.; Kumta, P. N., A Simple Facile Approach to Large Scale Synthesis of High Specific Surface Area Silicon Nanoparticles. *Journal of Solid State Chemistry* **2013**, *208*, 93-98.

231.Lu, X. T.; Bogart, T. D.; Gu, M.; Wang, C. M.; Korgel, B. A., In Situ Tem Observations of Sn-Containing Silicon Nanowires Undergoing Reversible Pore Formation Due to Fast Lithiation/Delithiation Kinetics. *Journal of Physical Chemistry C* **2015**, *119*, 21889-21895.

232.Lu, X. T.; He, Y.; Mao, S. X.; Wang, C. M.; Korgel, B. A., Size Dependent Pore Formation in Germanium Nanowires Undergoing Reversible Delithiation Observed by in Situ Tem. *Journal of Physical Chemistry C* **2016**, *120*, 28825-28831.

233.Brug, G. J.; van den Eeden, A. L. G.; Sluyters-Rehbach, M.; Sluyters, J. H., The Analysis of Electrode Impedances Complicated by the Presence of a Constant Phase Element. *Journal of Electroanalytical Chemistry and Interfacial Electrochemistry* **1984**, *176*, 275-295.

234.Germain, P. S.; Pell, W. G.; Conway, B. E., Evaluation and Origins of the Difference between Double-Layer Capacitance Behaviour at Au-Metal and Oxidized Au Surfaces. *Electrochimica Acta* **2004**, *49*, 1775-1788.

235.Aurbach, D., Review of Selected Electrode–Solution Interactions Which Determine the Performance of Li and Li Ion Batteries. *Journal of Power Sources* **2000**, *89*, 206-218.

236.Wang, B. B.; Jin, P.; Yue, Y. Z.; Ji, S. D.; Li, Y. M.; Luo, H. J., Synthesis of Nacl Single Crystals with Defined Morphologies as Templates for Fabricating Hollow Nano/Micro-Structures. *RSC Advances* **2015**, *5*, 5072-5076.

237.Liu, R.; Yang, S. C.; Wang, F.; Lu, X. G.; Yang, Z. M.; Ding, B. J., Sodium Chloride Template Synthesis of Cubic Tin Dioxide Hollow Particles for Lithium Ion Battery Applications. *Acs Applied Materials & Interfaces* **2012**, *4*, 1537-1542.

238.Xiao, X., et al., Scalable Salt-Templated Synthesis of Two-Dimensional Transition Metal Oxides. *Nat Commun* **2016**, *7*.

239.Fan, X.; Jiang, X. P.; Wang, W.; Liu, Z. P., Green Synthesis of Nanoporous Si/C Anode Using Nacl Template with Improved Cycle Life. *Mater Lett* **2016**, *180*, 109-113.

240.Grass, R. N.; Stark, W. J., Flame Synthesis of Calcium-, Strontium-, Barium Fluoride Nanoparticles and Sodium Chloride. *Chemical Communications (Cambridge, United Kingdom)* **2005**, 1767-1769.

241.Halim, S. C., Application of Reactive and Partly Soluble Nanomaterials. *Doctoral Thesis* **2008**.

242.S.M.Scholz; J.Dutta; H.Hofmann; H.Hofmeister, Raman Spectroscopic Study of Silicon Nanopowders. *J. Mater. Sci. Technol. (Shenyang, China)* **1997**, *13*, 327-332.

243.Breaux, G. A.; Benirschke, R. C.; Jarrold, M. F., Melting, Freezing, Sublimation, and Phase Coexistence in Sodium Chloride Nanocrystals. *J Chem Phys* **2004**, *121*, 6502-6507.

244.Kana, N.; Khamlich, S.; Kana, J. B. K.; Maaza, M., Peculiar Surface Size-Effects in Nacl Nano-Crystals. *Surf Rev Lett* **2013**, *20*.

245.Sang, L. V.; Huong, T. T. T.; Minh, L. N. T., Molecular Dynamics Simulations of the Melting of Kcl Nanoparticles. *Eur Phys J D* **2014**, *68*.

246.Sharma, S.; Sunkara, M. K., Direct Synthesis of Single-Crystalline Silicon Nanowires Using Molten Gallium and Silane Plasma. *Nanotechnology* **2004**, *15*, 130-134.

247.Chen, L.; Lu, W.; Lieber, C. M., Chapter 1 Semiconductor Nanowire Growth and Integration. In *Semiconductor Nanowires: From Next-Generation Electronics to Sustainable Energy*, The Royal Society of Chemistry: 2015; pp 1-53.

248.Choi, H.-J., Vapor–Liquid–Solid Growth of Semiconductor Nanowires. In *Semiconductor Nanostructures for Optoelectronic Devices: Processing, Characterization and Applications*, Yi, G.-C., Ed. Springer Berlin Heidelberg: Berlin, Heidelberg, 2012; pp 1-36.

249.Schmidt, V. Silicon Nanowires: Synthesis, Fundamental Issues, and a First Device. PhD Thesis, The Martin Luther University, Halle-Wittenberg, 2006.

250.Conesa-Boj, S.; Dunand, S.; Russo-Averchi, E.; Heiss, M.; Ruffer, D.; Wyrsch, N.; Ballif, C.; Morral, A. F. I., Hybrid Axial and Radial Si-Gaas Heterostructures in Nanowires. *Nanoscale* **2013**, *5*, 9633-9639.

251.Gattu, B.; Epur, R.; Datta, M. K.; Manivannan, A.; Kumta, P. N., Pulse Electrodeposition of Amorphous Si Film Anodes for Li-Ion Battery. *ECS Meeting Abstracts* **2014**, *MA2014-01*, 502.

252.Gattu, B.; Epur, R.; Shanti, P.; Jampani, P.; Kuruba, R.; Datta, M.; Manivannan, A.; Kumta, P., Pulsed Current Electrodeposition of Silicon Thin Films Anodes for Lithium Ion Battery Applications. *Inorganics* **2017**, *5*, 27.

253.Obrovac, M. N.; Christensen, L., Structural Changes in Silicon Anodes During Lithium Insertion/Extraction. *Electrochemical and Solid State Letters* **2004**, *7*, A93-A96.

254.Gattu, B.; Epur, R.; Jampani, P. H.; Kuruba, R.; Datta, M. K.; Kumta, P. N., Silicon-Carbon Core-Shell (C@Si@C) Hollow Nanotubular Configuration - High Performance Lithium-Ion Anodes. *The Journal of Physical Chemistry C* **2017**.

255.Xu, Q.; Li, J. Y.; Yin, Y. X.; Kong, Y. M.; Guo, Y. G.; Wan, L. J., Nano/Micro-Structured Si/C Anodes with High Initial Coulombic Efficiency in Li-Ion Batteries. *Chem-Asian J* **2016**, *11*, 1205-1209.

256.Wu, L. L.; Yang, J.; Zhou, X. Y.; Zhang, M. F.; Ren, Y. P.; Nie, Y., Silicon Nanoparticles Embedded in a Porous Carbon Matrix as a High-Performance Anode for Lithium-Ion Batteries. *Journal of Materials Chemistry A* **2016**, *4*, 11381-11387.

257.Li, W. Y.; Tang, Y. B.; Kang, W. P.; Zhang, Z. Y.; Yang, X.; Zhu, Y.; Zhang, W. J.; Lee, C. S., Core-Shell Si/C Nanospheres Embedded in Bubble Sheet-Like Carbon Film with Enhanced Performance as Lithium Ion Battery Anodes. *Small* **2015**, *11*, 1345-1351.

258.Zhang, Y. C.; You, Y.; Xin, S.; Yin, Y. X.; Zhang, J.; Wang, P.; Zheng, X. S.; Cao, F. F.; Guo, Y. G., Rice Husk-Derived Hierarchical Silicon/Nitrogen-Doped Carbon/Carbon Nanotube Spheres as Low-Cost and High-Capacity Anodes for Lithium-Ion Batteries. *Nano Energy* **2016**, *25*, 120-127.

259.Yin, Y. X.; Xin, S.; Wan, L. J.; Li, C. J.; Guo, Y. G., Electrospray Synthesis of Silicon/Carbon Nanoporous Microspheres as Improved Anode Materials for Lithium-Ion Batteries. *Journal of Physical Chemistry C* **2011**, *115*, 14148-14154.

260.Xu, Q.; Li, J. Y.; Sun, J. K.; Yin, Y. X.; Wan, L. J.; Guo, Y. G., Watermelon-Inspired Si/C Microspheres with Hierarchical Buffer Structures for Densely Compacted Lithium-Ion Battery Anodes. *Adv Energy Mater* **2017**, *7*.

261.Zhou, X. S.; Wan, L. J.; Guo, Y. G., Electrospun Silicon Nanoparticle/Porous Carbon Hybrid Nanofibers for Lithium-Ion Batteries. *Small* **2013**, *9*, 2684-2688.

262.Chen, X. L.; Gerasopoulos, K.; Guo, J. C.; Brown, A.; Wang, C. S.; Ghodssi, R.; Culver, J. N., A Patterned 3d Silicon Anode Fabricated by Electrodeposition on a Virus-Structured Current Collector. *Adv Funct Mater* **2011**, *21*, 380-387.

263.Gobet, J.; Tannenberger, H., Electrodeposition of Silicon from a Nonaqueous Solvent. *Journal of The Electrochemical Society* **1988**, *135*, 109-112.

264.Munisamy, T.; Bard, A. J., Electrodeposition of Si from Organic Solvents and Studies Related to Initial Stages of Si Growth. *Electrochimica Acta* **2010**, *55*, 3797-3803.

265.Nicholson, J. P., Electrodeposition of Silicon from Nonaqueous Solvents. *Journal of The Electrochemical Society* **2005**, *152*, C795-C802.

266.Nishimura, Y.; Fukunaka, Y., Electrochemical Reduction of Silicon Chloride in a Non-Aqueous Solvent. *Electrochimica Acta* **2007**, *53*, 111-116.

267.Agrawal, A. K.; Austin, A. E., Electrodeposition of Silicon from Solutions of Silicon Halides in Aprotic Solvents. *Journal of The Electrochemical Society* **1981**, *128*, 2292-2296.

268.Zein El Abedin, S.; Borissenko, N.; Endres, F., Electrodeposition of Nanoscale Silicon in a Room Temperature Ionic Liquid. *Electrochem. Commun.* **2004**, *6*, 510-514.

269.Schmuck, M.; Balducci, A.; Rupp, B.; Kern, W.; Passerini, S.; Winter, M., Alloying of Electrodeposited Silicon with Lithium—a Principal Study of Applicability as Anode Material for Lithium Ion Batteries. *J Solid State Electrochem* **2010**, *14*, 2203-2207.

270.Sharma, A.; Bhattacharya, S.; Das, S.; Das, K., A Study on the Effect of Pulse Electrodeposition Parameters on the Morphology of Pure Tin Coatings. *Metallurgical and Materials Transactions A* **2014**, *45*, 4610-4622.

271.Rezaei-Sameti, M.; Nadali, S.; Rajabi, J.; Rakhshi, M., The Effects of Pulse Electrodeposition Parameters on Morphology, Hardness and Wear Behavior of Nano-Structure Cr–Wc Composite Coatings. *Journal of Molecular Structure* **2012**, *1020*, 23-27.

272.Gummow, R. J.; He, Y., Morphology and Preferred Orientation of Pulse Electrodeposited Magnesium. *Journal of The Electrochemical Society* **2010**, *157*, E45-E49.

273.Tury, B., A Study on Pulse Electrodeposition of Ni-Co Alloys: Physical and Electrochemical Characterisation. **2006**.

274.Song, T.; Li, D. Y., Tribological, Mechanical and Electrochemical Properties of Nanocrystalline Copper Deposits Produced by Pulse Electrodeposition. *Nanotechnology* **2006**, *17*, 65.

275.Nee, C. C.; Kim, W.; Weil, R., Pulsed Electrodeposition of Ni-Mo Alloys. *Journal of The Electrochemical Society* **1988**, *135*, 1100-1103.

276.Boonyongmaneerat, Y.; Saengkiettiyut, K.; Saenapitak, S.; Sangsuk, S., Corrosion Behavior of Reverse-Pulse Electrodeposited Zn-Ni Alloys in Saline Environment. *Journal of Materials Engineering and Performance* **2014**, *23*, 302-307.

277.Ul-Hamid, A.; Dafalla, H.; Quddus, A.; Saricimen, H.; Al-Hadhrami, L. M., Microstructure and Surface Mechanical Properties of Pulse Electrodeposited Nickel. *Applied Surface Science* **2011**, *257*, 9251-9259.

278.Minakshi, M., Examining Manganese Dioxide Electrode in Koh Electrolyte Using Tem Technique. *Journal of Electroanalytical Chemistry* **2008**, *616*, 99-106.

279.Osaka, T.; Nara, H.; Momma, T.; Yokoshima, T., New Si-O-C Composite Film Anode Materials for Lib by Electrodeposition. *Journal of Materials Chemistry A* **2014**, *2*, 883-896.

280.Momma, T.; Aoki, S.; Nara, H.; Yokoshima, T.; Osaka, T., Electrodeposited Novel Highly Durable Sioc Composite Anode for Li Battery above Several Thousands of Cycles. *Electrochem. Commun.* **2011**, *13*, 969-972.

281.Nara, H.; Yokoshima, T.; Momma, T.; Osaka, T., Highly Durable Sioc Composite Anode Prepared by Electrodeposition for Lithium Secondary Batteries. *Energy & Environmental Science* **2012**, *5*, 6500-6505.

282.Nara, H.; Yokoshima, T.; Otaki, M.; Momma, T.; Osaka, T., Structural Analysis of Highly-Durable Sioc Composite Anode Prepared by Electrodeposition for Lithium Secondary Batteries. *Electrochimica Acta* **2013**, *110*, 403-410.

283.Mayers, M. Z.; Kaminski, J. W.; Miller, T. F., Suppression of Dendrite Formation Via Pulse Charging in Rechargeable Lithium Metal Batteries. *The Journal of Physical Chemistry C* **2012**, *116*, 26214-26221.

284.Choo, R. T. C.; Toguri, J. M.; El-Sherik, A. M.; Erb, U., Mass Transfer and Electrocrystallization Analyses of Nanocrystalline Nickel Production by Pulse Plating. *Journal of Applied Electrochemistry* **1995**, *25*, 384-403.

285.Ibl, N., Some Theoretical Aspects of Pulse Electrolysis. *Surface Technology* **1980**, *10*, 81-104.

286.Richoux, V.; Diliberto, S.; Boulanger, C.; Lecuire, J. M., Pulsed Electrodeposition of Bismuth Telluride Films: Influence of Pulse Parameters over Nucleation and Morphology. *Electrochimica Acta* **2007**, *52*, 3053-3060.

287.Shanthi, C.; Barathan, S.; Jaiswal, R.; Arunachalam, R. M.; Mohan, S., The Effect of Pulse Parameters in Electro Deposition of Silver Alloy. *Mater Lett* **2008**, *62*, 4519-4521.

288.Maranchi, J. P.; Hepp, A. F.; Evans, A. G.; Nuhfer, N. T.; Kumta, P. N., Interfacial Properties of the a-Si/Cu : Active-Inactive Thin-Film Anode System for Lithium-Ion Batteries. *Journal of the Electrochemical Society* **2006**, *153*, A1246-A1253.

289.Pal, S.; Damle, S. S.; Patel, S. H.; Datta, M. K.; Kumta, P. N.; Maiti, S., Modeling the Delamination of Amorphous-Silicon Thin Film Anode for Lithium-Ion Battery. *Journal of Power Sources* **2014**, *246*, 149-159.

290.Iwamura, S.; Nishihara, H.; Ono, Y.; Morito, H.; Yamane, H.; Nara, H.; Osaka, T.; Kyotani, T., Li-Rich Li-Si Alloy as a Lithium-Containing Negative Electrode Material Towards High Energy Lithium-Ion Batteries. *Scientific Reports* **2015**, *5*.

291.Agarwala, R. C.; Agarwala, V., Electroless Alloy/Composite Coatings: A Review. *Sadhana* **2003**, *28*, 475-493.

292.Epur, R.; Ramanathan, M.; Datta, M. K.; Hong, D. H.; Jampani, P. H.; Gattu, B.; Kumta, P. N., Scribable Multi-Walled Carbon Nanotube-Silicon Nanocomposites: A Viable Lithium-Ion Battery System. *Nanoscale* **2015**, *7*, 3504-3510.

293.Gattu, B.; Epur, R.; Shanti, P. M.; Jampani, P. H.; Kuruba, R.; Datta, M. K.; Manivannan, A.; Kumta, P. N., Pulsed Current Electrodeposition of Silicon Thin Films Anodes for Lithium Ion Battery Applications. *Inorganics* **2017**, *5*.

294.Yan, K.; Lu, Z. D.; Lee, H. W.; Xiong, F.; Hsu, P. C.; Li, Y. Z.; Zhao, J.; Chu, S.; Cui, Y., Selective Deposition and Stable Encapsulation of Lithium through Heterogeneous Seeded Growth. *Nat Energy* **2016**, *1*.

295.Najim, M.; Modi, G.; Mishra, Y. K.; Adelung, R.; Singh, D.; Agarwala, V., Ultra-Wide Bandwidth with Enhanced Microwave Absorption of Electroless Ni-P Coated Tetrapod-Shaped Zno Nano- and Microstructures. *Physical Chemistry Chemical Physics* **2015**, *17*, 22923-22933.

296.Sharma, S. B.; Agarwala, R. C.; Agarwala, V.; Satyanarayana, K. G., Development of Electroless Composite Coatings by Using in-Situ Co-Precipitation Followed by Co-Deposition Process. *Metall Mater Trans B* **2005**, *36*, 23-31.

297.Sepahvand, S.; Safaei, P.; Sanaee, Z., Growth of Carbon Nano Tubes on Copper Substrate Suitable for Lithium Ion Battery Anode. *Procedia Materials Science* **2015**, *11*, 634-638.

298.DiLeo, R. A.; Landi, B. J.; Raffaelle, R. P., Purity Assessment of Multiwalled Carbon Nanotubes by Raman Spectroscopy. *Journal of Applied Physics* **2007**, *101*.

299.Dresselhaus, M. S.; Dresselhaus, G.; Saito, R.; Jorio, A., Raman Spectroscopy of Carbon Nanotubes. *Phys Rep* **2005**, *409*, 47-99.

300.Puech, P.; Nanot, S.; Raquet, B.; Broto, J. M.; Millot, M.; Anwar, A. W.; Flahaut, E.; Bacsa, W., Comparative Raman Spectroscopy of Individual and Bundled Double Wall Carbon Nanotubes. *Phys Status Solidi B* **2011**, *248*, 974-979.

301.Shang, N. G.; Silva, S. R. P.; Jiang, X.; Papakonstantinou, P., Directly Observable G Band Splitting in Raman Spectra from Individual Tubular Graphite Cones. *Carbon* **2011**, *49*, 3048-3054.

302.Gattu, B.; Epur, R.; Jampani, P. H.; Kuruba, R.; Datta, M. K.; Kumta, P. N., Silicon-Carbon Core-Shell Hollow Nanotubular Configuration High-Performance Lithium-Ion Anodes. *Journal of Physical Chemistry C* **2017**, *121*, 9662-9671.

303.Gattu, B.; Jampani, P. H.; Datta, M. K.; Kuruba, R.; Kumta, P. N., Water-Soluble-Template-Derived Nanoscale Silicon Nanoflake and Nano-Rod Morphologies: Stable Architectures for Lithium-Ion Battery Anodes. *Nano Res* **2017**, *10*, 4284-4297.

304.Wang, W.; Favors, Z.; Ionescu, R.; Ye, R.; Bay, H. H.; Ozkan, M.; Ozkan, C. S., Monodisperse Porous Silicon Spheres as Anode Materials for Lithium Ion Batteries. *Scientific Reports* **2015**, *5*.

305.Zhao, J.; Yin, H. Y.; Lim, T. H.; Xie, H. W.; Hsu, H. Y.; Forouzan, F.; Bard, A. J., Electrodeposition of Photoactive Silicon Films for Low-Cost Solar Cells. *Journal of the Electrochemical Society* **2016**, *163*, D506-D514.

306.Grimes, S. A.; Cowley, A. H.; Bard, A. J.; Cho, S., Electrodeposition of Silicon in a Phosphonium Ionic Liquid. *Abstr Pap Am Chem S* **2012**, *243*.

307.Cho, S. K.; Fan, F. R. F.; Bard, A. J., Electrodeposition of Crystalline and Photoactive Silicon Directly from Silicon Dioxide Nanoparticles in Molten Cacl2. *Angew. Chem.-Int. Edit.* **2012**, *51*, 12740-12744.

308.Seko, S.; Nara, H.; Jeong, M.; Yokoshima, T.; Momma, T.; Osaka, T., Carbonate-Based Additive for Improvement of Cycle Durability of Electrodeposited Si-O-C Composite Anode in Glyme-Based Ionic Liquid Electrolyte for Use in Lithium Secondary Batteries. *Electrochimica Acta* **2017**, *243*, 65-71.

309.Baraton, L.; He, Z. B.; Lee, C. S.; Cojocaru, C. S.; Chatelet, M.; Maurice, J. L.; Lee, Y. H.; Pribat, D., On the Mechanisms of Precipitation of Graphene on Nickel Thin Films. *Epl-Europhys Lett* **2011**, *96*.

310.Swartzendruber, L. J.; Itkin, V. P.; Alcock, C. B., The Fe-Ni (Iron-Nickel) System. *Journal of Phase Equilibria* **1991**, *12*, 288-312.

311.Lander, J. J.; Kern, H. E.; Beach, A. L., Solubility and Diffusion Coefficient of Carbon in Nickel - Reaction Rates of Nickel-Carbon Alloys with Barium Oxide. *Journal of Applied Physics* **1952**, *23*, 1305-1309.

312.Lopez, G. A.; Mittemeijer, E., The Solubility of C in Solid Cu. *Scripta Mater* **2004**, *51*, 1-5.

313.Dahal, A.; Batzill, M., Graphene-Nickel Interfaces: A Review. *Nanoscale* **2014**, *6*, 2548-2562.

314.von Goldbeck, O. K., Iron—Copper Fe—Cu. In *Iron—Binary Phase Diagrams*, von Goldbeck, O. K., Ed. Springer Berlin Heidelberg: Berlin, Heidelberg, 1982; pp 35-37.

315.Romig, A. D.; Goldstein, J. I., Determination of the Fe-Rich Portion of the Fe-Ni-C Phase Diagram. *Metallurgical Transactions A* **1978**, *9*, 1599-1609.

316.Raghavan, V., Cu-Fe-Ni (Copper-Iron-Nickel). *J. Phase Equilib. Diffus.* **2012**, *33*, 232-235.

317.Xiong, W., et al., Solid-State Graphene Formation Via a Nickel Carbide Intermediate Phase. *Rsc Advances* **2015**, *5*, 99037-99043.